Inverter Reactive Power Control for the Integration of Distributed Generation

Matthew Deakin

Christ Church

University of Oxford

A thesis submitted for the degree of

Doctor of Philosophy

October 2019

Abstract

This thesis sets out to answer the following question:

To what extent can inverter reactive power control, combined with voltage regulators, increase network efficiency and hosting capacity of distributed generation?

The first part of this thesis is concerned with analytic methods for studying this question; therefore, a two-bus network model is used. Two aspects of the problem are considered using this model. Firstly, the maximum power transfer capabilities of distributed generation are considered. This bounds the maximum generation of a network, even if the marginal costs of both real and reactive power are zero. It is shown that losses caused by the reactive power and generation result in maximum power transfer before stability limits, in networks with high impedance (R/X) ratios.

Secondly, analytic bounds on a proposed 'relative energy loss fraction' are derived in closed form, using the LinDistFlow approximate solution. The bounds are validated by comparison with both the exact solution of the two-bus equations, and on a set of unbalanced distribution networks. The relative energy loss fraction was found to be as high as 30%, with the approximate bounds able to estimate the true bounds to within 5%.

The next part of this thesis studies how reactive power and taps can be used to increase hosting capacity under uncertainty in the locations and sizes of domestic generation. A linear method is proposed that is shown to reduce the computing runtime by as much as 1000 times. A proposed hosting capacity sensitivity is shown empirically to correlate well with the error caused by linearization. Centralised control of taps and regulators are shown to increase hosting capacity by as much as 70%.

Finally, an optimization is proposed to study the impact of taps and domestic inverter control on the feeder total power draw. The use of regulator control in isolation results in benefits of up to a 5% reduction in feeder power; the use of inverter reactive power control further reduces the feeder power by up to 0.5% of the load. A control scheme is proposed with a reduced communications overhead, which can obtain up to 97% of the potential benefits of full inverter control.

Acknowledgements

My gratitude first extends to my supervisor Professor Malcolm McCulloch for his guidance and support throughout my time at Oxford, and for the freedom he gave me to pursue my interests. I would like to particularly thank Dr Thomas Morstyn, who has always been available to provide a critical ear, and to my collaborators and colleagues Dr Dimitra Apostolopoulou and Constance Crozier, with whom I have had many fruitful discussions. All of these people have put in many hours of work to help me develop as a researcher, and for that I am very grateful.

My thanks also extend to my examiners, Professor Dan Rogers and Professor Andrew Keane, whose time and helpful comments helped to refine those parts of this thesis that required clarification.

This work was funded by the Clarendon Scholarship, with contributions from Oxford University Press, Sir John Aird and Christ Church. Without the generosity of this fund this work would not have been possible.

I am indebted to the many friends and colleagues from EPG who have supported me by providing feedback on my work, including Fili, Gwilym, Liyang, Jorn, Stratos, Ren, Pete, and Andreas. Particular thanks go to Dr Anna Clements, from whom I learned of the importance of teamwork in challenging situations.

I would also like to thank Dr Jouni Peppanen and Dr Miguel Hernandez, from whom I learned a huge amount during my internship at EPRI in 2018; and Dr Frank Johnson, who inspired the work that became the first chapter of this thesis, and has provided guidance throughout my engineering career. Of course, thank you to all my friends at Christ Church and the wider university with whom I shared this second half of my time at Oxford, who all made the PhD such an enjoyable time.

Finally, I am grateful for the love and support of my family. My parents Ralph and Sarah have supported me in so many ways through all of my studies. My partner Bel has helped me through many hours of work that have gone into this D. Phil, particularly in the past year. Without Bel's support I would not have got to where I am now.

Contents

1 Introduction **1**
- 1.1 Motivation: Distributed Energy Resources and Decarbonization . . . 2
  - 1.1.1 The Transition from DNO to DSO . . . 3
- 1.2 Opportunities and Challenges in the Integration of Distributed Energy Resources . . . 4
  - 1.2.1 Losses in Distribution Networks . . . 4
  - 1.2.2 Increasing the Hosting Capacity of Distribution Networks . . . 5
  - 1.2.3 Increasing the Efficiency of Loads . . . 7
- 1.3 Inverter Reactive Power for DG Integration . . . 7
  - 1.3.1 Studying the Properties of Reactive Power Control in Distribution Networks . . . 8
  - 1.3.2 Reasons for Considering Computational Complexity . . . 9
  - 1.3.3 Research Scope . . . 10
- 1.4 Thesis Roadmap . . . 12
- 1.5 Main Contributions . . . 12

2 Literature Review **15**
- 2.1 DER Reactive Power Control and Losses . . . 16
  - 2.1.1 Losses and Increasing Hosting Capacity with Reactive Power . 16
  - 2.1.2 State of the Art: Impacts of DG Reactive Power Control on Losses and Curtailment . . . 20
  - 2.1.3 Gap Analysis: Reactive Power Control, Losses and Curtailment 21
- 2.2 Stochastic Hosting Capacity considering Reactive Power Control . . . 22
  - 2.2.1 State of the Art: Stochastic Hosting Capacity Network Analysis 23
  - 2.2.2 Gap Analysis: Stochastic Hosting Capacity Methods . . . 26
- 2.3 Domestic Inverter Reactive Power Control for Volt-Var Control . . . 27
  - 2.3.1 Optimization via Conservation Voltage Reduction . . . 27
  - 2.3.2 State of the Art: Volt-Var Control Considering Inverter Control 28
  - 2.3.3 Gap Analysis: Volt-Var Control . . . 31
- 2.4 Review of Linearization Methods in Multiphase Networks . . . 31
  - 2.4.1 Multiphase Network Model . . . 32
  - 2.4.2 Multiphase Network Linear Models . . . 34
- 2.5 Distribution Network Case Studies . . . 36
  - 2.5.1 The EPRI K1 Circuit . . . 38

3 Methods for Characterising Impacts of Reactive Power Control on Curtailment and Losses **40**
3.1 Two-Bus Load Flow in Distribution Networks 42
3.1.1 The Two-Bus Network Model 43
3.1.2 Two-Bus Load Flow Solutions 44
3.2 Maximum Power Transfer in the Two-Bus Network 45
3.2.1 Heuristics for Maximum Power Transfer 45
3.2.2 Voltage Constrained Maximum Power Transfer 47
3.3 Converting Distribution Network Models to Two-Bus Representations 52
3.3.1 Calculating Line Impedance Z 52
3.3.2 Two-Bus Network Voltages 54
3.3.3 Calculating the Line Power S_{Snd} 54
3.4 Maximum Power Transfer Case Studies 55
3.4.1 Case Study Network 56
3.5 Relative Loss Fractions Considering Voltage Control 60
3.5.1 Reactive Power and Reducing Energy Curtailment 60
3.5.2 The Relative Loss Fraction 61
3.6 Two-Bus Relative Loss Fraction Bounds 63
3.6.1 Generator Control 64
3.6.2 Relative Loss Fraction Bounds Using LinDistFlow 65
3.6.3 Comparing Exact and LinDistFlow Relative Loss Fractions . . 69
3.7 Case Studies 74
3.7.1 Case Study Setup 76
3.7.2 Case Study Example: IEEE 34 Bus, Study A 78
3.7.3 Results of Case Studies 80
3.8 Summary 83

4 Linear Methods for Calculating Stochastic Hosting Capacity **87**
4.1 Stochastic Hosting Capacity Analysis 89
4.1.1 Hosting Capacity Curves and Quantiles 89
4.1.2 Hosting Capacity Parameters 92
4.1.3 Hosting Capacity Constraints 93
4.1.4 Calculating Stochastic Hosting Capacity 94
4.2 Linear Models for Hosting Capacity Analysis 97
4.2.1 Linear Network Model and RLF Model 97
4.2.2 Linear Load Flow with Taps 100
4.2.3 Linear Regulated Load Flow Model (Local Control) 101
4.2.4 Linear DERMS model (Centralised Control) 106
4.3 Regulated Load Flow Model Stochastic Analysis 107
4.3.1 Characterisation of Bus Power Injections 107
4.3.2 Voltage Mean and Covariance 108
4.3.3 Properties of Voltage Statistics 110
4.3.4 Network Preconditioning 112
4.3.5 Geographic Bus Vulnerability 116
4.4 Stochastic Hosting Capacity Curve Case Studies 116

4.4.1 Problem Setup . . . 118
4.4.2 Regulated Load Flow Model Hosting Capacity Analysis 118
4.4.3 Comparing Centralised (DERMS) and Local (Regulated Load Flow) Control . . . 122
4.5 Calculating Stochastic Hosting Capacity Quantile Values 124
4.5.1 Calculating Hosting Capacity Quantiles . . . 125
4.6 Hosting Capacity Quantiles: Case Studies . . . 127
4.6.1 Problem Size and Method Effectiveness . . . 128
4.6.2 Stochastic Hosting Capacity Variation with Penetration 129
4.7 Summary . . . 133

5 Inverter Reactive Power Control for Minimization of Total Feeder Power 135
5.1 Minimizing Operating Costs using Inverters and Taps 137
5.1.1 Conservation Voltage Reduction Load Models 138
5.1.2 Conservation Voltage Reduction: A Two-Bus Example 139
5.1.3 Case Studies . . . 140
5.2 Modelling a Network with Smart Inverters and Voltage-Sensitive Loads 142
5.2.1 Load Flow Considering Voltage Sensitive Loads 142
5.2.2 Linear Load Model . . . 145
5.2.3 Linear Model of Branch Currents . . . 146
5.2.4 Real Power Loss Quadratic Model . . . 149
5.2.5 Inverter Model . . . 150
5.2.6 Optimization Formulation . . . 153
5.3 Necessity of Load and Inverter Losses in QCQP Cost Function 156
5.3.1 Unconstrained Optimization Solution . . . 156
5.3.2 Inverter Losses in the Unconstrained QP . . . 158
5.3.3 Impact of Load Model . . . 164
5.4 Constrained Optimization: Case Studies . . . 166
5.4.1 Preliminary Case Study: IEEE 123 Bus . . . 168
5.4.2 Results Across Feeders . . . 171
5.4.3 Sensitivity Analysis . . . 174
5.4.4 Time Series Analysis using Phase Control 176
5.5 Summary . . . 184

6 Conclusion 186
6.1 Conclusion of Research Questions . . . 186
6.1.1 Conclusions of Thesis Research Question . . . 191
6.2 Future Work . . . 193
6.2.1 Losses and Curtailment: Distributed Droop Control 193
6.2.2 Stochastic Hosting Capacity: Load Flow Calculation Errors . 193
6.2.3 Stochastic Hosting Capacity: Robustness to Tap Bandwidth and Load Uncertainty . . . 194
6.2.4 Volt-Var control: Value Stacking . . . 194

A Derivations and Supporting Results **196**
A.1 Two-Bus Derivations (Chapter 3) 196
A.1.1 Two-bus Load Flow Solution 196
A.1.2 Power at the Stability Boundary 197
A.1.3 Derivation of Maximum Power Transfer 198
A.1.4 Upper and Lower Bounds of Relative Loss Significance 198
A.1.5 LinDistFlow Relative Loss Fractions 200
A.1.6 Loss-Minimizing Two-Bus Reactive Power 200
A.1.7 The Loss-Voltage Crossover Point 201
A.1.8 Inclusion of Voltage Regulators in the Two-Bus Model 201
A.2 Fixed Point Linearization: Validation and Computational Complexity (Chapter 4) 204
A.2.1 Validation of Load Flow Linearization 204
A.2.2 Complexity of Linearization 205
A.3 The Semidefiniteness of Quadratic Models in Losses (Chapter 5) . . . 206
A.3.1 Physical Basis for Semidefinite Quadratic Loss Matrix 206
A.3.2 Minimum Singular Values for Asymptotic Analysis of Indefinite Systems 207
A.3.3 Divergence of Neumann Series for Positive Definite Symmetric Matrices 208

Bibliography **210**

List of Figures

2.1 The two-bus model 17
2.2 A 'spy' plot of admittance matrix sparsity patterns, with i, j indicated with a dot if there is a non-zero matrix element. This demonstrates (i) relatively high levels of sparsity, (ii) a block-like structure, and (iii) symmetry in the sparsity pattern. 34
2.3 The EPRI K1 feeder 38

3.1 Two-bus power flow model (sign convention as indicated). 43
3.2 Comparison of heuristic methods and the marginal loss-induced maximum power $P_{\text{Snd, MPT}}$. Parameters are set as $V_{\text{Rcv}} = 1.0, V_+ = 1.05, |Z| = 1$. Powers calculated with the true maximum power transfer values (3.15) are denoted by $(\cdot)_{\text{MPT}}$; powers calculated using unity power factor control (3.11) are denoted $(\cdot)_{\text{UPF}}$; powers calculated at the stability boundary (3.10) are denoted $(\cdot)_{\text{Stb}}$, ... 49
3.3 Performance metrics at the loss-induced maximum power transfer point, with $V_+ = 1$. (a) Thermal efficiency (zero if positive real power cannot be transferred). (b) Power factor of the generator. 51
3.4 Two-bus power flow model considering a generator located within a distribution network. Two-bus parameters match the parameters described in the previous section. The additional parameters N_{reg}, S_{lds} model regulator taps and the network load respectively. 52
3.5 Boxplot of the positive sequence R/X ratios λ at all three-phase buses of a set of feeders, by calculating the equivalent Thévenin impedance to the voltage source. 53
3.6 IEEE 34 Bus test distribution feeder and buses considered for case studies. 56
3.7 P_{gen} versus network power received at the substation P_{Rcv}. 57
3.8 Phase current and reactive power flows at bus 834 versus generated power P_{gen}. The maximum power transfer point is reached prior to the current limit in this case. 58
3.9 The marginal and thermal induced power transfer limits for four buses of the IEEE 34 Bus network. $S_{\text{base}} = 2.5$ MVA. 59
3.10 Increasing the reactive power available to a generator can reduce the curtailment, by increasing the maximum real power that can be generated from the base case, $\mathring{P}_{\text{gen}}^{\text{base}}$, to the change case, $\mathring{P}_{\text{gen}}^{\text{chng}}$, yielding additional generated energy ΔE_{gen}. 61

3.11 Operating characteristic (3.41) with respect to the generated power P_{Snd}, Q_{Snd} 64
3.12 Calculations of the initial load compensated relative loss fraction $\epsilon_{\text{P}}^{\text{X}}$. In (a) the values are calculated using the Exact load flow solution; in (b) the values are calculated using the LinDistFlow solution; in (c) the absolute error between these two solutions is plotted. 72
3.13 Calculations of the initial relative loss fraction $\epsilon_{\text{P}}^{\text{init}}$ as a function of reactive power. In (a) the values are calculated using the Exact load flow solution; in (b) the values are calculated using the LinDistFlow solution; in (c) the absolute error between these two solutions is plotted. 73
3.14 Calculations of the initial value of the relative loss fraction 20% between the UPF and MPT control points (as described in Section 3.6.3.2). In (a) the values are calculated using the Exact load flow solution; in (b) the values are calculated using the LinDistFlow solution; in (c) the absolute error between these two solutions is plotted. 75
3.15 Voltages (left) and powers (right) for Study A. The 'base' case (subfigure (a) and (b)) has a reactive power limit $Q_{-}^{\text{base}} = 0$ kVAr, whilst the 'change' case (subfigure (c) and (d)) has the limit $Q_{-}^{\text{chng}} = -400$ kVAr. This leads to an increase in losses; plotting the relative power loss fraction ϵ_{P} illustrates that this reduces the efficacy of reactive power by 8-14% (subfigure (e)). Note that 'base' and 'change' case min/max/gen voltages do not change much from subfigure (b) to (d) as reactive power control (i.e., voltage control) acts to maintain voltages at a constant level. 79
3.16 Histogram of the relative power loss fraction values for Studies A, C, D and F. The three sets of dashed vertical lines correspond to three load weightings (as described in Section 3.7.2). 82

4.1 A stochastic hosting capacity curve. In this curve the stochastic hosting capacity 50%-quantile, $p^{50\%}$, occurs at a penetration level of 60%. 91
4.2 The linearization point for the linear model is found by identifying the maximum linearly scaled load point at which a constraint is violated (i.e. by multiplying all loads by a loading factor). In this figure, the maximum and minimum voltages on both the MV and LV nodes of the EPRI K1 feeder are plotted with the loading point. In this network (EPRI K1) the linearization scaling factor is at -0.72, as an LV upper voltage constraint is violated at this point. 101
4.3 Calculated errors for the IEEE 123 bus network in aggregate (a) and at individual loading points (b). 105
4.4 Saturation limits the region of validity for the IEEE 34 bus network. . 105
4.5 Solar PV sizes for this chapter are modelled as a gamma distribution, fitted to California residential solar data [1]. The scale parameter of 1.261 kW and shape parameter with value 4.214 was chosen using maximum likelihood estimation [2]. 107

4.6 Visualization of the variance (a) and correlation matrix (b) of the linear model for EPRI's 'Circuit 5'. It is observed that the variance changes by several orders of magnitude between the most and least sensitive bus, and that there is significant correlation between buses. 111
4.7 The indices that sort the number of standard deviations in increasing order with respect to the number of standard deviations to a constraint. Two values are plotted: the index at 0% penetration, and the index at 100% penetration. Orange points indicate that the mean voltage is outside of a constraint at the 100% penetration point. This figure demonstrates that strong buses remain strong (i.e. that there is a collection of indexes in the upper right in each of these figures). . . . 112
4.8 The use of preconditioning reduces the time for the linear model to solve by reducing the number of calculations required. The worst-case error (across nine networks) increases rapidly below a cutoff of 70%, and for a correlation cutoff below 98%. 114
4.9 The use of preconditioning reduces the time for the linear model to solve by reducing the number of calculations required. The worst-case error (across nine networks) increases rapidly below a cutoff of 70%, and for a correlation cutoff below 98%. 115
4.10 Number of standard deviations from the voltage mean to a constraint, for EPRI Ckt. 24, at 90% PV penetration. Negative values indicate the mean voltage is outside a constraint; grey values indicate the distance is greater than six standard deviations. At three-phase buses, the minimum number of standard deviations (i.e., the 'brightest colour') is plotted. 117
4.11 Stochastic hosting capacity for Circuit J1; both the overall hosting capacity (upper) and four of nine individual constraints are plotted (lower). The solid lines denote linear model approximation and the dashed lines the non-linear OpenDSS solution. 119
4.12 Box and whisker plot of the stochastic hosting capacity f_{Pen} (4.8) as calculated by OpenDSS and the regulated load flow model (4.26). The 0% and 100% hosting capacity values are plotted as triangles; the box-and-whisker plots the 5%, 25%, 50%, 75% and 95% values of f_{Pen}. A conservative estimate for f_{Pen} can be found using the linear model by increasing the generator sizing by 10% ($\hat{f}_{\text{Pen}}^{100\%}$). 120
4.13 There is a strong correlation between the hosting capacity sensitivity $f_{\text{Pen,S}}$ (calculated as in (4.7)) and the MAE of the linear (RLF) model with respect to the non-linear OpenDSS (DSS) solution. The small dots denote one Monte Carlo set (of which there are five for each network), and the cross denotes the mean MAE and hosting capacity sensitivity $f_{\text{Pen,S}}$. The Pearson correlation coefficient for the mean values is 0.878. 121
4.14 The hosting capacity curve for Circuit J1 changes significantly if generator power factors are reduced to 0.95 inductive (upper), and the impact on individual constraints (lower). 123

4.15 Hosting capacity curves for the centralised (DERMS) control and regulated load flow (RLF) curves. DERMS control with both reactive power (Q) and tap (T) control increases the hosting capacity the most. 124
4.16 A comparison between traditional, local control (regulated load flow, RLF) and centralised (DERMS) control for four networks. The benefits of centralised control vary significantly between circuits. 124
4.17 The fixed-power hosting capacity method (l), and the fixed-voltage hosting capcity method (r). Enforcing the constraint in the fixed-voltage method reduces the number of scenarios required for the same accuracy. 127
4.18 Boxplot of the total generation P_{PV} (a) and power per generator P_{gen} (b) as a function of the penetration for the EU LV feeder. 130
4.19 Boxplot of the total generation P_{PV} (a) and power per generator P_{gen} (b) as a function of the penetration for the EPRI K1 circuit. 130
4.20 Boxplot of the total generation P_{PV} (a) and power per generator P_{gen} (b) as a function of the penetration for the IEEE 8500 Node circuit. . 131

5.1 The two-bus model, assuming controls in the reactive power Q and regulator turns ratio T (the turns ratio is modifiable by a tap changer). The load P_{lds} is a function of the voltage magnitude at that point V_{lds}. 139
5.2 The Augmented EU LV (EULVa) network has 4 feeders connected to the same secondary substation; the EU LV network is to the Southeast of the substation. 142
5.3 The load variation in with reactive power injections, due to voltage sensitivity. The OpenDSS model ('DSS') uses the full exponential model as solved by the full non-linear load flow equations, whilst the linear model linearizes both the exponential load model and the voltage magnitudes assuming constant injections. 147
5.4 The Taylor-series based linear model leads to an excellent prediction of the voltage sensitivity around the linearization point, for both constant power loads and voltage sensitive loads. 147
5.5 A comparison between the current magnitudes as calculated in OpenDSS and for two linear models. The first linear model 'Lin. clx.' calculates the complex current as a linear function of the control vector, whilst the second 'Lin. mag.' calculates the linear current magnitude directly from the control vector, showing much worse performance. The complex model is much more accurate than the model in magnitudes for reactive power (a, b); either model was found to be acceptable for calculating the change in current with taps (c). 148
5.6 The losses as calculated by OpenDSS and the quadratic loss model, demonstrating that the model predicts loss characteristics of the circuit well. 150
5.7 Inverter loss and throughput as a function of the power through the inverter. 151
5.8 Inverter capability chart, for reactive power cutoff value $\alpha_{\mathrm{invr}} = 0.6$. . 152

5.9 The voltages and currents at the solution of the unconstrained quadratic program for the EPRI 5 Circuit. 157
5.10 Varying the inverter loss coefficient c_R changes the solution $x^{\dagger}_{\mathrm{Q,\,Unc}}$ significantly (plotted here is the augmented EU LV (a) and 123 Bus circuit (b) networks at 100% load). The two lines associated with each inverter size correspond to 'high' and 'low' calculations of the inverter loss coefficient c_R (these values vary with inverter size, as discussed in Section 5.2.5). 159
5.11 Varying the inverter loss coefficient changes the unconstrained solution $x^{\dagger}$ significantly (plotted here is EPRI Circuit 5 at 100% load). The 'true' solution is found by solving (5.25), whilst the asymptotic approximations are found by considering the first term of the Neumann series of (5.28) and (5.29) (as in (5.35)). The singular values are of the matrix $\Theta_{\mathrm{Q,\,lss,\,ntwk}}$ and the 95% cutoff values (whereby the solution has changed by 5% from it's nominal value) are found using the asymptotic approximation (5.35). 163
5.12 The quadratic program linear sensitivity for the EPRI K1 and EULVa network, at 100% load, with load voltage sensitivity $\alpha_{\mathrm{CVR}} = 0.6$. . . . 165
5.13 Solution of the 123 Bus circuit in terms of (a) voltages and (b) the optimal control solution. Three sets of voltages are plotted: the voltages according the the MI-QCQP solution (the 'QP Sln.'), with voltages as calculated using the MI-QCQP model; the solution prior to either tap or reactive power control ('Nom. Sln'); and, the solution in OpenDSS when optimal reactive power and taps are applied ('DSS. Sln'). The controls (b) are decomposed into reactive power (in terms of phase A, B, or C), and the tap. $\pm$100% represents the maximum and minimum values of each control. 168
5.14 Daisy plot of the optimal control for the IEEE 123 Bus feeder, minimizing the operating cost. Each hexagon represents an inverter, with tick angles at 0°, 120°, 240° representing phase A, B and C respectively; red marks indicate a regulator. There is a strong correlation between the optimal inverters control points and the phase information, suggesting that control on a per-phase basis could perform well. 169
5.15 The total feeder power P_{feeder} at the optimal point $x^{\dagger}$ under different control schemes, compared to the solution with no control $P_{\mathrm{feeder}}(0)$. . 170
5.16 The solution error for the 123 Bus test feeder in voltages and currents, demonstrating a very good fit between the changes predicted by the linear model and the true solution from OpenDSS. 171
5.17 The total feeder power P_{feeder} at the optimal point $x^{\dagger}$ under different control schemes, compared to the nominal solution with no control $P_{\mathrm{feeder}}(0)$, across all feeders, at 100% load. The first four circuits have no regulators ('No regs.') whilst the three final circuits have at least one regulator each ('With regs.') 172
5.18 Powers, voltages, benefits (in power) and phase control points for July and October days for EPRI Circuit 5. 178

5.19 Control efficacy for October and July days for EPRI Circuit 5. 180
5.20 Powers, voltages, benefits (in power) and phase control points for July and October days for the EPRI K1 circuit. 181
5.21 Tap position and control efficacy for October and July days for the EPRI K1 circuit. 182

A.1 The 'True' and 'Proposed' two-bus models with regulators the latter approximates the former by moving the regulator to the generator. The 'Base' model is the same as the 'Proposed' model but with the turns ratio set to unity, i.e., $\epsilon_N = 1$ 201
A.2 IEEE 37 Bus network case study. 204
A.3 Singular value decomposition of the 34 Bus networks, demonstrating the singular value corresponds to two buses that contain a combination of three-phase wye- and delta- connected loads. 207

List of Tables

1.1 Questions that can be considered a part of hosting capacity analysis (adapted from [3]). 6
1.2 Perception of system response times by users (adapted from [4, Ch. 5.5]). 10

2.1 The circuits studied in this thesis and the chapters in which they appear. 'Regs.' refers to the number of regulator controls for a given feeder (including load tap changers at primary substations). 39

3.1 Network Parameters (pu). $S_{\text{base}} = 2.5$ MVA, $V_{\text{base}} = 69$ kV. 56
3.2 Two-Bus properties of buses used in case studies D-F. The base voltages are 0.416, 13.2 kV and the power bases are 800, 12000 kVA for the EU LV and EPRI K1 circuits, respectively. 75
3.3 Generator sizes and operational constraints for all six case studies. . . 77
3.4 Voltage regulator parameters for the 34 Bus circuit (units as in OpenDSS). 78
3.5 Generation and losses for each case study. From these the corresponding relative energy loss fraction ϵ_{E} is also calculated (from (3.30b)). . 81
3.6 Predicted (two-bus) and actual (OpenDSS) relative power loss fraction bounds. The two-bus values are based on the LinDistFlow load flow solution. 84

4.1 Descriptor of vector/matrix linear multiplication operations implemented in BLAS [5], with α, β as scalars, x, y as vectors and A, B, C as full matrices and T as a triangular matrix. Matrices and vectors are assumed to be dimensioned according to n. 95
4.2 Comparison of the solutions of the regulated load flow (RLF) and OpenDSS (DSS) models; and, comparing two Monte Carlo runs RLF (i)–(ii), by calculating the MAE between them. 121
4.3 Estimated hosting capacity and error for two monte carlo runs ($N_{\text{MC}} = 1000$, $\alpha_{\text{PV}} = 50\%$) 128
4.4 Comparison of timings and estimated hosting capacities for the fixed power and fixed voltage methods 129
4.5 DG Policy Decisions, based on stochastic hosting capacity results. All powers are in kW per generator. 133

5.1 Qualitative operating zones for loss, load, and total feeder power minimization objectives. Key: ↑ (↓) – increase (decrease) the control variable; 0 – set to zero; × – no effect; ↑/↓ – positive or negative, depending on α_{CVR}. Double arrows (e.g. ⇊) indicate a strong effect, such that voltage constraints would likely be active at a solution. 140
5.2 Constraint extrema at the unconstrained optimization point $x^{\dagger}_{\text{Q, Unc}}$ (i.e. solved in reactive power only). **Bold** font indicates a constraint violation–four of the unconstrained problems are feasible, and constraint violations in the other circuits are not too great. This illustrates that the cost function will play a very important role in the global solution value of the QCQP, compared to if all problems were infeasible. 158
5.3 Minimum/maximum singular values of the network loss quadratic matrices $\Theta_{\text{Q, lss, ntwk}}$, and the estimate of the 95% inverter loss coefficient cutoff value. For values of the inverter loss coefficient c_R between 2 and 50 W/kVAr^2, inverter losses should always be taken into account, and network losses should usually be taken into account. 164
5.4 Summary of sensitivities to reactive power injections in load, loss, and the total for both of these combined. The angle θ_{ψ} is calculated between the load and loss sensitivity vectors; N_{Q} is the number of elements in the sensitivity vector ψ_{Q}. 166
5.5 Smart inverter benefits, as a % of load, compared to the Nominal control case (which only has tap controls activated, if there are any), calculated using the MI-QCQP model. With the exception of Network 10, the minimum ratio of phase to full load is 73%, and the maximum ratio of benefits is 98% 173
5.6 Maximum error across all three loading points (10%, 60%, 100%), when the optimal solution $x^{\dagger}$ is applied to both OpenDSS and the MI-QCQP model. Voltage, current and power errors are as calculated in (5.38a), (5.38b) and (5.38c). 174
5.7 Smart inverter load benefit (%) and efficacy (W/kVAr, defined in (5.23)). Values are as calculated using the MI-QCQP model. 175
5.8 Smart inverter load benefit (%) and efficacy (W/kVAr, defined in (5.23)) against α_{CVR}. Values are as calculated using the MI-QCQP model. 176

A.1 Sparsity properties of nine admittance matrices, and the corresponding time required to build the linear model, t_{Lin}. 205

Nomenclature

Acronyms

CVR	Conservation Voltage Reduction
DERMS	Distributed Energy Resource Management System
DG	Distributed Generation
DNO	Distribution Network Operator
DSO	Distribution System Operator
DSS	Distribution System Simulator
EPRI	Electric Power Research Institute
EV	Electric Vehicle
FOT	First Order Taylor
FPL	Fixed Point Linearization
LDF	LinDistFlow
LP	Linear Program
LV	Low Voltage ($\leq$ 1 kV Line-Neutral)
MI-QCQP	Mixed-Integer Quadratically Constrained Quadratic Program
MPT	Maximum Power Transfer
MV	Medium Voltage ($>$ 1 kV Line-Neutral)
PDF	Probability density function
pu	Per unit
PV	(Solar) Photovoltaic
QP	Quadratic Program

QSTS	Quasi-Static Time Series
RLF	Regulated Load Flow

Shared Notation: Operators

$(\cdot)^*$	Complex conjugate
$(\cdot)^{[i,j]}$	(i,j)th element (of a matrix)
$(\cdot)^{[i]}$	ith element (of a vector)
$(\cdot)^\intercal$	Matrix transpose
$(\cdot)_\Delta$	Associated with delta-connected loads (or generators)
$(\cdot)_\curlyvee$	Associated with wye-connected loads (or generators)
$\arg(\cdot)$	Complex argument
$\breve{(\cdot)}$	Associated with the linearization point
$\jmath$	The imaginary unit
$\mathbb{1}^\alpha$	Vector of all ones with dimension α
$\text{diag}(\cdot)$	Diagonal matrix with entries given by the vector argument *or* elements on the diagonal the matrix argument
$\text{nnz}(\cdot)$	Number of nonzero elements in matrix
$\Pr(\alpha \mid \beta)$	Probability of α given β.
$\Pr(\alpha)$	Probability of α
$\Re(\cdot)$, $\Im(\cdot)$	Real/imaginary part of an complex quantity

Shared Notation: Variables

$(\cdot)_+$, $(\cdot)_-$	Upper/lower constraint on a quantity
Λ	A diagonal matrix containing the ordered singular values
$a_{(\cdot)}$	Offset vector for linear model of complex voltages in power injections or taps
$b_{(\cdot)}$	Offset vector for linear model of voltage magnitudes in power injections or taps
$c_{(\cdot)}$	Offset vector for linear model of complex currents in power injections or taps

H_{Δ}	Wye-delta conversion matrix
I	Identity matrix
I_{bus}	Bus current injections, Amps (or %)
$K_{(\cdot)}$	Sensitivity matrix for linear model of voltage magnitudes in power injections or taps
$M_{(\cdot)}$	Sensitivity matrix for linear model of complex voltages in power injections or taps
$P_{(\cdot)}$	Real power, kW
P_{lss}	Real power losses
$Q_{(\cdot)}$	Reactive power, KVAr
$S_{(\cdot)}$	Complex power, kVA
$W_{(\cdot)}$	Sensitivity matrix for linear model of complex currents in power injections or taps
$Y_{(\cdot)}$	Admittance, Siemens
Y_{Branch}	Network branch (primitive) admittance matrix (Ohms)
Y_{bus}	Network bus admittance matrix, Siemens
$Z_{(\cdot)}$	Impedance, Ohms

Chapter 3

$(\cdot)^{[\text{case}]}$	Associated with either the 'base' or 'change' case
$(\cdot)^{\text{base}}$	Associated with the 'base' case
$(\cdot)^{\text{chng}}$	Associated with the 'change' case
$(\cdot)^{\text{init}}$	Initial (minimum) value
$(\cdot)^{\text{trml}}$	Terminal (maximum) value
$(\cdot)_{\text{gen}}$	Generated power
$(\cdot)_{\text{MPT}}$	Quantity at the Maximum Power Transfer point
$(\cdot)_{\text{net}}$	Net generated power (gen. less loss)
$(\cdot)_{\text{Rcv}}$	Two-bus 'receive' quantity
$(\cdot)_{\text{reg}}$	Regulator parameter

$(\cdot)_{\text{Snd}}$	Two-bus 'send' quantity
$(\cdot)_{\text{Stb}}$	Quantity at a stability-constrained point
$(\cdot)_{\text{UPF}}$	Quantity at a unity power factor point
ϵ_E	Relative energy loss fraction, %
ϵ_P	Relative power loss fraction, %
λ	R/X ratio of a line impedance
$\mathring{P}_{(\cdot)}^{[case]}$	Maximum real power point, constrained by a network constraint, kW
τ	Time, hr
$E_{(\cdot)}$	Total energy over some period, MWh
k_S	Two-bus load weighting
P_{ipt}	Generator power input (available power), kW
S_{SC}	Two-bus short circuit impedance
T_τ	Time period of interest, hr
Z_{bus}	Network impedance matrix, Ω

Chapter 4

$(\cdot)^{\text{LDC}}$	Line Drop Compensation Control Parameter
α_{PV}	Fraction of all load with PV connected, %
η_{Cor}	Correlation cutoff for removing rows during MC analysis
η_{Var}	Variance cutoff for removing rows during MC analysis
$\hat{f}_p$	Approx. hosting capacity curve, with respect to parameter p, calculated using Monte Carlo analysis and a linear load flow
$\hat{V}$	A known load flow solution, V
$\mu_{(\cdot)}$	Mean vector of a random variable
Ω	Monte Carlo scenario in the locations of PV
$\Sigma_{(\cdot)}$	Covariance matrix of a random variable
σ_γ	Variance of a gamma distribution
ζ_{Tol}	Bisection algorithm tolerance

f_{S}	Hosting capacity sensitivity to changes in generation
F_p	Hosting capacity curve with respect to parameter p
f_p	Approx. hosting capacity curve, with respect to parameter p, calculated using Monte Carlo analysis and a non-linear load flow
N_{MC}	Number of Monte Carlo runs
N_{Vltn}	Number of Monte Carlo runs with a violation
P_{PV}	Total power of all PV generation installed, kW

Chapter 5

$(\cdot)^{\dagger}$	Quantity at an optimal point
$(\cdot)_{\mathrm{invt}}$	Associated with an inverter
$(\cdot)_{\mathrm{ntwk}}$	Associated with the network
$(\cdot)_{\mathrm{QP}}$	Quantity calculated using the quadratic network model
α_{CVR}	Load CVR (voltage sensitivity) factor
$\psi_{(\cdot)}$	Linear vector of a quadratic program
$\rho_{(\cdot)}$	Constant term of a quadratic program
$\Theta_{(\cdot)}$	Quadratic matrix of a quadratic program
$c_{\mathrm{Turn,\,on}}$	Inverter turn on losses, W
c_R	Inverter quadratic loss coefficient, W/kVA^2
I_{rated}	Vector of transformer ratings, A
I_{xfmr}	Vector of transformer currents, A
M_{α}	Sensitivity matrix for linear model of load in power injections or taps
P_{feeder}	Total feeder power, W
S_{Rated}	Inverter apparent power rating, kVA

Chapter 1

Introduction

The main research question of this thesis is:

To what extent can inverter reactive power control, combined with voltage regulators, increase network efficiency and hosting capacity of distributed generation?

This topic is broken down further into three specific research topics as follows.

1. *How can the impact of inverter reactive power control on the efficiency of distributed generation be analytically characterised, considering power flow up to the maximum power transfer point?*

2. *How can the stochastic hosting capacity of a distribution network be calculated in a computationally efficient manner, considering voltage regulators and reactive power control from distributed generators?*

3. *How can the benefits of domestic-scale inverter reactive power control be evaluated with respect to minimising total power demand on a feeder, with load voltage sensitivity, inverter losses and distribution network losses taken into account?*

This chapter outlines the wider context and issues surrounding these questions, providing a basis for the research carried out through this thesis.

Chapter roadmap In Section 1.1, the motivation for the main research question is outlined, including a brief overview of the wider technological and regulatory challenges facing network operators. Following from this, Section 1.2 describes the opportunities for smart inverter control in this context. The research themes based on these opportunities are then discussed in Section 1.3, as well as covering the scope of the research undertaken. The structure of the rest of the thesis is given in Section 1.4. Finally, Section 1.5 summarises the key contributions to knowledge arising from this research.

1.1 Motivation: Distributed Energy Resources and Decarbonization

The International Renewable Energy Agency (IRENA) has identified three pillars for the decarbonization of the world's energy supply: an increase in electrification, energy efficiency, and renewable electricity generation capacity [6]. Distribution networks will be particularly affected by these targets–electrification of loads will increase demand in networks, whilst renewable generation is much more likely than traditional generation to be located in distribution networks. For example, in the UK, there is 40% more renewable generation (wind, solar and natural flow hydro) at the distribution level than the transmission level. For the case of solar, this is even more stark, with 89.9% of solar located in distribution networks [7].

Load-based distributed energy resources (DERs) such as electric vehicle chargers and heat pumps are often located in LV networks as they are generally installed directly at a consumer's property. On the other hand, the shift of generation from transmission to distribution networks is a significant change compared to how networks are traditionally operated. The reasons to locate small- or medium-scale generation in distribution networks are as follows:

- Although smaller assets may have higher costs associated with them, the financ-

ing and construction of these projects is easier as the ownership can be spread over many people and risks are therefore easier to manage [8, Ch. 1].

- If the generation profile of a generator correlates with the load profile, then line flows (and losses) are reduced, resulting in lower stress on network components [9]. This allows for the deferral of investment in assets, leading to savings.

- Controllable resources could empower consumers to become more engaged with energy systems, enabling them to collaborate and offer services that are more valuable than individually controlled assets [10].

Generators which are connected to a distribution network (rather than directly to a transmission network) are referred to as *distributed generators* (DGs)[1]. Various methods have been proposed to quantify the technical benefits of DG (e.g., [12, 13]).

This thesis is particularly focussed on the integration of solar photovoltaics (PV) in distribution networks. Solar PV is an interesting example of a DG, as the power ratings of these generators vary from a few kilowatts to tens of megawatts. For example, 93% of over one million PV plants in the UK have capacity less than 4 kW, yet 78% of the total capacity is medium- to large-scale (> 50 kW) [14]. This is similar to other power systems around the world [15]–in fact, rooftop PV is being mandated for all new buildings in some jurisdictions [16].

1.1.1 The Transition from DNO to DSO

Distribution networks have historically been operated with the 'fit-and-forget' approach, whereby assets are oversized to avoid later having to consider them which can lead to suboptimal solutions from a system-wide economic point of view (i.e., once long-term economic cost considerations are taken into account) [17]. Given the uptake of DG (and DERs more generally) in distribution networks, it has been recognised that the complexity of network management has increased. As such, governments and regulators have recognised that the traditional 'Distribution Network

[1]DGs are sometimes referred to as 'embedded generators' [11].

Operator' (DNO) must evolve; the new style of operator is often referred to as a 'Distribution System Operator' (DSO) [18], with it implicit that such an organisation will have additional responsibilities compared to DNOs.

The UK regulator Ofgem has identified that there are three main functions of traditional DNOs (network planning; monitoring active network management; and outage restoration and maintenance). The responsibilities of a DNO could increase from these three core functions to as many as nineteen with the transition to a DSO. Each of the new functions are categorised under the broader themes of markets, real-time processes (including operations), and long-term planning. All the research questions of this thesis are relevant to future DSO functionality, falling under categories of 'DER hosting capacity analysis', 'Supply of grid-operational services using DER assets' and 'DER net local value analysis' [19].

1.2 Opportunities and Challenges in the Integration of Distributed Energy Resources

There are a range of challenges faced by distribution networks in the integration of distributed energy resources. In [8], voltage magnitude violations, overloading of equipment, power quality, and changes to protection schemes are listed as being key network integration challenges. Similarly, [11] and [20] list the above issues, alongside changes to losses, operations and stability. The focus of this thesis is at the intersection of voltage magnitude, losses, and overloads, and how these factors interact with the planning and operation of distribution networks. The impact of these challenges on three opportunities for DGs are now considered.

1.2.1 Losses in Distribution Networks

Losses are known to be a key part of distribution network planning and operations [21, 22]. This is due to their size with respect to the total generation mix–the transmission

system operator of the UK, National Grid, estimates transport losses are 1.7% of total demand in the transmission network, with further transport losses of 5-8% in distribution networks [23,24]. As a result, in the UK DNOs are required to keep their losses within acceptable limits, and are required to publish a losses strategy [25].

The picture in the US is similar–the EPRI Green Circuits project studied the losses from 22 operators across a range of 66 networks [26]. Through detailed modelling it was estimated that 3.6% of total load on the feeders in distribution networks is due to losses, although peak losses were as great as 16% of this value in some networks. As the penetration of DGs increase, it is well-known known that losses first decrease up to a point, before they then start to increase again [9]. Changes to losses caused by DGs should be accounted for where possible, to incentivize the building of assets in locations that reduce losses [27].

1.2.2 Increasing the Hosting Capacity of Distribution Networks

Distributed generators impact on the *hosting capacity* of a network. The hosting capacity of a distribution network is defined according to the amount (in kW or %) that a DER that can connect prior to the violation of an operational constraint [8, Ch. 3], [28]. There are a range of questions that are related to hosting capacity calculations, with the aim of helping network operators with decision making (see Table 1.1).

The impact of DGs on voltage magnitude is particularly pertinent for hosting capacity as distribution networks are usually operated assuming unidirectional power flow. A result of this is that substation voltages are high to allow for voltage drops (e.g., [26, Section 2]). In fact, maintaining voltage magnitudes within bounds more consistently is the main technical recommendations discussed in a recent review for UK distribution network regulations [29]. The IET's 'Methods and Tools for Planning the Future Power System: Issues and Priorities' also identifies that UK DNOs require

Table 1.1: Questions that can be considered a part of hosting capacity analysis (adapted from [3]).

DSO Query	Approach/Outcome
How much DER can be connected to a given network?	Determine the existing hosting capacity for each feeder under the appropriate configuration
Can DER connect without causing adverse issues?	Screen the proposed feeder to consider if there is enough DER capacity at that location
Where is the 'optimal' DER location for maximising total feeder hosting capacity?	Identify locations that can minimize upgrades necessary to accommodate further DERs
What is the aggregate level of DER that can be accommodated at the substation level?	Improve visibility into substation-level capacity for accommodating DER connected at the multi- and individual-feeder level
When a feeder changes, how is hosting capacity impacted?	Re-run hosting capacity, with a method capable of considering feeder reconfigurations and upgrades
Is there locational value to DER?	Calculate the sensitivities of appropriate quantities with respect to location and study how values change
How can I visualise where DER impacts my feeder/system the most?	Calculate the hosting capacity, then plot the locational sensitivity geographically
Are smart inverters needed?	Identify voltage constrained hosting capacity locations and recalculate hosting capacity values with controls activated

new methods for the understanding challenges of DG integration–it concludes that 'established methods are not yet evident in respect of voltage and reactive power and evaluation of curtailment of generation' [30].

1.2.3 Increasing the Efficiency of Loads

As well as the impact of DGs on voltage resulting in changes to hosting capacity of networks, changes to voltage magnitude also change the power that is drawn by many types of load. In particular, loads are typically known to reduce their power draw as voltages are reduced to the lower end of their operating range. Despite a move towards a grid with more power electronic-interfaced devices (which do not show this effect), recent large-scale studies have suggested that 'conservation voltage reduction' (CVR) on a large scale could reduce US demand by as much as 2-3% per year [31,32].

DGs and DERs can influence voltages on the network if they change the reactive power they draw. There is therefore the opportunity to enhance the capabilities of this sort of efficiency measure if DGs can be controlled effectively.

1.3 Inverter Reactive Power for DG Integration

One of the most promising technologies for the integration of DGs with respect to the aforementioned issues is reactive power control. Reactive power control from DERs is possible if it is connected to a network with a power-electronic based grid interface with the appropriate functionality. The past decade has seen a significant development with respect to this functionality: IEEE Standard 1547 has been updated from a case whereby all DERs were prohibited from reactive power control [33] to the situation whereby there are now a wide range of potential operating strategies for inverters [34]. In fact, the California Energy Commission's 'Rule 21' mandates that inverters have reactive power priority, such that the full reactive power capability is realisable at full generation (i.e., the inverter must be oversized) [35]. Similar rules apply to inverters in other jurisdictions, such as Hawaii [36].

Reactive power control from inverter-based DGs can make a positive impact on all three of the opportunities for DGs. Sinking reactive power (using inductive vars) tends to lead to a reduction in voltage, which has the effect of reducing voltage rise that might have otherwise been caused by PV, and reducing load demand at the same time (assuming a positive load sensitivity to voltage). On the other hand, sourcing reactive power (capacitive vars) tends to improve the power factor of a circuit and reduce losses. As such, there is a natural tension in the use of reactive power in networks, leading to a trade-off between competing objectives.

1.3.1 Studying the Properties of Reactive Power Control in Distribution Networks

There are a wide range of model types that are appropriate for the study of any system [37]. In the context of distribution system analysis, there are broadly three types of models that can be used for the analysis or planning of a system [38].

- Analytic models (in closed form). These models are necessarily simple and have few parameters, each of which can be readily interpreted. The focus of these models is the study of the qualitative behaviour of a system, with relatively limited quantitative accuracy; the scope of applications may be entirely didactic.

- Models for planning. These models have many more parameters and are used to understand the behaviour of systems under significant uncertainty about future power flows, and their accuracy should be considered in this respect.

- Models for operations (i.e., for active network management). These models should be of the highest fidelity as is reasonable, taking into account the true state of the network where possible, to ensure safe and reliable network operation. These models can be combined with some cost function to achieve 'optimal' network operation, according to some sense[2].

[2]The definition of 'optimal' varies between stakeholders in an energy system; these inherent tradeoffs may result in non-uniqueness of optima.

The scope and properties of a good model vary between these types. For example, analytic models should explain the qualitative behaviour of a particular system well, whilst models for operations should take into account as much information about the true state of the network as possible.

1.3.2 Reasons for Considering Computational Complexity

For models for planning and operations, a recurring theme through this thesis is a consideration of the computational complexity. There are two main reasons for considering the complexity: firstly, optimization problems can become intractable as the number of variables increases. For example, integer programming is 'NP hard' [39], such that the computational complexity increases extremely quickly with the problem size. By considering less complex problems, either through relaxing integer constraints or linearizing non-linear systems, it is possible to find approximate solutions that are of high quality.

The second reason is the challenge of human-machine interaction. It has been known for many decades that humans struggle to interact with repetitive tasks that take longer than a few seconds [40, 41]. This fact continues to drive software design to this day [42, 43]. For reference, Table 1 summarises the perceived experience of software users to system response times, as described in [4, Ch. 5.5]. It is noted, if a model of a system takes longer than 10 seconds to run, it is unlikely that a user will be able to tolerate interacting with such a program for extended periods. Indeed, one of four 'issues and priorities' identified for the UK power systems industry was 'the provision of methods and tools to allow the engineering questions to be addressed as conveniently as possible' [30].

These two issues impact on the three models of Section 1.3.1 in different ways. Human-machine interaction is most important for the analytic and planning models, as humans are 'in-the-loop': these tools are intended to develop insight to network behaviour and enable efficient decision making, respectively. Some planning-type optimizations are large-scale and tractability is a key feature of algorithms [44], although

Table 1.2: Perception of system response times by users (adapted from [4, Ch. 5.5]).

Response time, s	User's perception
< 0.1	The system appears to be reacting almost instantaneously to a user's commands.
0.1-1.0	Flow of thought for the user remains uninterrupted, but the delay is likely to be noticed.
1.0-10	The user will maintain attention on the task, but simple feedback is advised to keep the user attentive.
> 10	Users will be unlikely to keep attention on a task. Users should be given estimates of time-to-completion so that they can do other tasks as the program runs.

it is worth highlighting that in real-world situations investment decisions are made by planners, not by automatic algorithms [45, Ch. 2]. On the other hand, operational decisions can largely be automated, and it is instead critical that calculations are successfully terminated within the specified control timeframe. For example, [46] suggests 'real-time' DG control actions might be updated on a sub-second basis, with optimal setpoints updated every five to fifteen minutes.

1.3.3 Research Scope

As stated in the research question at the start of this chapter, the focus of this thesis is the application of reactive power control for DERs in distribution networks. The main topics of consideration within the integration of DERs have now been introduced as the losses, hosting capacity, and load efficiency. The scope of the research carried out is now considered.

1.3.3.1 Types of DGs and DERs

There are a range of generators and load types that can be considered as DGs or DERs, including electric vehicles (EVs), induction motors, wind turbines etc. [8, 34]. The key distinction between DERs and general other components of a distribution system is the element of some controllability (therefore controllable DGs can be considered

a type of DER). The methods throughout this thesis are mostly focussed on the integration of solar PV, as it has been argued in this chapter that this is of particular interest to network operators (Section 1.1). Case studies are therefore focused on PV scenarios, and time series analysis and DG sizing reflects this. Nevertheless, the methods developed are applicable to the study of other DER types with reactive power control capabilities.

1.3.3.2 Control Paradigms

There are several competing paradigms by which it is envisioned that DERs may be integrated into power systems in the future (e.g. ownership of DERs, who is responsible for DER scheduling, etc.). These paradigms include Distributed Energy Management Systems (DERMS) [47], Virtual Power Plants (VPPs) [48] and peer-to-peer energy trading platforms [10].

This work is largely agnostic with respect to the control paradigm, with the focus mainly on 'societal' benefits (in terms of reduced curtailment, increased hosting capacity etc.). Nevertheless, it is assumed that a DERMS system is the simplest and most likely system to gain widespread adoption. A DERMS has functionalities to 'aggregate, simplify, optimize, translate' the control of DERs [47]. A DERMS system is assumed to have information from DGs as to their availability and the state of the network, and it can optimize and send optimization signals to devices to minimize some cost function (e.g. minimize losses subject to voltage constraints).

1.3.3.3 Dynamic Reactive Power Control

Many proposed reactive power schemes include a dynamic element (particularly droop control [34]). The choice of such droop coefficients was also not considered as a part of this work, as the accurate dynamic analysis of distribution networks requires very high fidelity models for accurate results [49]. Instead, it is assumed that once a 'steady state' optimal control point has been found (according to some suitable cost function), that a dynamic control scheme could be developed based on necessary

stability requirements (as in, e.g., [46]).

1.4 Thesis Roadmap

Chapter 2 reviews the state-of-the-art in the literature around the main research question. This allows for the key research gaps to be identified; additionally, it introduces the networks and background theory that are required for subsequent chapters. Chapter 3 considers the first research question: the study and validation of two analytic models for considering of the impact of reactive power on losses and curtailment, to identify what parameters will result in high losses when reactive power is used for voltage control. Chapter 4 considers the efficient calculation of the stochastic hosting capacity of a network, with a focus on the impact of reactive power on hosting capacity and sensitivity analysis (as some error is naturally introduced by the linear model). This method enables a DSO to understand the likelihood of hosting capacity capacities being reached. In Chapter 5 a method is proposed for calculating the optimal reactive power output of domestic generators, considering not only network losses but also inverter losses and load voltage sensitivity. Finally, in Chapter 6 the conclusion of the main research question is discussed with respect to the contributions of the thesis, and topics for further research are identified.

1.5 Main Contributions

The key contributions to knowledge from this research are as follows.

Contribution 1 (Ch. 3, I): The generation leading to maximum power transfer in a two-bus circuit is studied in the context of a distribution network. There are two novel aspects of this study: a comparative analysis demonstrates that conclusions drawn from maximum power transfer in transmission are very different to those in distribution; secondly, for the first time, a case study demonstrates that losses cause the maximum power transfer point on an unbalanced IEEE

test network. It is demonstrated that, for line impedance 'R/X ratios' greater than 0.7, losses result in maximum power transfer prior to traditional stability constraints.

Results based on this first contribution are published in the following papers.

- M. Deakin, T. Morstyn, D. Apostolopoulou, M. D. McCulloch, "*Loss Induced Maximum Power Transfer in Distribution Networks*". 20th Power Systems Computation Conference (Dublin, Ireland), 2018.
- M. Deakin & M. McCulloch, "*Voltage Regulation of Large Scale PV: A Comparative Case Study*". IEEE Powertech 2017 (Manchester, UK), 2017.

Contribution 2 (Ch. 3, II): The 'relative energy loss fraction' is proposed to study the impact of reactive power on losses. Analytic bounds on this relative energy loss fraction are derived and analysed, using the LinDistFlow load flow linearization[3]. These bounds are validated by comparison with both the closed-form solution of the two-bus load flow equations, and a set of three unbalanced distribution networks. The relative energy loss fraction was found to be as high as 30%, with the derived bounds able to estimate the true bounds to within 5% in the case studies considered.

The results from the second contribution are published in the following work.

- M. Deakin, T. Morstyn, D. Apostolopoulou, M. D. McCulloch, "*The Value of Reactive Power for Voltage Control in Lossy Networks*". IEEE PES General Meeting (Portland, US), 2018.

Contribution 3 (Ch. 4): A computationally efficient method for calculating stochastic hosting capacity is proposed, accounting for regulator controls and reactive power setpoints. This allows for stochastic hosting capacity of large networks to be calculated in less than 10 seconds, where detailed methods can take over one hour. Additionally, a hosting capacity sensitivity is proposed, which is shown empirically to correlate well with the error caused by linearization. The control

[3]LinDistFlow is a well-known load flow linearization, introduced by Baran and Wu in [50]; this is described in detail in Chapter 3.

of taps and regulators by a centralised DERMS-style controller is demonstrated to increase the hosting capacity in feeders with voltage constraints by as much as 70%.

The results from the third contribution are contained in the following work.

- M. Deakin, T. Morstyn, D. Apostolopoulou, M. D. McCulloch, "*Stochastic Hosting Capacity in LV Distribution Networks*". IEEE PES General Meeting 2019 (Atlanta, US), 2019.

Contribution 4 (Ch. 5): A MI-QCQP has been proposed to study the impact of domestic inverter control on the total feeder power, demonstrating reductions of 0.5% compared to only controlling taps. The main innovation of this chapter is the inclusion of network losses, inverter losses, and load voltage sensitivity in the cost function, leading to a more accurate assessment of the benefits of reactive power control than in previous works. The necessity of all components of the cost function of the MI-QCQP has been demonstrated analytically and empirically. As an extension to the full MI-QCQP, a control scheme with a smaller communications overhead is proposed, capturing more than 73% of the potential benefits of inverter control in all case studies.

Results from the final contribution are contained in the following work.

- M. Deakin, T. Morstyn, D. Apostolopoulou, M. D. McCulloch, "*Control of Pervasive Domestic-Scale Inverters for Minimizing Total Feeder Power*". 21st Power Systems Computation Conference (PSCC 2020)–conditionally accepted.

Chapter 2

Literature Review

In the introduction, the reasons for the consideration of losses, hosting capacity and load response to voltage for a DSO were described in broad terms. This chapter reviews the literature on the impact of reactive power control on these topics. The networks that will be studied for the remainder of the thesis will also be introduced. A review of methods of linearizing three-phase load flow is also undertaken, as linear models provide a computationally efficient method of analysing distribution networks.

Chapter Roadmap In Section 2.1, analytic methods for considering the impact of reactive power control on losses are considered, to consider what methods exist for studying the broad impacts of distributed generation on losses. Section 2.2 investigates methods for calculating the hosting capacity for domestic-scale DGs, and how reactive power can impact on this control. Section 2.3 describes the use of reactive power for total feeder demand reduction in networks. A literature review of linear models for three-phase distribution network modelling is carried out in Section 2.4, as background to the technical work of Chapters 4 and 5. Finally, Section 2.5 describes the set of distribution network models that will be used for the rest of this thesis.

2.1 DER Reactive Power Control and Losses

The first topic of interest when utilising reactive power is that of losses. Given their importance, losses have been studied for many years, and there are numerous methods for estimating losses in distribution networks using approximate formulae [22, 51–55].

Distribution losses are typically broken down into two categories: technical losses and non-technical losses. Technical losses consist of losses that are due to thermal losses in lines and transformers. Non-technical (commercial) losses are due to errors in metering equipment or energy theft.

Technical losses can be broken down further into load- and no-load losses. Load losses are dependent on the load that is drawn on the network, and so fluctuate with time. No-load losses are independent of the load and are caused by transformer eddy current and hysteresis losses [56, Ch 5.6]. Technical, 'load' losses are the focus of this work, as the control of DGs directly impacts on them.

2.1.1 Losses and Increasing Hosting Capacity with Reactive Power

Voltages in power systems are strongly influenced by the injection of reactive power. In a steady-steady alternating current (AC) power system, reactive power represents energy which is stored and released each cycle without doing work, and is non-zero when the AC voltage and current waveforms across an element are out of phase. This short-term energy is often stored in electric or magnetic fields; for example, cables have a significant shunt capacitance that 'sources' reactive power (i.e., the sign convention is that reactive power is generated), whilst overhead lines have a large series reactance that 'sinks' reactive power. Much like real power, reactive power is conserved in a steady-state AC system; it is typically given the symbol Q, and is measured in Volt Amps-reactive (VAr).

Fundamentally, therefore, DGs can therefore inject or sink reactive power by injecting current that is out of phase with the measured local voltage waveform (which

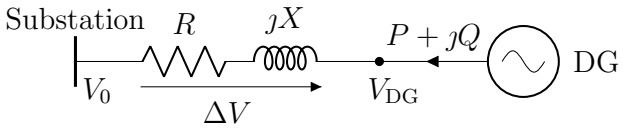

Figure 2.1: The two-bus model

is required to be measured in the first instance to ensure that real power is injected). A discussion of the reactive power capabilities of four types of DG grid interface (directly-coupled induction generators, inverters, directly-coupled synchronous generators and doubly-fed induction generators) is given in [57]. A summary of the operation of power electronic inverters, which are the focus of this thesis, is given in, e.g., [11, Ch. 4.3].

The voltage rise ΔV along a line, and the resulting power losses P_{lss}, can be approximated by

$$\Delta V = \frac{PR + QX}{V_0}\,, \tag{2.1}$$

$$P_{\mathrm{lss}} = R\frac{P^2 + Q^2}{V_0^2}\,, \tag{2.2}$$

where ΔV is the voltage between the substation V_0 and the DG V_{DG}, the line has resistance and reactance of R, X respectively, and P, Q are the generated real and reactive powers respectively [58]. The system as described is shown in Figure 2.1. These equations can be used to broadly explain the effect of reactive power on distribution networks at low powers: when the voltage rise ΔV due to generation is large, then the voltage increase can be mitigated by sinking reactive power (i.e., by reducing Q). This has the effect, however, of increasing the real power losses P_{lss}.

The injection of reactive power for increasing hosting capacity has been proposed at all voltage levels, including on LV feeders [58–62]. In this work, the *net* generated energy, consisting of net energy changes in both generation and losses, is considered to represent the true value of reactive power control [27, 63][1].

[1]Note that loss allocation [64] is not explicitly considered in this work—the design of loss charges for users of a power system is a policy decision with an inherent arbitrariness [65].

Nevertheless, there are contradictory claims as to the significance of losses in distribution networks. For example, reactive power control was found to be the most cost-effective network intervention in Germany [66], whilst the authors of [67] suggest that curtailment is the *only* worthwhile method of voltage control in low voltage networks. Other studies that propose reactive power control do not discuss losses at all (e.g., [17,68,69]). In fact, in a recent survey of voltage control methods in distribution networks (of which a large majority included reactive power control), more than 70% of papers did not consider losses as an optimization objective [70]. In some economic analyses, the value of generated power and of losses are not weighted equally [71–73]. Interestingly, the reason for loss reduction was stated as being motivated by government regulation in [74] (rather than efficient operation in itself).

As part of the broader literature review, a set of distribution system analysis monographs were also studied from (amongst others) the IEEE Press Power Series and IET Power and Energy Series, with topics on distributed generation and power quality [8, 11, 45, 56, 75–77]. The monographs by Short [56, pp. 833-838] and Bollen and Hassan [8, pp. 210-218] discuss the use of reactive power control from distributed generators and how this can be used to reduce voltage magnitudes. Both references note that reactive power control can impact on losses, but the impact of this reactive power on these losses is not calculated or considered numerically.

Before considering analytic methods for study losses, a review of maximum power transfer in lossy networks is first considered.

2.1.1.1 Studying Power Flows with the Maximum Power Transfer

One of the goals of the analytic method is to study how losses vary across a wide range of parameters. The maximum power that can be generated and then transferred to the transmission network is referred to as the *maximum power transfer* point.

There are some works considering maximum power transfer in distribution networks, but they are not common. A recent work on maximum power transfer noted that 'formulae [for maximum power transfer] with non-negligible resistance are not

easily found in the existing literature' [78]. The R/X ratios seen in transmission networks are typically from 0.05 to 0.3 [79], whilst they are typically between 0.4 and 3.1 in distribution networks [80].

It was found that works that did consider network resistance with maximum power transfer typically considering either wind or HVDC lines in subtransmission networks. The solution to the maximum power transfer point for a generator with non-zero resistance is reported in [81], based on a network with a Voltage Source Convertor High Voltage DC (VSC-HVDC) asset. In [82], the authors consider a system with a line R/X ratio of 0.08, and it is recognised that losses may cause maximum power transfer.

There are a few works that do study concepts related to the maximum power transfer in networks with R/X ratios appropriate to distribution networks. In [83, Ch. 4], the author studies the impact of the R/X ratio on the stability boundary of a distribution network connected to a transmission network. It is concluded that the R/X ratio can improve the stability boundary (the stability boundary is defined according to the upstream transmission network Thévenin impedance). In [80] the authors study the loadability problem in unbalanced distribution networks, although the effect of losses is not considered within the framework. In other words, the likelihood of operating near the identified stability boundary is not considered, which is particularly pertinent as distribution networks are operated very differently to transmission networks. The authors of [84] study the capability of wind turbines for providing reactive support to transmission networks through an MV network, concluding that reactive power support is possible even though MV circuits have higher losses than HV circuits. It is concluded that losses are not usually considered in the treatment of maximum power transfer, which is particularly pertinent in the case of distribution network analysis due to high R/X ratios.

2.1.2 State of the Art: Impacts of DG Reactive Power Control on Losses and Curtailment

Methods for studying the impact of DG reactive power control can be split into energy-focussed and power-focussed methods, depending on whether they study losses across a time period of interest or at an individual point in time [63, 85].

2.1.2.1 Energy-Focussed Loss Analysis

It is known that energy losses on distribution feeders follow a 'U-shape' curve with respect to DG penetration: losses first decline as the penetration of distributed generation (DG) increases, before they then start to increase [9]. The authors conclude that numerical results vary significantly between networks, but do not explicitly study this sensitivity with respect to any network parameters. A black-box method of estimating the impact of distributed photovoltaic generation on losses is given in [86], with inputs as penetration level, distance from a generator to the substation, secondary transformer ratings, and a 'critical PV value'. The method shows good agreement between the correlation index and losses. The black-box nature of the method limits the generality of the method, however.

A probabilistic method in [87] considers the impact of distributed generation on losses; again, the method focusses on a single case study, and the aforementioned U-shaped impact is observed. Similarly, the U-shaped curve is demonstrated in [88] for an active distribution network, with losses increased by up to 28% when reactive power of generators is taken into account. It is concluded that losses 'should not be ignored, even if the simulated system is an LV one'. In [73] reactive power is scheduled to reduce total system loss, but the simulation-based method does not allow for general conclusions to be considered. A maximum significance of losses value of 6.5% is found in the case studies of [27] (in terms of increased generation versus losses), although the study only considers the impact of changes in DG real power, rather than reactive power.

2.1.2.2 Power-Focussed Loss Analysis

There are fewer methods which consider the study of powers. Marginal loss factors are a power-based method for studying losses, and are calculated as the partial derivative of total losses with respect to bus injections (see, e.g. [89]). By definition, this then only explicitly considers a single loading point (and as such only explicitly takes into account power losses, rather than energy). In [90], marginal loss factors are ascribed to distributed generation (notably, also considering the impact of reactive power injections), and are described heuristically as being 'up to 2.5%' of DG output. The authors of [91] derive a loss sensitivity metric for generic networks, although they do not attach a clear meaning to this metric, with the impact of losses appearing to be several orders of magnitude smaller than changes in bus power injections. The method of loss allocation in [92] does account for generator reactive power within loss allocation, but the case studies considered are limited.

The other main power-based methods of loss estimation use simplified models to estimate losses. For example 'loss factors' can be used to convert peak load-losses to an average load-loss value, by using a conversion factor based on the generation or load profile [56, Ch. 6.6]. Others methods use small-scale equivalent models to identify technical losses [93]. The losses associated with distributed load models (rather than traditional 'lumped' load models) are considered in [77, Ch. 3], although only constant power models are considered.

2.1.3 Gap Analysis: Reactive Power Control, Losses and Curtailment

In general, these works do not study losses in the context of a wide range of distribution network parameters, and are sensitive to changes in temporal load and generation profiles. Predictions of these profiles is generally non-trivial, and networks vary a large amount in their topology and configurations. This gap motivates our search for an analytic method for studying the impact of reactive power on energy losses. Indeed,

it has been noted by a Cigré working group that 'future planning methods should be able to deal with real, large-scale cases but [it] is crucial to investigate the role of simplified approaches in providing acceptable solutions' [38].

Given that the goal is an analytic model for understanding, the number of parameters should be kept to a minimum. Additionally, it should take place over as wide a range of powers as can be seen in a distribution network. This motivates the study of maximum power transfer in distribution networks, and the subsequent validation of the method with respect to maximum power transfer points.

The first gap in literature, G1, can be summarised as follows:

G1. There is currently no analytic method that considers the impact of reactive power control by a distributed generator on energy losses across a wide range of network parameters and powers.

From this research gap, the first research question is identified:

How can the impact of inverter reactive power control on the efficiency of distributed generation be analytically characterised, considering power flow up to the maximum power transfer point?

Research to answer this question is carried out in Chapter 3.

2.2 Stochastic Hosting Capacity considering Reactive Power Control

Stochastic hosting capacity refers to the approach of studying the amount of some DER that can be connected (the hosting capacity), given uncertainty in input parameters. This extends the nominal definition of (deterministic) hosting capacity, considering the probability of a constraint being violated as a function (the most common definition considers uncertainty on the location and sizes of DER [94]). Deterministic hosting capacity calculations can be computationally intensive if calculated exhaustively [95]. Uncertainty in generator locations further increases the computational

burden [96]. It is worth noting that the importance of methods considering uncertainty are recognised in industry as well as academia [30, 38].

A basic approach to study the stochastic hosting capacity of a network is via Monte Carlo simulation. One Monte Carlo scenario consists of a set of DERs at given locations and sizes; a load flow is run on a small number of loading points with this set (typically fewer than 12), and the solutions assessed for violations [94, 96–101]. Scenarios are then created at each penetration level, resulting in thousands of non-linear load flow evaluations. This is a significant computational burden, making hosting capacity analysis of distribution networks slow. This makes sensitivity analysis challenging, which should be an integral part of distribution system analysis [96].

2.2.1 State of the Art: Stochastic Hosting Capacity Network Analysis

In this section, methods of studying the stochastic hosting capacity of distribution networks are categorised into feasibility and optimization methods. These approaches are differentiated according to whether or not there are active or passive controls. Active controls are optimization-based, and controls are set with full knowledge of generator locations within a given scenario. Passive controls, on the other hand, are considered to act independently of the locations of generation (although generation may impact on their operation, for example, through line drop compensation).

2.2.1.1 Stochastic Hosting Capacity: Feasibility Methods

A majority of hosting capacity methods consider the load-flow feasibility problem, by increasing the DER penetration and then calculating the resulting load flow. It is then often the case that hosting capacity is analysed indirectly in terms of the sensitivity to a particular parameter. For example, many methods consider the analysis of DER locations on the final hosting capacity value by studying how the hosting capacity varies with the solutions obtained.

The authors of [102] determine the hosting capacity, considering PV sizes based on historical data, concluding that locations far from the head of the feeder lead to a reduced hosting capacity. In [103], the authors study the hosting capacity of fifteen feeders and consider how the hosting capacity values correlate with six feeder characteristics. It is concluded that impedance, voltage class and peak load have the greatest correlation with hosting capacity values. The authors of [100] go one step further: the authors propose that the hosting capacity of over 50,000 LV feeders can be calculated by sampling just 1% of all feeders and extrapolating, showing promising results. In [104], the authors study the susceptibility of feeders to constraints caused by voltage unbalance, concluding that it is unlikely to be a binding hosting capacity constraint in distribution networks. In [96], the authors calculate hosting capacity calculations over a day using the full load flow solution, demonstrating the importance of sensitivity analysis.

Other methods take a more analytic approach to make more general claims about the behaviour of networks. In both [105] and [106], simplified two-bus models are studied for radial distribution systems, to consider the impact of various network parameters on the hosting capacity of networks—the authors conclude that substation voltage, DG power factor and network impedance have a large impact on hosting capacity values. In [98], the authors study the impact of an increase in low-carbon technologies, including PV, on voltage violations in networks. It was demonstrated that the highest correlation between hosting capacity values and the variables studied was the feeder's total path resistance and minimum load. In [107], probabilistic load flows are used for hosting capacity calculations, and the calculations compared to 'true' expert judgements, concluding that the predicted and actual calculations of hosting capacity were well correlated.

One method of reducing the computational burden of load flow calculations is to use a linear model. The Electric Power Research Institute (EPRI) has developed a 'Streamlined' method that uses a linear model based on network resistances to calculate hosting capacity [3] (and is contrasted with the authors previous 'detailed'

approach [108]). A linear power flow method is used in [109] to calculate the hosting capacity of a centralised PV system, concluding that the linear method has superior computational efficiency (although the authors study only the hosting capacity of a single generator). A method using linear models to perform high-resolution PV impact analysis using Quasi-Static Time Series (QSTS) analysis is implemented in [110], although the method is most suited to centralised PV analysis; indeed, there are significant computational challenges associated with QSTS for such impact analysis even for a single generator [49]. A linear model is used for stochastic hosting capacity in [101]; however, the approach does not consider voltage regulators and is only validated on two small networks.

2.2.1.2 Stochastic Hosting Capacity: Optimization Methods

Other methods consider the explicit optimization of the stochastic hosting capacity. In both [97] and [111], the authors consider optimizing stochastic hosting capacity, overcoming the non-linear nature of the hosting capacity problem for optimization by using heuristic optimization methods. In the former, the authors optimize capacitors, regulator taps, and switches on the IEEE 123 bus feeder to increase hosting capacity. This shows moderate improvements compared to alternative control strategies (e.g., adjusting the power factor of all inverters uniformly); the approach was not demonstrated on a large-scale system, however. The latter considers the sizing and placement of static compensators (STATCOMs) and energy storage for increasing hosting capacity, demonstrating that in some cases energy storage can be the most cost-effective method of increasing hosting capacity.

A small number of works consider the linearization of the three-phase load flow for optimization as part of hosting capacity calculations. In [112] the authors study a linear model for increasing hosting capacity using reconfiguration, concluding that minimizing the Thévenin impedance increases the hosting capacity. The authors consider stochasticity of loads and generation for the maximisation of (centralised) PV in [113] using a linear method, highlighting that constraints on different networks

lead to very different solutions in terms of maximum hosting capacity values. In [99], the stochastic hosting capacity is calculated using a three-step process. Six control schemes are implemented (including an OPF-based method), although the authors only demonstrate the method on a circuit with fewer than 300 DERs, and the computational scalability of the solution is not demonstrated. (For comparison, the EPRI Circuit 24 network, introduced in Section 2.5, has 3891 loads fed from a single regulator. As there is only the regulator at the head of the feeder, the voltage magnitudes for all of these loads are coupled and need to be modelled together.)

2.2.2 Gap Analysis: Stochastic Hosting Capacity Methods

None of the previous works calculate the stochastic hosting capacity analysis using a linear model that considers voltage regulators explicitly, either in the case of fixed regulation or regulators with line drop compensation (LDC). This is particularly pertinent as regulator controls are most commonly implemented in this fashion [77], with hosting capacity constraints showing high sensitivity to assumptions about voltage setpoints [100]. In fact, surveys of probabilistic load flow methods show that a large percentage of methods utilise a linear method, further providing evidence that a linearized method could provide benefits [114].

The second gap identified, G2, is summarised as follows:

G2. At present, there is no method of calculating stochastic hosting capacity values of distribution networks in a computationally efficient manner, taking into account both legacy voltage regulation equipment and reactive power control by distributed generators.

From this research gap, the next research question is identified:

How can the stochastic hosting capacity of a distribution network be calculated in a computationally efficient manner, considering voltage regulators and reactive power control from distributed generators?

Research to answer this question is carried out in Chapter 4.

2.3 Domestic Inverter Reactive Power Control for Volt-Var Control

In this final research topic, the question arises as to how domestic-scale inverters can be controlled to minimize the total power that a feeder draws, when inverters are not being used for curtailment avoidance. When hundreds or thousands of domestic generators are considered, a scalable optimization strategy is required [115].

The idea of conservation voltage reduction due to voltage sensitive loads is first considered, as it is hypothesised that this will influence the optimal operation of inverters substantially. The literature of volt-var control of domestic scale reactive power control is then surveyed, before the final research question is introduced.

2.3.1 Optimization via Conservation Voltage Reduction

Conservation voltage reduction considers the impact of reducing voltages on energy demand. The 'CVR factor' (or 'voltage sensitivity factor') α_{CVR} is given by [116]

$$\alpha_{\text{CVR}} = \frac{\Delta P}{\Delta |V|}\,, \tag{2.3}$$

for changes to load power P and the feeder voltage magnitude $|V|$.

Load devices which exhibit a non-constant power characteristic include incandescent bulbs, street lighting, fridge/freezer units, and fans [117]. More modern devices sometimes actually show slightly negative values of the CVR coefficient α_{CVR}, although this is never more than 0.1% [31, 32, 118]. In addition to reductions in load, implementing CVR causes reductions in the no-load losses of transformers (although over 90% of energy savings seen are due to load reduction [56, Ch. 6]).

The value of the load-voltage sensitivity α_{CVR} is typically a function of time. For example, resistive thermostatic loads will initially display a value of α_{CVR} of 2, but over a long time period will appear to have a value of $\alpha_{\text{CVR}} = 0$ due to the effect of thermostatic control. In this work, CVR techniques are considered as either

short-term or long-term. Short-term CVR acts to reduce loads for short periods (typically for an hour or less) to provide transmission-scale flexibility or avoid asset overloading [119]; long-term CVR acts to minimise the total energy continuously, to reduce resource requirements [116, 120]. It is worth noting that there are risks that reducing voltages could case additional power quality issues, as summarised in [121].

In general, the range of load-voltage sensitivities is typically between 0.3–1.2%, with most studies finding an aggregate sensitivity between 0.5–0.8% [32, 116]. This ultimately depends on the load composition [117], which varies with geographic location, season and time of day.

Control of reactive power for CVR applications has historically used discrete switched capacitor banks and regulators with taps. Legacy CVR methods can be split into open-loop and closed-loop methods. Open-loop methods are based on line drop compensation (LDC), whilst closed-loop methods utilise feeder voltage measurements to more accurately identify when voltages can be reduced by lowering taps [116].

Most previous schemes that have been implemented in practise only use open-loop control, reducing voltages a set amount [32, 119, 122]. As the availability of measurements on distribution systems has increased, however, more recent papers do take into account distribution system measurements for more accurate closed-loop control. For example, a complex scheme that utilises measurements for total feeder power reduction has been implemented in [31].

2.3.2 State of the Art: Volt-Var Control Considering Inverter Control

The optimization of taps and capacitors banks for loss reduction and CVR is often called 'Volt-Var optimization' or simply 'voltage optimization' [56, Ch. 6]. There is a wide range of papers that propose 'traditional' volt-var control based on the optimization of tap and regulator setpoints, with the goal of minimizing total energy

or providing flexibility services [120,123,124]. It is only more recently that the control of DERs has been considered a potential part of this optimization [125].

Methods for the optimal operation of distribution networks can be split into 'numerical' methods and 'heuristic' methods [126]. The former considers mathematical programming techniques based on linear or non-linear programming, whilst the latter focusses on the optimization using 'black-box' methods such as the genetic algorithm to overcome challenges with non-convexity of integer constraints.

2.3.2.1 Numerical Methods

Because of the large number of decision variables, all surveyed numerical optimizations studying the impact of domestic inverter control relied on a linearization of the power flow equations for tractability. The objective function can broadly be split into methods that consider load minimization and those that do not.

The authors of [127] minimize total feeder demand on radial distribution networks, considering DER and capacitor bank switching, using the LinDistFlow linearization formulation, concluding that there are good opportunities for reactive power control to increase the possible penetrations of PV. In [128] the authors study an approach to assess the benefits of inverter reactive power control on losses, with a detailed inverter model to account for inverter losses on the solution, again using LinDistFlow. They conclude that modelling the lifetime of inverter components is important when using inverters for reactive power dispatch, but the work does not consider the load response to voltage magnitudes.

Papers that consider the minimization of load also often consider the minimization of network losses. In [129] the impact of voltage sensitive loads and network losses is captured, although the approach is only tested on a small-scale network and the load-flow model used for calculating voltages and losses is not described, so it is difficult to assess the accuracy of the approach.

The authors of [130] consider a single-phase linearized load flow model to study CVR in a network with capacitors and tap changers. A comparison with the true

non-linear model is not considered (phase angles of currents are assumed constant), but losses and load reduction are incorporated into the constraints. The authors of [131] propose an Alternative Direction Method of Multipliers (ADMM) based multi-period volt-var control scheme for CVR and loss reduction. The authors do not, however, take into account inverter losses, and only study cases with a small number (up to 20) smart inverter locations. In [132] the authors use a linearized load flow to compare loss and load minimizing strategies in four-wire networks, although the study is limited to tap changers only.

2.3.2.2 Heuristic Methods

Other methods use heuristic optimization strategies to overcome non-linearities in their formulations, avoiding the need to consider the accuracy of load flow equations at the cost of potentially inefficient optimization strategies.

In [133] the authors use a genetic algorithm to increase the benefits of CVR in two utility scale feeders, demonstrating savings of 0.3-0.9% load reduction compared to a case with no inverter functionality—the impact of inverter losses is not considered, however. A multi-objective analysis of enabling smart inverter droop functions is presented in [134] to study the impact of smart inverters on energy reductions, including the total feeder energy, but losses are monitored, rather than considered explicitly within the main cost function considered.

In [135] the authors study the effect of load models on total load in the IEEE 123 Bus distribution network using a genetic algorithm. The author's work is extended in [136] to study changes in the optimal control of devices. It is noted by the authors that load models appear to have a significant impact on the operation of devices; but only the modestly-sized 123 Bus circuit is studied, however, and the impacts of smart inverter losses are not considered. In [137], network losses, CVR and inverter losses are considered as a part of the load flow. Regulator taps and droop coefficients are modified manually and the impact studied, although the authors do not explicitly optimize these parameters. As such, the benefits of the inverter control could be

understated.

2.3.3 Gap Analysis: Volt-Var Control

From surveying the literature on domestic inverter reactive power support, it has been observed that there are no works which optimize the use of domestic inverters and reactive power control considering inverter losses, network losses, and voltage sensitive loads. Given the large number of domestic properties, a linear method is most appropriate as this leads to scalability and much more predictable optimization performance. In this case, the error at the approximate solution should be carefully verified against the non-linear value of the solution.

The final gap that has been identified, G3, is summarised as follows:

G3. There is no scalable method that considers the potential for domestic-scale DG to reduce total feeder demand, taking into account load voltage sensitivity, inverter losses and distribution network losses.

The final question this thesis considers is therefore:

How can the benefits of domestic-scale inverter reactive power control be evaluated with respect to minimising total power demand on a feeder, with load voltage sensitivity, inverter losses and distribution network losses taken into account?

This research question is considered in Chapter 5.

2.4 Review of Linearization Methods in Multiphase Networks

The two final chapters of this thesis make use of linear multiphase network models, considering both wye- and delta-connected loads. To understand these linear models, the general multiphase load flow problem is outlined, before a review of three-phase linearization methods is undertaken.

2.4.1 Multiphase Network Model

The multiphase load flow problem is now outlined for the case of constant power loads. For a more detailed discussion of the properties of multiphase load flow problem (e.g., uniqueness and existence) see [138, 139].

The basic element of a power system model is the primitive (or branch) admittance matrix. This describes the branch currents of the ith branch element (e.g. line, transformer etc) according to the equation

$$I^{[i]}_{\text{branch}} = Y^{[i]}_{\text{branch}} V^{[i]}_{\text{branch}} \,, \tag{2.4}$$

where $I^{[i]}_{\text{branch}}$ collects the current injections of the ith circuit element, and $Y^{[i]}_{\text{branch}}, V^{[i]}_{\text{branch}}$ are the associated branch admittance matrix and voltages of the element respectively. The model (2.4) describes passive series elements, including general multiphase lines, transformers and regulators. The dimensions of Y_{branch} are given by the total number of terminals of the branch element (e.g. a three-phase line with neutral will have an 8×8 primitive admittance matrix).

Loads (and generators) are either wye-connected or delta-connected. The governing equations for the ith load are

$$S^{[i]}_{\curlyvee} = V^{[i]}_{\text{lds}} \left(I^{[i]}_{\curlyvee} \right)^* \tag{2.5a}$$

$$S^{[i]}_{\Delta} = \Delta V^{[i]}_{\text{lds}} \left(I^{[i]}_{\Delta} \right)^* \,, \tag{2.5b}$$

where $S_{\curlyvee\,(\Delta)}$ are the powers of each of the wye- (delta-) connected loads, $(\Delta)V_{\text{lds}}$ are the voltages across each of the wye- (delta-) loads, and $I_{\curlyvee\,(\Delta)}$ are the wye- (delta-) currents flowing through each of the loads.

By using Kirchhoff's laws, the multiphase load flow equations can be written

$$I_{\text{bus}} = Y_{\text{bus}} V \tag{2.6a}$$

$$S_{\curlyvee} = \text{diag}(V) I_{\curlyvee}^{*} \tag{2.6b}$$

$$S_{\Delta} = \text{diag}(H_{\Delta} V) I_{\Delta}^{*} \tag{2.6c}$$

$$I_{\text{bus}} = I_{\curlyvee} + H_{\Delta}^{\intercal} I_{\Delta} \,, \tag{2.6d}$$

where Y_{bus} is the bus admittance matrix, I_{bus} are the bus current injections, V are the node voltages, and H_{Δ} is a block-diagonal matrix given by

$$H_{\Delta} = \begin{bmatrix} H_0 & 0^{3\times3} & \cdots & 0^{3\times3} \\ 0^{3\times3} & H_0 & \cdots & 0^{3\times3} \\ \vdots & \vdots & \ddots & \vdots \\ 0^{3\times3} & 0^{3\times3} & \cdots & H_0 \end{bmatrix}, \qquad H_0 = \begin{bmatrix} 1 & -1 & 0 \\ 0 & 1 & -1 \\ -1 & 0 & 1 \end{bmatrix}. \tag{2.7}$$

The bus admittance matrix Y_{bus} is composed of the primitive admittance matrices as

$$Y_{\text{bus}} = A_{\text{icd}}^{\intercal} \text{diag}(Y_{\text{branch}}) A_{\text{icd}} \,, \tag{2.8}$$

where A_{icd} is the network incidence matrix [140]. The admittance matrix is generally sparse, with a characteristic block structure (see Figure 2.2), as the degree of most nodes is usually small. (Note that if any of the delta loads are zero then the corresponding row of H_{Δ} can then be removed from (2.7).)

The solution of the load flow problem in a multiphase network consists of the complex voltages V at each node [139]. From this, the branch currents and losses can be calculated (from (2.4)), as well as losses, line-line voltages, voltage unbalance and load currents. Therefore, for the purposes of this work, the load flow problem (2.6) is summarised as

$$V = G_{\text{LF}}(S_{\text{bus}}) \,, \tag{2.9}$$

where S_{bus} is a concatenation of the wye- and delta-connected power injections $S_{\curlyvee}$, S_{Δ},

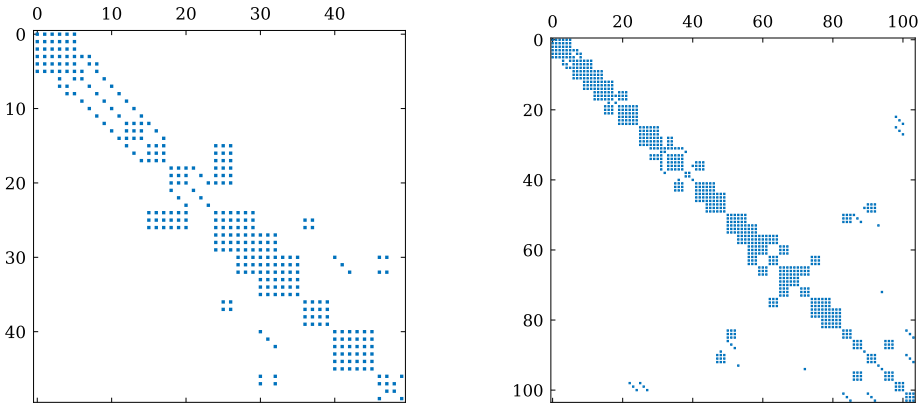

(a) IEEE 13 bus network (b) IEEE 34 bus network

Figure 2.2: A 'spy' plot of admittance matrix sparsity patterns, with i, j indicated with a dot if there is a non-zero matrix element. This demonstrates (i) relatively high levels of sparsity, (ii) a block-like structure, and (iii) symmetry in the sparsity pattern.

and G_{LF} is the load flow function. (Although there are generally multiple solutions to (2.9), uniqueness can be enforced by restricting the co-domain of G_{LF}, as in [139].)

Taps and the load flow problem Tap controls are not included within the multiphase load flow problem. Changing taps changes the gain matrix of the regulator transformers. This alters their primitive admittance and subsequently the system admittance matrix. Taps are therefore often chosen 'outside the loop'—once the load flow has been solved, the tap position is updated as specified by control logic. The load flow is then rerun with the updated position until convergence.

The order of operations of this control can be non-trivial, as there are often multiple feasible tap combinations, and so the order of operation of taps matters. The study of this operation is the focus of detailed QSTS analysis [49] and is beyond the scope of this work.

2.4.2 Multiphase Network Linear Models

Given the power flow problem (2.9), a power flow linearization takes the form

$$V = M_S S_{\text{bus}} + a\,, \qquad M_S = \begin{bmatrix} M_\curlyvee & M_\Delta \end{bmatrix} \tag{2.10}$$

where M_S, a represent the linear sensitivity and offset matrices, and $M_\curlyvee$, M_Δ are the sensitivity matrices with respect to the wye- and delta-connected loads respectively. Representations of V and S_{bus} can be in either rectangular or polar coordinates [141].

Traditional methods of power system linearization include DC power flow [142], Linear Coupled Power Flow [141], and LinDistFlow [58]. Other methods have also recently been proposed, such as the linear load flow in rectangular coordinates [143], and linear load flow considering logarithmic scaling [144]. These traditional methods of power flow linearization are focussed on balanced equivalent models (or symmetric models), and therefore extensions are required if arbitrary connections are considered (e.g., a mixture of wye- and delta- loads).

For works which study three-phase linearizations, models are now classified as analytic, approximate, or data-driven.

Analytic Methods Analytic methods utilise the power flow equations explicitly, and sensitivities are calculated using vector calculus. Methods based on Taylor series expansions (i.e., for calculating the Jacobian) include the method of [139] and of [145], although the latter does not consider delta connected loads. The authors of [139] also develop a novel fixed-point based linearization, with the model being particularly attractive as (i) it provides a 'global approximant', which may reduce error in some instances, and (ii) building the linearization matrices using the fixed-point method requires a matrix inverse which is four times smaller than calculating the Jacobian explicitly. In [146] a linearization is developed that accounts for PV (voltage controlled) buses explicitly, but the analysis is limited to small-scale test networks and error analysis is not considered.

Approximate Methods Approximate methods are based on the fact that power systems locally behave linearly, with non-linearity only significantly impacting on results when loads are large. The method of [147] approximates ZIP loads as a constant current and a constant impedance term. The method of [148] makes three approximations, assuming that phase angle and voltage deviations in the solution

are small (so that second order terms can be neglected), and that load models are approximately linear in voltage magnitude. A small error is shown in the case study considered by the authors. In [149] the author develops a method based on the assumption that voltage magnitudes remain close to unity, although again there is no systematic study of the error properties.

Data-driven Methods The data-driven approach linearizes based either on known load flow solutions or on measurements taken from field measurements. One such method is the so-called perturb-and-observe approach: for each variable of interest the linearization is evaluated using (non-linear) load flow evaluations, with the sensitivity matrices found using a central-difference based method [150]. That is, the sensitivity to changes in a variable x are given by

$$\frac{\partial f(x)}{\partial x} \approx \frac{f(x+\delta x) - f(x-\delta x)}{2\delta x}\,. \tag{2.11}$$

However, there are challenges associated with this approach in systems with very large numbers of variables, as the number of non-linear evaluations of (2.11) that are required increases with the number of buses. Other data driven methods find sensitivities using only smart meter measurements [151] or inverter measurements [152].

The benefits of each of these methods varies with the application. Therefore, in Chapters 4 and 5 (both of which utilise a linear model) the appropriate model shall be chosen for the application at hand.

2.5 Distribution Network Case Studies

It is well known that the properties of the network have a significant impact on the effectiveness of reactive power control for voltage control and loss minimization. Therefore, a range of networks are studied in this thesis.

In total, seventeen networks are studied, with the properties of these networks

summarised in Table 2.1. These cases include both US and European-style networks (LV networks in European-style networks have many more loads than US-style networks [56, Ch. 1.6]). The complexity of a feeder can be considered to be dependent on the number of loads, the number of nodes, and the number of controls (regulators and capacitors).

It is interesting to note that the IEEE feeders are outliers in terms of regulators: in a survey of 216 US feeders, 80.1% of them did not have a regulator in the feeder itself [153]. Note that, for the purposes of this thesis, the tap changer at the primary substation at the head of a feeder is referred to as a (voltage) regulator.

Each of the feeders are available in OpenDSS natively, with the exception of the EULVa network and Network 10. (The latter two circuits are created assuming all individual feeders from Network 1 and 10 of [154] all share a single secondary transformer.) These networks are deliberately chosen to ensure the repeatability of calculations with the minimum possible overhead.

IEEE Test Feeders The first five networks are from the IEEE Test Feeders set. Some of these circuits are based on real feeders, and some are deliberately heavily unbalanced. For example, the IEEE 13 Bus network is a heavily unbalanced feeder for evaluating the performance of load flow solvers under heavily unbalanced conditions; the 8500 Node feeder, on the other hand, is based on a real feeder and is designed for demonstrating the scalability of control algorithms [155].

EPRI Circuits 5, 7, 24 and J1, K1, M1 EPRI has released 6 feeders for the study of the impacts of DERs on distribution networks. These are reported as being the largest publicly available distribution network testbeds in [156]—the scale of EPRI Circuit 24 is like that of the 8500 Node network.

Electricity Northwest LV Networks The final set of networks are from the Low Voltage Network Solutions project. These feeders were developed for developing an understanding of the impact of DERs on LV networks.

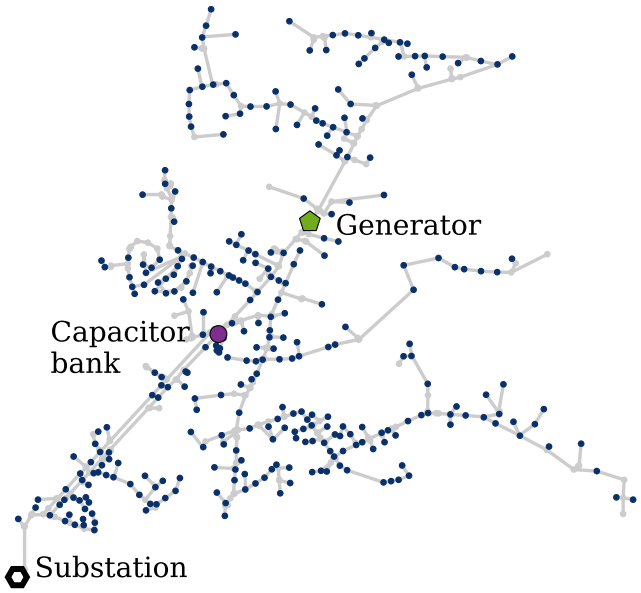

Figure 2.3: The EPRI K1 feeder

2.5.1 The EPRI K1 Circuit

The EPRI K1 circuit [157] is used as a recurring case study through this thesis. This network has modest complexity: it has a single gang-operated load tap changer (regulator) at the substation, a fixed capacitor, and two separate feeders coming from the primary substation (the second feeder is modelled as a lumped load at the substation). There is a mixture of commercial and residential load. This feeder has a 1 MW generator proposed at a location two miles from the substation (see Figure 2.3). The feeder is particularly suited to case studies as it is of modest complexity, is a real network, and contains regulator controls which are important for the study of voltage regulation problems.

Table 2.1: The circuits studied in this thesis and the chapters in which they appear. 'Regs.' refers to the number of regulator controls for a given feeder (including load tap changers at primary substations).

Feeder	Loads	Nodes	Median load, kW	Tot. Power, MW	Length, km	Regs.	Caps.	Ch. 3	Ch. 4	Ch. 5	Ref.
13 Bus	15	95	194.2	3.6	1.5	3	2		∘		IEEE, [155]
34 Bus	68	117	11.3	2.0	50	6	2	∘	∘		IEEE, [155]
123 Bus	92	278	44.7	3.6	3	7	4		∘	∘	IEEE, [155]
8500 Node	2355	8541	3.72	12.1	6	12	4		∘		IEEE, [155]
EU LV	55	1170	1.05	0.055	0.7	0	0	∘	∘		IEEE, [155]
Ckt. J1	1384	4245	3.1	11.6	18	9	5		∘		EPRI, [157]
Ckt. K1	332	1751	4.5	12.7	7	1	1	∘	∘	∘	EPRI, [157]
Ckt. M1	1470	3153	3.8	15.7	3.4	1	3		∘		EPRI, [157]
Ckt. 5	1379	3437	5.5	16.3	5	0	4		∘	∘	EPRI, [158]
Ckt. 7	868	2452	4.2	19.3	4	0	2		∘	∘	EPRI, [158]
Ckt. 24	3891	7522	1.5	69.4	10	1	3		∘		EPRI, [158]
N1.F1	55	2721	1.05	0.055	0.3	0	0		∘		ENWL, [154]
N2.F1	175	6861	1.05	0.175	0.5	0	0		∘		ENWL, [154]
N3.F1	94	3912	1.05	0.094	0.45	0	0		∘		ENWL, [154]
N4.F1	24	1125	1.05	0.024	0.18	0	0		∘		ENWL, [154]
EULVa	200	9444	1.05	0.200	0.7	0	0			∘	ENWL, [154]
Ntwk. 10	64	8214	1.05	0.064	0.4	0	0			∘	ENWL, [154]

Chapter 3

Methods for Characterising Impacts of Reactive Power Control on Curtailment and Losses

In this chapter, the following research question is addressed:

How can the impact of inverter reactive power control on the efficiency of distributed generation be analytically characterised, considering power flow up to the maximum power transfer point?

The two-bus model is particularly well suited to the research question, as the load flow solution of this network has a closed-form, analytic solution. The efficiency of distributed generation is considered in terms of the total power transferred to a transmission network (that is, the fraction of power that is not lost as thermal ('load') losses).

The load flow solution shall be considered in terms of the 'Exact' and 'LinDistFlow' approaches; the former represents the closed-form, non-linear solution of the two-bus load flow equations, whilst the latter approach (originally proposed by Baran and Wu [50]) is a linearization of the load flow equations that assumes relatively small losses. The linearity of the LinDistFlow model makes it easier to analyse algebraically, at

the cost of some linearization error.

This first contribution of this chapter takes the form of a consideration of the qualitative and quantitative properties of the maximum power transfer in lossy networks. The aim is to consider the properties of the maximum power transfer in a distribution network, and crucially, how the lossiness of the network and reactive requirements change at this point (compared to transmission network maximum power transfer). The study of this problem is pertinent for the study of losses because (i) the maximum power transfer point is shown to be caused by losses in many cases (rather than a stability limit), and (ii) it gives the widest possible range of powers that generators could operate over, and so conclusions can be made on the two-bus model with full generality. The first half of the chapter is concluded by considering a method to represent real distribution networks as a two-bus model, and then demonstrating the predictions made by the two-bus model are accurate on an unbalanced IEEE test feeder.

The second half of this chapter considers the impact of reactive power control on losses when the amount of available reactive power increases from a 'base' to a 'change' case. The relative loss fraction is proposed to study how losses change when reactive power control is introduced (i.e., increased) in a system.

The main contribution with this topic is the derivation and validation of an analytic method for calculating *bounds* on the relative loss fraction. The bounds are based on the LinDistFlow load flow solution, and two complementary validation steps are carried out. Firstly, the properties and numerical values of the bounds are compared against the analytic bounds that are calculated using the Exact two-bus load flow solution. This first validation considers what fraction of the derived maximum power transfer point can be reached and the LinDistFlow solution remain accurate.

Secondly, a set of pertinent case studies demonstrate that the numerical predictions of the proposed bounds are accurate in terms of a range of network parameters. These relative loss fraction bounds are particularly useful for network planners and operators as they provide a fast, analytic method to identify numerically the impact

of parameters that will lead to unavoidable losses, if reactive power is used for voltage control.

Chapter roadmap In Section 3.1 the two-bus network is described. The LinDistFlow and Exact load flow solutions are given as these are used throughout the rest of this chapter. In Section 3.2 the maximum power transfer is parametrised in terms of the R/X ratio, and the qualitative properties investigated in terms of this parameter to understand the implications for distribution networks. This is followed in Section 3.3 by the description of a proposed method for converting distribution networks to a two-bus representation for further analysis, so that two-bus calculations can be made on unbalanced distribution networks. Section 3.4 demonstrates the maximum power transfer point on a full distribution network model, to illustrate that losses do cause maximum power transfer. In Section 3.5 the relative energy loss fraction is introduced, for comparing network losses with and without reactive power control. Bounds on this relative loss fraction are derived in Section 3.6 using the LinDistFlow load flow solution, for quick analysis of the impact of losses on reactive powers. In Section 3.7 a set of detailed time series analysis are carried out on three feeders, representing a wide range of network parameters, to validate the predictions made by the two-bus model. A summary of the contributions from this chapter is given in Section 3.8.

3.1 Two-Bus Load Flow in Distribution Networks

In this section, the two-bus network model is introduced. The two load flow solution to this (the Exact and LinDistFlow models) are also given, as these form the basis of the rest of this chapter.

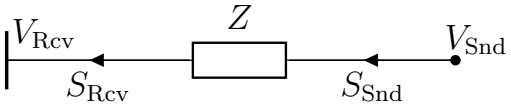

Figure 3.1: Two-bus power flow model (sign convention as indicated).

3.1.1 The Two-Bus Network Model

The two-bus load flow problem is plotted in Figure 3.1[1]. The impedance of the line is given as $Z = R + \jmath X$ and the network resistance and reactance are given by R, $X \in \mathbb{R}^+$. $V_{\text{Rcv}} \in \mathbb{R}$ is the fixed reference voltage at the receiving node, usually the substation. $V_{\text{Snd}} \in \mathbb{C}$ denotes the voltage at the sending node, usually a generator bus. $S_{\text{Rcv}}, S_{\text{Snd}} \in \mathbb{C}$ represent the apparent power at the receiving and sending bus respectively. The operators $(\cdot)^*$, $|\cdot|$, $\angle(\cdot)$ denote complex conjugate, magnitude, and argument respectively. The short-circuit power is given by $S_{\text{SC}} = |V_{\text{Rcv}}|^2/|Z|$.

Throughout the thesis, there is always a generator at the 'sending' bus (sending bus quantities are given the subscript $(\cdot)_{\text{Snd}}$), and sometimes a load. The 'receiving' bus models a primary distribution substation, which sends power to the upstream transmission (or subtransmission) network (quantities associated with this bus use the subscript $(\cdot)_{\text{Rcv}}$).

In this chapter the R/X ratio is of particular interest, as this value varies significantly between networks. This parameter is given the symbol λ, i.e.,

$$\lambda = R/X\,. \tag{3.1}$$

Complex powers are decomposed into real and reactive power injections as

$$S_{(\cdot)} = P_{(\cdot)} + \jmath Q_{(\cdot)}\,. \tag{3.2}$$

[1]The two-bus model used through this thesis uses a series impedance model, as is common in analytic distribution network analysis [77, Ch. 2]. This ignores shunt capacitance which is often modelled using 'π-model' (see, e.g., [140, Ch. 6]).

3.1.2 Two-Bus Load Flow Solutions

The two-bus model can be solved exactly. The solution (derived in the appendix, Section A.1.1) can be given in terms of voltage magnitude at the sending bus $|V_{\mathrm{Snd}}|$ and real power losses P_{lss} as

$$|V_{\mathrm{Snd}}|^2 = S_{\mathrm{SC}}|Z| \left(\frac{\lambda P_{\mathrm{Snd}} + Q_{\mathrm{Snd}}}{S_{\mathrm{SC}}\sqrt{1+\lambda^2}} + \frac{1}{2} \pm D, \right) , \tag{3.3}$$

$$P_{\mathrm{lss}} = S_{\mathrm{SC}} \frac{\lambda}{\sqrt{1+\lambda^2}} \left(\frac{\lambda P_{\mathrm{Snd}} + Q_{\mathrm{Snd}}}{S_{\mathrm{SC}}\sqrt{1+\lambda^2}} + \frac{1}{2} \mp D \right) , \tag{3.4}$$

where D is given by

$$D = \sqrt{\frac{1}{4} + \frac{\lambda P_{\mathrm{Snd}} + Q_{\mathrm{Snd}}}{S_{\mathrm{SC}}\sqrt{1+\lambda^2}} - \frac{(-P_{\mathrm{Snd}} + \lambda Q_{\mathrm{Snd}})^2}{S_{\mathrm{SC}}^2(1+\lambda^2)}} \tag{3.5}$$

The solutions (3.3), (3.4) is referred to from here as the 'Exact' solution of the two-bus problem.

An alternative, approximation load flow solution is the LinDistFlow solution (as discussed in Section 2.1.1). Voltages and losses are given by [159]

$$|V_{\mathrm{Snd,\,LDF}}|^2 = |V_{\mathrm{Rcv}}|^2 + 2(P_{\mathrm{Snd}}R + Q_{\mathrm{Snd}}X) \tag{3.6}$$

$$P_{\mathrm{lss,\,LDF}} = R\frac{P_{\mathrm{Snd}}^2 + Q_{\mathrm{Snd}}^2}{|V_{\mathrm{Snd}}|^2}. \tag{3.7}$$

The approximate load flow solution given by (3.6), (3.7) shall be referred to as the 'LinDistFlow' solution.

For the first half of this chapter (considering maximum power transfer) the Exact solution shall be used, as the power flows at the maximum power transfer point are large.

The following useful identities are also derived in the appendix (Section A.1.1):

$$P_{\text{lss}} = \frac{\lambda}{\sqrt{1+\lambda^2}}\left(\frac{|V_{\text{Rcv}}|^2 - |V_{\text{Snd}}|^2}{|Z|} + 2\frac{\lambda P_{\text{Snd}} + Q_{\text{Snd}}}{\sqrt{1+\lambda^2}}\right) \tag{3.8}$$

$$\left(P_{\text{Snd}} - \frac{R|V_{\text{Snd}}|^2}{|Z|^2}\right)^2 + \left(Q_{\text{Snd}} - \frac{X|V_{\text{Snd}}|^2}{|Z|^2}\right)^2 = \left(\frac{|V_{\text{Rcv}}||V_{\text{Snd}}|}{|Z|}\right)^2. \tag{3.9}$$

3.2 Maximum Power Transfer in the Two-Bus Network

The aim of this section is to consider how the properties of the maximum power transfer point vary with the R/X ratio, and what can be deduced about losses in distribution networks from this model. This analysis will utilise the Exact load flow model. First, two heuristics are considered for the calculation of maximum power transfer, assuming either fully resistive or inductive lines. Following from this the true maximum power transfer is derived and then the properties studied.

3.2.1 Heuristics for Maximum Power Transfer

By taking the difference between the sending power and the losses (calculate from (3.8)) the power received at the substation can be parametrized in terms of λ as

$$\begin{aligned} P_{\text{Rcv}} = P_{\text{Snd}}\left(\frac{\lambda^{-1} - \lambda}{\lambda + \lambda^{-1}}\right) - Q_{\text{Snd}}\frac{2}{\lambda + \lambda^{-1}} \\ + \frac{(|V_{\text{Snd}}|^2 - |V_{\text{Rcv}}|^2)}{|Z|}\frac{\lambda}{\sqrt{\lambda^2+1}}. \end{aligned} \tag{3.10}$$

The maximum power transfer cases for mostly inductive or mostly resistive lines are now considered.

3.2.1.1 Unity Power Factor Control

Consider a resistive line such that the R/X ratio $\lambda \to \infty$. Then,

$$\lim_{\lambda \to \infty} P_{\text{Rcv}} = -P_{\text{Snd}} + \frac{|V_{\text{Rcv}}|^2 - |V_{\text{Snd}}|^2}{|Z|} \,. \tag{3.11}$$

This demonstrates that, if a voltage limit has been reached (such that $(|V_{\text{Rcv}}|^2 - |V_{\text{Snd}}|^2)/|Z|$ is a constant), then P_{Snd} should be *minimized* along the locus of points described by (3.3) (all of which give a constant value of $|V_{\text{Snd}}|$). In other words, even if the marginal cost of power is zero, one should refrain from using reactive power to generate additional power, because the real power losses increase at a greater rate than the rate at which additional real power is generated.

Using little or no reactive power agrees with how distribution networks are traditionally operated. This heuristic of setting $Q_{\text{Snd}} = 0$ is referred to as Unity Power Factor (UPF) control. That is, once a voltage limit is reached, additional generated real power is curtailed. At this point the sent real power is given by

$$P_{\text{Snd, UPF}} = \frac{|V_{\text{Snd}}|^2}{|Z|} \left(\frac{\lambda}{\sqrt{\lambda^2 + 1}} - \sqrt{\frac{\lambda^2}{\lambda^2 + 1} - \left(1 - \frac{|V_{\text{Rcv}}|^2}{|V_{\text{Snd}}|^2} \right)} \right) \,, \tag{3.12}$$

which is found by setting $Q_{\text{Snd}} = 0$ in (3.3) and solving for P_{Snd}.

3.2.1.2 Solution Boundary ('Stb') Control

In the case $\lambda \to 0$, (3.10) yields

$$\lim_{\lambda \to 0} P_{\text{Rcv}} = P_{\text{Snd}} \,,$$

as expected. Therefore, reactive power should be used to simply avoid voltage violations, as there is no cost (in a real power sense) of increasing the reactive power.

If the real power continues to increase then the stability boundary will be reached (i.e. 'critical points', or the 'knee' of the P-V curve [160]). If a converter controls

the complex power, then this will limit power transfer, as the gradient is unbounded. These points occur when the discriminant in (3.3) and (3.4) is equal to zero. It is shown in the appendix (Section A.1.2) that the received power when this happens is given by

$$P_{\mathrm{Rcv,\,Stb}} = \frac{|V_{\mathrm{Rcv}}|^2}{|Z|}.\frac{1}{\sqrt{1+\lambda^2}}\left(-\frac{\lambda}{2}+\sqrt{\frac{|V_{\mathrm{Snd}}|^2}{|V_{\mathrm{Rcv}}|^2}-\frac{1}{4}}\right). \tag{3.13}$$

3.2.2 Voltage Constrained Maximum Power Transfer

The point of maximum power transfer point is defined by the optimization

$$\max_{S_{\mathrm{Snd}}} \quad P_{\mathrm{Rcv}} \tag{3.14a}$$

$$\text{s.t.} \quad |V_{\mathrm{Snd}}| \leq V_+ \,. \tag{3.14b}$$

The solution to (3.14), $S_{\mathrm{Snd,\,MPT}}$, is derived in the appendix (Section A.1.3) and is given by

$$P_{\mathrm{Snd,\,MPT}} = \frac{V_+^2}{|Z|}.\frac{1}{\sqrt{1+\lambda^2}}\left(\lambda+\frac{1-\lambda^2}{\sqrt{1+\lambda^2}}.\frac{|V_{\mathrm{Rcv}}|}{V_+}\right), \tag{3.15}$$

$$Q_{\mathrm{Snd,\,MPT}} = \frac{V_+^2}{|Z|}.\frac{1}{\sqrt{1+\lambda^2}}\left(1-2\frac{\lambda}{\sqrt{1+\lambda^2}}.\frac{|V_{\mathrm{Rcv}}|}{V_+}\right), \tag{3.16}$$

with the corresponding received power, $P_{\mathrm{Rcv,\,MPT}}$, given by

$$P_{\mathrm{Rcv,\,MPT}} = \frac{|V_{\mathrm{Rcv}}|^2}{|Z|}\left(\frac{V_+}{|V_{\mathrm{Rcv}}|}-\frac{\lambda}{\sqrt{1+\lambda^2}}\right). \tag{3.17}$$

The maximum of (3.14a) is reached when the marginal increase in losses is greater than the marginal increase in generated power P_{Snd}. Real power generation should always be curtailed beyond $P_{\mathrm{Snd,\,MPT}}$ due to these marginal losses, even if additional power could be generated.

As was identified in the literature review, the properties of the maximum power transfer in distribution networks has not been studied in previous works. The voltage-constrained maximum power transfer point is now compared to the Maximum Power

Transfer Theorem, then to UPF and stability-constrained control described previously. Finally, the power factor and thermal efficiency of generation is then considered, to consider the practicalities of operating at the voltage-constrained maximum power transfer point.

3.2.2.1 Comparison with the Maximum Power Transfer Theorem

The Maximum Power Transfer Theorem (or, 'Impedance Matching Theorem' [78]) states that the impedance that draws the greatest load from a voltage source through an impedance Z is given by Z^*. The theorem does not consider operating constraints (i.e. voltages) [161]. The LinDistFlow equations suggest that an unconstrained maximum power will exist in the two-bus model as well—the losses are quadratic in generation (from (3.7)), and so at some point the losses will increase at a greater rate than generation.

However, the Exact model shows that unconstrained maximum power transfer is unbounded. To see this, note that received power at the substation for a given voltage constrained maximum power transfer is an affine function of the upper voltage limit (from (3.17)). As such, if there is no voltage limit, then the maximum power that can be received by the grid is unbounded. This apparent contrast with the Maximum Power Transfer Theorem is because it is generation, rather than load, which is being considered.

3.2.2.2 Comparison with UPF and Stability Boundary Control

Figure 3.2 plots the maximum power transfer points in terms of both the generated and sent power, across a range of R/X ratio λ (for two-bus parameters $|Z| = 1$, $V_+ = 1.05$, $V_{\text{Rcv}} = 1.0$). The purpose of this figure is to consider the range of validity of the two heuristic methods (UPF and 'Stability' control), in comparison to the voltage-constrained maximum power transfer point.

For resistive networks (high λ) the true maximum power transfer approaches that of UPF control, with little use for reactive power. As λ is reduced below 10, the

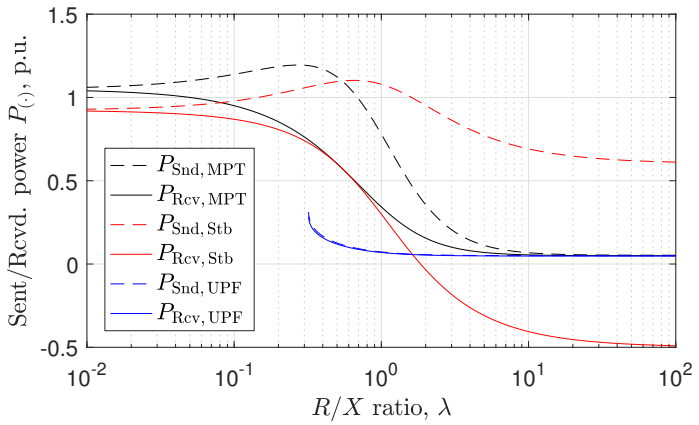

Figure 3.2: Comparison of heuristic methods and the marginal loss-induced maximum power $P_{\mathrm{Snd,\,MPT}}$. Parameters are set as $V_{\mathrm{Rcv}} = 1.0, V_{+} = 1.05, |Z| = 1$. Powers calculated with the true maximum power transfer values (3.15) are denoted by $(\cdot)_{\mathrm{MPT}}$; powers calculated using unity power factor control (3.11) are denoted $(\cdot)_{\mathrm{UPF}}$; powers calculated at the stability boundary (3.10) are denoted $(\cdot)_{\mathrm{Stb}}$,

maximum generation point $P_{\mathrm{Snd,\,MPT}}$ starts to increase, approaching the stability boundary generation $P_{\mathrm{Snd,\,Stb}}$. Eventually, as the R/X ratio λ drops further the maximum generated power surpasses the stability boundary generation—that is, it moves from the 'high voltage, low loss' solution to the 'low voltage, high loss' solution.

The R/X ratio at which the stability generation is less than the voltage-constrained maximum power transfer, denoted by λ_{Stb}, is found from (3.17) and (3.13) as

$$\lambda_{\mathrm{Stb}} = \frac{1}{\sqrt{4\dfrac{V_{+}^{2}}{|V_{\mathrm{Rcv}}|^{2}} - 1}}. \tag{3.18}$$

For the parameters chosen here, $\lambda_{\mathrm{Stb}} = 0.542$, as in Figure 3.2. If $V_{\mathrm{Rcv}} = 1$, $V_{+} \in [0.9, 1.1]$, then $\lambda_{\mathrm{Stb}} \in [0.51, 0.67]$. When $|V_{\mathrm{Rcv}}| = |V_{\mathrm{Snd}}|$, $\lambda_{\mathrm{Stb}} = 1/\sqrt{3}$.

As discussed previously, in this region where $P_{\mathrm{Snd,\,MPT}} > P_{\mathrm{Snd,\,Stb}}$, the network is being operated in a region that is associated with stability issues [78], so it will not be feasible to operate in this region. In other words, in the case $\lambda \leq \lambda_{\mathrm{Stb}}$ stability will become a problem prior to voltage-constrained maximum power transfer.

In contrast to stability control, using no reactive power (UPF control) always leads to less received power. However, there are regions for which this control in fact

yields no solution, as the upper voltage constraint is never reached. For example, for a purely inductive line, injecting a small amount of real power with no reactive power leads to a reduction in voltage. The critical R/X ratio for which there is no solution for UPF control is denoted by λ_{UPF}, calculated as

$$\lambda_{\mathrm{UPF}} = \sqrt{\frac{V_+^2}{|V_{\mathrm{Rcv}}|^2} - 1} \tag{3.19}$$

If $V_{\mathrm{Rcv}} = 1$, $V_+ \in [1.01, 1.2]$, then $\lambda_{\mathrm{UPF}} \in [0.141, 0.663]$. It is concluded that UPF control is only a good model for high R/X ratios (for λ roughly greater than 10).

3.2.2.3 Thermal Efficiency and Reactive Power Utilisation at Loss-Induced Maximum Power Transfer

Thermal efficiency and power factor at the receiving bus are indices that represent the 'performance' of the network in some sense. The efficiency operating at the maximum power transfer point for a range of R/X and voltage parameters is shown in Figure 3.3a. For very resistive or very inductive lines, $P_{\mathrm{Rcv,\,MPT}}$ is generally efficient with $P_{\mathrm{Rcv,\,MPT}}/P_{\mathrm{Snd,\,MPT}} > 90\%$ for a range of powers. However, for λ from 0.4–2 the efficiency of exported power is less than 60%.

The power factor at the sending (generating) bus is shown in Figure 3.3b. Low power factors require the oversizing of the inverter to which are generators connected. For intermediate R/X ratios λ from 0.3-1.0 the power factor at the generator at the maximum power transfer point is above 0.9. In other words, in these regions, an inverter would not have to be over-sized too much for large generators to reach the maximum power transfer point. In this region, the relatively low thermal efficiency and stability limit λ_{Stb} may instead result in uneconomical (or infeasible) operation of generators.

The power factor at the receiving bus (substation) follows a similar pattern and so is not plotted. Poor power factors at the substation increase the reactive power drawn from the transmission network, which is typically very 'lossy' with respect to

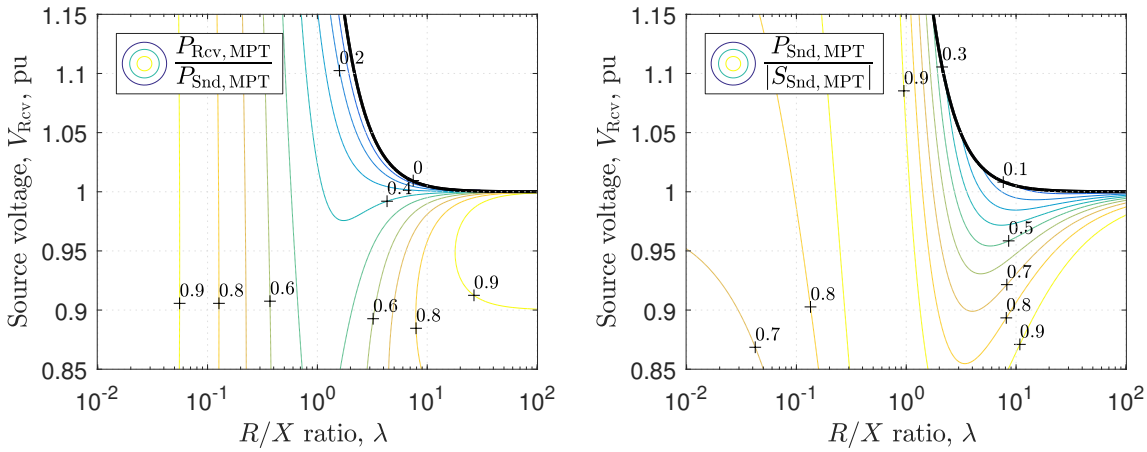

(a) Efficiency

(b) Sending (generator) bus power factor

Figure 3.3: Performance metrics at the loss-induced maximum power transfer point, with $V_+ = 1$. (a) Thermal efficiency (zero if positive real power cannot be transferred). (b) Power factor of the generator.

reactive power due to high X/R ratios. Additionally, this requires the substation transformer to be oversized, and there can be stability challenges associated with distribution networks that draw large amounts of reactive power [84].

Regions of interest in distribution networks Considering the previous analysis, it is concluded that the maximum power transfer point demonstrates that losses are likely to become relevant in many networks. As discussed, for unity voltage regulation (i.e., $|V_{\text{Rcv}}| = |V_{\text{Snd}}|$), this transition from stability- to loss-constrained networks occurs at $\lambda = 1/\sqrt{3}$ (around 0.58).

It is yet to be seen if the predictions made by the two-bus model about the maximum power transfer point hold true in an unbalanced distribution system model. Therefore, a method for representing a distribution network as a two-bus model is presented next, before case studies are considered to demonstrate that losses can result in maximum power transfer.

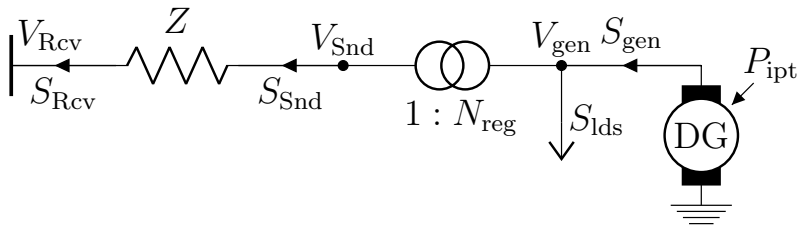

Figure 3.4: Two-bus power flow model considering a generator located within a distribution network. Two-bus parameters match the parameters described in the previous section. The additional parameters N_{reg}, S_{lds} model regulator taps and the network load respectively.

3.3 Converting Distribution Network Models to Two-Bus Representations

In this section a method is considered to convert full distribution network models to a two-bus representation. The model will be used to consider the accuracy of the maximum power transfer point first, as well as for studying losses directly in the second half of this chapter. There are four quantities that must be chosen for the two-bus approximation: the reference voltage, V_{Rcv}; the voltage at the sending node, V_{Snd}; the line impedance, Z; and the sending power, S_{Snd}.

Figure 3.4 is an augmented two-bus model, with additional network components for determining the required two-bus quantities. A regulator with turns ratio N_{reg} steps the voltage up to the voltage at the generator node V_{gen}. The available generating power for the distributed generator DG is P_{ipt}, which exports the complex power S_{gen}. (From Section 3.5, generator inverter constraints are considered so the available power P_{ipt} may not be the same as the generator power P_{gen}.) Finally, there is a load S_{lds}, modelling loads which are co-located with the generator. The calculation of each of these parameters is now considered.

3.3.1 Calculating Line Impedance Z

The impedance between two nodes in a circuit is called the Thévenin impedance [140, pp. 287-294]. To calculate this value, the impedance matrix $Z_{\text{bus}} \in \mathbb{C}^{n \times n}$ is first

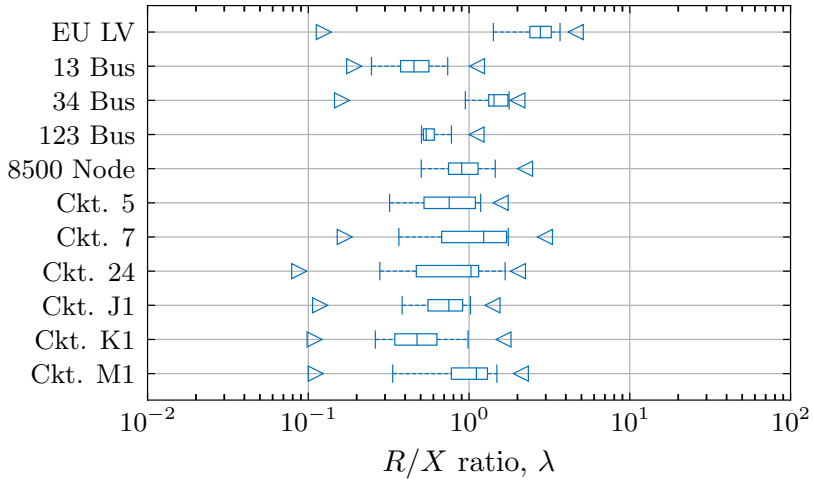

Figure 3.5: Boxplot of the positive sequence R/X ratios λ at all three-phase buses of a set of feeders, by calculating the equivalent Thévenin impedance to the voltage source.

obtained, which is defined as

$$V_{\text{bus}} = Z_{\text{bus}} I_{\text{bus}} \,, \tag{3.20}$$

where V_{bus}, $I_{\text{bus}} \in \mathbb{C}^n$ are the bus voltages and current injections respectively.

The Thévenin impedance between two nodes in single phase, per unit equivalent circuit (i.e. not considering transformers) is calculated by injecting current δI at the sending (generator) bus and $-\delta I$ at the receiving (substation) bus. The voltage drop δV is then calculated as $\delta V = V_{\text{bus}}^{\text{Src}} - V_{\text{bus}}^{\text{Snd}}$ from (3.20). The Thévenin impedance Z is then calculated as the ratio of these two quantities, $\delta V / \delta I$.

A boxplot of the R/X ratio λ of the Thévenin impedance between all three-phase buses and the grid is given in Figure 3.5 for a set of eleven networks. It is interesting to see that, although the R/X ratio λ of individual lines may be as great as 40 (for example, in the EU LV network), the R/X ratio of most networks is no greater than 5. The R/X ratio does not usually drop below 0.1 (a small number of nodes with very low R/X ratios are upstream of some substation transformers). For eight of the eleven networks the R/X is greater than 0.7, and so the two-bus model suggests that the maximum power transfer will be loss-constrained, rather than stability-constrained.

3.3.2 Two-Bus Network Voltages

Voltage regulators can act to increase or decrease voltages and currents. An ideal voltage regulator is modelled as a lossless element, and so the power into each terminal of the regulator is equal in magnitude (and opposite in sign). The voltage changes across a regulator according to the turns ratio as

$$\frac{V_{(\cdot),\,\mathrm{Reg}}}{V_{(\cdot)}} = N_{\mathrm{Reg}}\,, \tag{3.21}$$

where N_{Reg} is the regulator turns ratio and $V_{(\cdot),\,\mathrm{Reg}}$ is the voltage at the regulated bus. The current through the transformer changes by the same ratio. If there is a regulator at the head of the feeder or a regulator co-located very close to a generator, then the voltages on the feeder can therefore be modelled as stepping up/down the voltage at the head of the feeder or at the generator accordingly.

If there is a regulator at a mid-point of a feeder, then the approximation is made that it only acts to increase the voltage at the end of the feeder (as in Figure 3.4), and the effective change in impedance (due to changes to currents downstream of the regulator) is ignored. Where there are multiple operated single-phase regulators on a three-phase line, the mean of the turns ratio is taken. There will of course be some error introduced by each of these approximations,–a non-linear unbalanced system is being represented by a balanced system of just two buses. For example, it is shown in the Appendix section A.1.8 that aggregating regulators at the generator leads to some error being introduced in the calculation of both voltage drop and losses, although the error is demonstrated to be small relative the typical magnitudes of those variables.

3.3.3 Calculating the Line Power S_{Snd}

The final parameter to choose is the load power S_{lds}. This power is such that

$$S_{\mathrm{Snd}} = S_{\mathrm{gen}} - S_{\mathrm{lds}}\,. \tag{3.22}$$

If load is distributed along the length of a long feeder then it is not clear what this load should be chosen as. If the total feeder load is denoted by $S_{\text{lds, Tot}}$ then the load power is chosen according to

$$S_{\text{lds}} = k_S S_{\text{lds, Tot}} \tag{3.23}$$

where $k_S \in \mathbb{R}$ is a scale parameter.

It is proposed that k_S be chosen according to one of the following methods.

1. Full load ($k_S = 1$). The total feeder load is connected to generator node.

2. No load ($k_S = 0$). No load is connected at the generator node.

3. Weighted load. Load is connected according to the load flowing through the generator bus towards the substation $S_{\text{to sub}}$ as:

$$k_S = \frac{|Q_{\text{to sub}}|}{|Q_{\text{lds, Tot}}|}\,. \tag{3.24}$$

Only the Full load model will be used in the first half of the chapter (studying the maximum power transfer point), whilst all three of the models are utilised in the second half of this chapter. (In the Weighted load case, the reactive power is considered in (3.24) as it is shown in Section 3.6.2.1 that the reactive power of loads makes more of an impact on losses than the real power, when considering voltage control, as real power generation compensates the real power of the load in the control scheme considered there.) Note that other options could be explored beyond those described here—for example, considering real and reactive power separately.

3.4 Maximum Power Transfer Case Studies

In this section, the accuracy of the two-bus 'Exact' load flow solution is considered for a set of case studies on the IEEE 34 Bus test network. The aim is to evaluate if the predictions of the two-bus method hold true in a real distribution network.

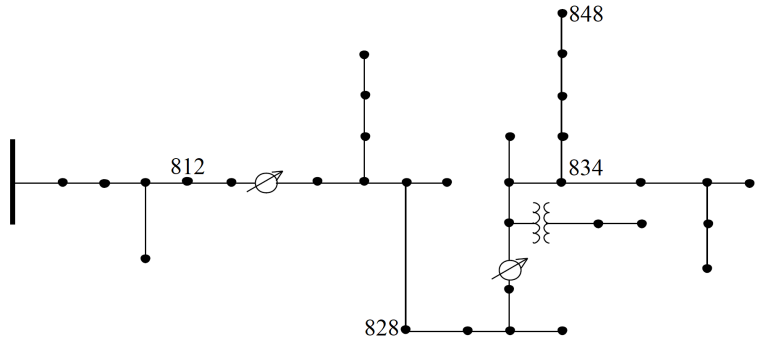

Figure 3.6: IEEE 34 Bus test distribution feeder and buses considered for case studies.

Table 3.1: Network Parameters (pu). $S_{\text{base}} = 2.5$ MVA, $V_{\text{base}} = 69$ kV.

Parameter	Bus 812	Bus 828	Bus 834	Bus 848
R/X ratio λ	1.41	1.52	1.85	1.87
Impedance magnitude $\lvert Z\rvert$, pu	0.078	0.119	0.203	0.203
Substation maximum power S_+, pu	1.0			
Max phase current I_+, A	180			
Maximum voltage V_+, pu	1.06			
Substation voltage V_{Rcv}, pu	1.05			
Total feeder load $S_{\text{lds, Tot}}$, pu	$0.72\angle 9.4°$			

In addition to the maximum power transfer point as caused by a voltage constraint, the maximum power transfer as caused by a current constraint will also be considered, $P_{\text{Snd, Imx}}$, which is caused when the maximum phase current in a network, $|I_{\max}|$ is equal to it's limit I_+ (permissible phase currents are taken from [162]). The maximum power through the substation S_+ will be assumed to be capped at the substation transformer rating (1 pu).

3.4.1 Case Study Network

For this case study the IEEE 34 Bus test feeder is used. Four buses are identified from this circuit for analysis (see Figure 3.6), with the two-bus parameters of each of these buses given in Table 3.1. There are a range of R/X ratios λ between these feeders, and the magnitude of the impedance $|Z|$ varies.

To calculate the maximum power transfer at each bus, a grid search method is chosen. A range of real and reactive powers are generated at the bus that is studied,

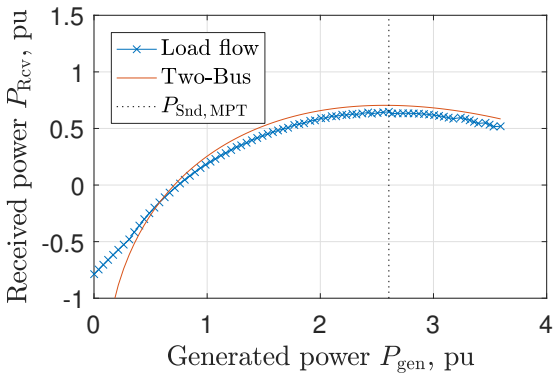

Figure 3.7: P_{gen} versus network power received at the substation P_{Rcv}.

and the losses and substation power recorded. This method is required as OpenDSS converts constant power loads (or generators) to constant impedance if the solver is not converging. The powers considered in these load flow studies are relatively large, and the solver often is therefore not able to converge in a number of cases considered. Because of the constant impedance model, the real and reactive power flows at the generator must therefore be found after convergence.

Once the mesh of load flow solutions is found, points for which the voltage constraint is not satisfied are removed. For each value of real power generated, the reactive power is chosen which maximises the real power transferred through the substation. This procedure yields the curve shown in Figure 3.7. The solution as found by the two-bus model for a fixed generator voltage $|V_{\text{Snd}}|$ is also plotted, assuming all load is located at the generator ($k_S = 1$). The generator powers are relatively large compared to the nominal load, and so this was found to be a good approximation. It is observed that the two-bus model corresponds well to the behaviour seen at high generator powers.

Figure 3.8a shows the maximum network phase current and predicted currents. Vertical lines indicate the values of $P_{\text{Snd, MPT}}$ and $P_{\text{Snd, Imx}}$ as found by the mesh of load flow solutions from OpenDSS. The network is not overloaded at the measured value of $P_{\text{Snd, MPT}}$, as the maximum network current is below the permitted value. It is noted that the voltage constrained MPT $P_{\text{Snd, MPT}}$ is below the thermal limit $P_{\text{Snd, Imx}}$; generating at the higher thermal limit would yield less power transfer due

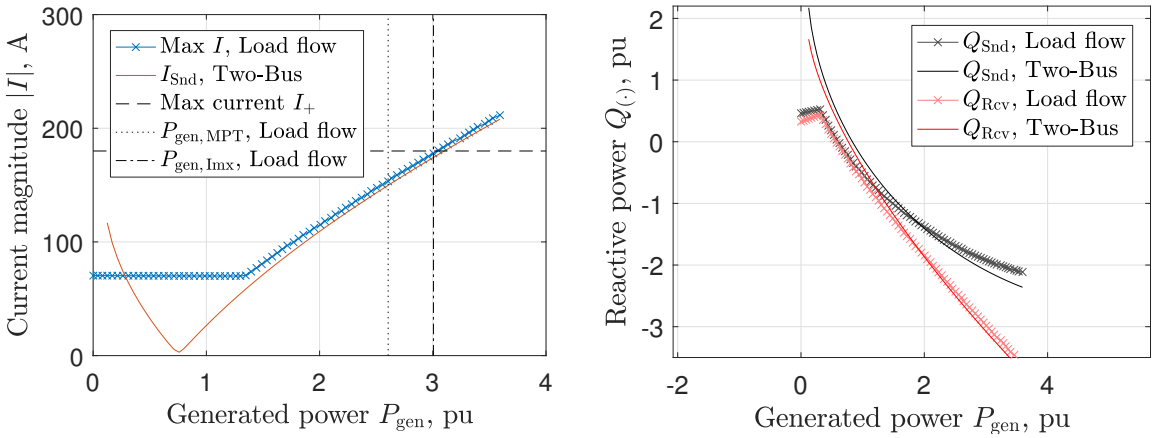

(a) Network currents

(b) Network reactive powers

Figure 3.8: Phase current and reactive power flows at bus 834 versus generated power P_{gen}. The maximum power transfer point is reached prior to the current limit in this case.

to increased losses.

Finally, in Figure 3.8b, estimated and measured reactive power flows are observed to be estimated reasonably well across a range of generated powers (again diverging at low generation). The reactive flows are much greater than 1 pu, and (by comparison with Figure 3.7) the power factor at the substation and generator are both very poor. A large amount of shunt compensation would be required at the substation to avoid overloading the transformer, and the inverter at the generator would require oversizing by a large amount. Thus, in this system the maximum power transfer point could be reached before a thermal limit on a line, but a large amount of compensation would be required to avoid overloading the substation.

3.4.1.1 Discussion: Model Accuracy

The maximum power transfer points for both voltage and current constraints are plotted in Figure 3.9 for all four considered locations. The relative error between the predicted and true values of both of these values is less than 15% in all cases, and the two-bus model correctly identifies if the thermal or voltage constraint causes the maximum power transfer at all buses.

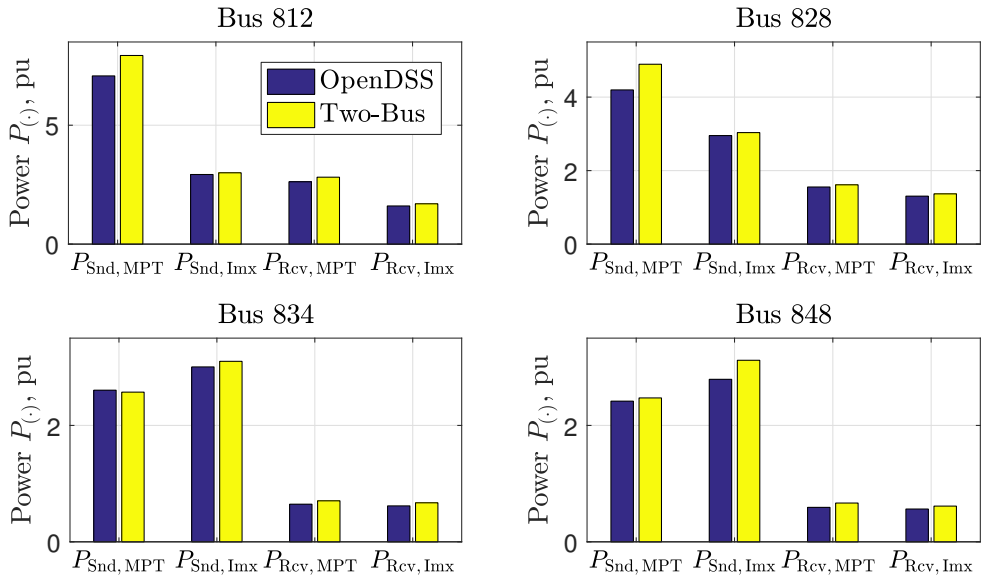

Figure 3.9: The marginal and thermal induced power transfer limits for four buses of the IEEE 34 Bus network. $S_{\text{base}} = 2.5$ MVA.

The conclusions about the maximum power transfer hold true in this case study. The qualitative nature of the results is accurate using the two-bus model, even with the simple method described here. Of course, detailed simulations are required for the most accurate results, but from this case study it is concluded that there are good opportunities to understand better the properties of distribution networks using the two-bus model.

It is concluded that the maximum power transfer point is an interesting point to study as it reveals a lot about the behaviour of distribution networks with reactive power control. The properties of the maximum power transfer vary significantly between networks, particularly for networks with R/X ratio greater than 0.7.

It has been demonstrated that the maximum power transfer capabilities of many distribution networks will be limited by losses. In the next section, the two-bus model is revisited to consider the behaviour with *small* amounts of reactive power and their impact on losses using the LinDistFlow model. The behaviour up to the maximum power transfer point will be considered to consider the range of validity of the LinDistFlow approximation.

3.5 Relative Loss Fractions Considering Voltage Control

For the rest of this chapter, the impact of reactive power is on *energy* losses as the primary topic of interest (rather than power losses). This means that the quantities of interest are defined over a range of time τ. The approach to this problem is similar, however, to that of the previous section: the energy losses are considered by studying the power losses of the two-bus model.

In this section, the quantities that will be studied to understand the impact of reactive power on losses will be introduced.

3.5.1 Reactive Power and Reducing Energy Curtailment

When reactive power is introduced into a network for voltage control, the generation and losses will change. The network power flows will be considered before and after changing some generator reactive power constraint. The case with the 'nominal' reactive constraint is referred to as the *base* case, with variables associated with this case denoted by the superscript $(\cdot)^{\text{base}}$. The case with an increased reactive power provision is called the *change* case, likewise denoted by superscript $(\cdot)^{\text{chng}}$. The superscript $(\cdot)^{[\text{case}]}$ is used to indicate conditions which hold for either the change and base case. The reactive power constraint for each case is indicated by $Q_{-}^{[\text{case}]}$, and the associated real power generated at this point is given by $\mathring{P}_{\text{gen}}^{[\text{case}]}$.

As the amount of reactive power that can be supplied by a generator for voltage control is increased, generation will be increased from the base power limit $\mathring{P}_{\text{gen}}^{\text{base}}$ to the new level of $\mathring{P}_{\text{gen}}^{\text{chng}}$ (Figure 3.10). The total amount of additional generated energy over the time period is denoted by ΔE_{gen}.

The useful, *net* power available to drive loads at any point in time P_{net} is the difference between the generated and losses,

$$P_{\text{net}} = P_{\text{gen}} - P_{\text{lss}}\,. \tag{3.25}$$

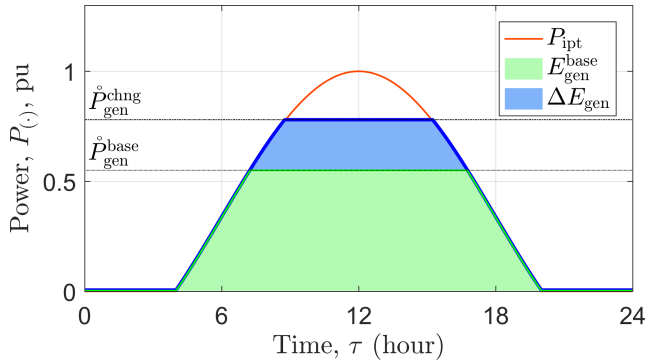

Figure 3.10: Increasing the reactive power available to a generator can reduce the curtailment, by increasing the maximum real power that can be generated from the base case, $\mathring{P}_{\text{gen}}^{\text{base}}$, to the change case, $\mathring{P}_{\text{gen}}^{\text{chng}}$, yielding additional generated energy ΔE_{gen}.

It is only the case that generated energy is a good metric if the losses component is small. Often losses are neglected as they can be challenging to measure accurately [55]. Additionally, it can be difficult to directly attribute losses to a specific 'cause' due to their inherent non-linearity [65]. Nevertheless, by making the assumption that loads (and any other generators) in the network are not controllable, then this attribution is meaningful [27, 63].

The remainder of this chapter considers methods for estimating if losses are significant across a range of R/X ratios in distribution networks. To consider this, the 'relative loss fraction' is first described.

3.5.2 The Relative Loss Fraction

The energy that can be generated by a generator E_{gen}, and the net generation E_{net}, are defined over a period T_τ as a function of the input power $P_{\text{ipt}}(\tau)$ and power constraint $\mathring{P}_{\text{gen}}^{[\text{case}]}$ as

$$E_{\text{gen}}^{[\text{case}]} = \int_0^{T_\tau} P_{\text{gen}}\left(P_{\text{ipt}}(\tau), \mathring{P}_{\text{gen}}^{[\text{case}]}\right) d\tau\,, \tag{3.26}$$

$$E_{\text{net}}^{[\text{case}]} = \int_0^{T_\tau} P_{\text{net}}\left(P_{\text{ipt}}(\tau), \mathring{P}_{\text{gen}}^{[\text{case}]}\right) d\tau\,, \tag{3.27}$$

The change control scheme results in an increase in actual and net generated energy compared to the base case as

$$\Delta E_{\text{gen}} = E_{\text{gen}}^{\text{chng}} - E_{\text{gen}}^{\text{base}}\,, \tag{3.28}$$

$$\Delta E_{\text{net}} = E_{\text{net}}^{\text{chng}} - E_{\text{net}}^{\text{base}}\,. \tag{3.29}$$

The *relative energy loss fraction* metric ϵ_{E} is now proposed, given by

$$\epsilon_{\text{E}}(\mathring{P}_{\text{gen}}^{\text{chng}}, \mathring{P}_{\text{gen}}^{\text{base}}) = \frac{\Delta E_{\text{gen}} - \Delta E_{\text{net}}}{\Delta E_{\text{gen}}} \tag{3.30a}$$

$$= \frac{\Delta E_{\text{lss}}}{\Delta E_{\text{gen}}}\,. \tag{3.30b}$$

This fraction can be interpreted in three ways. Firstly, it represents the fraction of energy losses, compared to the total energy that is generated, (3.30b). Alternatively, it is the calculated error if losses were ignored when valuing reactive power (3.30a) as providing additional energy. Finally, if the efficiency of the additional generated energy is $\eta_{\text{E}} = \Delta E_{\text{net}}/\Delta E_{\text{gen}}$, then it is related to the efficiency by

$$\epsilon_{\text{E}} = 1 - \eta_{\text{E}} \tag{3.31}$$

The temporal, steady state power increase in generation (ΔP_{gen}), losses (ΔP_{lss}), and net generation (ΔP_{net}) are given by

$$\Delta P_{\text{gen}} = P_{\text{gen}}^{\text{chng}} - P_{\text{gen}}^{\text{base}}\,, \tag{3.32}$$

$$\Delta P_{\text{lss}} = P_{\text{lss}}^{\text{chng}} - P_{\text{lss}}^{\text{base}}\,, \tag{3.33}$$

$$\Delta P_{\text{net}} = P_{\text{net}}^{\text{chng}} - P_{\text{net}}^{\text{base}}\,. \tag{3.34}$$

These values are set to be undefined for $P_{\text{gen}} < \mathring{P}_{\text{gen}}^{\text{base}}$, if the state of all controls (taps, capacitors banks) in the network are identical. The *relative power loss fraction* is

defined as

$$\epsilon_{\mathrm{P}}(P_{\mathrm{gen}}, \mathring{P}_{\mathrm{gen}}^{\mathrm{base}}) = \frac{\Delta P_{\mathrm{lss}}}{\Delta P_{\mathrm{gen}}}\,, \tag{3.35}$$

in a direct analogy to the relative energy loss fraction. Note that the relative energy loss fraction ϵ_{E} is implicitly defined with a profile P_{ipt}, whereas the relative power loss fraction ϵ_{P} is defined only at a given time. In other words, in the case that S_{net} does not change with time τ, it can be observed that

$$\epsilon_{\mathrm{E}} = \epsilon_{\mathrm{P}}\,. \tag{3.36}$$

The relative power loss fraction clearly provides a lot of information about the relative energy loss fraction, as the latter is found by averaging the former across the time period of interest. Therefore, the approach in the next section is to calculate properties of the relative *power* loss fraction, as a means of bounding the relative *energy* loss fraction.

3.6 Two-Bus Relative Loss Fraction Bounds

In this section the relative energy loss fraction is studied in the context of the two-bus network. To characterise real power losses in the two-bus model, assumptions are required to be made about the operation of a DG. It is assumed that the reactive power is chosen to maximise net generation P_{net}. Although there are many types of reactive power control, this is a well-accepted objective function [70].

The control strategy that maximises net generation, subject to voltage constraints, is first described. Following from this, the second main contribution of this chapter is given: an analytic method for studying the impact of voltage control on losses, as a function of load, voltage regulation, and the R/X ratio of the Thévenin impedance at the DG. The method is given using the LinDistFlow equations, and therefore the validity of the conclusions drawn are considered in terms of a comparison with the Exact two-bus solution.

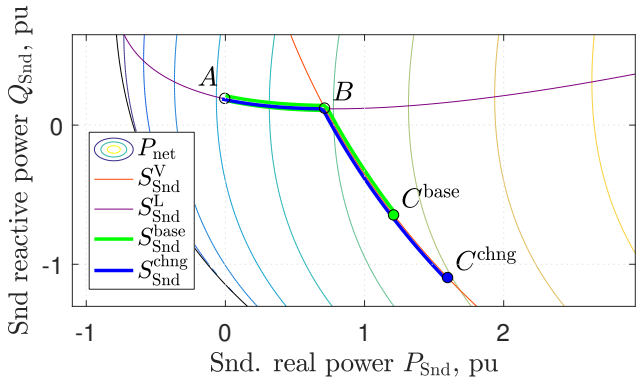

Figure 3.11: Operating characteristic (3.41) with respect to the generated power P_{Snd}, Q_{Snd} .

3.6.1 Generator Control

For the objective of maximising net generation subject to operational constraints, the optimal generator power export is found as

$$S^{[\text{case}]}_{\text{gen}} = \arg\max_{S_{\text{gen}}} P_{\text{net}} \tag{3.37a}$$

$$\text{s.t.} \quad Q_{\text{gen}} \geq Q^{[\text{case}]}_{-} \tag{3.37b}$$

$$0 \leq P_{\text{gen}} \leq P_{\text{ipt}} \tag{3.37c}$$

$$|S_{\text{gen}}| \leq S_{+} \tag{3.37d}$$

$$V_{-} \leq |V| \leq V_{+}\,. \tag{3.37e}$$

The generator has limited reactive power availability (3.37b), a generation limit (3.37c), and a fixed inverter size (3.37d). Additionally, it is required that all network voltages V must remain within bounds (3.37e).

The operation of a generator can be decomposed into different operating modes, depending on which constraints are active, illustrated in Figure 3.11. Firstly, when the available generation P_{ipt} is relatively small, the generator acts to minimize losses in the network by compensating reactive load (as a 'P-Q generator', from A to B in Figure 3.11). At these points, the generated loss compensating generator power is denoted by $S^{\text{L}}_{\text{gen}} = P_{\text{ipt}} + \jmath Q^{\text{L}}_{\text{gen}}$, where the load compensating reactive power $Q^{\text{L}}_{\text{gen}}$ is

given by

$$Q_{\text{gen}}^{\text{L}} = \arg\max_{Q_{\text{gen}}} P_{\text{net}} \quad \text{s.t.}\,(3.37\text{c})\,. \tag{3.38}$$

Eventually, as the generation increases, the voltage constraint will become active, at a loss-voltage crossover point denoted by $S_{\text{gen}}^{\text{X}}$ (point B). After this crossover point, the generator is operated as a voltage-constrained generator (as a 'P-V generator', from B to $C^{[\text{case}]}$). This voltage constrained power generation is denoted as $S_{\text{gen}}^{\text{V}} = P_{\text{ipt}} + \jmath Q_{\text{gen}}^{\text{V}}$, defined by

$$Q_{\text{gen}}^{\text{V}} = \arg\max_{Q_{\text{gen}}} P_{\text{net}} \quad \text{s.t.}\,(3.37\text{c}),\,(3.37\text{e})\,. \tag{3.39}$$

The inverter or reactive power limit will be reached at point $C^{[\text{case}]}$, denoted by

$$\mathring{S}_{\text{gen}}^{[\text{case}]} = \arg\max_{S_{\text{gen}}} P_{\text{net}} \quad \text{s.t.}\,(3.37\text{b}),\,(3.37\text{d}),\,(3.37\text{e}). \tag{3.40}$$

The full control scheme can be summarised succinctly in terms of these three operating modes (loss minimization, voltage constrained, power constrained) as

$$S_{\text{gen}}^{[\text{case}]} = \begin{cases} P_{\text{ipt}} + \jmath Q_{\text{gen}}^{\text{L}} & \text{if } P_{\text{ipt}} \leq P_{\text{gen}}^{\text{X}} \\ P_{\text{ipt}} + \jmath Q_{\text{gen}}^{\text{V}} & \text{if } P_{\text{gen}}^{\text{X}} < P_{\text{ipt}} \leq \mathring{P}_{\text{gen}}^{[\text{case}]} \\ \mathring{S}_{\text{gen}}^{[\text{case}]} & \text{if } P_{\text{ipt}} > \mathring{P}_{\text{gen}}^{[\text{case}]}\,. \end{cases} \tag{3.41}$$

3.6.2 Relative Loss Fraction Bounds Using LinDistFlow

The optimal two-bus operation has now been described and so the main result, bounding the relative energy loss fraction, is considered in this section. The contribution consists of a demonstration that both two-bus models (Exact and LinDistFlow) have positive curvature, so that the bounds are simply the maximum and minimum values of the relative loss fractions. It is then demonstrated that the neighbourhood over which the LinDistFlow matches the Exact solution is reasonable, being up to 20% of the maximum potential benefits of voltage control. The LinDistFlow model has the distinct advantage that the equations have a simple algebraic form.

3.6.2.1 Relative Loss Fraction Bounds

The relative power loss fraction is not defined for powers less than the base real power constraint $\mathring{P}^{\text{base}}_{\text{gen}}$. However, as this power is approached from above, the relative energy loss fraction tends to a constant value.

More concretely: for a power limit $\mathring{P}^{\text{base}}_{\text{Snd}}$ the initial relative power loss fraction $\epsilon^{\text{init}}_{\text{P}}$ is defined by

$$\epsilon^{\text{init}}_{\text{P}}(\mathring{P}^{\text{base}}_{\text{Snd}}) = \lim_{P_{\text{Snd}} \to \mathring{P}^{\text{base}}_{\text{Snd}}} \epsilon_{\text{P}}(P_{\text{Snd}}, \mathring{P}^{\text{base}}_{\text{Snd}}) \tag{3.42}$$

$$= \frac{dP_{\text{lss}}}{dP_{\text{Snd}}}\,. \tag{3.43}$$

This is holds simply by the definition of the derivative of a function. This initial relative power loss fraction $\epsilon^{\text{init}}_{\text{P}}$ requires the use of a limit to calculate the lower bound for ϵ_{P} (setting $P_{\text{Snd}} = \mathring{P}^{\text{base}}_{\text{Snd}}$ in (3.42) results in the indeterminate form 0/0). Note also that the required derivatives for the evaluation of $\epsilon^{\text{init}}_{\text{P}}$ in (3.43) can be derived for either the Exact or LinDistFlow solutions.

The first part of this results is given as follows: the relative energy loss fraction ϵ_{E} is bounded by the initial and terminal relative power loss fraction as

$$\epsilon^{\text{init}}_{\text{P}} < \epsilon_{\text{E}} \leq \epsilon^{\text{trml}}_{\text{P}}\,, \tag{3.44}$$

where the initial relative loss fraction $\epsilon^{\text{init}}_{\text{P}}$ is given by (3.42) and the terminal relative loss fraction $\epsilon^{\text{trml}}_{\text{P}}$ is given by

$$\epsilon^{\text{trml}}_{\text{P}} = \epsilon_{\text{P}}(\mathring{P}^{\text{chng}}_{\text{Snd}}, \mathring{P}^{\text{base}}_{\text{Snd}})\,. \tag{3.45}$$

Additionally, for any network constrained on the voltage curve, following (3.41), then

$$\epsilon^{\text{X}}_{\text{P}} < \epsilon^{\text{init}}_{\text{P}}(\mathring{P}^{\text{base}}_{\text{gen}})\,, \tag{3.46}$$

where the *load compensated relative loss fraction* $\epsilon_{\mathrm{P}}^{\mathrm{X}}$ is given by $\epsilon_{\mathrm{P}}^{\mathrm{X}} = \epsilon_{\mathrm{P}}^{\mathrm{init}}(P_{\mathrm{Snd}}^{\mathrm{X}})$.

The proof of (3.44) is given in the appendix (Section A.1.4). This result is useful practically because it justifies the calculation of relative loss fraction bounds using the two-bus model using just two points.

A notable feature of this proof is that it is given in terms of P_{Snd} rather than P_{gen} explicitly. This is because it is the line power S_{Snd}, rather than the generator or load power that defines when the voltage constraint is hit. A corollary of this is that, under a reactive power generation limit (3.37b), the load real power does not impact on the initial relative loss fraction $\epsilon_{\mathrm{P}}^{\mathrm{init}}$, but the reactive power of the load does.

Calculating Relative Loss Fractions with LinDistFlow With the LinDistFlow equations, the values of the initial and terminal relative loss fractions can all be calculated algebraically. These are given in two forms; in terms of the base and change reactive power, and in terms of the base and change real powers.

By substituting (3.6) into (3.7) and differentiating with respect to P_{Snd}, the initial relative loss fraction (3.43) is given by

$$\epsilon_{\mathrm{P}}^{\mathrm{init}} = 2\frac{P_{\mathrm{Snd}}^{\mathrm{base}}}{S_{\mathrm{SC}}}\frac{|V_{\mathrm{Rcv}}|^2}{V_+^2}\lambda\sqrt{1+\lambda^2} - \lambda^2\left(1 - \frac{|V_{\mathrm{Rcv}}|^2}{V_+^2}\right), \tag{3.47}$$

$$= -2\frac{Q_{\mathrm{Snd}}^{\mathrm{base}}}{S_{\mathrm{SC}}}\frac{|V_{\mathrm{Rcv}}|^2}{V_+^2}\sqrt{1+\lambda^2} + \left(1 - \frac{|V_{\mathrm{Rcv}}|^2}{V_+^2}\right). \tag{3.48}$$

It shown in the appendix (Section A.1.5) the relative loss fractions are calculated similarly as

$$\epsilon_{\mathrm{P}}^{\mathrm{trml}} = \frac{(P_{\mathrm{Snd}}^{\mathrm{base}} + P_{\mathrm{Snd}}^{\mathrm{chng}})}{S_{\mathrm{SC}}}\frac{|V_{\mathrm{Rcv}}|^2}{V_+^2}\lambda\sqrt{1+\lambda^2} - \lambda^2\left(1 - \frac{|V_{\mathrm{Rcv}}|^2}{V_+^2}\right) \tag{3.49}$$

$$= -\frac{(Q_{\mathrm{Snd}}^{\mathrm{base}} + Q_{\mathrm{Snd}}^{\mathrm{chng}})}{S_{\mathrm{SC}}}\frac{|V_{\mathrm{Rcv}}|^2}{V_+^2}\sqrt{1+\lambda^2} + \left(1 - \frac{|V_{\mathrm{Rcv}}|^2}{V_+^2}\right). \tag{3.50}$$

The two (3.49), (3.50) complement each other, and both forms are useful to consider the properties of networks with reactive power control. The first equation in generated powers (3.49) shows that the sensitivity of the relative loss fraction ϵ_{P} is super-linear

with the R/X ratio λ (with respect to the change real power $P_{\text{Snd}}^{\text{chng}}$).

The second form is in reactive powers (3.50). This form demonstrates that increasing reactive powers leads only to a sub-linear increase in losses. The increase in generated power is also diminished, however: along lines of constant voltage, changes in real power are inversely proportional to the R/X ratio, as $\Delta P_{\text{Snd}} = -\dfrac{\Delta Q_{\text{Snd}}}{\lambda}$.

Finally, given the fact that LinDistFlow suggests that losses are minimized when $Q_{\text{Snd}} = 0$ (from (3.7)), it is concluded that the load compensated relative power loss fraction $\epsilon_{\text{P}}^{\text{X}}$ is given by

$$\epsilon_{\text{P}}^{\text{X}} = \left(1 - \frac{|V_{\text{Rcv}}|^2}{V_+^2}\right) . \tag{3.51}$$

The conclusion of the analysis of the two-bus model using the LinDistFlow solution is as follows. Not only does the effectiveness of reactive power reduce with the R/X ratio (in terms of voltage drop per unit of reactive power), but the losses also increase, reducing the benefits further. Equations (3.50), (3.48) give a simple heuristic for calculating this impact on losses *numerically*.

The next two sections will consider the accuracy and limitations of the calculated values of (3.50). The first comparison will be to compare the model to the Exact two-bus model, to consider if the benefits of the algebraic simplicity of the LinDistFlow method are not to the detriment of their accuracy. Secondly, their accuracy in comparison to full time-series analysis of a range of unbalanced networks is then considered.

Calculating Relative Loss Fractions with the Exact Model The relative loss significance for the Exact model is found from (3.8) to be

$$\epsilon_{\text{P}}^{\text{trml, Exact}}(P_{\text{Snd}}^{\text{chng}}, P_{\text{Snd}}^{\text{base}}) = 2\frac{\lambda}{1+\lambda^2}\left(\lambda + \frac{\zeta_{P\to Q}(P_{\text{Snd}}^{\text{chng}}) - \zeta_{P\to Q}(P_{\text{Snd}}^{\text{base}})}{P_{\text{Snd}}^{\text{chng}} - P_{\text{Snd}}^{\text{base}}}\right) , \tag{3.52}$$

where the mapping from real to reactive powers $\zeta_{P\to Q}$ is (from (3.9))

$$\zeta_{P\to Q}(P_{\text{Snd}}) = \frac{X|V_{\text{Snd}}|^2}{|Z|^2} - \sqrt{\left(\frac{|V_{\text{Rcv}}||V_{\text{Snd}}|}{|Z|}\right)^2 - \left(P_{\text{Snd}} - \frac{R|V_{\text{Snd}}|^2}{|Z|^2}\right)^2}. \tag{3.53}$$

To find the initial relative loss fraction, first note (from (3.9))

$$\frac{dQ^V_{\text{Snd}}}{dP_{\text{Snd}}} = \frac{P_{\text{Snd}} - \dfrac{R|V_{\text{Snd}}|^2}{|Z|^2}}{Q_{\text{Snd}} - \dfrac{X|V_{\text{Snd}}|^2}{|Z|^2}}, \tag{3.54}$$

so that

$$\epsilon_{\text{P}}^{\text{init, Exact}}(P_{\text{Snd}}^{\text{base}}) = 2\frac{\lambda}{1+\lambda^2}\left(\lambda + \frac{P_{\text{Snd}}^{\text{base}} - \dfrac{R|V_{\text{Snd}}|^2}{|Z|^2}}{\zeta_{P\to Q}(P_{\text{Snd}}^{\text{base}}) - \dfrac{X|V_{\text{Snd}}|^2}{|Z|^2}}\right). \tag{3.55}$$

Whilst this is in closed form, it is challenging to analyse due to the relatively large number of terms compared to the LinDistFlow characterisation (3.50). (This is why the LinDistFlow expression is considered analytically, instead of the Exact model.)

3.6.3 Comparing Exact and LinDistFlow Relative Loss Fractions

The initial and terminal relative loss fractions can be calculated using either the Exact model or the LinDistFlow model. In this section, the qualitative and quantitative values of calculated relative loss fractions of the LinDistFlow model are compared with the Exact model, to consider the accuracy of the conclusions drawn using the LinDistFlow model.

3.6.3.1 Qualitative Differences

There are a number of qualitative differences between the solutions of both the Exact and LinDistFlow models. Four differences which are relevant to calculations of the relative loss significance are summarised here.

1. There is always a solution to the LinDistFlow equations; this is not the case for the two-bus Exact solution. For example, $Q_{\mathrm{Snd}} = 0$ will always have a solution for any $|V_{\mathrm{Snd}}|$, $|V_{\mathrm{Rcv}}|$ for the LinDistFlow problem, whilst it was demonstrated in Section 3.2.2.2 this is not the case for the Exact non-linear solution.

2. Squared voltage magnitude level sets are linear in powers in the LinDistFlow model; voltage level sets are described by circles in the Exact two-bus solution (see, e.g., (3.9), (3.6)). Therefore, there is a many-to-one relation from real to reactive powers on voltage level sets in the Exact model, but not in the LinDistFlow model.

3. The LinDistFlow model suggests that losses are minimized when $Q_{\mathrm{Snd}} = 0$, whilst the Exact solution has a slightly positive reactive power (Section A.1.6).

4. The calculation of the load compensated reactive power $Q^{\mathrm{X}}_{\mathrm{Rcv}}$ for the Exact load flow requires the solution of a quartic equation, rather than a quadratic (see appendix, Section A.1.7). Therefore, the calculation of $\epsilon^{\mathrm{X}}_{\mathrm{P}}$ (as a lower bound for $\epsilon^{\mathrm{init}}_{\mathrm{P}}$) cannot practically be given in closed form. This is in contrast to the solution given by the LinDistFlow model, which is simply given as (3.51).

As the LinDistFlow model is qualitatively very different from the Exact model, quantitative calculations are now considered to study where the LinDistFlow model is accurate. For this, an absolute error of 10% is used as criterion for acceptable error in calculations. (If this error is too conservative (or relaxed) a tighter error value could be chosen.)

3.6.3.2 Numerical Comparison Between Exact and LinDistFlow Load Flow Solutions

The impact of the LinDistFlow model on the numerical accuracy of the model is now compared to the Exact two-bus load flow solution. In particular, three different properties of the LinDistFlow model are considered. The first points two are the

loss-voltage intersection relative loss fraction and the initial relative loss fraction with reactive power. The third point is the initial relative loss fraction, where the load point is chosen between the zero reactive power and maximum power transfer points. The purpose is to demonstrate the accuracy of the solution at low powers, and then to consider the region of validity of the method. This comparison is across reactive powers, voltage ratios, and R/X ratios.

Loss-voltage Intersection Relative Loss Fraction The first point that is considered is the loss-voltage intersection point (defined by (3.46)). As has been pointed out, for the Exact two-bus solution, this is calculated using a numerical method (see Section 3.6.3.1). The value of the relative loss fraction is plotted in Figure 3.12a for the Exact model. Likewise, the value of this quantity is plotted in Figure 3.12b for the calculation using the LinDistFlow model, and the absolute value of the difference between these values is plotted in Figure 3.12c

In Figure 3.12a, the impact of the non-linearity of voltages on the initial load-compensated relative loss fraction $\epsilon_{\mathrm{P}}^{\mathrm{X}}$ is clear in the Exact model–for a voltage ratio greater than unity and R/X less than 0.1, there is a wide range of areas where there is no load compensated relative loss fraction $\epsilon_{\mathrm{P}}^{\mathrm{X}}$. This is because loss minimization requires a small amount of reactive power export, causing the voltage to increase. The upper voltage boundary is therefore never reached (i.e. the voltage never drops to reach the voltage constraint).

These figures demonstrate that the difference between the LinDistFlow approximation, given by (3.51), and the solution obtained using the Exact model is less than 10% for $\lambda > 0.6$. In fact, the difference is less than 3% for values of $\lambda > 1.05$.

Initial Relative Loss Fraction with Reactive Power The point that is considered is the initial relative loss fraction, as a function of R/X ratio λ and reactive power. In this figure, the sending and receiving voltage magnitudes are identical, i.e. $|V_{\mathrm{Rcv}}| = |V_{\mathrm{Rcv}}|$, and the line impedance is 0.1. The solution from the Exact solution is given in Figure 3.13a; the solution in terms calculated using the LinDistFlow model is

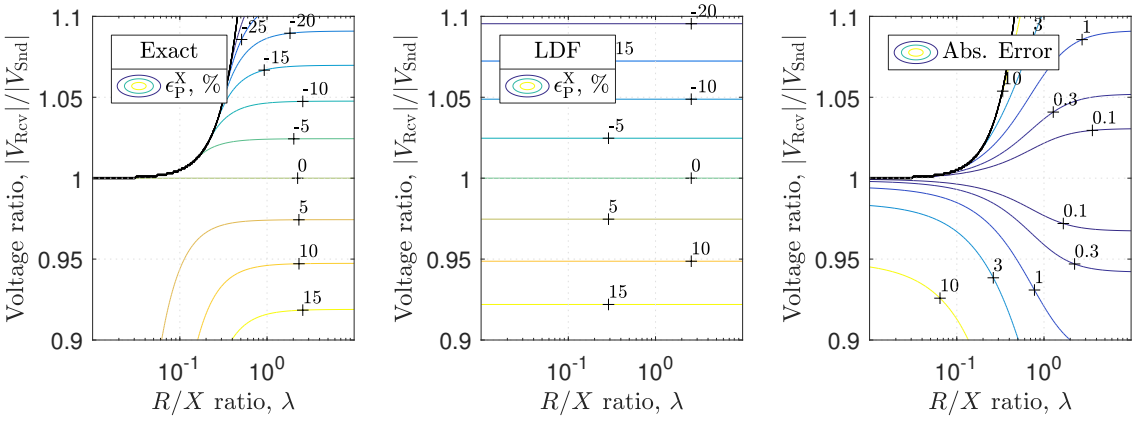

(a) Exact model ϵ_P^X (b) LinDistFlow model ϵ_P^X (c) Absolute error, Exact vs. LinDistFlow ϵ_P^X

Figure 3.12: Calculations of the initial load compensated relative loss fraction ϵ_P^X. In (a) the values are calculated using the Exact load flow solution; in (b) the values are calculated using the LinDistFlow solution; in (c) the absolute error between these two solutions is plotted.

given in Figure 3.13b; the absolute difference between the values of these calculations are given in Figure 3.13c.

In this case, the non-linearity is clear, with negative (inductive) reactive power sometimes not yielding a solution for R/X less than 0.3. (The range of points where a solution does not exist occurs when the reactive power is less than the minimum obtained from, e.g., (3.53).) The behaviour of the LinDistFlow model again deviates for low values of R/X (Figure 3.13b), but the shape of the Exact and LinDistFlow models are similar for R/X ratios greater than 0.5.

In this case, it can be seen that the LinDistFlow calculations show the smallest error when the reactive power is zero and when λ is close to 0.7 (Figure 3.13c). The region over which this calculation is accurate is larger than the loss-voltage intersection point. This is unsurprising, as the generator complex power at which this point is calculated matches for the two models (whereas, the powers generated at the load compensated reactive loss fraction of the previous section varies between the Exact and LinDistFlow models).

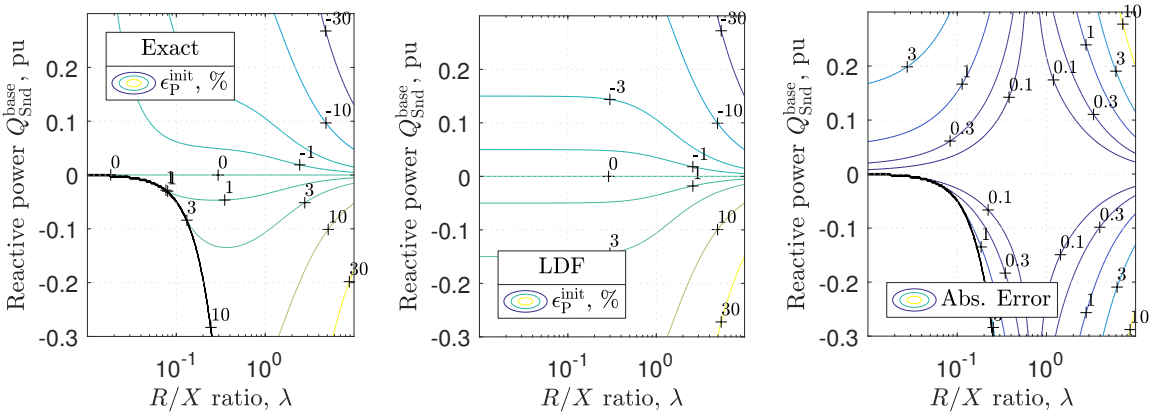

(a) Exact model $\epsilon_{\mathrm{P}}^{\mathrm{init}}$ (b) LinDistFlow model $\epsilon_{\mathrm{P}}^{\mathrm{init}}$ (c) Absolute error, Exact vs. LinDistFlow $\epsilon_{\mathrm{P}}^{\mathrm{init}}$

Figure 3.13: Calculations of the initial relative loss fraction $\epsilon_{\mathrm{P}}^{\mathrm{init}}$ as a function of reactive power. In (a) the values are calculated using the Exact load flow solution; in (b) the values are calculated using the LinDistFlow solution; in (c) the absolute error between these two solutions is plotted.

Terminal Relative Loss Fraction at Maximum Power Transfer In this final validation with respect to the Exact model, the error introduced by the LinDistFlow equations as a fraction of the maximum power transfer is considered. Specifically, the region of validity of the LinDistFlow method for estimating the relative loss fraction is compared to the Exact model at some fraction of the voltage-constrained maximum power transfer point.

This is calculated from the following steps.

1. The point which the voltage constraint is hit using UPF control, $P_{\mathrm{Snd,\,UPF}}$, and the maximum power transfer point, $P_{\mathrm{Snd,\,MPT}}$, are calculated for the Exact model. These are calculated from (3.12), (3.15).

2. The reactive power $Q_{\mathrm{UPF-MPT}}$ at some fraction $F_{\mathrm{UPF-MPT}}$ between $P_{\mathrm{Snd,\,UPF}}$ and $P_{\mathrm{Snd,\,MPT}}$ is found according to

$$Q_{\mathrm{UPF-MPT}} = \zeta_{P\to Q}\left(P_{\mathrm{Snd,\,UPF}} + F_{\mathrm{UPF-MPT}}(P_{\mathrm{Snd,\,MPT}} - P_{\mathrm{Snd,\,UPF}})\right), \quad (3.56)$$

where $\zeta_{P\to Q}$ is defined in (3.53).

3. The initial relative loss fraction at the fraction $F_{\text{UPF}-\text{MPT}}$, denoted $\epsilon_{\text{P}}^{F_{\text{UPF}-\text{MPT}}\%}$, is calculated from (3.48) for the LinDistFlow model, and from (3.55) for the Exact model.

For example, if the fraction $F_{\text{UPF}-\text{MPT}}$ is equal to unity, then the chosen point is the maximum power transfer point at the voltage constraint, and so the value of $\epsilon_{\text{P}}^{100\%}$ is 100% for the Exact model at all points.

The results of this calculation are plotted in Figure 3.14 for the fraction $F_{\text{UPF}-\text{MPT}} = 20\%$. The solution from the Exact solution is given in Figure 3.14a; the solution in terms calculated using the LinDistFlow model is given in Figure 3.14b; the absolute difference between the values of these calculations are given in Figure 3.14c.

There are a two things to note. Firstly, for the Exact model, the value of $\epsilon_{\text{P}}^{20\%}$ is sometimes much less than 20%, and sometimes much more. This is interesting to note, as it demonstrates the non-linearity of the increase in ϵ_{P}.

More importantly, at this point there is still a relatively wide region of validity of the LinDistModel. Assuming acceptable results for a maximum error of 10%, it is demonstrated here that $\epsilon_{\text{P}}^{20\%}$ as calculated by the LinDistFlow model is accurate for R/X ratios λ between 0.7 and 4. As shown in Figure (3.5), this covers most distribution network buses (similarly, [80] suggests R/X ratios in distribution networks are typically between 0.4 and 3.1). Where calculations are required for the highest accuracy, the Exact model could be used for calculations. However, it is demonstrated that, for reactive powers required for up to 20% of the power increase afforded by reactive power control, the model is accurate for almost all distribution network parameters.

3.7 Case Studies

To further consider the applicability of the conclusions drawn from the two-bus model, three networks are considered for case studies. These consist of the EU LV network, the IEEE 34 Bus network, and the EPRI K1 network, representing high, moder-

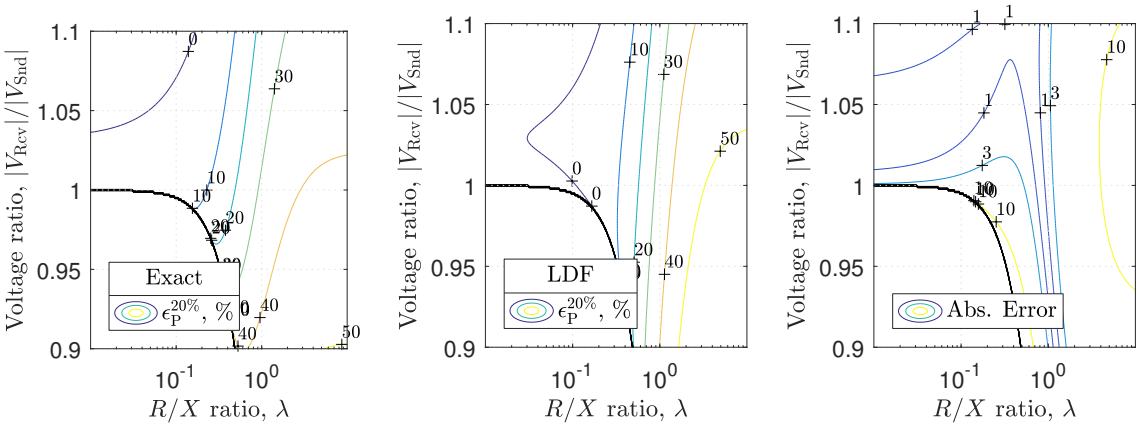

(a) Exact model $\epsilon_{\mathrm{P}}^{20\%}$ (b) LinDistFlow model $\epsilon_{\mathrm{P}}^{20\%}$ (c) Absolute error, Exact vs. LinDistFlow $\epsilon_{\mathrm{P}}^{20\%}$

Figure 3.14: Calculations of the initial value of the relative loss fraction 20% between the UPF and MPT control points (as described in Section 3.6.3.2). In (a) the values are calculated using the Exact load flow solution; in (b) the values are calculated using the LinDistFlow solution; in (c) the absolute error between these two solutions is plotted.

Table 3.2: Two-Bus properties of buses used in case studies D-F. The base voltages are 0.416, 13.2 kV and the power bases are 800, 12000 kVA for the EU LV and EPRI K1 circuits, respectively.

Study	Circuit	Gen. Bus	λ	$\lvert Z\rvert$, pu	$\lvert V_{\mathrm{Rcv}}\rvert$, pu	V_+, pu	$S_{\mathrm{lds,Tot}}$, pu
D	EPRI K1	34096115	0.26	0.18	1.038	1.03	$0.78\angle 6.4°$
E, F	EU LV	801	3.34	0.46	1.096	1.10	$0.011\angle 18.2°$

ate, and low R/X ratios. Additionally, the 34 Bus network has two in-line voltage regulators.

These case studies are designed to investigate the impact of reactive power, voltage drop, and the R/X ratio on the relative loss fraction. Additionally, the numerical predictions made by the two-bus LinDistFlow model are also investigated.

The two-bus properties at the chosen generator buses on the EU LV and EPRI K1 networks are given in Table 3.2. Neither feeder has line drop compensation, and the EU LV network does not have a voltage regulator. The taps in the EPRI K1 circuit are free to change as specified in their controls. The two-bus properties of the 34 Bus circuit are in Table 3.1 (only bus 834 is used for these studies).

3.7.1 Case Study Setup

Before presenting the result of the case studies, the assumptions made for the time series analysis are first considered.

Load and Generation profiles A solar profile was obtained using typical meteorological data for London Gatwick from [163]. The power factor of all loads remains fixed at their nominal values. The 'total load' (as required for (3.23)) was taken as the average load throughout the year; the ratio (3.24) was calculated at maximum load.

A representative load profile for each of the loads in the 34 Bus and EPRI K1 circuits was obtained from smart meter data from [164] by averaging and normalising 23 annual residential profiles. This aggregate profile was then applied to all loads.

For the EU LV network, individual profiles were used for each load. In contrast to the previous case studies, all three values of the load scaling factor k_S will be considered in the analysis (as described in Section 3.3.3).

For the 34 Bus circuit, voltage bounds of $V_+ = 1.05$ pu and $V_- = 0.95$ pu result in a load flow which is initially infeasible, as there are undervoltages at full load. The maximum load at which the network is feasible (with zero generation) is when all loads are scaled to 78% of their nominal kVA ratings. This scaled value of load was chosen as the peak value for simulations.

Loss Minimization and Relative Loss Fraction Calculations To minimize losses for (3.41) within OpenDSS, the golden search method was used. The secant method was utilised to find the reactive power required to have an active voltage constraint (for details of both of these algorithms see [165, Ch. 4]).

As a numerical method is used to find these voltage and loss minimization points in OpenDSS, a tolerance is required to determine if there is a 'zero' or 'non-zero' value of ΔP_{gen}, ΔP_{lss}. A tolerance of 4×10^{-5} times the generator size as chosen. Under this tolerance, the total relative values of ΔE_{lss}, ΔE_{gen} changed by less than 2×10^{-5}

Table 3.3: Generator sizes and operational constraints for all six case studies.

Study ID	Circuit	Generator power rating, kW	Generator inverter rating, kVA	'Base' reactive power, kVAr	'Change' reactive power, kVAr
A	34 Bus	1250	1400	0	400
B	34 Bus	1250	1400	400	800
C	34 Bus	3000	3200	0	400
D	EPRI K1	15000	16000	0	750
E	EU LV	55	68	0	20
F	EU LV	55	68	20	40

in all cases using this tolerance (across the whole year's simulation).

3.7.1.1 Generator Specifications and Regulator Settings

The generator size, inverter size, and reactive power capabilities for each case study are given in Table 3.3. The reactive power increases from Study A to Study B and Study E to Study F. Study C has the same reactive power constraint as Study A, but voltage regulator settings are modified to allow for an increase in generation (these modifications are described in the next section). In all cases the inverter is assumed to be sized so that reactive power can always be generated if required ('VAR priority'), following the 'Rule 21' standard [35].

Modification of Nominal Network Controls For the 34 Bus circuit, voltage regulator line drop compensation (LDC) settings were changed (see Table 3.4). 'Cogen' mode was enabled to allow for reverse power flow, with the same LDC parameters forwards as backwards. Tap limits were required to avoid undervoltages on branches coming off the main feeder. For Study A and Study B the substation (source) voltage was reduced by 0.5% and the fixed tap ratio on the substation transformer 'xfm1' was increased by one tap. For Study C, the substation was additionally assumed to have a load tap changer (LTC) installed, with LDC enabled.

Additionally, in the 34 Bus network case studies the capacitors at the end of the feeder were switched out. This was done as the generator (located close to these

Table 3.4: Voltage regulator parameters for the 34 Bus circuit (units as in OpenDSS).

					Min tap	
Reg. ID	R_{reg}, V	X_{reg}, V	V_{reg}, V	Max tap	Study A & B	Study C
Reg. 1	4	1.6	118	+16	-1	-6
Reg. 2	0.8	0.8	124	+16	-2	-16
LTC	15	6	120	+2	NA	-6

capacitors) was available to provide compensation more accurately.

3.7.2 Case Study Example: IEEE 34 Bus, Study A

In this section, a two-day time series analysis is undertaken to demonstrate the method, and show how the two-bus model can be used to predict the behaviour of a circuit over a longer time period.

The generator power for Study A on two illustrative days is shown in Figures 3.15a, 3.15c, and the corresponding voltages from the network are plotted in Figures 3.15b, 3.15d. It is demonstrated that the voltages remain in bounds across the whole network in both cases, and that the amount of real power that can be generated increases in the 'change' case. There is an increase in generation on these two days of 2.72 MWh, and an increase in losses of 0.36 MWh. The relative energy loss fraction is therefore 13.2%.

The corresponding relative power loss fraction ϵ_{P} is plotted in Figure 3.15e. At the times when the reactive power of the 'change' case drops below the reactive power of the 'base' case, there is a difference in the generation and losses in the network. For times when the powers in both circuits are identical, the relative power loss fraction is undefined (and so not plotted on Figure 3.15e).

Additionally, Figure 3.15e has three pairs of bounds plotted, calculated using the two-bus LinDistFlow model.

- The black pair of dashed lines are the bounds calculated by the LinDistFlow model, assuming that all load is co-located with the generator ($k_{\text{S}} = 1$). The

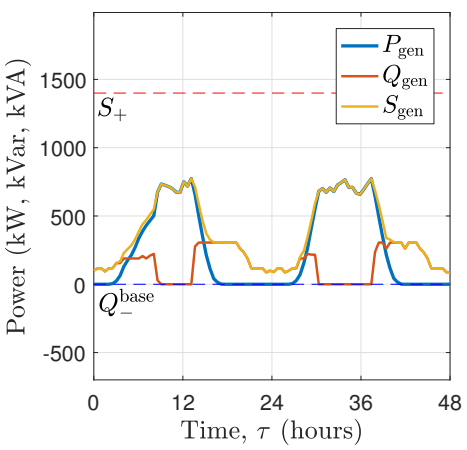

(a) Study A: Base Case Powers

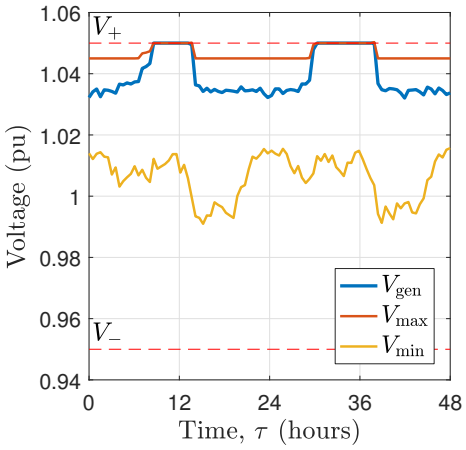

(b) Study A: Base Case Voltages

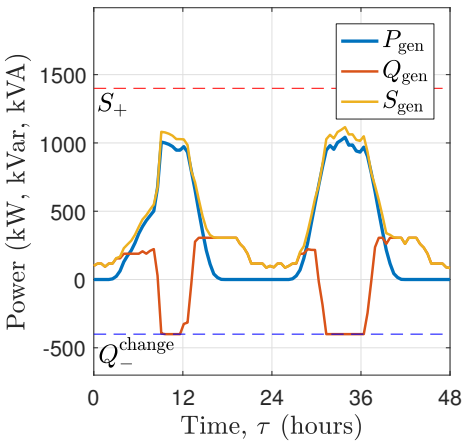

(c) Study A: Change Case Powers

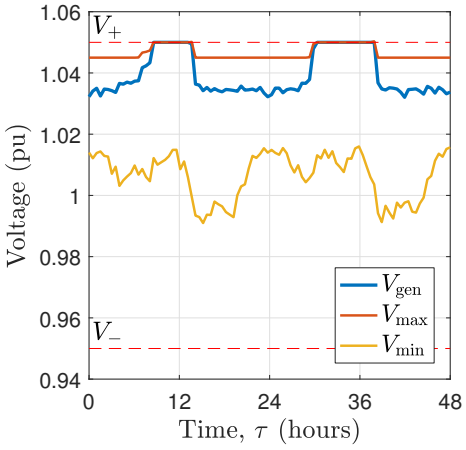

(d) Study A: Change Case Voltages

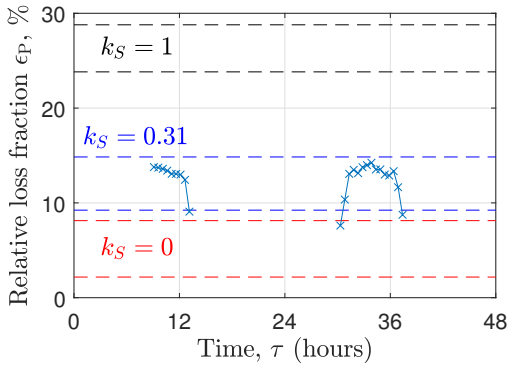

(e) Study A: Relative Loss Fraction ϵ_{P}.

Figure 3.15: Voltages (left) and powers (right) for Study A. The 'base' case (subfigure (a) and (b)) has a reactive power limit $Q_-^{\text{base}} = 0$ kVAr, whilst the 'change' case (subfigure (c) and (d)) has the limit $Q_-^{\text{chng}} = -400$ kVAr. This leads to an increase in losses; plotting the relative power loss fraction ϵ_{P} illustrates that this reduces the efficacy of reactive power by 8-14% (subfigure (e)). Note that 'base' and 'change' case min/max/gen voltages do not change much from subfigure (b) to (d) as reactive power control (i.e., voltage control) acts to maintain voltages at a constant level.

upper (terminal) value is calculated using (3.50) and the lower (initial) bound is calculated using (3.47).

- The red pair of dashed lines are calculated assuming that there is no load at the generator ($k_S = 0$). The upper and lower bounds are calculated in the same way as for $k_S = 1$.

- Finally, the blue dashed lines are the calculated bounds for the 'weighted' load method from Section (3.24) (again the bounds are calculated as in the previous two load points).

Figure 3.15e demonstrates three things. Firstly, the relative loss fraction ϵ_{P} values are close to the calculated relative energy loss fraction of 13.2%. Secondly, the predicted bounds with the 'weighted' load (the blue dashed lines) give reasonably accurate bounds on the relative loss fraction values. Finally, it is interesting to observe how much the reactive load in the two-bus (i.e., as k_S increases from 0 to 1 for red, blue or black dashed lines) impacts on the bounds predicted by the LinDistFlow model.

3.7.3 Results of Case Studies

In this section, the results of all of case studies are considered. The aim is to consider if the predictions of the two-bus LinDistFlow model are accurate qualitatively and quantitatively. Specifically, the aim is to consider (i) how the R/X ratio λ impacts on the relative loss fraction; (ii) how the voltage drop at the voltage constraint impacts on relative loss fraction; and (iii) the numerical accuracy of the two-bus calculations.

3.7.3.1 Relative Energy Loss Fraction Analysis

Table 3.5 summarises the results of the time series simulation of the six case studies. There were no under- or over-voltages recorded in any simulations.

For Studies A-D the generator capacity factor (in terms the ratio of actual generation to the potential generation) is 87% or better. For Studies E and F this generation

Table 3.5: Generation and losses for each case study. From these the corresponding relative energy loss fraction ϵ_E is also calculated (from (3.30b)).

Study ID	Circuit	Potential Gen., MWh	Gen., MWh		Loss, MWh		Rel. loss frac. ϵ_E, %
			Base	Chng.	Base	Chng.	
A	34 Bus	1414.9	1308.8	1397.8	237.0	248.5	13.0 %
B	34 Bus	1414.9	1397.8	1414.9	248.5	252.1	21.4 %
C	34 Bus	3395.9	3274.2	3359.5	346.0	371.6	30.0 %
D	EPRI K1	16979	14786	16979	1550	1602	2.4 %
E	EU LV	62.26	32.04	43.01	0.46	0.95	4.5 %
F	EU LV	62.26	43.01	50.94	0.95	1.83	11.1 %

capacity factor is lower, reaching 81% in Study F. In other words, the generator sizing in the EU LV circuit is not particularly efficient, even though the generator size matches the peak load of the feeder of 55 kW.

Comparing Studies A-B and Studies E-F, it can be observed that the relative loss fraction increases by more than 6%. Increasing the amount of reactive power clearly increases the relative energy loss fraction in these cases. Interestingly, however, this increase is less than the increases between Study A and Study C; the relative energy loss fraction in that case increases by 17%. This is driven by the increase in the voltage drop along the line (and thus the power at which the voltage constraint becomes active).

The R/X ratio of the EPRI K1 circuit is much lower than the EU LV and 34 Bus circuit. There is therefore a corresponding reduction in the relative loss fraction for this circuit (for example, comparing Study D with A and E). However, as pointed out, the EU LV circuit has a lower relative loss fraction than the 34 Bus circuit, even though the R/X ratio of the EU LV circuit is higher. As predicted by the two-bus model, the R/X ratio is just one factor, with other parameters (the load reactive power and voltage drop) also making a large difference.

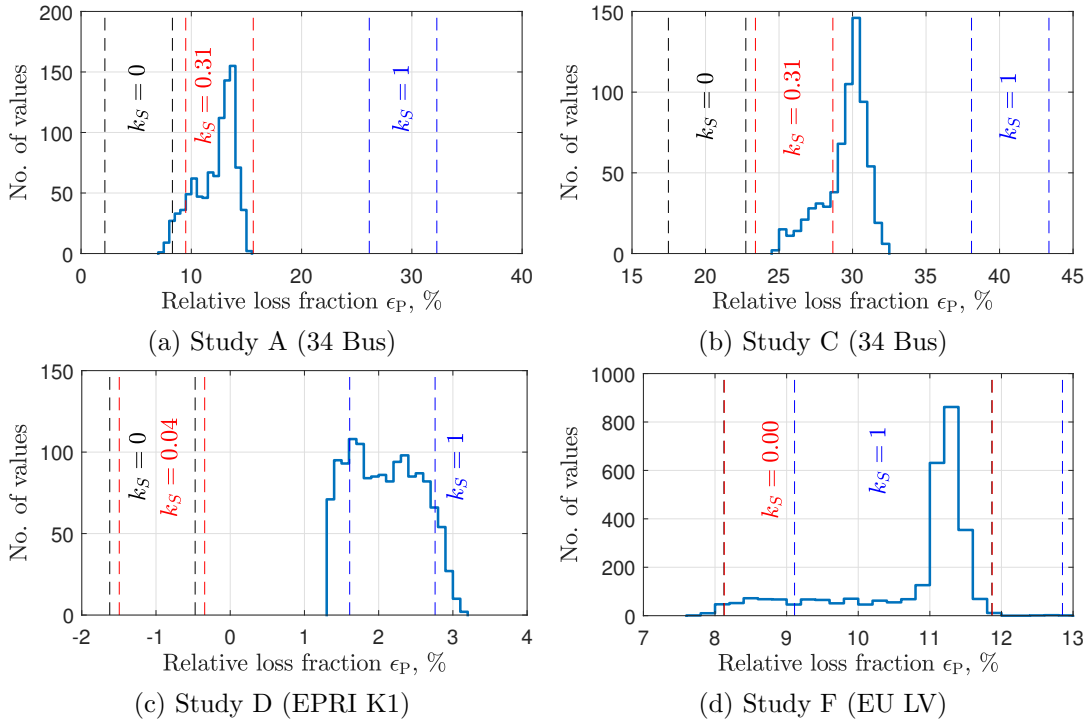

(a) Study A (34 Bus)

(b) Study C (34 Bus)

(c) Study D (EPRI K1)

(d) Study F (EU LV)

Figure 3.16: Histogram of the relative power loss fraction values for Studies A, C, D and F. The three sets of dashed vertical lines correspond to three load weightings (as described in Section 3.7.2).

3.7.3.2 Histograms of Relative Power Loss Fraction

To estimate the performance of the two-bus LinDistFlow model, the value of the relative power loss fraction ϵ_P is calculated throughout the year. Histograms of the relative power loss fraction are plotted in Figure 3.16 for four of the case studies.

There are three things that can be noted from this figure. Firstly, it is clear through the year that the predicted property of a non-trivial lower bound on the relative power loss fraction holds true. Comparing these figures with the relative energy loss fraction from Table 3.5 shows that the relative energy loss fraction is always within 6% of the maximum and minimum relative power loss fraction.

Secondly, the range of values of ϵ_P are increased compared to the LinDistFlow model (i.e. the difference between the maximum and minimum values of ϵ_P is greater than the difference between each pair of dashed lines). To some extent, this is expected—the method using the LinDistFlow model only considers a single reactive

power point, whilst the reactive power will in fact fluctuate throughout the year.

Finally, it is clear that the method for calculating the load by choice of k_S is not always as accurate as it could be. This is particularly noticeable on the EPRI K1 circuit, where the weighted load coefficient $k_S = 0.04$ leads to a relatively poor estimate of the relative loss fraction. To some extent, this can be explained—there is a bulk capacitor upstream of the generator (see Figure 2.3). This leads to a different reactive power profile to the other feeders which only have inductive loads.

3.7.3.3 Relative Power Loss Fraction Bounds

To summarise the results of this section, the minimum and maximum values of the relative power loss fraction from OpenDSS calculations are compared against the bounds calculated using the two-bus LinDistFlow model, using the 'weighed' load method (i.e., corresponding to the red dashed lines from Figure 3.16). These values are tabulated in Table 3.6.

From this table, it can be seen that there is no more than 5% difference between the predicated and actual terminal (maximum) relative loss fraction $\epsilon_{\mathrm{P}}^{\mathrm{trml}}$. Similarly, there is no more than a 4% difference between the predicted and actual values of the initial (lower) relative loss fraction $\epsilon_{\mathrm{P}}^{\mathrm{init}}$. Correspondingly, it is concluded that the two-bus method is predicting the behaviour of the network with reasonable accuracy. It is evident, however, the most accurate results will require the full load flow solution from OpenDSS to be used.

3.8 Summary

Fine-grained reactive power control is set to become an integral part of DSO planning and operations. It is paramount that the impact of reactive power on distribution system operations and planning is well understood. To this end, the following research question was studied:

How can the impact of inverter reactive power control on the efficiency of distributed

Table 3.6: Predicted (two-bus) and actual (OpenDSS) relative power loss fraction bounds. The two-bus values are based on the LinDistFlow load flow solution.

Study ID	Circuit	OpenDSS		Two-Bus	
		$\epsilon_{\mathrm{P}}^{\mathrm{init}}$, %	$\epsilon_{\mathrm{P}}^{\mathrm{trml}}$, %	$\epsilon_{\mathrm{P}}^{\mathrm{init}}$, %	$\epsilon_{\mathrm{P}}^{\mathrm{trml}}$, %
A	34 Bus	7.5	15.2	9.5	15.6
B	34 Bus	18.1	23.0	21.7	27.9
C	34 Bus	24.6	32.3	23.4	28.7
D	EPRI K1	1.3	3.1	−1.5	−0.3
E	EU LV	0.8	5.4	0.6	4.4
F	EU LV	7.8	12.9	8.1	11.9

generation be analytically characterised, considering power flow up to the maximum power transfer point?

The two-bus network has been studied to consider the impact of reactive power on losses. This model is advantageous as it contains relatively few parameters, and so the effect of each parameter can be studied explicitly and with full generality.

The first part of this chapter studied the voltage-constrained maximum power transfer. This point is interesting to study because it bounds, for example, the maximum amount of generation that can be installed even if the generation is at zero marginal cost (e.g., inverter interfaced PV). On the other hand, it demonstrates the maximum amount that a network could ever generate, even if there are no reactive power constraints at a generator or substation.

It was demonstrated that for a purely resistive network that no reactive power should be used. To the contrary, however, for R/X ratios close to unity (as seen in many distribution networks), reactive power can increase the amount of generation significantly. For R/X ratios greater than 0.7, it was demonstrated that losses limit power transfer prior to stability constraints caused by the loadability boundary.

The analysis of the properties showed that the behaviour of distribution network losses changes rapidly with the R/X ratio around unity, motivating a study of the impact of reactive power on losses at lower powers in the second half of the chapter. Specifically, the impact of reactive power control on *energy* losses across some time

period (as opposed to *power* losses) is considered. To study these losses, the relative energy loss fraction was proposed. If the value of this is high, it implies that the measures used to increase generation provide less benefit than expected (compared to a case where losses are ignored).

Novel bounds are derived for the relative energy loss fraction on the two-bus circuit, using the LinDistFlow solution (under the assumption that the network is controlled to minimize total feeder power draw). The bounds are shown to be dependent on the 'base' case and 'change' case reactive powers; the load reactive power; voltage regulation of the feeder; and the R/X ratio. These bounds are useful as they allow a network operator to quickly identify the range of relative loss fractions, and understand the amount that changes to parameters will have on these values. This could be used to compare locations for reactive power, or identify if separate loss charges may be required in some networks.

The chapter closes with a twofold validation of the bounds based on the LinDistFlow model. Firstly, the LinDistFlow bounds are compared against the Exact non-linear bounds with respect to reactive power and voltage drop parameters, as well as the bounds at a fraction of the power at the maximum power transfer point. It was found that the model is less accurate at low R/X ratios and at high powers. The error was less than 10% for networks with R/X ratio between 0.7 and 4 (i.e., covering distribution network line parameters), so long as generation was below 20% of the maximum potential generation gain that can be realised using reactive power control.

The second validation step considers a set of case studies demonstrating the accuracy of the bounds on three unbalanced distribution networks. The relative loss fraction lower bounds (as calculated by OpenDSS) were as high as 25% in a high-penetration scenario. It was found that the absolute difference between the predicted and actual relative energy loss fractions was less than 5% in case studies. However, given that calculated bounds are all less than 33%, there is clearly still a need for detailed load flow calculations.

This chapter has focussed on the study of losses for large-scale PV. These DGs are

likely to have good communications infrastructure and an ability to modify its control actively according to the voltages within the network. On the other hand, in a scenario with a large amount of small-scale PV generation, the methods considered by network planners need to include a full network model as there are potentially thousands of customers connected to a network. Secondly, there is significant uncertainty as to the potential locations of PV generators that will be installed. As such, stochastic methods are the focus of the next chapter.

Chapter 4

Linear Methods for Calculating Stochastic Hosting Capacity

In this chapter, the following research question is addressed:

How can the stochastic hosting capacity of a distribution network be calculated in a computationally efficient manner, considering voltage regulators and reactive power control from distributed generators?

For this chapter, two stochastic hosting capacity problems are considered. The *stochastic hosting capacity curve* describes the likelihood of a constraint violation over the range of some parameter (for example, the penetration of rooftop PV). The first problem considered in this chapter is the calculation of the stochastic hosting capacity curve across the whole range of customer DER penetrations, up to 100% penetration. This allows a utility to understand the hosting capacity properties of a network. Uncertainty is in terms of the location and size of solar PV generators; it can therefore be considered as a planning-type problem, with the output leading to insights as to where and why the network is constrained, and if interventions will be required.

The second problem that is considered is the calculation of stochastic hosting capacity quantiles. These quantiles are the values of penetration that lead to a given

likelihood of a constraint violation. If a network operator is willing to accept the risk of having to upgrade a network early, then the resulting increase in generation would result in a greater utilisation of existing network infrastructure.

In this chapter a method using a linear model is proposed to calculate both the stochastic hosting capacity curve and stochastic hosting capacity quantiles. The proposed system method utilises a linear 'regulated load flow' (RLF) model, taking into account voltage regulator controls as the networks have traditionally been operated.

This new formulation allows for the properties of linear models to be exploited in three ways. Firstly, a linear feasibility problem is proposed to model the control a centralised DERMS system may have access to. This model considers if there is any tap and generator power factor set point that would lead to a feasible load flow solution. The second method takes advantage of the closed-form calculation of the mean and covariance bus voltages, for eliminating calculations which will not impact on the final hosting capacity curve. The final method considered is a direct method for calculating hosting capacity quantiles, under the assumption that uncertainty is with respect to a scale parameter.

To demonstrate the computational efficiency of the proposed linear method and the insights that can be drawn from it, two sets of case studies are developed. The first set of case studies validate the method for calculating hosting capacity curves against the full non-linear load flow solution. In addition, it illustrates the benefits of using both the linear regulated model and DERMS control. The second set considers the calculation of hosting capacity quantiles, and illustrates the benefits of stochastic hosting capacity calculations for decision making.

Chapter roadmap Definitions of a number of stochastic hosting capacity quantities are first described in Section 4.1. A 'linear network model' is proposed in Section 4.2 that combines linear load flow with a linearization in tap positions. This linear network model is combined with regulator controls in the proposed RLF model, described in Section 4.3; the DERMS-based centralised control scheme is also proposed

alongside a method for increasing the computational efficiency of the RLF model. Section 4.4 uses a number of case studies to demonstrate the performance of the method, including detailed error analysis and an illustration of the advantages of the proposed linear method. Section 4.5 describes a set of problems that are particularly well suited to the proposed linear methods due to the hosting capacity values being given in closed-form. A second set of case studies, based on this property, are demonstrated in Section 4.6, including a set of model scenarios that could be encountered by a DSO. The findings from this chapter are summarised in Section 4.7.

4.1 Stochastic Hosting Capacity Analysis

Stochastic hosting capacity is defined according to the probability of power quality constraints being violated, given uncertainty in DER locations and sizes. In some instances a hosting capacity curve is of interest, whilst in other cases the value of a parameter that results in a specific likelihood of a constraint violation is required. The parameter of interest varies between applications. In some cases, the penetration level is the quantity of interest (i.e., the number of customers that can connect prior to a constraint violation), whereas in other applications it is the power that causes the violation which must be determined.

In this section, the stochastic hosting capacity curve and quantiles are described, after which the considered network constraints are introduced. The Monte Carlo approach is then described; finally, a framework for analysing the computational complexity of affine operations is described for analysing the computational burden and scalability of the algorithms described through the chapter.

4.1.1 Hosting Capacity Curves and Quantiles

To define a stochastic hosting capacity curve, the stochastic hosting capacity function is first introduced. The stochastic hosting capacity function F_p specifies the probability of a power quality constraint violation given some parameter p (for example,

the fraction of locations with PV). More precisely, the stochastic hosting capacity function F_p satisfies

$$F_p(p) = \Pr(\mathcal{X} \leq \mathcal{X}_+ | \, p) \ , \tag{4.1}$$

where $\mathcal{X}$ is a random vector that contains all power quality indices of interest, $\mathcal{X}_+$ is a vector of associated constraints, and $\leq$ represents element-wise inequality.

The stochastic hosting capacity curve is the image of the hosting capacity function 4.1 over the range of the parameter p. For example, it is the curve that describes the likelihood of a constraint violation, from 0% to 100% penetration. For notational simplicity, the notation F_p shall be used to denote both the stochastic hosting capacity function and curve.

In general, the whole curve F_p is of interest for the following reasons.

- Different constraints are active as the penetration changes, with each constraint being impacted on by network interventions differently. This visibility helps to identify what can be done to increase hosting capacity.
- An estimate of F_p can be used to identify load levels where constraint violations are most impactful, which can then be investigated with more detailed techniques (e.g., using QSTS).
- Maximum and minimum hosting capacity calculations will identify very unlikely scenarios (e.g., all generators connected to one phase at the end of a feeder).

Figure 4.1 plots a (hypothetical) stochastic hosting capacity curve. Sections 4.3 and 4.4 of this chapter will focus on calculations of stochastic hosting capacity curves, as described by (4.1).

The stochastic hosting capacity quantile p^ϕ is the minimum value of p that results in a given hosting capacity violation,

$$p^\phi = F_p^{-1}(\phi) \, . \tag{4.2}$$

(In the case that F_P is many-to-one, then the smallest (principal) value of (4.2) can

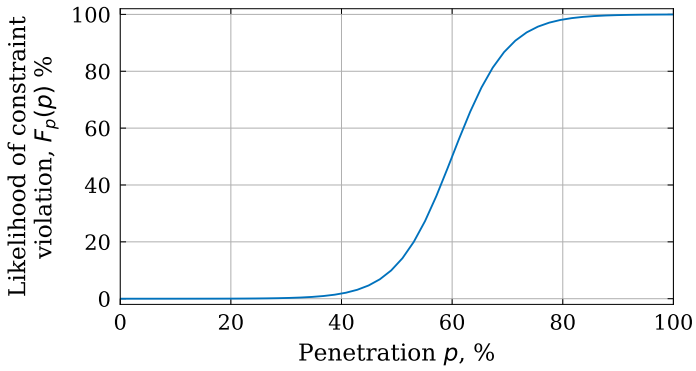

Figure 4.1: A stochastic hosting capacity curve. In this curve the stochastic hosting capacity 50%-quantile, $p^{50\%}$, occurs at a penetration level of 60%.

be taken.) This can alternatively be viewed in terms of a probability: the ϕ % hosting capacity quantile satisfies

$$\Pr(\mathcal{X} \leq \mathcal{X}_+ \,|\, p = p^\phi) = \phi\,. \tag{4.3}$$

The smallest and largest values of (4.3) are called the minimum and maximum hosting capacity values of a network [3]. Stochastic hosting capacity is not well-suited to finding maximum and minimum hosting capacity values: if these are required, then an optimization should be run explicitly to find these values (as in, e.g., [109]). Instead, the focus of stochastic hosting capacity is on estimating the shape of the majority of the probability mass.

The optimal location for DG in networks (for maximising hosting capacity) will usually be at the start of the feeder [3]. This is because the start of the feeder is the location for which the sensitivity to voltage is smallest. In any case, if the locations of DG are known, then there is no stochastic element and so the hosting capacity is unique.

Specific values of p^ϕ are of interest for the following reasons.

- If a network operator chooses the amount of DG that can connect under assumptions about DER growth rates, then some small acceptable level of risk (e.g., less than 10%) allows for a greater utilisation of assets compared to the

robust case [94, 100].

- The worst-case, robust scenario is likely to result in unrealistic penetration scenarios–the weakest parts of the network will end up with the highest penetrations of PV (e.g., the end of feeders tends to be the weakest part of the network [102]).

Sections 4.5 and 4.6 will focus on finding specific hosting capacity constraints of the form of (4.2).

Comparing hosting capacity curves There are a range of methods that can be used to compare predicted and true values of a given quantity. To compare the difference between hosting capacity curves, the mean absolute error is proposed to differentiate two curves F_p, $\hat{F}_p$ as

$$\text{MAE} = \frac{1}{p_1 - p_0} \int_{p_0}^{p_1} |F_p(p) - \hat{F}_p(p)| \, dp \,, \tag{4.4}$$

As the data will be studied under a unique scale (the range of F_p is 0% to 100%), this metric has clear advantages of being simple to calculate and interpret [166].

4.1.2 Hosting Capacity Parameters

In this chapter, the hosting capacity is studied as a function of two quantities (i.e., p as previously defined represents two different variables). Penetration-based stochastic hosting capacity analysis outputs a function F_{Pen} that specifies the probability of a power quality constraint violation for a given fraction of locations with PV, $\alpha_{\text{PV}} \in [0\%, 100\%]$. That is, the stochastic hosting capacity curve F_{Pen} is defined as

$$F_{\text{Pen}}(\alpha_{\text{PV}}) = \Pr(\mathcal{X} \leq \mathcal{X}_+ | \, \alpha_{\text{PV}}) \,. \tag{4.5}$$

Power-based stochastic hosting capacity is defined in a similar way: a function F_{Pwr} is found that specifies the probability of power quality constraint for a given generating

power that is installed,

$$F_{\mathrm{Pwr}}(P_{\mathrm{PV}}) = \Pr(\mathcal{X} \leq \mathcal{X}_{+} |\, P_{\mathrm{PV}}) \;, \tag{4.6}$$

where P_{PV} is the total power of all PV generators that are installed. These curves will generally not be the same, as PV penetration level α_{PV} gives rise to a range of generator powers P_{PV}.

4.1.2.1 Stochastic Hosting Capacity Sensitivity

To characterise the sensitivity of the hosting capacity to uncertainty in generator sizes, a new metric is proposed to capture changes in stochastic hosting capacity as may occur. The stochastic hosting capacity sensitivity $F_{p,\,\mathrm{S}}$ is defined as the change in hosting capacity with respect to changes in generator sizes,

$$F_{p,\,\mathrm{S}} = \lim_{k \to 0} \left(\frac{1}{2k} \int_{0\%}^{100\%} |F_p^{(1+k)P_{\mathrm{gen}}}(p) - F_p^{(1-k)P_{\mathrm{gen}}}(p)| \; dp \right) \;, \tag{4.7}$$

where $F_p^{(1+k)P_{\mathrm{gen}}}$ represents the hosting capacity function (4.1) with all generators scaled linearly by the factor $(1 + k)$.

If this value is high, it implies that the hosting capacity curve F_p changes quickly with bus injections. If this value is small, then the hosting capacity is robust to uncertainty in generation. Therefore, if there is an error in the calculation of power quality indices (e.g. steady state voltages), then this implies that the curve will introduce a larger error. This will be studied in the context of the linear models introduced later in this chapter, as these necessarily will introduce an error in the calculation of non-linear phenomenon.

4.1.3 Hosting Capacity Constraints

Two types of voltage constraint are studied in detail in this section: steady state voltage limits and voltage deviation limits. Per-unit values of steady state limits typ-

ically vary depending on their location in the network [167]. For this work, therefore, secondary (LV) and primary (MV) constraints take different numeric values. Voltage deviation limits consider changes in voltage magnitude as PV export ramps from 100% to 0% across the network, with the assumption that the ramp is sufficiently fast that regulation equipment (i.e. regulator taps and capacitors) does not act [95, 103].

It is known that both overvoltages and undervoltages can be caused by PV. Therefore a high-load and low-load solution is considered, as is suggested in the literature [95]. The choice of the exact values of these factors could be identified by finding, for example, midday minimum and maximum loading through the year.

To calculate voltage deviation values, the low-load solution is calculated and compared with the load flow solution with no PV (for the load flow with the same tap settings).

It is worth noting that these are not the only hosting capacity constraints that exist; Bollen and Hassan list increased risks of overload and losses, risk of overvoltages, increased levels of power quality disturbances, incorrect operation of protection, and system stability issues as hosting capacity challenges for DGs [8, Ch. 1]. The load-flow based methods of this chapter are well-suited for the study of overloads, overvoltages, and some power quality disturbances; however, as outlined in Section 1.2.2, voltage magnitude violations are a particular concern. The methods outlined here could naturally be extended to include overloads, as branch currents are related to voltages by a linear relation (as discussed in Section 2.4).

4.1.4 Calculating Stochastic Hosting Capacity

The Monte Carlo approach [114] approximates (4.5), (4.6) by running N_{MC} scenarios, approximating $F_{(\cdot)}$ with a function $f_{(\cdot)}$, given by

$$f_{\mathrm{Pen}}(\alpha_{\mathrm{PV}}) = \frac{N_{\mathrm{Vltn}}(\alpha_{\mathrm{PV}})}{N_{\mathrm{MC}}}\,, \tag{4.8}$$

$$f_{\mathrm{Pwr}}(P_{\mathrm{PV}}) = \frac{N_{\mathrm{Vltn}}(P_{\mathrm{PV}})}{N_{\mathrm{MC}}} \tag{4.9}$$

Table 4.1: Descriptor of vector/matrix linear multiplication operations implemented in BLAS [5], with α, β as scalars, x, y as vectors and A, B, C as full matrices and T as a triangular matrix. Matrices and vectors are assumed to be dimensioned according to n.

BLAS level	Level 1	Level 2	Level 3
Operations	Vector-vector	Matrix-vector	Matrix-matrix
Memory requirements	$\mathcal{O}(n)$	$\mathcal{O}(n^2)$	$\mathcal{O}(n^2)$
Processing requirements	$\mathcal{O}(n)$	$\mathcal{O}(n^2)$	$\mathcal{O}(n^3)$
Calculation examples	$x \leftarrow \alpha x + y$	$x \leftarrow Ax + y$	$A \leftarrow AB + C$
	$x \leftarrow \alpha \|x\|_2 + \beta$	$A \leftarrow A + \alpha xy^\intercal$	$B \leftarrow \alpha T^{-1} B$

where N_{Vltn} is the number of draws that result in a constraint violation. The approximations $f_{(\cdot)}$ are referred to as the hosting capacity curves from here. Similarly, the stochastic hosting capacity sensitivity (4.7) is approximated by

$$f_{p,\mathrm{S}} = \frac{1}{2k} \sum_{p=0\%}^{100\%} |f_p^{(1+k)P_{\mathrm{gen}}}(p) - f_p^{(1-k)P_{\mathrm{gen}}}(p)| \, \delta p \,, \tag{4.10}$$

for discretization step δp, and $f_p^{(1+k)P_{\mathrm{gen}}}(p)$ denoting the hosting capacity function with all generator sizes scaled by the constant factor $(1 + k)$. (In this work, a value of $k = 5\%$ is used.)

4.1.4.1 Computational Complexity of Affine Operations

As one of the goals is to create a workflow that can be solved by considering the nominal attention span of a human operator, the computational complexity of a number of the types of affine operations and linear algebra subroutines are briefly summarised.

The 'level' of an affine operation is based on the BLAS (Basic Linear Algebra Subprograms) functionality [5], based on memory and computation requirements and the type of operations used. The 'level' corresponds to the order of computational complexity involved (in terms of memory and floating point operation count) [168]. Table 4.1 briefly outlines the main features of the three levels.

In the case of Level 3 general matrix-matrix multiplication, the number of arith-

metic operations required for matrices $A \in \mathbb{R}^{m\times n}$, $B \in \mathbb{R}^{n\times p}$ is $m \times n \times p$. Reducing any of m, n, or p therefore decreases the computational complexity linearly. (Methods with smaller numbers of calculations are known, such as 'Strassen Multiplication', but usually have higher overhead or memory requirements [168] and are not considered here.) Matrix factorisations (e.g. the Cholesky or Singular Value Decomposition) typically require $\mathcal{O}(n^3)$ operations, and therefore they are also considered Level 3 operations in this work.

One operation which is not natively within the Level 2 library, but fits the memory and processing requirements is that of pre- (or post-) multiplication of a matrix by a diagonal matrix,

$$A \leftarrow \mathrm{diag}(x)A\,. \tag{4.11}$$

This operation is equivalent to scaling all rows of A by the factors in x. As such, there are n^2 multiplications and the memory requirement is n^2. For the purposes of this exposition this shall therefore be considered a Level 2 operation (much like the outer product update $A \leftarrow A + \alpha xy^\intercal$).

Sparsity In many cases, matrices only have a relatively small number of non-zero entries, in which case the matrix is referred to as *sparse*. In this case, operations are designed to roughly be independent of the number dimensions of the matrices and instead be proportional to the number of non-zero elements [169]. If a matrix is not sparse it is referred to as *dense*.

For dense matrices, solving matrix equations (and thus finding the inverse) is typically found by LU decomposition with partial pivoting and solving the subsequent triangular system [170], and so this problem is solved as a sequence of Level 3 operations. Admittance matrices (to be considered later in this chapter) are usually sparse, however, and so the inverse of matrices should be approximately proportional the number of non-zero elements, rather than the matrix dimension [169].

4.2 Linear Models for Hosting Capacity Analysis

In this section the linear network model for hosting capacity analysis is proposed, based on a combination of a fixed-point linearization for the linear load flow and a perturb-and-observe based linearization for taps. The control of regulators is combined to describe the regulated load flow (RLF) model. This models the three regulator types that are implemented in OpenDSS. These regulator types are (i) locked taps (e.g. a boost autotransformer), (ii) regulators with fixed setpoints (fixed regulation), and (iii) regulators with line drop compensation.

The final model assumes that regulator settings and inverter power factors are controllable by a central DERMS system with good network visibility. This linear model with centralised control is referred to as the 'linear DERMS' model. This identifies if there is any tap and reactive power combination that result in a feasible solution.

4.2.1 Linear Network Model and RLF Model

As described in the literature review, a load flow linearization is of the form

$$V = M_S S_{\text{bus}} + a\,, \tag{4.12}$$

where M_S, a represent the linear sensitivity and offset matrices, V is a vector of network voltages and S_{bus} collects all bus injections. The linearization method for this problem is first considered before considering the impact of taps on the linearization.

4.2.1.1 Chosen Load Flow Linearization Method

Following the literature review of linear models (Section 2.4), the fixed-point linearization model from [139] was chosen, which has two key advantages. Firstly, if the network impedance matrix is known or can be calculated in advance, that it is very fast to calculate, as it only requires level two operations. Secondly, it can be

considered a 'global' approximant, insofar as it shows zero error at the no-load point and the linearization point, leading to smaller overall error across a wider range of powers than Taylor-series based methods.

The method to calculate this value is now outlined. The voltage vector V is partitioned into a source voltage $V_0 \in \mathbb{C}^3$ and network voltages $V_\mathrm{L} \in \mathbb{C}^{N_V-3}$, and the admittance matrix similarly partitioned, i.e.,

$$V = \begin{bmatrix} V_0 \\ V_\mathrm{L} \end{bmatrix}, \qquad Y_\mathrm{bus} = \begin{bmatrix} Y_{00} & Y_{0\mathrm{L}} \\ Y_{\mathrm{L}0} & Y_{\mathrm{LL}} \end{bmatrix}, \tag{4.13}$$

then the complex fixed point linearization linear load flow model is calculated as [139]

$$M_\curlyvee = \begin{bmatrix} Y_{\mathrm{LL}}^{-1}\mathrm{diag}(\breve{V}^*)^{-1} & -\jmath Y_{\mathrm{LL}}^{-1}\mathrm{diag}(\breve{V}^*)^{-1} \end{bmatrix} \tag{4.14a}$$

$$M_\Delta = \begin{bmatrix} Y_{\mathrm{LL}}^{-1}H_\Delta^\intercal\mathrm{diag}(H_\Delta\breve{V}^*)^{-1} & -\jmath Y_{\mathrm{LL}}^{-1}H_\Delta^\intercal\mathrm{diag}(H_\Delta\breve{V}^*)^{-1} \end{bmatrix} \tag{4.14b}$$

$$a = -Y_{\mathrm{LL}}^{-1}Y_{\mathrm{L}0}V_0\,, \tag{4.14c}$$

where $\breve{V}$ is the known solution satisfying (2.9) at a given load point $\breve{S}_\mathrm{bus}$. It is shown in [139] that this method is equivalent to finding an interpolation between the no-load load-flow solution $(0,\, a)$, and the known load-flow solution $(\breve{S}_\mathrm{bus},\, \breve{V})$[1].

The method is validated against the accuracy of published results in the Appendix, section A.2.1, and the computational scalability of the method considered in the Appendix, section A.2.2.

4.2.1.2 Linear Calculations of Voltage Magnitudes

In this chapter, voltage magnitudes are constrained, rather than complex voltages. Calculating the magnitude of a complex number is a non-linear operation and so a

[1]To see this from [139], note that specifying the voltages in (18) results in a linear set of equations in power injections. Choosing the injections to be zero leads to the no-load solution; setting the injections to the linearization point yields the linearization solution; intermediate points are then an interpolation between these two points.

further linearization is required to calculate the voltage magnitude.

The following rule is stated without proof in [139]:

$$\frac{\partial|f(x)|}{\partial x} = \frac{1}{|f(\breve{x})|}\Re\left(\frac{\partial f(x)}{\partial x}f^*(\breve{x})\right). \tag{4.15}$$

This can be derived as follows. In the case of a complex-valued function f, the following holds:

$$|f(x)|^2 = f(x)f(x)^*, \tag{4.16a}$$

$$\frac{\partial|f(x)|^2}{\partial x} = \frac{\partial f(x)}{\partial x}f(x)^* + f(x)\frac{\partial f^*(x)}{\partial x} \tag{4.16b}$$

$$= 2|f(x)|\frac{\partial|f(x)|}{\partial x}. \tag{4.16c}$$

Combining the right hand of (4.16b), (4.16c) yields

$$\frac{\partial|f(\breve{x})|}{\partial x} = \frac{1}{|f(\breve{x})|}\Re\left(\frac{\partial f(x)}{\partial x}f^*(\breve{x})\right) \tag{4.17}$$

$$= \Re\left(\frac{\partial f(x)}{\partial x}e^{-\jmath\arg(f(\breve{x}))}\right). \tag{4.18}$$

As such, by (4.18) the approximation of (4.15) is equivalent to making the assumption that the argument of the complex value of the function f does not change too much.

This can be applied to the linearization (4.14) as

$$|V| = K_S S_{\text{bus}} + b \tag{4.19a}$$

$$K_S = \operatorname{diag}(|\breve{V}|)^{-1}\Re\left(\operatorname{diag}(\breve{V}^*)M_S\right) \tag{4.19b}$$

$$b = |\breve{V}| - K_S\breve{S}_{\text{bus}}, \tag{4.19c}$$

where $\breve{S}_{\text{bus}}$ is the linearization power that leads to the solution $\breve{V}$.

4.2.2 Linear Load Flow with Taps

In this section, linear models which account for both load flow models and for regulator taps are proposed. Bus voltage magnitudes $|V|$ in power injections S and (integer) tap positions T are calculated as

$$|V| = K_T T + K_S S_{\text{bus}} + b \tag{4.20a}$$

$$= K_T T + K_P P_{\text{bus}} + K_Q Q_{\text{bus}} + b\,, \tag{4.20b}$$

where K_T represents a sensitivity matrix of the tap positions T. The power injections vector S_{bus} is a stacked vector of real and reactive power injections P, Q, i.e.,

$$S_{\text{bus}} = \begin{bmatrix} P_{\text{bus}} \\ Q_{\text{bus}} \end{bmatrix}\,, \qquad K_S = \begin{bmatrix} K_P & K_Q \end{bmatrix}\,. \tag{4.21}$$

Both wye and delta connected loads are accommodated in this form.

For this linear load flow model with taps, a hybrid model is proposed: the load flow sensitivity K_S is calculated based on the fixed-point linearization of the previous section, whilst the tap sensitivity is calculated via a perturb-and-observe method (as described in Section 2.4). The latter method is conceptually simple, is relatively fast (the number of non-linear load flow calculations is proportional to the number of taps) and the linearization point can be chosen explicitly to improve accuracy.

4.2.2.1 Choice of Linearization Point

The error introduced by the linearization is dependent on the linearization point; a simple method is proposed to choose the linearization point. The method is to reduce the load step by step, and record the minimum and maximum voltages at each step. The first point at which there is a constraint violation is chosen as the linearization point. This method has the advantage that it is conceptually simple, and takes into account the changes in powers that could be caused by generators (compared to, for example, linearizing at a no-generation point).

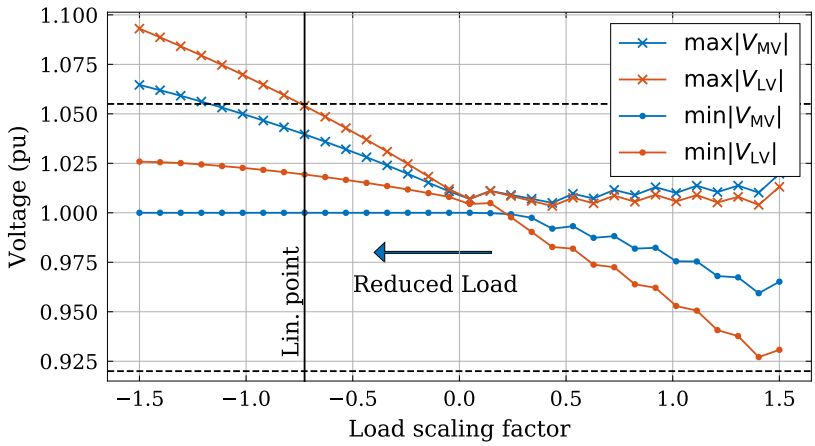

Figure 4.2: The linearization point for the linear model is found by identifying the maximum linearly scaled load point at which a constraint is violated (i.e. by multiplying all loads by a loading factor). In this figure, the maximum and minimum voltages on both the MV and LV nodes of the EPRI K1 feeder are plotted with the loading point. In this network (EPRI K1) the linearization scaling factor is at -0.72, as an LV upper voltage constraint is violated at this point.

This process is illustrate in Figure 4.2 for the EPRI K1 feeder. On this Figure, blue lines indicate upper the maximum and minimum voltages on the MV network, and orange lines indicate the same but for LV nodes. For this network, the linearization point is at a load scaling factor of -0.72.

With this point chosen, the linearization matrices can then be calculated. This involves the calculation of the load flow linearization (4.20); then, the tap sensitivity matrix is calculated using the central-difference based perturb and observe algorithm (2.11).

4.2.3 Linear Regulated Load Flow Model (Local Control)

The two main types of control for voltage regulators are fixed regulation and line drop compensation, with tap positions usually constrained to be in discrete multiples of 0.625% [77].

LDC control requires three parameters for each regulator: real and imaginary impedance parameters R^{LDC}, X^{LDC}, and a voltage parameter $V^{\text{LDC},0}$. These param-

eters act to hold the voltage at a regulated bus V^{LDC} according to

$$V^{\mathrm{LDC}} = |V^{\mathrm{LDC},0} + (R^{\mathrm{LDC}} + \jmath X^{\mathrm{LDC}})I^{\mathrm{LDC}}|\,, \tag{4.22}$$

$$\approx V^{\mathrm{LDC},0} + R^{\mathrm{LDC}}\mathfrak{R}(I^{\mathrm{LDC}}) + X^{\mathrm{LDC}}\mathfrak{I}(I^{\mathrm{LDC}}) \tag{4.23}$$

where I^{LDC} is the (complex) current measured by the regulator current transformer (and so the phase of I^{LDC} is relative to the local voltage phase), and $\mathfrak{R}(\cdot), \mathfrak{I}(\cdot)$ find the real and imaginary parts of a complex vector (or matrix) respectively. Fixed regulation is identical, but with $R^{\mathrm{LDC}} = X^{\mathrm{LDC}} = 0$.

To calculate the current phasor I^{LDC} the (complex) fixed point voltage model is combined with appropriate primitive admittances (as in [171]) to derive a model

$$I^{\mathrm{LDC}} = W_S S + b_I\,, \tag{4.24}$$

where W_S, b_I are the (complex) sensitivity matrix and offset, respectively. (Note each row of I^{LDC} must be rotated by the nominal regulator voltage angle, so that the phase angle of I^{LDC} in (4.22) is correct.)

4.2.3.1 Model Formulation

The regulated load flow model assumes that the control condition (4.22) holds exactly (relaxing the condition that each entry of T must be at an integer tap position). To construct this model, buses are partitioned into regulated buses, indexed by $(\cdot)^{\mathrm{Reg}}$, and passive (non-regulated) buses, indexed as $(\cdot)^{\mathrm{Psv}}$, written

$$V = \begin{bmatrix} V^{\mathrm{Psv}} \\ V^{\mathrm{Reg}} \end{bmatrix} = \begin{bmatrix} K_S^{\mathrm{Psv}} & K_T^{\mathrm{Psv}} \\ K_S^{\mathrm{Reg}} & K_T^{\mathrm{Reg}} \end{bmatrix} \begin{bmatrix} S \\ T \end{bmatrix} + \begin{bmatrix} b^{\mathrm{Psv}} \\ b^{\mathrm{Reg}} \end{bmatrix}\,. \tag{4.25}$$

Therefore, using the assumption $V^{\mathrm{Reg}} = V^{\mathrm{LDC}}$, (4.23) and (4.24) can be equated and solved for V as

$$|V| = K_{\mathrm{RLF}} S_{\mathrm{bus}} + b_{\mathrm{RLF}}\,, \tag{4.26}$$

where the network sensitivity matrix K_{RLF} and offset b_{RLF} are calculated as

$$K_{\text{RLF}} = \begin{bmatrix} K_T^{\text{Psv}} + K_T^{\text{Psv}} K_T^{\text{Reg}\,-1}(U_S - K_S^{\text{Reg}}) \\ U_S \end{bmatrix} \tag{4.27}$$

$$b_{\text{RLF}} = \begin{bmatrix} b^{\text{Psv}} + K_T^{\text{Psv}} K_T^{\text{Reg}\,-1}(c_I - b^{\text{Reg}}) \\ c_I \end{bmatrix}, \tag{4.28}$$

where

$$U_S = R^{\text{LDC}}\mathfrak{R}(W_S) + X^{\text{LDC}}\mathfrak{I}(W_S) \tag{4.29}$$

$$c_I = R^{\text{LDC}}\mathfrak{R}(b_I) + X^{\text{LDC}}\mathfrak{I}(b_I) + V^{\text{LDC},\,0}\,. \tag{4.30}$$

Secondly, the voltage deviation values $|\Delta V|$ must be calculated. For a ramp from 100% to 0% without tap changes, the voltage change is calculated as

$$|\Delta V| = (K_S S_{\text{bus}} + K_T T + b) - (K_S S_{\text{lds}} + K_T T + b) \tag{4.31a}$$

$$= K_S S_{\text{gen}}\,. \tag{4.31b}$$

The full regulated load flow model is therefore a combination of (4.26) and (4.31).

4.2.3.2 Model Validation

To demonstrate the requirement for taps and the control LDC to be taken into account, the linearized load flow (4.20) with locked taps (i.e. each of T fixed at their linearization value) is compared to the linear regulated load flow model (4.26).

Two different (non-linear) load flow solutions are calculated for a range of load scale factors: one with locked taps, one without.

The Necessity of Inclusion of LDC Parameters The relative error is calculated with respect to two non-linear models in Figure 4.3a, for the IEEE 123 bus network linearized with loads all scaled by -0.7 (following the procedure proposed in Section

4.2.2.1). One model has tap controls enabled, whilst the other has the taps locked. The solid black curve plots the error for the latter case, which follows the expected w-shaped error.

For the non-linear case with taps unlocked, the error varies a large amount depending on the model type. The linear model with taps locked has a relatively small error around the linearization point, but this quickly increases. The model with only 'fixed' regulation controls enabled has small errors around the origin, as at that point the current through the regulator is approximately zero (and so the regulator acts as if there is no LDC). The error remains below 1% for the case utilising LDC control. As such, it is concluded that the proposed LDC model can make a significant improvement to the accuracy of the linear model.

The error for individual nodes is plotted in Figure 4.3b. The error is distributed across buses spread throughout the network, with no buses with a significantly larger error than other buses. This indicates that the linearization is working well as an approximation across the whole range.

Tap Saturation A limitation of the model in the form (4.26) is that it does not assume constraints on the positions of taps. As such, if a tap reaches its maximum or minimum position, then the error between the linear model and the true solution will increase significantly. For example, in the IEEE 34 bus model the regulators saturate at (relatively) small levels. This leads to the region of validity of the linear model being constrained to a narrower region compared to the IEEE 123 bus network (Figure 4.4). It is interesting to note, however, the error remains below 1% even when the error of the fixed tap model has increased beyond 1%. It is assumed that this is because the action of the voltage regulator is to hold voltages in a tighter band than if they were not installed in the network.

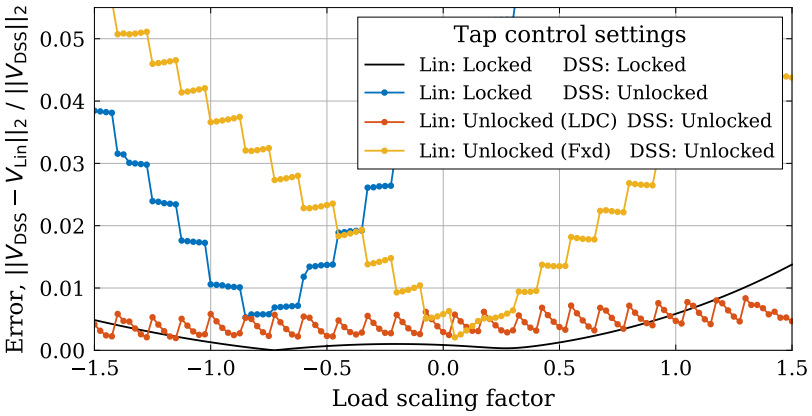

(a) Voltage error for four linear models, compared to (i) the OpenDSS model with taps locked, and (ii) the OpenDSS model with taps unlocked. Over the range considered, the linear model with LDC enabled (orange) shows comparable accuracy to the linear model with locked taps (black); the other models show large errors.

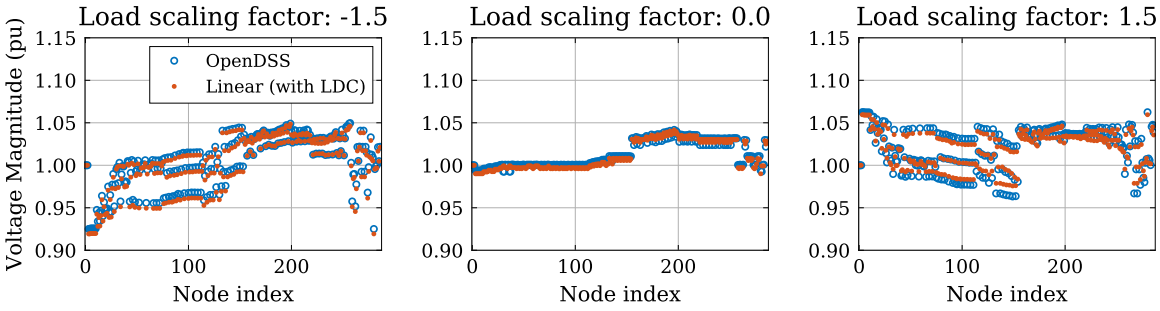

(b) Voltages calculated by OpenDSS and the linear model (with regulator LDC control), for the IEEE 123 bus network (taps unlocked).

Figure 4.3: Calculated errors for the IEEE 123 bus network in aggregate (a) and at individual loading points (b).

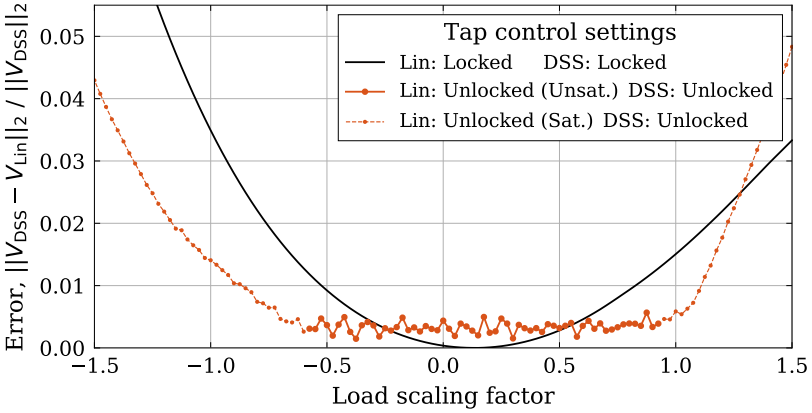

Figure 4.4: Saturation limits the region of validity for the IEEE 34 bus network.

4.2.4 Linear DERMS model (Centralised Control)

In this section, the proposed RLF model is extended, taking into account the centralised control of taps and generator inverter reactive power setpoints (as might be chosen by a DERMS controller with good network visibility). Generators are assumed to export at the same power factor, which is specified by the central controller. This is modelled by scaling a generator's real power scaled by a scalar q that determines the generator's reactive power, i.e.

$$Q_{\text{gen}} = qP_{\text{gen}}\,. \tag{4.32}$$

As such, for a given Monte Carlo scenario with real power generator sizes P_{gen}, the centralised control considers the feasibility over tap positions $T \in \mathbb{R}^{N_T}$ (i.e. there are N_T controllable taps) and generator reactive power scaling q. This can be formulated the set of linear inequalities

$$|V| = K_T T + K_P P_{\text{gen}} + K_Q q P_{\text{gen}} + K_S S_{\text{lds}} + b \tag{4.33a}$$

$$|\Delta V| = K_P P_{\text{gen}} + K_Q q P_{\text{gen}} \tag{4.33b}$$

$$V_- \leq |V| \leq V_+ \tag{4.33c}$$

$$\Delta V_- \leq |\Delta V| \leq \Delta V_+ \tag{4.33d}$$

$$q_- \leq q \leq q_+ \tag{4.33e}$$

$$T_- \leq T \leq T_+\,, \tag{4.33f}$$

where the notation $\leq$ considers elementwise inequalities and $(\cdot)_{+/-}$ represents upper/lower bounds. Equations (4.33) describe a linear feasibility problem, which is solved by formulating a linear program.

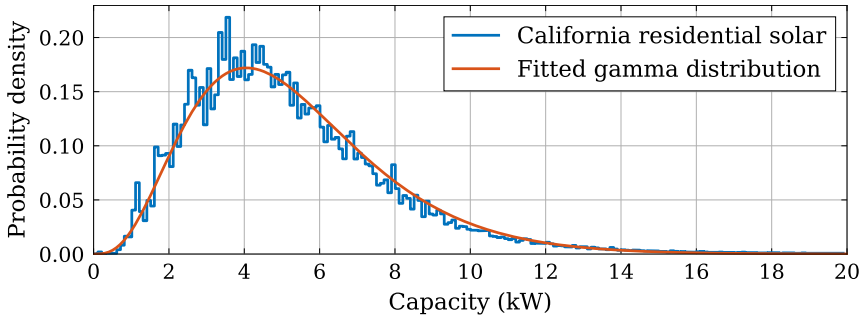

Figure 4.5: Solar PV sizes for this chapter are modelled as a gamma distribution, fitted to California residential solar data [1]. The scale parameter of 1.261 kW and shape parameter with value 4.214 was chosen using maximum likelihood estimation [2].

4.3 Regulated Load Flow Model Stochastic Analysis

In this section the stochastic properties of the proposed linear RLF model (4.26) are considered for improving computational efficiency and visualization of vulnerability of buses to constraint violations. Only the upper voltage constraint will be explicitly described; results for voltage deviation and voltage lower bounds are analogous.

4.3.1 Characterisation of Bus Power Injections

The uncertainty in this work is introduced by the location and size of any installed PV. Figure 4.5 plots domestic solar PV sizing in California, demonstrating marked differences between distribution parameters. The Californian dataset modelling domestic solar sizes will be considered for the remainder of this chapter, as the applicable case studies (of Section 4.4) consider US-style networks. For simplicity of modelling, a gamma distribution is fitted to this dataset using maximum likelihood estimation. This leads to a good fit compared to the reported data.

Real power injections P_{bus} at each bus are given by the difference between generation P_{gen} and load P_{lds},

$$P_{\text{bus}} = P_{\text{gen}} - P_{\text{lds}}\,, \tag{4.34}$$

where loads are assumed to be known. A similar expression holds for reactive power injections Q_{bus} where (for simplicity) installed generators are assumed to operate with a uniform power factor.

4.3.2 Voltage Mean and Covariance

If the voltage mean and covariance can be found efficiently, then this gives a significant amount of information about the likelihood of any one constraint being violated. More specifically, Chebyshev's inequality [172, pp. 388-389] states that, for a random variable ζ with known mean μ and variance σ, that

$$\Pr\left(|\zeta - \mu| \geq k\sigma\right) \leq \frac{1}{k^2}\,. \tag{4.35}$$

Seeking out buses with a mean voltage close to a violation and a large variance in the voltage can therefore reduce the number of calculations required–only one constraint violation is required for an infeasible load flow to be recorded.

4.3.2.1 Bus Injection Statistics

The mean of the bus injections, μ_S, is given by

$$\mu_S = \alpha_{\text{PV}}\mu_\gamma - S_{\text{lds}}\,, \tag{4.36}$$

where μ_γ is the mean of the gamma distribution modelling generator sizes, and S_{lds} are the (known) complex loads. The diagonal elements of the covariance matrix of bus injections Σ_S (i.e. bus variances) are calculated as

$$\Sigma_S^{[i,i]} = \alpha_{\text{PV}}(\sigma_\gamma^2 + \mu_\gamma^2) - (\alpha_{\text{PV}}\mu_\gamma)^2 \tag{4.37}$$

where σ_γ is the standard deviation of the gamma distribution representing generator sizes. Generation between buses is not independent, as a PV generator at load i implies that the chance of a generator at bus j is smaller (as a fixed number of buses

that have PV are assumed). The covariates $\Sigma_S^{[i,j]}$, for $i \neq j$, can be calculated to be

$$\Sigma_S^{[i,j]} = \frac{\mu_\gamma^2 \alpha_{\mathrm{PV}}(\alpha_{\mathrm{PV}} - 1)}{N_{\mathrm{lds}} - 1}\,, \tag{4.38}$$

where N_{lds} is the number of loads in the network.

4.3.2.2 Voltage Statistics

By construction, covariance matrices are symmetric positive semidefinite. As such, a covariance matrix Σ can be decomposed into a matrix square root by using the spectral decomposition as

$$\Sigma = U\Lambda U^\intercal = (U\Lambda^{1/2}U^\intercal)^2 = (\Sigma^{1/2})^2\,, \tag{4.39}$$

where $\Sigma^{1/2}$ is the unique positive semidefinite square root. This can be used to 'whiten' a random variable $\mathcal{X}$ with covariance matrix Σ and mean μ. That is, there exists a zero mean, unit variance random variable $\bar{\mathcal{X}}$ such that

$$\mathcal{X} = \Sigma^{1/2}\bar{\mathcal{X}} + \mu\,. \tag{4.40}$$

This follows from the linearity of the expectation operator.

As the mean and covariance of S_{bus} are known, this procedure can be followed to produce a 'white' random variable $\bar{S}_{\mathrm{bus}}$, rewriting (4.26) as

$$V = K_{\mathrm{RLF}}(\Sigma_S^{1/2}\bar{S}_{\mathrm{bus}} + \mu_S) + b_{\mathrm{RLF}}\,. \tag{4.41}$$

Steady state voltage constraints require that voltage magnitudes are within bounds, i.e.,

$$|V| \leq V_+\,. \tag{4.42}$$

Finally, in this last section on voltage statistics, a normalised model is formed. This is particularly simple to work with as it has zero mean, and all constraints

are normalised to unity. Therefore, the reciprocal of the standard deviation in this model is the number of standard deviations to a constraint. This normalised model is described by

$$\mathcal{Z} = K_Z \bar{S}_{\text{bus}} \,, \tag{4.43}$$

and is found by combining (4.41) and (4.42) such that

$$K_Z = \text{diag}(V_+ - b_{\text{RLF}} - K_{\text{RLF}}\mu_S)^{-1} K_{\text{RLF}} \Sigma_S^{1/2} \,. \tag{4.44}$$

The constraint (4.42) is equivalent to

$$\mathcal{Z}^{[i]} \leq 1 \quad \text{if } (V_+^{[i]} - K_{\text{RLF}}\mu_S^{[i]} - b_{\text{RLF}}^{[i]}) > 0 \tag{4.45a}$$

$$\mathcal{Z}^{[i]} > 1 \quad \text{otherwise.} \tag{4.45b}$$

Because $\bar{S}_{\text{bus}}$ is zero mean and unit covariance, the transformed model $\mathcal{Z}$ has zero mean and covariance matrix Σ_Z given by

$$\Sigma_Z = K_Z K_Z^{\intercal} \,. \tag{4.46}$$

As described, with the model in this form, the number of standard deviations $n_\sigma^{[i]}$ from the mean voltage to the voltage constraint at the ith bus is simply calculated as $(\Sigma_Z^{[i,i]})^{-1/2}$.

4.3.3 Properties of Voltage Statistics

The (normalised) variance and correlation matrix for all constraints are visualised in Figure 4.6 for a zero mean, unit variance variation in S_{bus} for the EPRI Circuit 5 [158]. The constraint variances change by four orders of magnitude, illustrating that some buses are much more likely than others to produce constraint violations. Additionally, there are large correlations between buses. If two buses are perfectly correlated, then this implies that a calculation does not need to be repeated as information obtained

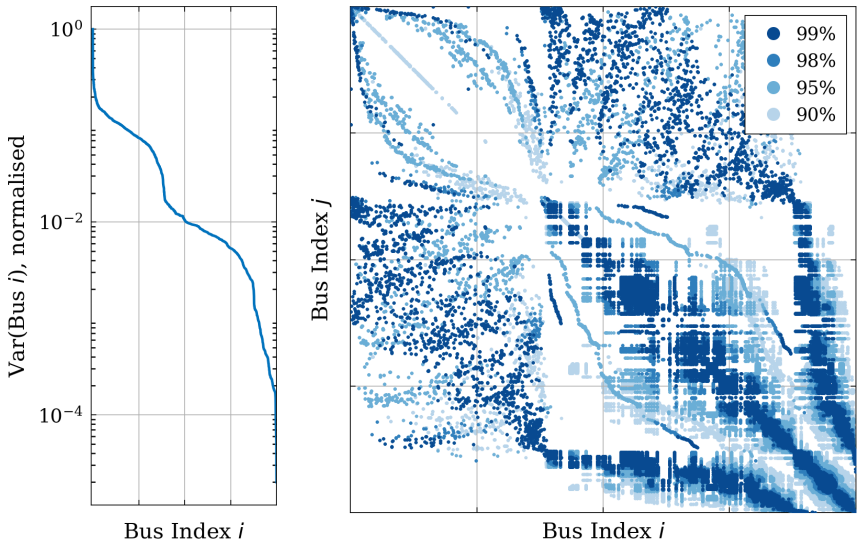

(a) Variance (b) Correlation

Figure 4.6: Visualization of the variance (a) and correlation matrix (b) of the linear model for EPRI's 'Circuit 5'. It is observed that the variance changes by several orders of magnitude between the most and least sensitive bus, and that there is significant correlation between buses.

from the first result gives perfect information about the second.

4.3.3.1 Correlation in Voltage Statistics between Penetration Levels

Initially, the mean voltage for all buses is within bounds. However, as the penetration increases, the mean voltage will tend to move towards a constraint and the variance of the voltage will also increase.

It is noted that if the initial number of standard deviations to a constraint (from (4.46)) is very large relative to other buses, then this number will likely remain large compared to the other buses. This can be seen by considering (4.46). If the distance to the constraint is large (i.e., $V_+^{[i]} - b_{\mathrm{LF}}^{[i]}$ is large for some index i) and the corresponding row of the sensitivity matrix $K_{\mathrm{RLF}}^{[i,:]}$ is also small (according to some norm), then the number of standard deviations will not tend to decrease much as the penetration increases. This is because as the value of $K_{\mathrm{RLF}}^{[i,:]}\mu_S$ will also remain small.

In other words: buses which are strong at low penetrations will remain strong as the penetration is increased. This can then be exploited as it is the weakest buses

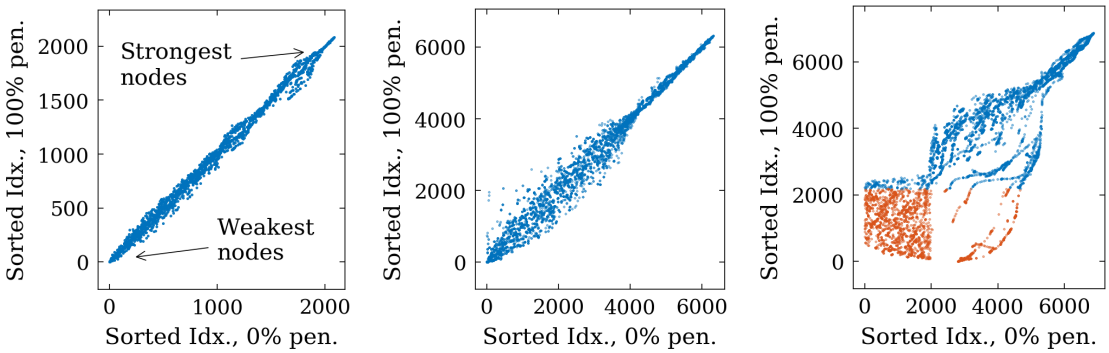

(a) Ckt. K1 (b) Ckt. M1 (c) Ckt. 5

Figure 4.7: The indices that sort the number of standard deviations in increasing order with respect to the number of standard deviations to a constraint. Two values are plotted: the index at 0% penetration, and the index at 100% penetration. Orange points indicate that the mean voltage is outside of a constraint at the 100% penetration point. This figure demonstrates that strong buses remain strong (i.e. that there is a collection of indexes in the upper right in each of these figures).

in the network determine the hosting capacity, and so calculations of voltages at the strongest buses can be avoided.

To test the hypothesis that 'strong buses remain strong', the number of standard deviations to a constraint is calculated at the 0% and 100% penetration point, and the indices that sort the two sets of vectors are compared. The results of this sorting is plotted in Figure 4.7 (note that this is for all constraints, not just upper voltage constraints). The sorting index at 0% penetration is clearly a good predictor of the sorting index at 100% penetration, particularly for strong buses. This indicates that the hypothesis is correct in the cases considered.

For the weakest buses, in some cases the number of standard deviations becomes 'negative' at 100% (indicating that the mean voltage is outside of a constraint, and plotted in orange in Figure 4.7). In networks for which this has happened, the ordering is not as accurate, as shown for the case of EPRI Circuit 5 (Figure 4.7c).

4.3.4 Network Preconditioning

Based on the observations of the previous section, a simple algorithm is proposed to remove rows of the normalised sensitivity matrix K_Z that are unlikely to cause

violations, or those which are highly correlated with other buses.

First, the normalised sensitivity matrix K_Z is calculated considering the smallest penetration of a single generator (i.e. the penetration $\alpha_{\mathrm{PV}} = 1/N_{\mathrm{lds}}$). Buses are then included in hosting capacity calculations only if:

- the magnitude of the correlation with already included buses is less than some fraction η_{Cor}; and,
- the variance is greater than some fraction of the largest variance η_{Var}.

The performance of this algorithm is determined in terms of an increased error (due to missed violations) versus the reduction in problem size and time required to run stochastic hosting capacity. The average size (across nine networks) is reduced by over 50%, even for a variance and correlation cutoff of 99% (see Figure 4.8). The maximum time required (across all networks) also reduces significantly.

The maximum allowable correlation of $\eta_{\mathrm{Cor}} = 98\%$ and variance ratio of $\eta_{\mathrm{Var}} = 70\%$ reduced the size of K_Z by between 74% and 97% (depending on the network) without introducing an error greater than 1% (in terms of the MAE (4.49)). This was therefore chosen as the best case estimate of the power of this method.

An exploration of alternative methods for reducing this burden was beyond the scope of this research; however, it is noted that alternative methods based on the bus variances directly could be used to check that buses with significant variance are not missed in this preconditioning step.

4.3.4.1 Implementation of Preconditioning Method

The matrix square root of a symmetric positive semidefinite matrix can be found by calculating the Cholesky or spectral decomposition, which are generally Level 3 operations [168]. In the case considered here, it is possible to exploit the structure of the covariance matrix to calculate the matrix square root directly to avoid this relatively expensive calculation. In particular, all of the diagonal and off-diagonal values are identical (from (4.37), (4.38)).

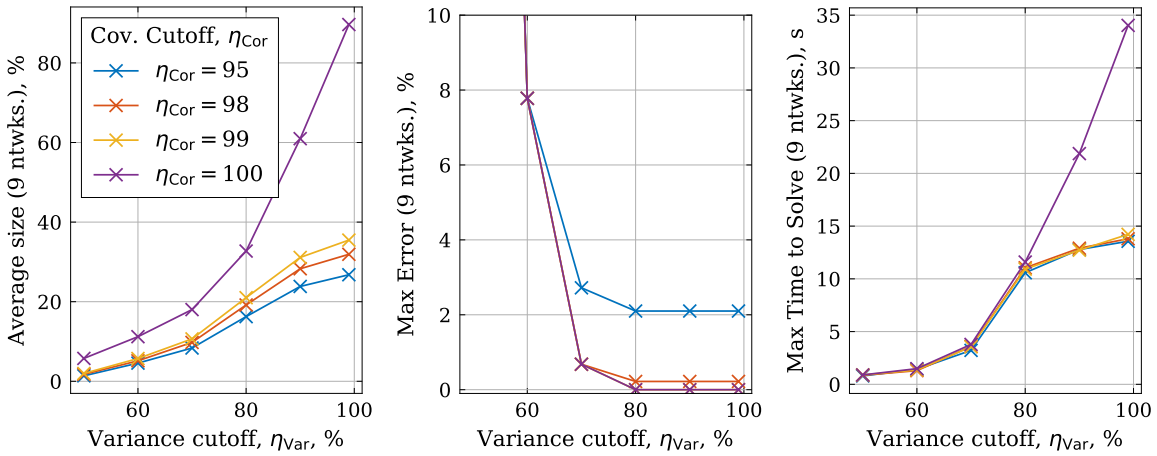

(a) Sizes (b) Error (c) Times

Figure 4.8: The use of preconditioning reduces the time for the linear model to solve by reducing the number of calculations required. The worst-case error (across nine networks) increases rapidly below a cutoff of 70%, and for a correlation cutoff below 98%.

For a matrix with diagonal γ and off-diagonal μ the matrix square root is found by solving for α, β in

$$\begin{bmatrix} \alpha & \beta & \cdots & \beta \\ \beta & \alpha & \cdots & \beta \\ \vdots & \vdots & \ddots & \vdots \\ \beta & \beta & \cdots & \alpha \end{bmatrix} \begin{bmatrix} \alpha & \beta & \cdots & \beta \\ \beta & \alpha & \cdots & \beta \\ \vdots & \vdots & \ddots & \vdots \\ \beta & \beta & \cdots & \alpha \end{bmatrix} = \begin{bmatrix} \gamma & \mu & \cdots & \mu \\ \mu & \gamma & \cdots & \mu \\ \vdots & \vdots & \ddots & \vdots \\ \mu & \mu & \cdots & \gamma \end{bmatrix}, \tag{4.47}$$

which can be expanded as follows:

$$\alpha^2 + (N-1)\beta^2 = \gamma \tag{4.48a}$$

$$2\alpha\beta + (N-2)\beta^2 = \mu\,. \tag{4.48b}$$

These simultaneous equations yield a quadratic in β^2, and α can therefore be found by back substitution. As such, there is no need to use a numerical implementation to find this square root.

Secondly, it is worth noting that the matrix-matrix calculation (4.44) only consists of Level 2 operations. This is because the matrix square root Σ_S consists of the sum

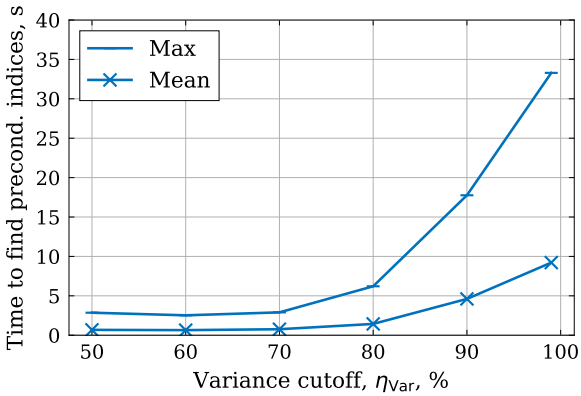

Figure 4.9: The use of preconditioning reduces the time for the linear model to solve by reducing the number of calculations required. The worst-case error (across nine networks) increases rapidly below a cutoff of 70%, and for a correlation cutoff below 98%.

of a diagonal and a rank-1 matrix. The multiplication and additions required are therefore all Level 2 calculations.

The final stage of the preconditioning is, however, a Level 3 operation (the calculation of the variance and correlation). To reduce the computational burden, the variance is first calculated for all buses–i.e. the 2-norm of all rows of K_Z are calculated, which is in total a Level 2 operation. Buses which are not included within the calculation can therefore be removed from correlation calculations, and so the operation then is dependent on the number of included buses, rather than on the matrix dimensions explicitly.

Because of this, the time taken to calculate the indices drops as the fraction of buses reduces, as low variance buses are removed (Figure 4.9). The time taken to calculate the indices reduces below 5 seconds for variance cutoffs below 80%.

Remark: Impacts of Network Reconfiguration on Complexity. One issue which is otherwise not discussed in this work is that of network reconfiguration, which in practise could mean that hosting capacity calculations would be required to be calculated for each possible network configuration. If this is the case, then the hosting capacity described in this chapter would need to be re-run, which would increase the corresponding running time.

It is worth noting, however, that the re-linearization using (4.14) would be efficient if the matrix inversion of the admittance matrix Y_{bus} has already been calculated, as an update of the inverted matrix would only require a small number of level-2 operations. To see this, note that changing the network configuration modifies only a small number of elements in the admittance matrix, so that the corresponding change to the admittance matrix is of a low rank–say, of rank n. The matrix inversion can then be carried out by using n unit-rank updates using the Sherman-Morrison formula (see e.g., [168, Ch. 2.1.4]).

4.3.5 Geographic Bus Vulnerability

A second application for the mean and variance calculations is the mapping of geographic estimates of the likelihood of a constraint violation. This allows for identification of vulnerable regions of a network and the impact of interventions designed to increase hosting capacity. Indeed, it is worth noting that visualization is considered an important part of hosting capacity analysis [3, 95].

For example, in Figure 4.10 the number of standard deviations to a constraint at each bus are plotted for cases with unity power factor and for a power factor of 0.98 inductive for EPRI Circuit 24 [158]. This approach is more meaningful than plotting (for example) the minimum or maximum bus voltage, as it also accounts for both the proximity to a constraint, and the sensitivity of a bus to changes in this proximity as generation is installed.

4.4 Stochastic Hosting Capacity Curve Case Studies

In this section the linear regulated load flow model is compared against the full OpenDSS model for nine circuits. To study how centralised control can improve the hosting capacity, the linear DERMS and regulated load flow models are then

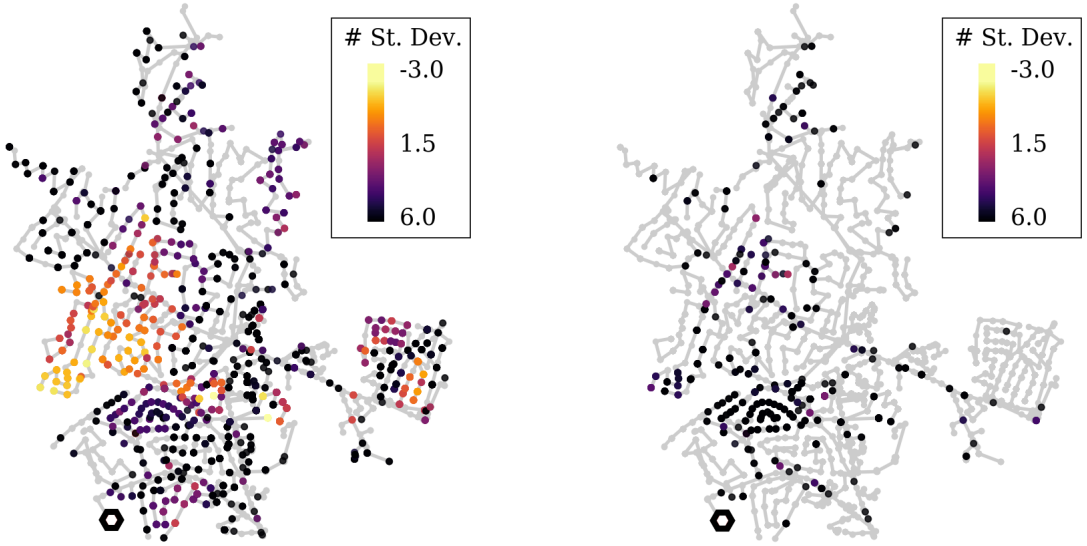

(a) PF = 1.00

(b) PF = 0.98 inductive

Figure 4.10: Number of standard deviations from the voltage mean to a constraint, for EPRI Ckt. 24, at 90% PV penetration. Negative values indicate the mean voltage is outside a constraint; grey values indicate the distance is greater than six standard deviations. At three-phase buses, the minimum number of standard deviations (i.e., the 'brightest colour') is plotted.

compared for four circuits. The IEEE 34 bus, 123 bus, and 8500 node models [155] are all studied, as well as EPRI's J1, K1, M1 feeders [157] and Circuits 5, 7, and 24 [158].

To compare the non-linear and linear hosting capacity curves, the MAE (4.4) is calculated across the sampled points as

$$\text{MAE} = \frac{1}{N_f} \sum_{i=0}^{N_f-1} |f_{\text{Pen}}(\alpha_{\text{PV}}^{[i]}) - \hat{f}_{\text{Pen}}(\alpha_{\text{PV}}^{[i]})| \tag{4.49}$$

where $\alpha_{\text{PV}}^{[i]}$ represents the ith value of N_f PV penetrations, and f_{Pen}, $\hat{f}_{\text{Pen}}$ are the true (OpenDSS) and approximate (linear) values of the hosting capacity curve (4.8).

For these case studies, $N_{\text{MC}} = 100$ Monte Carlo scenarios are run with 50 values of α_{PV} (equally spaced between 0% and 100%) over two loading points. Therefore, approximately 10^4 load flow solutions are required (a small number are additionally required for voltage deviation calculations).

4.4.1 Problem Setup

To calculate the hosting capacity, minimum and maximum midday loads of 20% and 66% of peak load are assumed (respectively), with generators/loads modelled as constant power. One capacitor was removed in each of the 8500 Node and IEEE 34 bus networks (to avoid overvoltages), but otherwise capacitors were free to switch in/out of OpenDSS as specified by their controls. The linear model assumed fixed capacitor bank positions as seen at the linearization point. Upper voltage limits of 1.055 pu were considered for both primary and secondary circuits, whilst a lower bound of 0.95 pu and 0.92 pu respectively [167]. (The slightly increased upper bounds were chosen to avoid infeasibility in networks with substation voltages around 1.05 pu.)

Uncertainty in PV panel sizes are modelled by the gamma distribution fitted to the Californian PV dataset, as described in Section 4.3.1. The parameters were modified for some circuit calculations due to the hosting capacity being extremely high or low (note that the distribution of PV sizes varies geographically). The scale factor of the gamma distribution was reduced by 50% for three circuits (8500 Node, Ckt. 5, Ckt. 7); three had the nominal scale factor (34 bus, Ckt. 24, J1), and three had the scale factor increased by 33% (123 bus, K1, M1). Voltage regulator bandwidths are set to 1 V. Computations are carried out on a desktop PC with Intel i7-5500U and 8 GB main memory.

4.4.2 Regulated Load Flow Model Hosting Capacity Analysis

The linearization of non-linear equations will always lead to some error in subsequent calculations. The accuracy of the linear load flow solutions across the nine networks is first calculated, including presenting a method to estimate accuracy *a priori*, before discussing the clear computational benefits of the models derived in this work.

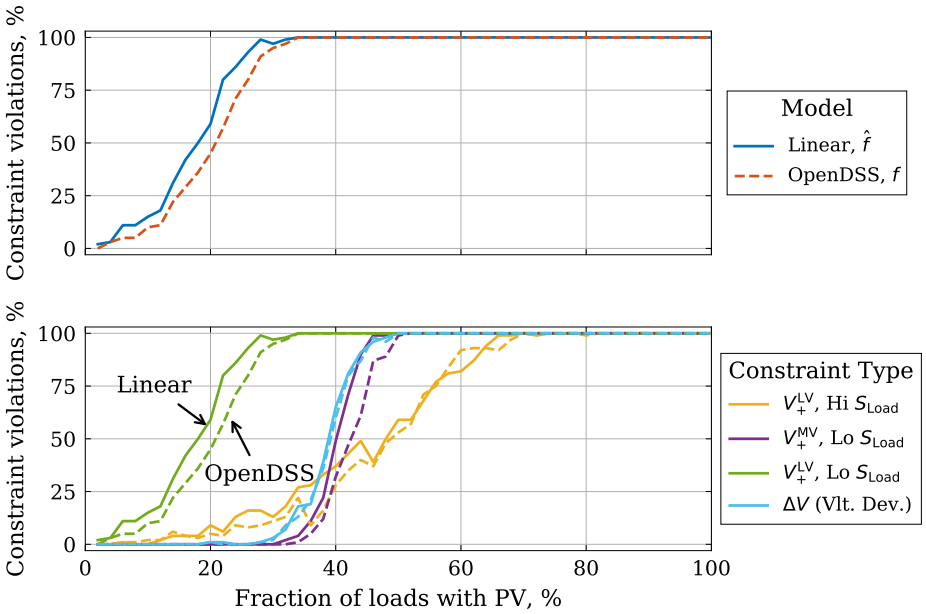

Figure 4.11: Stochastic hosting capacity for Circuit J1; both the overall hosting capacity (upper) and four of nine individual constraints are plotted (lower). The solid lines denote linear model approximation and the dashed lines the non-linear OpenDSS solution.

4.4.2.1 Detailed Results, Circuit J1

The outputs of the hosting capacity calculation for Circuit J1 are shown in Figure 4.11. The hosting capacity is mostly dominated by an upper voltage constraint on secondary circuits constraints at the low load point. (Lower voltage constraints are not plotted as these are not violated at any point for this network.) The linear model is able to accurately estimate both the total hosting capacity curve f_{Pen} and the curves for each of the individual constraints.

4.4.2.2 Model Accuracy

The stochastic hosting capacity curves for all nine circuits are plotted as box-and-whisker plots in Figure 4.12. In all cases, the linear prediction $\hat{f}_{\text{Pen}}$ closely matches the true hosting capacity curve f_{Pen} to a reasonable degree of accuracy. The calculated MAE is given in Table 4.2 and found to be less than 14% in all cases. (Note that previous works sometimes show significant error in their calculations, as great as

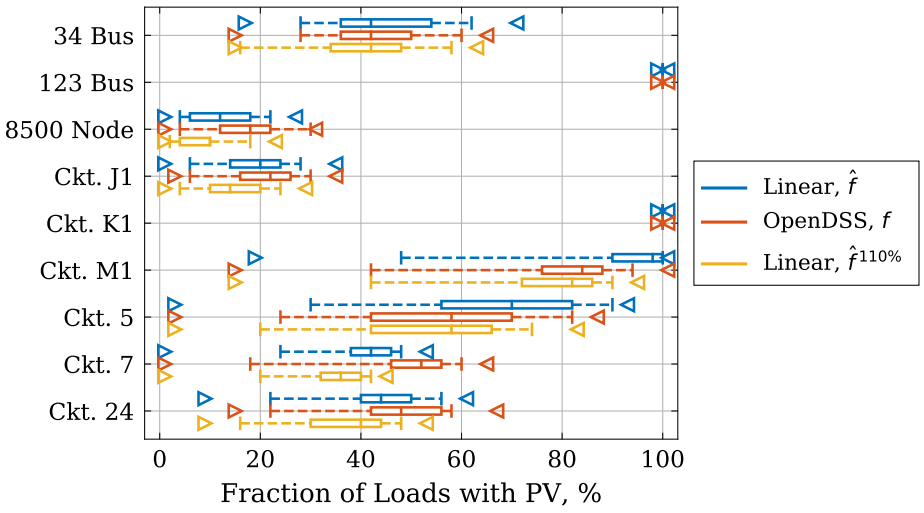

Figure 4.12: Box and whisker plot of the stochastic hosting capacity f_{Pen} (4.8) as calculated by OpenDSS and the regulated load flow model (4.26). The 0% and 100% hosting capacity values are plotted as triangles; the box-and-whisker plots the 5%, 25%, 50%, 75% and 95% values of f_{Pen}. A conservative estimate for f_{Pen} can be found using the linear model by increasing the generator sizing by 10% ($\hat{f}_{\text{Pen}}^{100\%}$).

50% in individual hosting capacity calculations in [3].) If a conservative estimate is required, a scaling of all generator sizes linearly by 110% (solution $\hat{f}_{\text{Pen}}^{110\%}$) was found to be a good heuristic for producing conservative curves (Figure 4.12).

4.4.2.3 Correlation between Sensitivity and Error

If the hosting capacity sensitivity $f_{\text{Pen,S}}$ (calculated as in (4.7)) is high then it can be expected that the error observed will be greater. This is because errors in voltages will affect the number of constraint violations that are observed.

To consider if this hypothesis is correct, the Pearson's correlation coefficient is calculated for the MAE and hosting capacity sensitivity $f_{\text{Pen,S}}$. The value of this coefficient (calculated from the mean value of $f_{\text{Pen,S}}$ and the MAE over five runs) is found to be 0.878. The values of both the raw data and the means are plotted in Figure 4.13. In other words, there is empirical evidence that the hosting capacity sensitivity provides a good means of estimating confidence in the accuracy of the linear solution.

Table 4.2: Comparison of the solutions of the regulated load flow (RLF) and OpenDSS (DSS) models; and, comparing two Monte Carlo runs RLF (i)–(ii), by calculating the MAE between them.

Model	DSS–RLF MAE, %	Solution time, s		RLF (i)–(ii) MAE, %
		DSS	RLF	
34 Bus	2.18	33.80	0.12	1.60
123 Bus	0.00	53.02	0.28	0.00
8500 Node	5.12	2861.16	1.77	1.14
Ckt. J1	2.54	1722.62	0.88	0.90
Ckt. K1	0.00	245.53	0.47	0.14
Ckt. M1	13.00	1123.80	0.59	2.04
Ckt. 5	8.50	778.86	1.06	2.36
Ckt. 7	9.02	857.05	1.30	1.40
Ckt. 24	3.70	5594.47	3.98	2.16

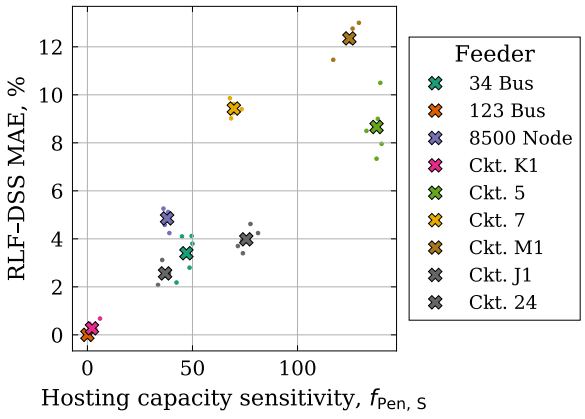

Figure 4.13: There is a strong correlation between the hosting capacity sensitivity $f_{\mathrm{Pen,S}}$ (calculated as in (4.7)) and the MAE of the linear (RLF) model with respect to the non-linear OpenDSS (DSS) solution. The small dots denote one Monte Carlo set (of which there are five for each network), and the cross denotes the mean MAE and hosting capacity sensitivity $f_{\mathrm{Pen,S}}$. The Pearson correlation coefficient for the mean values is 0.878.

4.4.2.4 Computational Performance

All hosting capacity calculations are significantly faster using the linear model than the OpenDSS model, particularly for large-scale networks (Table 4.2). The magnitude of speed increases are similar to the increases seen in other work that approximates non-linear load flows with linear models [110].

There are overheads associated with the calculations, as has been discussed in previous sections. The most significant of these is the matrix inversion required for calculating the linear load flow models. Other significant overheads are associated with random number generation and preconditioning; however, none of these are greater than 10 seconds.

To consider if 100 Monte Carlo simulations per penetration level is sufficient to estimate the stochastic hosting capacity, the (linear) stochastic hosting capacity was calculated for a second Monte Carlo run for all networks. Calculations of the MAE of these runs illustrate that the results are consistent, with the mean absolute error being less than 3% (Table 4.2).

4.4.3 Comparing Centralised (DERMS) and Local (Regulated Load Flow) Control

The stochastic hosting capacity curve and individual constraint curves are plotted in Figure 4.14 for Circuit J1 for two different generator power factors. The active upper voltage constraint indicates however that there is potential to increase the hosting capacity if taps can be controlled.

Figure 4.15 plots the hosting capacity for Circuit J1 for both DERMS-style centralised control and the regulated load flow model. With taps enabled, the hosting capacity is higher with DERMS control than regulated load flow control (both with unity power factor). With reactive power and tap control the hosting capacity is further increased significantly, with a minimum hosting capacity over 50% for DERMS control. If there is no reactive power control and locked taps, the problem is not

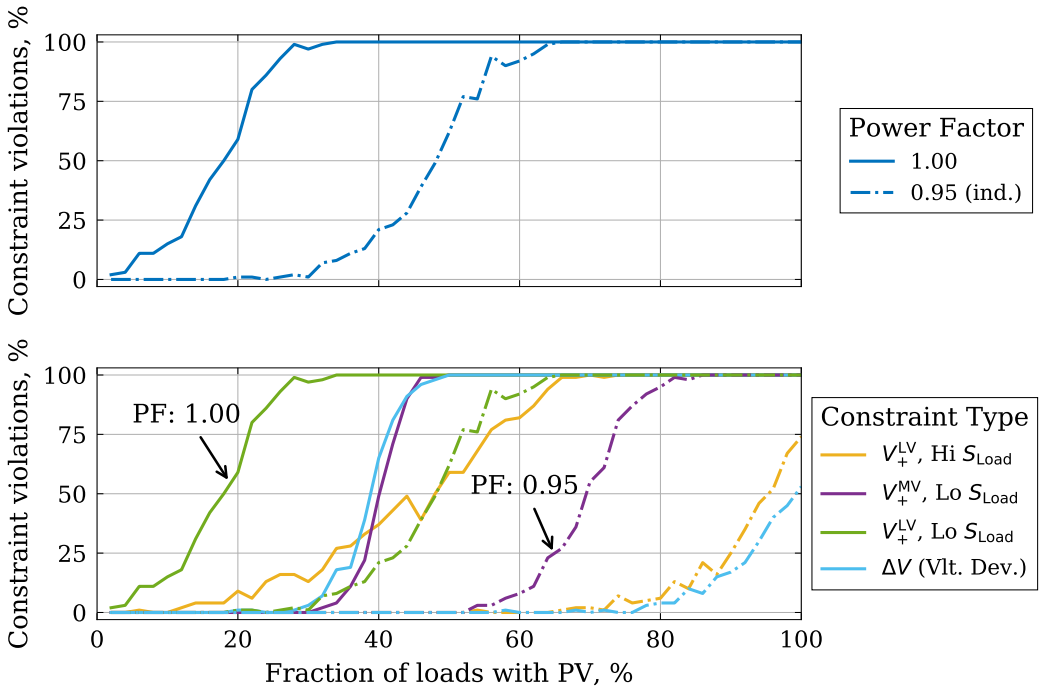

Figure 4.14: The hosting capacity curve for Circuit J1 changes significantly if generator power factors are reduced to 0.95 inductive (upper), and the impact on individual constraints (lower).

feasible (even without generation) due to the taps being locked at the linearization point.

4.4.3.1 Increasing Hosting Capacity on Four Circuits

Changes to hosting capacity for four circuits are plotted in Figure 4.16, comparing the linear regulated load flow model with unity and power factors of 0.95 inductive, as well as DERMS control with both tap and reactive power control. The use of DERMS control increases the 5% hosting capacity by 15% in all cases. The increase in minimum hosting capacity is as great as 82% in Circuit M1 for the case of 0.95 PF.

There is scope for increasing the hosting capacity in some circuits just by reducing the power factor. Circuit 24 is a particularly noticeable example, with all hosting capacity problems cleared even without DERMS, an increase in minimum hosting capacity of over 80%. It is therefore concluded that DERMS has significant potential

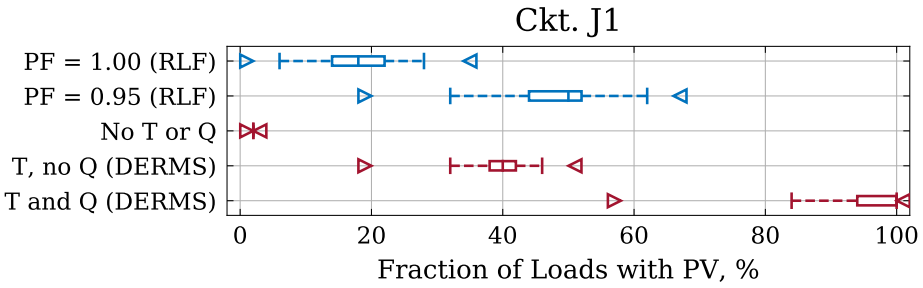

Figure 4.15: Hosting capacity curves for the centralised (DERMS) control and regulated load flow (RLF) curves. DERMS control with both reactive power (Q) and tap (T) control increases the hosting capacity the most.

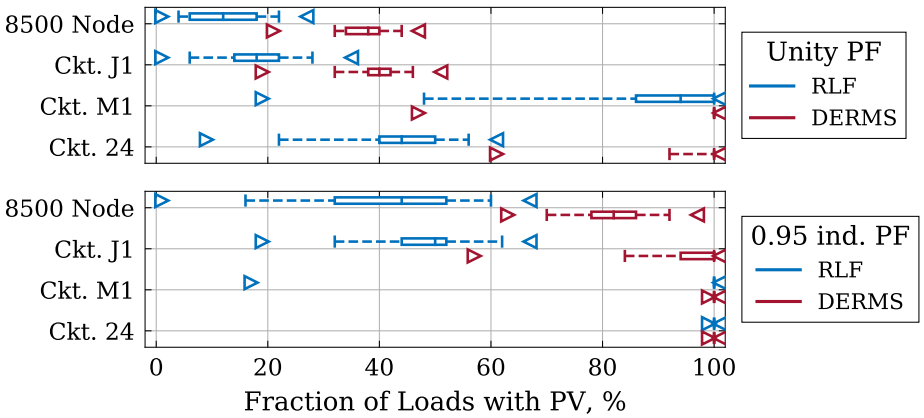

Figure 4.16: A comparison between traditional, local control (regulated load flow, RLF) and centralised (DERMS) control for four networks. The benefits of centralised control vary significantly between circuits.

to increase minimum hosting capacity, but there may be local controls actions that can be implemented (that may require less investment) that show similar improvements in hosting capacity.

4.5 Calculating Stochastic Hosting Capacity Quantile Values

In the previous section, the problem of finding bulk hosting capacity curves was discussed and the accuracy evaluated in detail. In this final section the problem of finding hosting capacity quantiles is discussed for the class of problems for which the parameter of interest is a scale parameter. That is, the aim is to calculate P_{PV}^{ϕ}, as

defined in (4.6). The limiting step is shown to be a Level 3 matrix-matrix multiplication. By exploiting the properties of the scale parameter just a single iteration is required, avoiding the use of iterative root-finding methods.

In contrast to the previous sections, generation sizes are assumed to be identical for all generators (and so the uncertainty is only in generation location). This is justified as:

- if a network operator allows customers on a network to install up to a maximum generator size, then the values calculated here are a worst case;
- levels of socio-economic development tend to be concentrated locally (and thus higher levels of load and abilities to purchase PV); and,
- the physical availability of space for PV is likely to be relatively similar in small geographical areas (e.g. within an LV network).

For simplicity, only voltage magnitude upper limits are considered, as these were the most common constraints that were violated in the previous section.

4.5.1 Calculating Hosting Capacity Quantiles

To calculate hosting capacity quantiles, a set of Monte Carlo draws $\Omega(p) \in \mathbb{R}^{N_{\text{lds}} \times N_{\text{MC}}}$ are drawn from a distribution with a set of parameters p. The voltages magnitudes are calculated and the voltage difference $\tilde{V}_{\text{MC}}$ is calculated according to

$$\tilde{V}_{\text{MC}} = \text{diag}(V_+ - b)^{-1} K_{\text{bus}} \Omega(p) \ \leq \ \mathbb{1}_V^N \,, \tag{4.50}$$

i.e. a Level 3 matrix operation. The sign of the minimum value of each column of $\tilde{V}_{\text{MC}}$ indicates if there is a violation. That is, the hosting capacity function f_{Pwr} evaluated at p is given by

$$f_{\text{Pwr}}(p) = \frac{\sum \mathbf{1}_{\leq 1}(\lfloor \tilde{V}_{\text{MC}} \rfloor)}{N_{\text{MC}}} \,, \tag{4.51}$$

where $\lfloor \cdot \rfloor$ finds the column-wise minimum value and $\mathbf{1}_X$ is the indicator function of condition X.

If the parameter of interest is simply a linear scaling, so that $\Omega(p) = \Omega_0 p$, then this can be solved directly and the set of smallest linear scalings $\hat{p}$ found that will result in a constraint violation as

$$\hat{p} = \text{diag}(\lceil \text{diag}(V_+ - b)^{-1} K_{\text{bus}} \Omega_0 \rceil)^{-1} \mathbb{1}^{N_{\text{MC}}} , \tag{4.52}$$

where $\lceil \cdot \rceil$ takes the column-wise maximum of a matrix. The stochastic hosting capacity quantile is therefore calculated as

$$p^{\phi} = \text{Quantile}^{\phi}(\hat{p}) . \tag{4.53}$$

The advantages of a linear method for solving in this way is illustrated graphically in Figure 4.17. If the PDF is found using a 'fixed power' characteristic (Figure 4.17, left) then a number of iterations are required to find the power that satisfies (4.53); whereas, the proposed 'fixed voltage' method (Figure 4.17, right) only requires a single set of calculations.

Beyond the primary aim of finding an individual hosting capacity quantile, the linear method has the benefit of providing an estimate of the PDF of all powers. This gives valuable information as to the potential benefits of locating generators in optimal locations. A wide spread indicates that some locations are much more suitable for generation than others. For example, if there is one weak bus at the end of a feeder then scenarios that include generation at this bus will not be able to host a significant amount of generation.

4.5.1.1 Bisection Algorithm

To demonstrate the advantages of a problem involving a scaling parameter, the method is compared to the Bisection method for finding the roots of non-linear equations. This algorithm can be briefly summarised as follows. Two initial guesses for

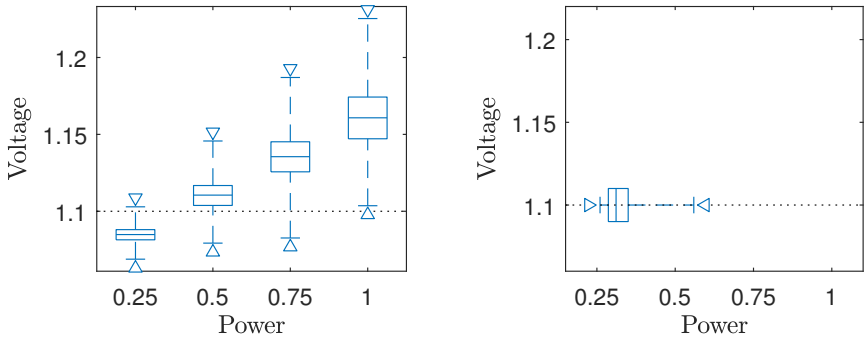

Figure 4.17: The fixed-power hosting capacity method (l), and the fixed-voltage hosting capcity method (r). Enforcing the constraint in the fixed-voltage method reduces the number of scenarios required for the same accuracy.

the penetration are chosen ($p_{[1]}$, $p_{[0]}$), then $\hat{\phi}_{[1]}$ and $\hat{\phi}_{[0]}$ are calculated according to (4.51). If the error function E for two function evaluations ($\hat{\phi}_{[j]}$, $\hat{\phi}_{[j-1]}$) is greater than some tolerance ζ_{Tol}, then a new value $p_{[j+1]}$ is chosen, according to the sign of $(\hat{\phi}_{[j]} - \phi) - (\hat{\phi}_{[j-1]} - \phi)$. The process is repeated until convergence is achieved, i.e. until

$$E(\hat{\phi}_{[j]}, \hat{\phi}_{[j-1]}) \leq \zeta_{\text{Tol}}\,. \tag{4.54}$$

The algorithm has the advantage that, if ($p_{[1]}$, $p_{[0]}$) have opposite signs (i.e. one is positive and one is negative), then the algorithm is guaranteed to converge to a zero. The following error metric function is used:

$$E(\hat{\phi}_{[j]}, \hat{\phi}_{[j-1]}) = \frac{|(\hat{\phi}_{[j]} - \phi) - (\hat{\phi}_{[j-1]} - \phi)|}{1 + |\hat{\phi}_{[j-1]} - \phi|}\,, \tag{4.55}$$

This is a 'combination' of relative and absolute error. For a more detailed description of the algorithm see, e.g., [165, Ch. 4].

4.6 Hosting Capacity Quantiles: Case Studies

To study the additional benefits of using a linear model for problems involving a scale parameter, a subset of three networks from the previous section are chosen. In addition, four small-scale LV feeders from [154] are also studied. These represent

smaller geographic areas, and so it is more likely that the uniform generator selection assumptions might hold.

For the cases of the previous section the linearization around 20% load was considered, whilst the LV feeders were assigned loads of 0.3 kW at 0.95 PF lagging. Voltage limits for the larger networks remained at their nominal values as in the last case studies; voltages for the LV networks follow the UK standard of ±10% at 230 V [173]. Variance and correlation cutoffs of 99% were used to reduce model sizes for the large networks.

4.6.1 Problem Size and Method Effectiveness

The number of runs required for the Monte-Carlo method N_{MC} to achieve good accuracy was determined considering a hosting capacity $P_{\mathrm{gen}}^{5\%}$. The calculated hosting capacity for two Monte Carlo runs is given in Table 4.3. Using $N_{\mathrm{MC}} = 1000$ gives an accuracy better than 3% in the networks studied. This is larger than the number required for the stochastic hosting capacity curve calculations, as the primary point of interest is no longer around the bulk of the probability mass, but instead focussed at the 5% point.

Table 4.3: Estimated hosting capacity and error for two monte carlo runs ($N_{\mathrm{MC}} = 1000$, $\alpha_{\mathrm{PV}} = 50\%$)

Feeder	$P_{\mathrm{gen}}^{5\%}$ (i), kW	$P_{\mathrm{gen}}^{5\%}$ (ii), kW	Rel. error, %
8500 Node	1.59	1.58	0.12
Ckt. 24	4.93	4.89	0.81
Ckt. K1	16.48	16.51	0.22
EU LV	0.45	0.45	1.43
N1.F1	3.30	3.21	2.68
N2.F1	2.61	2.61	0.15
N3.F1	2.46	2.48	0.71
N4.F1	10.05	10.22	1.70

A comparison of the computational time required for the analytic ('Linear Direct') and iterative ('Bisection') methods are given in Table 4.4. For the Bisection method

a tolerance $\zeta_{\text{Tol}} = 1\%$ in (4.54) is used, initialised with $p_{[0]} = 0$, and $p_{[1]}$ as the unique hosting capacity at $\alpha_{\text{PV}} = 100\%$.

In the cases considered, between 11 and 16 iterations lead to convergence, leading to a time improvement of at least seven times. The 'usability' of the method is much improved. For example, problems which were likely to cause a disruption in workflow (taking longer than 10 seconds to solve) can now naturally be incorporated (as discussed in Section 1.3.2). Given the computational speed, it is concluded that the benefits of linear models for studying problems with a scale parameter is even greater than for linear models in isolation.

Table 4.4: Comparison of timings and estimated hosting capacities for the fixed power and fixed voltage methods

Feeder	Linear Iterative (Bisection)			Linear Direct		Time ratio
	Time, s	$P_{\text{gen}}^{5\%}$, kW	Iterations	Time, s	$P_{\text{gen}}^{5\%}$, kW	
8500 Node	47.32	1.586	11	3.84	1.585	12.3
Ckt. 24	105.02	4.931	12	7.96	4.930	13.2
Ckt. K1	0.98	16.481	12	0.08	16.478	12.5
EU LV	0.14	0.453	16	0.02	0.452	7.9
N1.F1	0.97	3.301	13	0.09	3.300	11.0
N2.F1	8.06	2.616	11	0.66	2.615	12.2
N3.F1	1.82	2.458	11	0.20	2.458	9.3
N4.F1	0.25	10.049	12	0.03	10.046	7.6

4.6.2 Stochastic Hosting Capacity Variation with Penetration

In the decision making process, it is likely that the penetration level will be uncertain. If this is the case, then this method gives an efficient way of calculating stochastic hosting capacity quantiles over a range of penetrations. The PDF of the total generation and power per generator is shown in Figures 4.18 - 4.20. The 5% quantile is plotted explicitly alongside the calculated range, quartiles and median values at each penetration level.

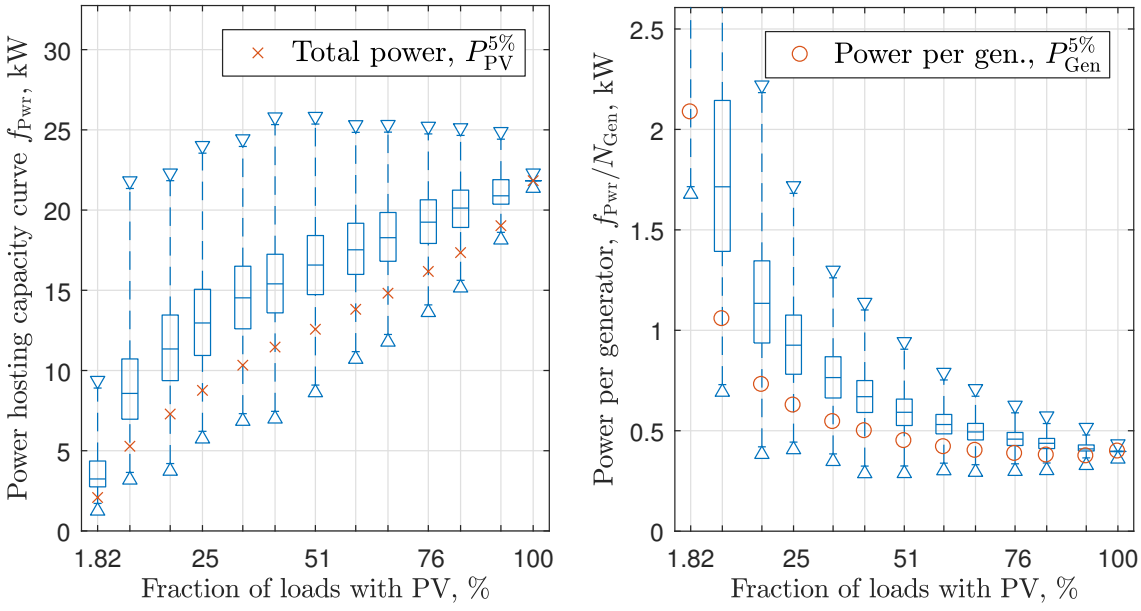

(a) EU LV, total gen.

(b) EU LV, power per gen.

Figure 4.18: Boxplot of the total generation P_{PV} (a) and power per generator P_{gen} (b) as a function of the penetration for the EU LV feeder.

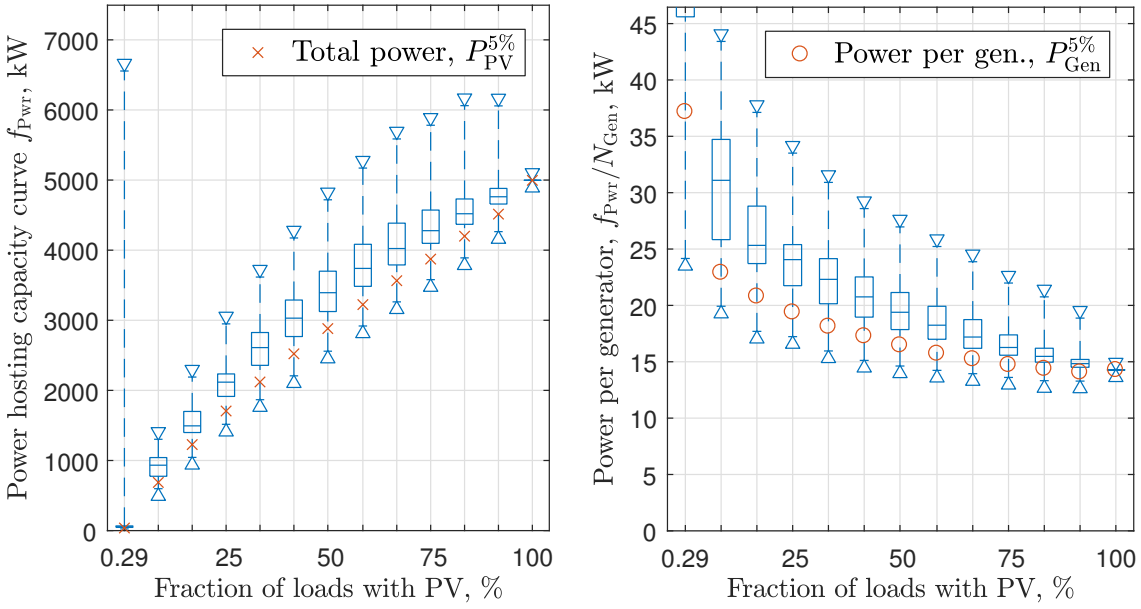

(a) EPRI K1, total gen.

(b) EPRI K1, power per gen.

Figure 4.19: Boxplot of the total generation P_{PV} (a) and power per generator P_{gen} (b) as a function of the penetration for the EPRI K1 circuit.

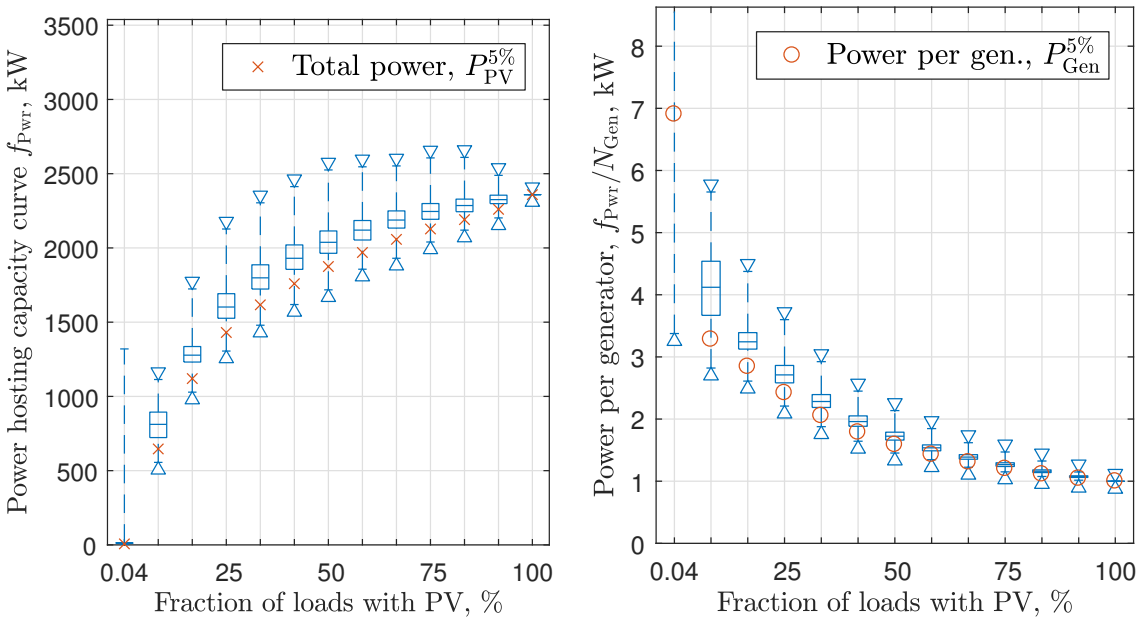

(a) 8500 Node circuit, total gen.

(b) 8500 Node circuit, power per gen.

Figure 4.20: Boxplot of the total generation P_{PV} (a) and power per generator P_{gen} (b) as a function of the penetration for the IEEE 8500 Node circuit.

It is clear that the hosting capacity is strongly affected by the fraction of loads connected. It is interesting to see that the 5% hosting capacity quantile follows a different shape depending on the feeder. For example, in the EPRI K1 feeder, the power per generator changes by 20% as the penetration increases from 50% to 100% (Figure 4.19b), where it changes by 50% in the 8500 Node network (Figure 4.20).

In all cases, the total generator power drops rapidly for small penetrations (below 25%), whilst the total power per generator increases rapidly. On the other hand, in some cases at high penetrations (above 80%), increasing the penetration increases the power per generator. This is presumed to be due to a more balanced network in the 100% penetration case.

In all feeders, the 100% penetration case leads to a smaller hosting capacity compared to the maximum hosting capacity. It is also interesting to note that the maximum hosting capacity points that have been found vary significantly. For example, in the EU LV network, cases at 42% reach the maximum recorded hosting capacity (Figure 4.18a), with the range at this penetration from 7 to 25 kW. In the EPRI K1

circuit, however, there is a maximum reached with just a single generator (Figure 4.19a). This appears to be because there are some loads which are located very close to the substation (see Figure 2.3). Given there is a load tap changer in the substation, the voltage sensitivity at these locations is very small. As such, unless all loads that are drawn in a scenario are all very close to the head of the feeder, a small number of generators will have a smaller hosting capacity that those single 'outlier' generator cases at the head of the feeder.

4.6.2.1 DG Policy Decisions Under Uncertainty

In this section two decision making scenarios are described, to demonstrate the benefits of stochastic hosting capacity calculations, when compared to deterministic or conservative calculations. These scenarios are given as follows:

C1. The DSO is mandated to determine the generator size such that 75% of customers can connect, and that fewer than one in 20 feeders will need to be upgraded.

C2. A DSO is incentivised to allow the connection of as much PV as possible to a network. Between 15% and 40% of generators will connect, with uniform probability. The utility wishes to find the generator sizing such that there is a 5% chance of having to upgrade the network.

The first decision making scenario (C1) is a straightforward application of the method presented. The societal benefit is that there will be an increase in the PV power that can be connected, increasing the utilisation of the network assets, whilst providing a 'fair' system whereby all customers on the network will have the opportunity to connect until the quota is filled.

The benefits for this case study vary (Table 4.5). In the EU LV network, using the value obtained for 100% hosting capacity leads to an overestimate of the amount of PV that can be connected, resulting in a 10% chance of overvoltages. On the other hand, allowing for 5% rather than 1% of generators to connect increases the average

Table 4.5: DG Policy Decisions, based on stochastic hosting capacity results. All powers are in kW per generator.

Feeder	$P_{\text{gen}\,100\%}$, kW (per gen.)	C1, $\alpha_{\text{PV}} = 75\%$			C2, $\alpha_{\text{PV}} \in (15\%, 40\%)$	
		$P^{1\%}_{\text{gen}}$	$P^{5\%}_{\text{gen}}$	$P^{10\%}_{\text{gen}}$	$P^{5\%}_{\text{gen}}$	$P^{1\%}_{\text{gen},\,\alpha_{\text{PV}}=40\%}$
EU LV	0.40	0.36	0.39	0.40	0.55	0.44
Ckt. K1	14.27	14.26	14.72	15.00	18.20	16.39
8500 Node	1.00	1.18	1.20	1.21	1.87	1.72

amount of connected power by 8%. In the other networks, there is an increase in the power that can be connected, by as much as 20% for the 8500 Node network.

The second decision making scenario (C2) is more complex. Here the PDF is approximated by sampling across a range of penetrations. A uniform sample is taken between 15% and 40%, then all solutions are combined into one large sample. From this, the 5% quantile can be taken across all samples. In this case, there is at least a 27% increase compared to the 100% penetration generator power, with an increase of 87% in the 8500 Node network. These values also compare favourably compared to, for example, a 'conservative' calculation at the highest penetration level with a 1% probability, with an increase of at least 8% in all networks.

4.7 Summary

Hosting capacity of domestic PV will always have a stochastic element to it, and finding computationally efficient methods of calculating PV hosting capacity is paramount given the large number of distribution feeders that exist. To this end, in this chapter the following question was studied:

How can the stochastic hosting capacity of a distribution network be calculated in a computationally efficient manner, considering voltage regulators and reactive power control from distributed generators?

The models developed in this chapter account for two standard regulator operation control types (including line drop compensation), as well as centralised DERMS-

style tap and reactive power control. It has been demonstrated that voltage means and variances can be calculated efficiently, and that this information is suitable for increasing the efficiency of Monte Carlo calculations.

The proposed hosting capacity analysis with DERMS-style control considers if there is any feasible load flow solution, and it is used to show that hosting capacity problems can (in some cases) be cleared completely. Without the implementation of regulators, some solutions are shown to be infeasible and therefore have no hosting capacity.

The linear model considering traditional regulator controls has the advantages of excellent computational efficiency, with reductions in computation times of up to three orders of magnitude. Additionally, sensitivity analysis can be calculated efficiently using the linear method, which would be impractical using traditional non-linear simulations. This calculation of sensitivity is particularly pertinent as it has been shown to provide useful information about the quality of the solution, when compared to the non-linear load flow solution.

In the case of individual hosting capacity quantiles, problems characterised by a scale parameter have been identified as being particularly suitable for calculations with linear models, as they avoid the requirement for iterative calculations. In the cases considered, this reduced the computation time by up to 14 times. This improves the usability significantly, make it much simpler for a user to tweak parameters and then see how the solution has changed.

Finally, given recent policy shifts towards larger-scale PV, in future it may be that relatively fewer PV systems connect, but the PV systems that connect are larger. It has been demonstrated that the hosting capacity varies significantly with the total number of PV generators that are connected. Depending on the expected uptake of PV, the methods present will help with decision making, by evaluating the hosting capacity in a fair, transparent way.

Chapter 5

Inverter Reactive Power Control for Minimization of Total Feeder Power

The final question studied in this thesis is:

How can the benefits of domestic-scale inverter reactive power control be evaluated with respect to minimising total power demand on a feeder, with load voltage sensitivity, inverter losses and distribution network losses taken into account?

It was shown in the previous chapter that changing the substation voltage can lead to a complete clearing of voltage problems; or, that simple constant power factor control schemes can be enabled to a similar effect. In these cases, the question arises as to what the optimal reactive power and tap positions are. In this chapter, the benefits of reactive power control are assumed to be in terms of reduced load (due to voltage-sensitive loads) and losses. This question is also applicable to circuits for which tap or reactive power control is not required for curtailment avoidance in the first instance.

The two-bus model is first revisited to study and understand the optimal behaviour of a simple circuit qualitatively. The true minimization of total feeder power

is compared against solutions from load and loss minimization objectives. It is demonstrated that, in contrast to load and loss minimization, for moderate values of load sensitivity to voltage it is not immediately clear how taps and reactive power devices should be operated.

A novel, detailed network model is then considered to model the power flows in the network, in terms of losses due to the network, inverter losses, and changes in load with voltage. These models are based on an alternative linear model in voltages to that described in the previous chapter, and has an increased expressivity compared to the models from the literature on which it is based, as it models exponential as well as constant power load models. The model is validated using OpenDSS, and takes the form of a mixed-integer quadratically constrained quadratic program (MI-QCQP).

Having developed the model, the remainder of the chapter is focussed on studying the properties of the MI-QCQP model in detail. Specifically, both the cost function and controls are studied in a number of contexts and on a range of case studies. The optimization is considered in two contexts: first, the closed-form solution of the unconstrained solution of the quadratic program (QP) is considered, after which the constrained solution to the full MI-QCQP is then found. Optimal reactive power control is shown to be qualitatively different in circuits with regulators and those without.

Two final case studies are considered as time series analyses on two representative days: one high-solar day and one high-load day. Both the fraction of load that is reduced is considered, and the control effort at the optimal point is also studied, after which the relative benefits of reactive power control are considered from an economic point of view.

Chapter Roadmap The rest of this chapter is organised as follows. Section 5.1 describes the load model used in this chapter, and how taps or reactive power controls should be scheduled for either load or loss minimization, to demonstrate the tension between these objectives on a simple network. Section 5.2 develops the full

network and inverter model in detail. With this basis, the analytic properties of the resulting unconstrained QP are considered in Section 5.3, considering the impact of each of the components of load and losses on the relaxed solution. In Section 5.4 case studies on the proposed MI-QCQP demonstrate the key differences between regulated and non-regulated optimal solutions, including two time-series based case studies that demonstrate how the benefits of inverter reactive power control change in time. Conclusions are drawn in Section 5.5.

5.1 Minimizing Operating Costs using Inverters and Taps

In this chapter, the primary operating cost of a network is assumed to be a real power cost (i.e. from losses and running loads at a sub-optimal voltage). This is justified as the marginal cost of reactive power is typically small compared to the cost of real power injections [174]–in fact, network operators in the UK charge only charge customers when reactive power injections are greater than 33% of real power load [175, pp. 582-583].

The total feeder power P_{feeder} can decomposed into load P_{lds}, generation P_{gen}, network losses $P_{\text{lss,ntwk}}$, and inverter losses $P_{\text{lss,invr}}$, as

$$P_{\text{feeder}} = P_{\text{lds}} + P_{\text{lss,ntwk}} + P_{\text{lss,invr}} - P_{\text{gen}} \,. \tag{5.1}$$

Minimization of the total power into the feeder, assuming all generators are exporting with no curtailment, is therefore equivalent to minimizing losses (in the network and inverters) and load, by the control of domestic-scale smart inverters directly with taps connected to a feeder. No prior work consider the impact of domestic inverter control with all four of the terms in (5.1) was identified as part of the literature survey (Section 2.3).

5.1.1 Conservation Voltage Reduction Load Models

Reducing the voltage in networks tends to change the amount of load drawn by loads. A common model for this is the *exponential model* that models sensitivity to voltage as a power law [176, 177]. For the ith load, this can be written

$$P^i_{\text{lds}} = P^i_{\text{lds},\,0} \left(\frac{|V^i_{\text{lds}}|}{V^i_{\text{lds},\,0}} \right)^{\alpha_{\text{CVR}}}, \tag{5.2}$$

where P^i_{lds} is the load power, $P^i_{\text{lds},\,0}$ is the load power 'demand', $V^i_{\text{lds},\,0}$ is a nominal voltage, $|V^i_{\text{lds}}|$ is the voltage at the load and α_{CVR} is the CVR coefficient.

Therefore, by reducing the voltage at a load the demand can be optimized to ensure maximum efficiency. It is assumed that the maximum efficiency is found when a device draws the lowest power.

It is well known that the CVR coefficient α_{CVR} varies significantly, depending on the type of load and the duration of voltage suppression [176]. In this work, the long-term value of α_{CVR} is the primary quantity of interest. Estimates for this parameter range from 0.06 to 1.30 [116], depending on the load composition, season, and time. For example, field trials as part of the Customer-Load Active System Services (CLASS) project in the UK demonstrated that the value of α_{CVR} can double, depending on the time of day, when considering a 10-minute voltage reduction window. Alternatively, EPRI studied nine circuits over a period of 11 to 24 months to determine the long-term voltage-load sensitivity factor (increasing and decreasing voltages on a daily basis). They similarly demonstrated significant changes in this value, with the energy decrease typically ranging from 2 to 4%, although the wide variation in values observed highlights the necessity of a detailed understanding of the underlying cause of the reduction in demand [26]. Other field trials and case studies are summarised in [116] and [56, Ch. 6.7].

For this chapter a value of α_{CVR} between 0 and 0.9 is used in simulations, with a central estimate of 0.6. This follows the best estimate for residential loads identified in [56, Ch. 6] as 0.63, and is slightly lower than value used in similar recent work

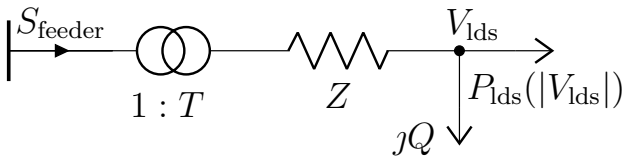

Figure 5.1: The two-bus model, assuming controls in the reactive power Q and regulator turns ratio T (the turns ratio is modifiable by a tap changer). The load P_{lds} is a function of the voltage magnitude at that point V_{lds}.

[133].

5.1.2 Conservation Voltage Reduction: A Two-Bus Example

In Chapter 3, the two-bus model was used to explore reactive and tap control for the minimization of losses, under an assumption of a constant power load (i.e., it was assumed that $\alpha_{\text{CVR}} = 0$). In this section, this model is briefly revisited to consider how tap and reactive control varies as a function of the CVR sensitivity factor α_{CVR}. Figure 5.1 illustrates the setup of the model in terms of the reactive power control Q and the turns ratio T (as impacted by the tap).

When the CVR sensitivity factor is an integer between 0 and 2, loads are referred to as one of the 'ZIP'-type loads. That is, either a load is an impedance 'Z' ($\alpha_{\text{CVR}} = 2$), a constant current load 'I' ($\alpha_{\text{CVR}} = 1$), or a constant power load 'P' ($\alpha_{\text{CVR}} = 0$). In the two-bus model, the qualitative optimal behaviour with respect to either load, loss, or total feeder power draw can be considered exactly for these integer values. That is, the 'direction' of the sensitivity of the real power at zero (for reactive power) or unity (for turns ratios) are identified as positive or negative.

The directions (i.e., sign) of the sensitivity, with respect to turns ratio and reactive power, are given in Table 5.1. For example, if losses are to be minimized with reactive power, then (as described in Chapter 3), for a constant power load, a small amount of reactive power should be injected. For constant current load, no reactive power should be injected as this will always increase the magnitude of the current through the impedance. For a constant impedance load, a small amount of reactive power

Table 5.1: Qualitative operating zones for loss, load, and total feeder power minimization objectives. Key: $\uparrow$ ($\downarrow$) – increase (decrease) the control variable; 0 – set to zero; $\times$ – no effect; $\uparrow/\downarrow$ – positive or negative, depending on α_{CVR}. Double arrows (e.g. $\Downarrow$) indicate a strong effect, such that voltage constraints would likely be active at a solution.

Minimization objective	$\alpha_{\text{CVR}} = 2$ ['Z']		$\alpha_{\text{CVR}} = 1$ ['I']		$\alpha_{\text{CVR}} = 0$ ['P']		$0 < \alpha_{\text{CVR}} < 1$	
	Q	T	Q	T	Q	T	Q	T
Losses	$\downarrow$	$\Downarrow$	0	$\times$	$\uparrow$	$\Uparrow$	$\uparrow$	$\Uparrow$
Load	$\Downarrow$	$\Downarrow$	$\Downarrow$	$\Downarrow$	$\times$	$\times$	$\downarrow$	$\Downarrow$
Feeder pwr.	$\downarrow$	$\Downarrow$	$\downarrow$	$\Downarrow$	$\uparrow$	$\Uparrow$	$\uparrow/\downarrow$	$\uparrow/\downarrow$

can be sunk to reduce the magnitude of the current flowing through the line. For the minimization of losses in taps T, then the voltage should be reduced as much as possible for a constant impedance load; the tap makes no difference to losses in a constant current load; and the tap should be increased as much as possible for a constant power load. Similar arguments apply for taps and reactive power for load reduction.

On the other hand, it is interesting to note that for intermediate values of voltage sensitivity α_{CVR} (between 0 and 1) the optimal operation in terms of total feeder power reduction varies with the exact value of α_{CVR}. This implies that the optimal tap and reactive power position will vary depending on the network, power draw, and the load voltage sensitivity. This is in contrast to load or loss reduction, which always act to reduce or increase the voltage respectively for α_{CVR} in this intermediate region. It is concluded that the two-bus circuit suggests that the optimal amount and direction of reactive power control could vary between networks, and that the load and loss sensitivities are likely to work in opposite directions.

5.1.3 Case Studies

Given the conclusions drawn from the two-bus problem, it is clear that a range of networks will need to be analysed to study the solution space of this problem. In particular, the presence of voltage regulators will likely have a significant impact on

the solution and action of reactive power support, and so a set of networks both with and without regulators must be chosen.

In this chapter, seven networks are studied with a range of R/X ratios and voltage levels. For networks without regulators, EPRI Circuit 5 and Circuit 7 are used to represent US-style networks, whilst Network 1 and Network 10 are utilised from the ENWL dataset to represent EU-style circuits. The former (Network 1) will from hereon be referred to as the augmented EU LV circuit (the 'EULVa' network), as it contains the EU LV network (see Figure 5.2). Network 10 shows a particularly low power, with just 64 houses connected to the substation, but otherwise is similar to the EULVa network.

For networks with regulators, the EPRI K1 feeder and 123 Bus network are used to represent US-style networks, whilst the EU-style network is represented by a 'regulated' EULVa network, or 'EULVa-r' network. The latter is assumed to have an on-load tap changer fitted at the substation to control all feeders (following installations in similar networks [178]). Between them these networks represent a range of R/X and power levels, as well as a range of tap changers (for example, the 123 Bus circuit has 7 separate voltage regulator controls on the feeder).

5.1.3.1 PV and Inverter Sizing

For residential PV (of installation size less than 20 kW), the median PV size for both the UK and California is 4 kW [1,14]. Alternatively, it is possible to generate reactive power from single phase electric vehicle chargers [179, 180]. A sample of 4000 single phase EV chargers in the UK shows that this is also a common size, with 48% of chargers between 3 and 4 kW [181]. For the purposes of this chapter, case studies therefore consider a fixed inverter size of 4 kVA with a corresponding PV size of 3.8 kW (inverters in some jurisdictions are required to be oversized to allow for volt-var control [16]).

Figure 5.2: The Augmented EU LV (EULVa) network has 4 feeders connected to the same secondary substation; the EU LV network is to the Southeast of the substation.

5.2 Modelling a Network with Smart Inverters and Voltage-Sensitive Loads

In this section, the optimization of total losses and demand in terms of reactive power and taps is proposed, making use of a linear load flow model and a linear model of loads in voltages. The utilisation of a linear load flow model renders the calculation of losses and voltages as a convex function of reactive powers [115]; a linear load model therefore loads to a convex optimization in reactive powers. The use of linearization avoids the use of heuristic optimization strategies.

5.2.1 Load Flow Considering Voltage Sensitive Loads

For the rest of the chapter, bus injections in reactive power from inverters Q_{invr} and taps are concatenated into the control vector x as

$$x = \begin{bmatrix} Q_{\text{invr}} \\ T \end{bmatrix} \tag{5.3}$$

This vector is made by partitioning the power injection vector S_{bus} as appropriate.

The linear load flow model can be summarised as

$$V = M_x x + a_x \,, \tag{5.4}$$

$$|V| = K_x x + b_x \tag{5.5}$$

where M_x, a_x are the linear sensitivity matrix and offset for complex voltages and K_x, b_x are the sensitivity matrix and offset for voltage magnitudes. As in the previous chapter, K_x is determined from M_x using the linearization (4.15). The calculations of voltage sensitivities to taps follows the same perturb-and-observe approach as previously considered, but with the exponential load model utilised in OpenDSS.

With respect to reactive power sensitivities, there are two key differences between the linear model M_s considered in the previous chapter and the model M_x considered here. Firstly, the injections in reactive power are assumed to be relatively small, and so the 'global' error is not as important. Additionally, accuracy of the linear sensitivities is more important in optimization than in the function evaluation, as the gradient of the linearization is used to determine the optimal point. Taylor-series based expansions find the local gradient exactly; therefore this is used instead of the fixed-point linearization method.

This Taylor-series representation is now derived following [139]. From (2.6) and (4.13), the wye- and delta-connected loads can be found as

$$S_{\curlyvee,\,\mathrm{L}} = \operatorname{diag}(V_{\mathrm{L}})\left(Y^*_{\mathrm{L0}} V^*_0 + Y^*_{\mathrm{LL}} V^*_0 - H_\Delta I^*_\Delta\right) \tag{5.6a}$$

$$S_{\Delta,\,\mathrm{L}} = \operatorname{diag}(H_{\Delta,\,\mathrm{L}} V_{\mathrm{L}}) I^*_{\Delta,\,\mathrm{L}} \,, \tag{5.6b}$$

where the notation $(\cdot)_{\mathrm{L}}$ follows the previous convention in (4.13), referring to all nodes except for those at the source. Taking partial derivatives of (5.6) with respect

to voltages and delta currents yields

$$\operatorname{diag}(H_{\Delta,\mathrm{L}}V)\frac{\partial I^*_{\Delta,\mathrm{L}}}{\partial S_{\Delta,\mathrm{L}}} + \operatorname{diag}(I^*_{\Delta,\mathrm{L}})H_{\Delta,\mathrm{L}}\frac{\partial V}{\partial S_{\Delta,\mathrm{L}}} = I_{1+\jmath} \tag{5.7a}$$

$$\begin{aligned}\operatorname{diag}(H^\intercal_{\Delta,\mathrm{L}}I^*_{\Delta,\mathrm{L}} - Y^*_{\mathrm{L0}}V^*_0 - Y^*_{\mathrm{LL}}V^*)\frac{\partial V}{\partial S_{\Delta,\mathrm{L}}} \\ +\operatorname{diag}(V)\left(H^\intercal_{\Delta,\mathrm{L}}\frac{\partial I^*_{\Delta,\mathrm{L}}}{\partial S_{\Delta,\mathrm{L}}} - Y^*_{\mathrm{LL}}\frac{\partial V^*}{\partial S_{\Delta,\mathrm{L}}}\right) = 0\end{aligned} \tag{5.7b}$$

$$\operatorname{diag}(H_{\Delta,\mathrm{L}}V)\frac{\partial I^*_{\Delta,\mathrm{L}}}{\partial S_{\curlyvee,\mathrm{L}}} + \operatorname{diag}(I^*_{\Delta,\mathrm{L}})H_{\Delta,\mathrm{L}}\frac{\partial V}{\partial S_{\curlyvee,\mathrm{L}}} = 0 \tag{5.7c}$$

$$\begin{aligned}\operatorname{diag}(H^\intercal_{\Delta,\mathrm{L}}I^*_{\Delta,\mathrm{L}} - Y^*_{\mathrm{L0}}V^*_0 - Y^*_{\mathrm{LL}}V^*)\frac{\partial V}{\partial S_{\curlyvee,\mathrm{L}}} \\ +\operatorname{diag}(V)\left(H^\intercal_{\Delta,\mathrm{L}}\frac{\partial I^*_{\Delta,\mathrm{L}}}{\partial S_{\curlyvee,\mathrm{L}}} - Y^*_{\mathrm{LL}}\frac{\partial V^*}{\partial S_{\curlyvee,\mathrm{L}}}\right) + I_{1+\jmath} = 0\,,\end{aligned} \tag{5.7d}$$

where $I_{1+\jmath} = [I,\, \jmath I]$ (for identity matrices of the correct dimension). To find the Taylor-series expansion, one solves the set of linear equations (5.7) for the voltage partial derivatives $\dfrac{\partial V}{\partial S_{\Delta,\mathrm{L}}}$, $\dfrac{\partial V}{\partial S_{\curlyvee,\mathrm{L}}}$. By collecting the wye- and delta-connected loads into the vector S_{bus}, and choosing a_s as the linearization point, the model is then of the same form as in the last chapter,

$$V = M_s S_{\mathrm{bus}} + a_s\,, \tag{5.8}$$

but with the values of M_S, a_S calculated using the Taylor-series method.

The second key difference between the model of the previous chapter and this model is that the real power of the loads is assumed to vary with the voltage magnitude at the node, as given by the exponential model (5.2). It is assumed that the bus injections S_{bus} can (approximately) be found as a linear function of the control vector x,

$$S_{\mathrm{bus}} = M_\alpha x + S_\alpha\,, \tag{5.9}$$

where M_α is the sensitivity of loads to the control vector x and S_α is the load injections at the linearization point. The total real power load of the feeder $P_{\mathrm{lds,\,tot}}$ is then

calculated by summing real parts of the rows of (5.9), denoted by

$$P_{\text{lds, tot}} = \phi_{\text{lds}} x + \rho_{\text{lds}} \,, \tag{5.10}$$

where ϕ_{lds}, ρ_{lds} are the gradient and offset vectors respectively.

Combining the models of bus injections in the control vector (5.9) and the model (5.8) leads to the linearization

$$M_x = M_s M_\alpha \,, \qquad a_x = M_s S_\alpha + a_s \,, \tag{5.11}$$

which is of the form of (5.4). Therefore, the exact model (5.9) of the loads in terms of reactive power injections is determined next so that the full model can be determined.

5.2.2 Linear Load Model

The exponential model (5.2) is non-linear in voltage magnitudes, and therefore the first step for determining the linearization (5.9) is to linearize this model around a solution point. Considering a small changes in injections, it is found that

$$P^i_{\text{lds}} = P^i_{\text{lds, 0}} \left(\frac{|\breve{V}^i_{\text{lds}}| + |\delta V^i_{\text{lds}}|}{V^i_{\text{lds, 0}}} \right)^{\alpha_{\text{CVR}}} \tag{5.12a}$$

$$\approx P^i_{\text{lds, 0}} \left(\alpha_{\text{CVR}} \frac{|\delta V^i_{\text{lds}}|}{V^i_{\text{lds, 0}}} + \left(\frac{|\breve{V}^i_{\text{lds}}|}{V^i_{\text{lds, 0}}} \right)^{\alpha_{\text{CVR}}} \right) \,, \tag{5.12b}$$

where δV^i_{lds} is the voltage deviation around the linearization point $\breve{V}^i_{\text{lds}}$ across the ith load.

Secondly, the change in voltage magnitude δV^i_{lds} must be found as a linear function of the control vector. To do so, the linear load model (5.4) is first obtained, assuming constant power loads. For wye-connected loads, the voltage magnitude is found using (4.15).

The voltage magnitude for delta-connected loads is obtained in a similar fashion: the voltage across the load is found as the difference between the appropriate rows

of (5.4), and the magnitude linearization obtained from that point. As the phase angle does not vary too much with changes in power injections, this remains a good approximation. Using this approach, (5.12b) yields a linear model in both wye and delta connected loads which is of high quality (see Figure 5.3).

5.2.2.1 Summary of Modified Taylor-Series Method

To summarise: finding the linear model in control variables (5.4) involves the following steps.

- The set of equations (5.7) are solved to find M_s, a_s for the intermediate load flow model (5.8), assuming constant power injections.
- The load model in reactive power, (5.9), is determined using the intermediate load flow model (5.8).
- The load flow model (5.4) in control vector x is then found using the update (5.11) (with the exception of the columns of M_x representing sensitivity to taps, which are instead found using the perturb-and-observe based approach, as described in Section 2.4.2).

The approximations for the Taylor-series based approximation obtained using this method are of high quality, as evidenced by the graphs of the errors seen in Fig. 5.4. The error profile is very different from that of the fixed-point linearization method (as in, e.g., Figure A.2), as the method finds the tangent plane rather than fitting a hyperplane through two points. Furthermore, it is interesting to note that increasing the CVR factor from zero to 0.6 has the effect of reducing the error. This is presumed to be because the model is getting closer to being a constant impedance load (when $\alpha_{\text{CVR}} = 2$), for which the load flow solution is linear.

5.2.3 Linear Model of Branch Currents

With the linear model of complex voltages in the control vector determined in (5.4), the branch admittance matrix (2.4) can be used to find the branch currents of trans-

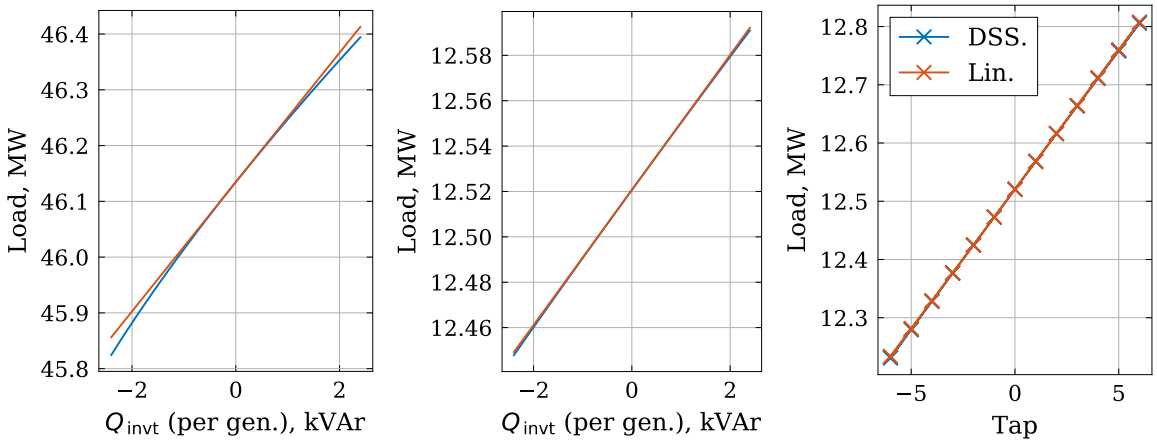

(a) EPRI Ckt. 7 (b) EPRI K1 (c) EPRI K1

Figure 5.3: The load variation in with reactive power injections, due to voltage sensitivity. The OpenDSS model ('DSS') uses the full exponential model as solved by the full non-linear load flow equations, whilst the linear model linearizes both the exponential load model and the voltage magnitudes assuming constant injections.

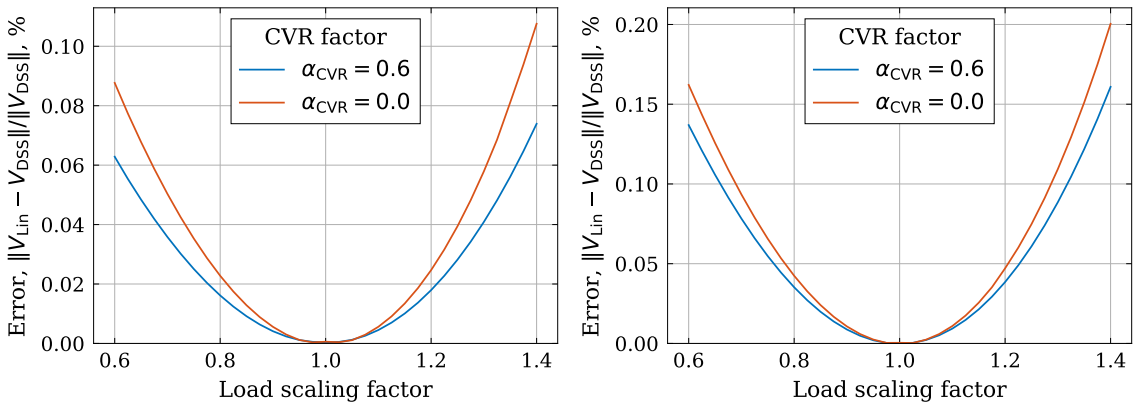

(a) 123 Bus Circuit (b) EPRI Ckt. 7

Figure 5.4: The Taylor-series based linear model leads to an excellent prediction of the voltage sensitivity around the linearization point, for both constant power loads and voltage sensitive loads.

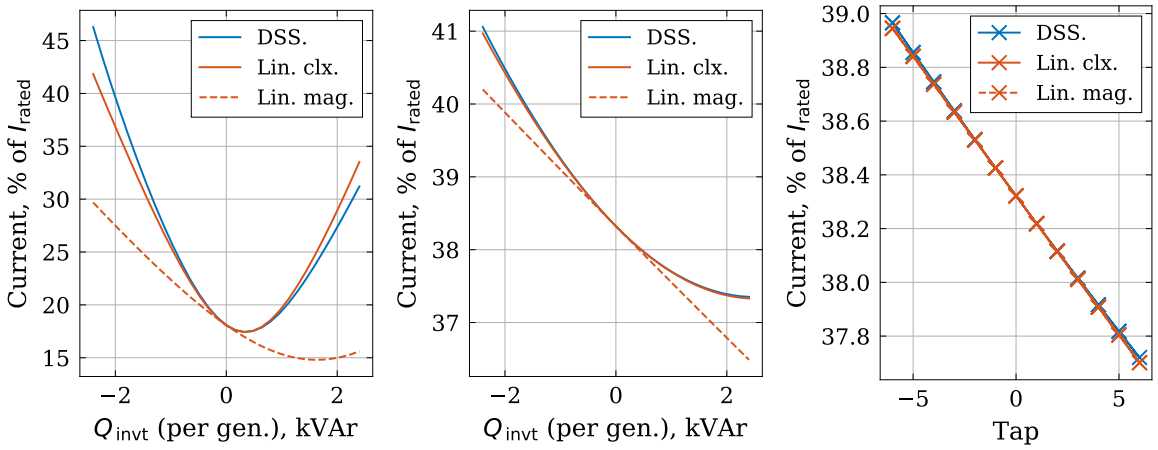

(a) EPRI Ckt. 7 (b) EPRI K1 (c) EPRI K1

Figure 5.5: A comparison between the current magnitudes as calculated in OpenDSS and for two linear models. The first linear model 'Lin. clx.' calculates the complex current as a linear function of the control vector, whilst the second 'Lin. mag.' calculates the linear current magnitude directly from the control vector, showing much worse performance. The complex model is much more accurate than the model in magnitudes for reactive power (a, b); either model was found to be acceptable for calculating the change in current with taps (c).

formers I_{xfmr} as

$$I_{\text{xfmr}} = W_x x + a_I \,, \tag{5.13}$$

where W_x, a_I are the branch current sensitivity matrix and offset vectors respectively.

It is interesting to note that it was found that the linear complex current model was much more accurate than a linear model of current magnitudes in reactive power injections (found by linearization of the complex current magnitude (5.13) using (4.15)). This is illustrated in Figure 5.5 - the linear model in current magnitudes is close to the true model only for very small current injections in both of the circuits considered here, in contrast to the linear model in complex current.

It is assumed that the linear model in current magnitudes is unreliable as the accuracy of the linearization (4.15) requires that the argument of the complex quantity does not change too much. This is true in the case of voltages, as demonstrated previously, but not true of currents (for example, if the power flow changes direction then the phase changes by 180°).

5.2.3.1 Determining Current Constraints

In this work the thermal (current) constraints considered are those of transformers in the circuit, as these often limit the amount of PV (and load) that can be connected at a domestic level. For a single phase transformer with a known power and voltage rating the current rating is immediately apparent: the transformer current rating is applied based on the ratio of the power and voltage rating of the transformer.

For a three-phase transformer a conservative equivalent limit is therefore considered. The transformer kVA rating is divided between the three phases, and then the current rating determined according to the per-phase value of the voltage.

It is worth noting that nominal transformer ratings are typically conservative as they assume worst-case conditions [56, Ch. 5]. That is, transformers can generally be loaded to a higher value than their rated power [182, 183]; 'thermal' power ratings are assumed to be 120% of their nominal values in all circuits. (In a small number of transformers this is further increased to ensure feasibility at 100% load; this is never more than 170% of the rated power.)

Finally, the European-style LV networks considered in this chapter (the EULVa, EULVa-r and Network 10) show very conservative kVA ratings (for example, the 64-house Network 10 network has an 800 kVA transformer). In these cases, a more restrictive current rating is considered at 2 kVA per household. This is approximately the rating at which new-build houses might be expected to be rated [184].

5.2.4 Real Power Loss Quadratic Model

Given the linear model of complex bus voltages and currents, the losses in any element can found by summing the real power injected into all the terminals of the device. Therefore, given the linear models in currents (5.13) and voltages (5.4), the total

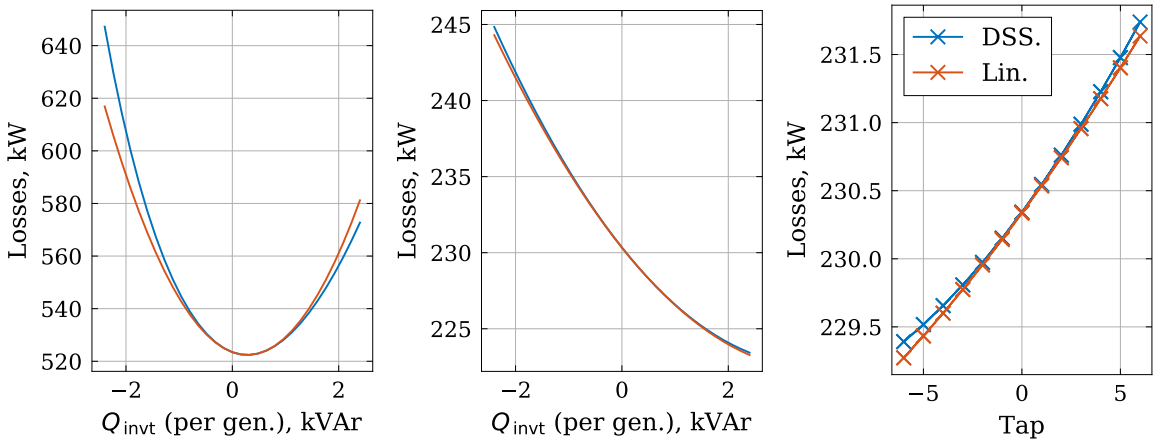

(a) EPRI Ckt. 7 (b) EPRI K1 (c) EPRI K1

Figure 5.6: The losses as calculated by OpenDSS and the quadratic loss model, demonstrating that the model predicts loss characteristics of the circuit well.

network losses $P_{\text{lss, ntwk}}$ are found to be given by a quadratic model as

$$P_{\text{lss, ntwk}} = \Re\left(V_{\text{branch}}^{\mathsf{T}} I_{\text{branch}}^{*}\right) \tag{5.14}$$

$$= x^{\mathsf{T}} \Theta_{\text{lss,ntwk}} x + \psi_{\text{lss,ntwk}}^{\mathsf{T}} x + \rho_{\text{lss,ntwk}} \tag{5.15}$$

where V_{branch}, I_{branch} are the voltages and currents across the branch elements of the network (the former is found by identifying the corresponding nodes for each branch). Given the voltages and currents show good error characteristics, the losses are also found to be approximated well by the model (5.15) (as plotted in Figure 5.6).

As losses are non-negative, the matrix $\Theta_{\text{lss,ntwk}}$ is positive semidefinite. The physical cause and consequences of the loss matrix being semidefinite (as opposed to positive definite) are discussed in the Appendix (Section A.3.1).

5.2.5 Inverter Model

The losses of an inverter depend on the magnitude of the apparent power that they generate. In this chapter a quadratic model is used for inverter losses $P_{\text{lss, invr}}$ in the

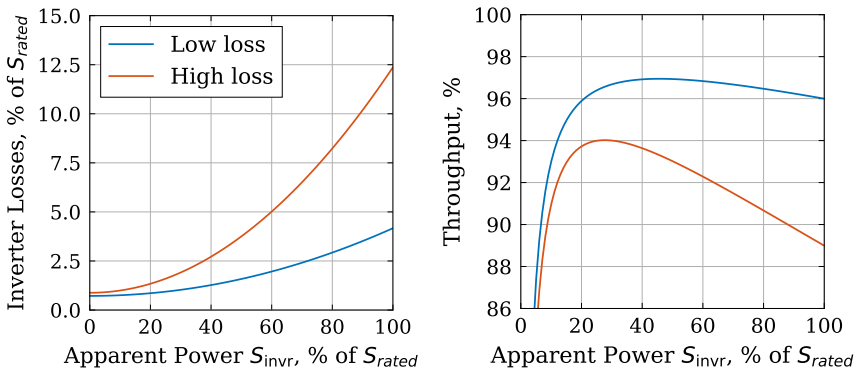

(a) Inverter losses (b) Inverter throughput

Figure 5.7: Inverter loss and throughput as a function of the power through the inverter.

inverter apparent power, S^i_{invr}, given by

$$P^i_{\text{lss, invr}} = c^i_{\text{Turn on}} + c^i_R |S^i_{\text{invr}}|^2 \,, \tag{5.16}$$

where $c^i_{\text{Turn on}}$, c^i_R model the turn on and ohmic loss coefficients respectively. Two cases are considered for this work, a 'low loss' and 'high loss' case (a 'Type 1' and 'Type 3' inverter as in [185]). Assuming a uniform inverter size, this cost is therefore given by

$$P_{\text{lss, invr}} = c_R \left(\|P_{\text{invr}}\|_2^2 + \|Q_{\text{invr}}\|_2^2 \right) + N_{\text{Lds}} c_{\text{Turn on}} \tag{5.17}$$

$$= x^\intercal \Theta_{\text{lss, invr}} x + \rho_{\text{lss, invr}} \,, \tag{5.18}$$

where $\Theta_{\text{lss, invr}}$, $\rho_{\text{lss, invr}}$ are the components of the inverter quadratic loss model in the control vector x. The losses for this type of inverter are plotted in Figure 5.7a and the corresponding throughput in Figure 5.7b. (Throughput here is defined by taking inverter apparent power less real losses, divided by inverter apparent power.)

It is interesting to note that the losses per unit of reactive power are a function of the inverter size. The value of the offset coefficient $c_{\text{Turn on}}$ increases linearly with inverter size, whilst the quadratic coefficient c_R is *inversely* proportional to the inverter size. A larger inverter therefore has a higher turn-on cost; but, under the assumption

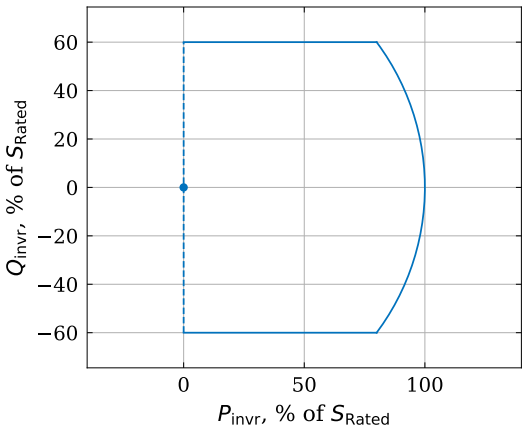

Figure 5.8: Inverter capability chart, for reactive power cutoff value $\alpha_{\text{invr}} = 0.6$.

that an inverter is already on (to export PV generation) it will then be able to export reactive power with a lower marginal cost than a smaller inverter.

The converter output capability is considered as,

$$|Q^i_{\text{invr}}| \leq \alpha_{\text{invr}} S_{\text{Rated}} \,, \tag{5.19}$$

$$|S^i_{\text{invr}}| \leq S_{\text{Rated}} \,, \tag{5.20}$$

where α_{invr} models the capability of the inverter to provide reactive power at low power. Generation priority is assumed, so that (at a given generation point P^i_{invr}) the equivalent constraint on the inverter is

$$|Q^i_{\text{invr}}| \leq \min \left\{ \alpha_{\text{invr}} S_{\text{Rated}}, \sqrt{S^2_{\text{Rated}} - P^i_{\text{invr}}} \right\} \,. \tag{5.21}$$

A value of α_{invr} is chosen to be 0.6 following previous work [133], with the capability chart for this inverter plotted in Figure 5.8. This is comparative to the reactive requirement of 0.44 of rated power, down to 20% of rated real power, specified by IEEE 1547 [34]. Similarly, California 'Rule 21' specifies that an inverter must be able to operate to a power factor of 0.85 or 0.9, depending on size, down to 20% of rated power [16], corresponding to limits of 0.53 and 0.44 of the rated power.

It is assumed in this work that if the real power generated by the inverter is zero,

then so is the reactive power, as inverters are not assumed to have accurate reactive power capabilities at very low power ratings as described in the previous paragraph. This may still overstate real capabilities at low powers (both IEEE 1547 and Rule 21 reactive power requirements taper to zero), although some works do suggest that in future the 'full semi-circle' could be utilised [57]. As-is, however, the results could potentially exaggerate reactive power capabilities in real systems during times of low power (i.e., during cloudy periods, or at dawn and dusk).

If the work here is considered in a specific jurisdiction, then the results should therefore be re-run to ensure the validity of the conclusions–as long as the region over which calculations are made is convex, the complexity of the optimization will not be impacted. (It is also worth highlighting here, however, that in many of the cases discussed the reactive power limit of the devices is not reached, as reactive power use tends to increase losses–this point is considered in Section 5.3.1.2.)

The limit provided here is larger than this limit, although it will be noted that, in many cases, the reactive power generated by the specified systems will be far below this rated reactive power.

5.2.6 Optimization Formulation

Combining all models together, the proposed optimization formulation takes the form of a mixed integer QCQP,

$$\min_{x} \quad P_{\text{feeder}}(x) = x^{\intercal}\Theta x + \psi^{\intercal} x + \rho \tag{5.22a}$$

$$|I_{\text{xfmr}}|^2 \leq I_{\text{rated}}^2 \tag{5.22b}$$

$$V_{-} \leq |V| \leq V_{+} \tag{5.22c}$$

$$x_{-} \leq x \leq x_{+} \tag{5.22d}$$

$$T \in \mathbb{Z}^{N_T} . \tag{5.22e}$$

where (for notational simplicity) $|\cdot|$, $(\cdot)^2$, $\leq$ are all elementwise operations. The cost function (5.22a) minimizes losses and load, with the cost function taken by summing (5.10), (5.14) and (5.17). This is subject to current constraints (5.22b) (from (5.13)) and voltage magnitude constraints (5.22c) (from (5.5)). Current constraints are set as discussed in Section 5.2.3.1; voltage constraints in EU-style networks are within $\pm 10\%$ of nominal, whilst MV and LV constraints in US-style networks are the same as considered in the previous chapter (see Section 4.4.1). Engineering constraints (5.22d) hold reactive power and taps within bounds (taps are constrained to ± 16, with reactive power constraints are given in (5.21)). Finally, taps are constrained to integer positions (5.22e).

This problem is technically non-convex (due to the integer constraints). In practise, however, standard conic solvers can handle mixed-integer convex conic problems with integer variables using branch-and-bound. In the case studies considered here the largest number of integer variables considered here is seven, which was found to be well within the capabilities of the MI-conic solver within Mosek [186].

Remark: Scalability beyond Single Timesteps. 'Slow' distribution network control actions, such as those taken by tap changers, are likely to only occur every five to fifteen minutes [46]; therefore, this is the time over which optimizations need to be calculated. It is worth noting that traditional volt-var control typically looks to minimise the number of tap changes as a part of the optimization objective function in (5.22), in order to minimise maintenance requirements [124]. This introduces coupling between timesteps, increasing the number of integer control variables. Nevertheless, if a known, feasible solution exists, this greatly improves the performance of branch-and-bound based optimizations [187, Ch. 7], [188]. Practically, therefore, it is expected that the optimization solutions, found by the method of this chapter, could lead to a practical algorithm that minimises tap changes as well as demand. Specifically, an algorithm could use of branch and bound, with a set of initially feasible solutions to (5.22) at each timestep, then even if the global optimal point cannot be found

then at least upper and lower bounds on the solution would be known (such that the quality of the solution can be determined *ex post*). In, general, however, the non-convexity of integer constraints does make integer programming a computationally 'hard' problem, and generally is by no means guaranteed to find a globally optimal (or even good solution) within a reasonable time [187].

5.2.6.1 Quality of Solution

The immediate benefit of a solution is given by the difference between the power with and without a given solution. This number is usually reported as a relative benefit– for example, as the amount of load reduction that is possible. For CVR applications (utilising load and loss reduction) this number is typically less than 5% of load, and more commonly up to 2% of load [133], [56, Ch. 6].

A second parameter which will be considered is that of the reactive power control efficacy. For the purposes of this chapter, this efficacy is found as the average power saving (in W) divided by the total change in reactive power injected (in kVAr):

$$\text{Efficacy} = \frac{P_{\text{feeder}}(x^{\dagger}) - P_{\text{feeder}}(x^{\text{Nom}})}{\|Q^{\dagger}_{\text{invr}} - Q^{\text{Nom}}_{\text{invr}}\|_1}\,, \tag{5.23}$$

where the notation $(\cdot)^{\dagger}$ denotes the optimal solution, and $(\cdot)^{\text{Nom}}$ is some nominal solution (usually the case that $Q^{\text{Nom}}_{\text{invr}}$=0). The efficacy is useful to consider as it describes the control effort required to effect the reduced feeder power. Although the benefit (in terms of the fraction of load) might be small, if the control effort is also small then this may justify the requirements required to active the control. Alternatively, if only a small amount of reactive power is required then a subset of inverters could instead be activated for the appropriate control scheme.

5.3 Necessity of Load and Inverter Losses in QCQP Cost Function

The cost function (5.22a) has three parts: load, network losses and inverter losses. The properties of this cost function in terms of inverter reactive power are now studied explicitly. There are two aims for this section. The first aim is to demonstrate that it is meaningful to consider the unconstrained QP (i.e., just the cost function (5.22a)) when considering reactive power control in isolation. This is done by showing that the unconstrained QP is almost feasible in all cases.

Having shown the unconstrained problem is almost feasible, the second purpose of this section is then to demonstrate the necessity of the inclusion of all components of the cost function. This is done by comparing norms of the quadratic models of the network losses, inverter losses, and load.

5.3.1 Unconstrained Optimization Solution

First, denote $\psi_{\mathrm{Q}}, \Theta_{\mathrm{Q}}$ as the partitions of ψ, Θ in reactive power injections, i.e.,

$$\psi = \begin{bmatrix} \phi_{\mathrm{Q}} \\ \phi_{\mathrm{T}} \end{bmatrix} \qquad \Theta = \begin{bmatrix} \Theta_{\mathrm{Q}} & \Theta_{\mathrm{QT}} \\ \Theta_{\mathrm{QT}}^{\intercal} & \Theta_{\mathrm{T}} \end{bmatrix}, \tag{5.24}$$

where dimensions are according to the number of inverters and taps respectively. It is assumed that the matrix Θ_{Q} is positive definite. (If this is not the case and Θ_{Q} is instead positive semidefinite, it is argued in the appendix, Section A.3.2 that, in the following analysis, in *some* cases the use of the Moore-Penrose inverse may be justified as an alternative to the matrix inverse.)

By differentiating the objective of the optimization (5.22a) and solving, the un-

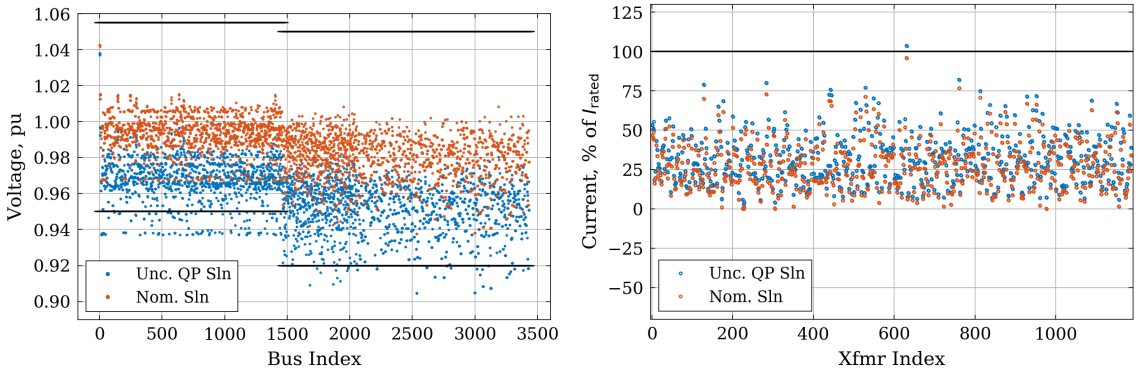

(a) EPRI Ckt. 5 Voltages

(b) EPRI Ckt. 5 Currents

Figure 5.9: The voltages and currents at the solution of the unconstrained quadratic program for the EPRI 5 Circuit.

constrained optimal solution $x^{\dagger}_{\text{Q Unc.}}$ and cost (feeder power) are given as

$$x^{\dagger}_{\text{Q Unc.}} = -\frac{1}{2}\Theta_{\text{Q}}^{-1}\psi_{\text{Q}} \tag{5.25a}$$

$$P_{\text{feeder}}(x^{\dagger}_{\text{Q Unc.}}) = -\frac{1}{4}\psi_{\text{Q}}^{\intercal}\Theta_{\text{Q}}^{-1}\psi_{\text{Q}} + \rho\,. \tag{5.25b}$$

If the unconstrained QP is feasible then it is also the optimal solution of the original problem, as it represents a relaxed optimization.

5.3.1.1 Initial Case Study: EPRI Circuit 5

The solution of the unconstrained QP is first found for EPRI Circuit 5. The voltages and currents are plotted in Figure 5.9–all load buses have a 'low' loss inverter (as discussed in Section 5.2.5) with a load voltage sensitivity factor of 0.6, at 100% load. The largest reactive power exported at this condition was 1.97 kVAr, compared to the upper bound of 2.4 kVAr.

In this case, the voltages and currents are not all in bounds, but the magnitude of the constraint violations are not too great–the minimum voltage is 0.905, and 6.8% of buses have undervoltages. The constrained solution will therefore have a higher optimal cost.

Table 5.2: Constraint extrema at the unconstrained optimization point $x^{\dagger}_{\mathrm{Q,\,Unc}}$ (i.e. solved in reactive power only). **Bold** font indicates a constraint violation–four of the unconstrained problems are feasible, and constraint violations in the other circuits are not too great. This illustrates that the cost function will play a very important role in the global solution value of the QCQP, compared to if all problems were infeasible.

Feeder	max(V), pu	min(V), pu	max(I_{xfmr}), %	max(Q_{invr}), kVAr
Ckt. 5	1.038	**0.905**	**103.9**	1.98
Ckt. 7	1.001	**0.898**	**133.3**	**3.25**
EULVa	1.041	0.997	58.4	0.28
Nwk. 10	1.043	0.999	58.3	0.05
123 Bus	1.049	0.976	79.6	2.05
Ckt. K1	1.015	**0.944**	**109.1**	**4.04**
EULVa-r	1.048	0.998	58.6	0.28

5.3.1.2 Feasibility of Seven Networks

It was found that the unconstrained problem was close to being feasible in all networks–the constraints are tabulated in Table 5.2; for example, no voltages in any of the networks are below 0.898 pu. There are some low voltages and high currents in EPRI Circuits 5 and 7, and some high currents and reactive powers in EPRI Circuit K1. The problem is feasible in the EULVa, EULVa-r, Network 10 and 123 Bus cases.

Given that the unconstrained QP is close to being feasible in the cases considered, this motivates a more thorough study of the objective function in reactive powers. The aim of is to study relative impact of load sensitivity and inverter losses on the solution, to understand how these change the solution and to demonstrate necessity of the consideration of all of these components.

5.3.2 Inverter Losses in the Unconstrained QP

First our attention turns to the inverter losses. These losses only change the quadratic matrix Θ_{Q}. To consider how this impacts on the solution $x^{\dagger}_{\mathrm{Q\,Unc.}}$, this quadratic term Θ_{Q} can be decomposed in terms of network and inverter losses as

$$\left(\Theta_{\mathrm{Q,\,lss,\,inv}} + \Theta_{\mathrm{Q,\,lss,\,ntwk}}\right) x^{\dagger}_{\mathrm{Q\,Unc.}} = -\frac{1}{2}\psi_{\mathrm{Q}}\,, \tag{5.26}$$

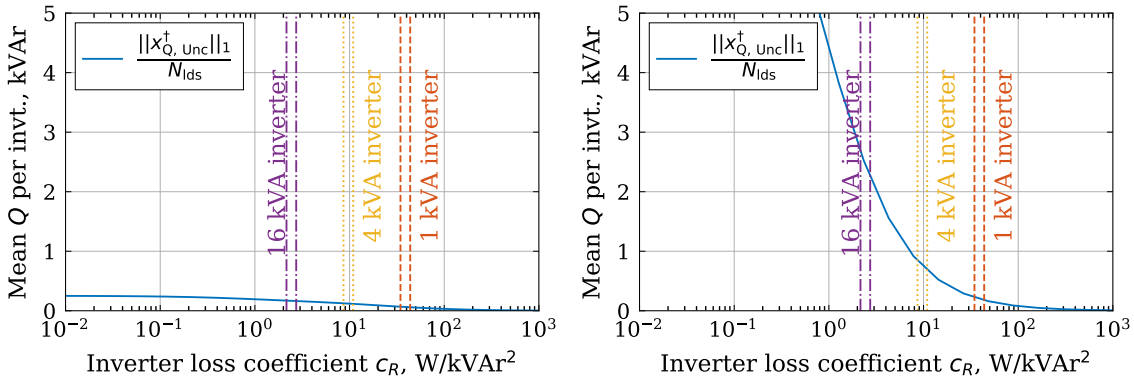

(a) Augmented EU LV

(b) IEEE 123 Bus

Figure 5.10: Varying the inverter loss coefficient c_R changes the solution $x^{\dagger}_{\mathrm{Q,\,Unc}}$ significantly (plotted here is the augmented EU LV (a) and 123 Bus circuit (b) networks at 100% load). The two lines associated with each inverter size correspond to 'high' and 'low' calculations of the inverter loss coefficient c_R (these values vary with inverter size, as discussed in Section 5.2.5).

noting that

$$\Theta_{\mathrm{Q,\,lss,\,inv}} = c_R I\,. \tag{5.27}$$

Equation (5.26) is solved for $x^{\dagger}_{\mathrm{Q\,Unc.}}$ over a range of inverter loss parameters c_R, and then the normalised norm of the solution plotted in Figure 5.10. Both 'low' and 'high' inverter loss parameters are considered for three inverter sizes of 1, 4 and 16 kVA. There are two things to note from these figures. As observed previously, the amount of reactive power at the optimal solution can vary by more than an order of magnitude, depending on the network. Secondly, the size of the inverter has a much larger influence on the loss coefficient c_R than whether an inverter is 'high' or 'low' loss. A sensible choice of inverter sizing, as well as loss coefficients, is therefore necessary.

5.3.2.1 Asymptotic Analysis

Given the large variation seen across solutions in Figure (5.10), our attention turns to consider if there is a way to demonstrate if the inverter losses will always result in a significant impact on the unconstrained solution. In studying this question, the converse also naturally arises: do the network losses need to be taken into account,

given inverter loss coefficient values?

The equation (5.26) can be rewritten in terms of the per-inverter losses c_R as

$$\left(I - \frac{1}{c_R}\left(-\Theta_{\mathrm{Q,\,lss,\,ntwk}}\right)\right) x^{\dagger}_{\mathrm{Q\,Unc.}} = \frac{-1}{2c_R}\psi_Q \tag{5.28}$$

$$\left(I - c_R\left(-\Theta^{-1}_{\mathrm{Q,\,lss,\,ntwk}}\right)\right) x^{\dagger}_{\mathrm{Q\,Unc.}} = \frac{-1}{2}\Theta^{-1}_{\mathrm{Q,\,lss,\,ntwk}}\psi_Q \tag{5.29}$$

These are both of the form

$$(I - \kappa A)\, x = b\,, \tag{5.30}$$

where κ is given by either c_R or $1/c_R$. In this form, it can be observed that (5.28) represents network losses causing a perturbation to the solution obtained by only considering inverter losses; likewise, (5.29) represents the smart inverter losses causing a perturbation on the solution considering only network losses.

If $\|\kappa A\| < 1$ (for any induced matrix norm), then (5.30) can be solved according to the Neumann series [168, pp. 74-75]

$$x = \sum_{k=0}^{\infty} (\kappa A)^k\, b \tag{5.31}$$

$$= b + \kappa A b + (\kappa A)^2 b + \dots\,. \tag{5.32}$$

Given that $\|\kappa A\| = |\kappa|\|A\|$, the norm of A yields important information about the convergence of this series, and thus if the solution is (in some sense) 'close' to the nominal solution b (for a given value of κ).

More specifically, it is shown in the appendix (Section A.3.3) the series (5.31) diverges if $\|\kappa A\|_2 \geq 1$. Therefore, the Neumann series non-convergence value κ_{Cnvg} is defined by $\kappa_{\mathrm{Cnvg}}\|A\|_2 = 1$, i.e.,

$$\kappa_{\mathrm{Cnvg}} = \frac{1}{\|A\|_2}\,. \tag{5.33}$$

For the two cases (5.28), (5.29) over the matrix 2-norm, this leads to convergence

regions (in c_R and $1/c_R$) as the maximum and minimum singular values of $\Theta_{\mathrm{Q,\,lss,\,ntwk}}$. This follows from the fact that the 2-norm of the inverse of a matrix is the reciprocal of the minimum singular value of that matrix (see, e.g., [189, pp. 94-95]). In other words, the spectral radius of the quadratic loss matrix $\Theta_{\mathrm{Q,\,lss,\,ntwk}}$ and its inverse determine if a solution is, in a sense, far from being a 'small' perturbation in either the network or inverter losses.

An second, alternative way to see the condition (5.33) is based on the following bound [190][pp. 124-125]:

$$\frac{\|b - x\|_2}{\|b\|_2} \leq \frac{\kappa\|A\|_2}{1 - \kappa\|A\|_2}\,. \tag{5.34}$$

In other words, the condition (5.33) results in an uninformative upper bound on the relative error of the solution to (5.30).

Asymptotic changes in the unconstrained solution Assuming that $\|\kappa A\| \ll 1$, (5.31) leads to the asymptotic approximation

$$x \approx b + \kappa A b \tag{5.35}$$

Using this result it is now possible to consider how x changes with κ, compared to the unperturbed solution b. Specifically, if the aim is to find the point at which x changes by some percentage k (for example, when $\|x\|_2$ reduces by, say, 5%), then this can be solved for $\kappa_{k\,\%}$ as a quadratic as

$$\|k\,b\|_2 = \|b + \kappa_{k\,\%} A b\|_2\,, \tag{5.36}$$

$$\rightarrow \quad \kappa_{k\,\%}^2\|Ab\|_2^2 + 2\kappa_{k\,\%}(Ab)^\intercal b + (1 - k^2)\|b\|_2^2 = 0\,. \tag{5.37}$$

Solving for κ, yields the point at which the solution $x^{\dagger}_{\mathrm{Q,\,Unc}}$ changes significantly from the low (or high) values of c_R. If this inverter loss coefficient 'cutoff value' κ_{Cnvg} is well within the region of convergence (as calculated by the singular value) then it can be concluded that the calculated value will be accurate; if it is outside the region of

convergence then it will not be accurate.

To summarise:

- If the value of the inverter loss coefficient c_R is between the maximum and minimum singular values of the quadratic network loss matrix $\Theta_{\mathrm{Q,\,lss,\,ntwk}}$ then both network and inverter losses should be accounted for.

- If the value of the inverter loss coefficient c_R is smaller than both the minimum singular value and some reasonable inverter loss coefficient cutoff value κ_{Cnvg} (e.g., 95%) with respect to the network loss perturbation (5.29), then inverter losses can reasonably be ignored.

- If the value of the inverter loss coefficient c_R is larger than both the maximum singular value and some reasonable inverter loss coefficient cutoff value κ_{Cnvg} (e.g., 95%) with respect to the inverter loss perturbation (5.28), then network losses can reasonably be ignored.

5.3.2.2 Case Study: EPRI Circuit 5

To demonstrate the method, the true solution (5.25) is found, alongside the asymptotic approximations as calculated from (5.35) (for (5.28) and (5.29)), for EPRI Circuit 5 (Figure 5.11). Additionally, on this figure the singular values of the network loss matrix $\Theta_{\mathrm{Q,\,lss,\,ntwk}}$ are plotted, alongside the 95% inverter loss coefficient cutoff values, as calculated by the Neumann series approximation (5.35).

The figure illustrates a number of important points.

- Between the maximum and minimum singular value, neither of the asymptotic linear approximations accurately model the behaviour of the solution. In their region of their convergence (outside of the region between minimum and maximum singular values), however, they model the solution well with a maximum absolute error of 13%.

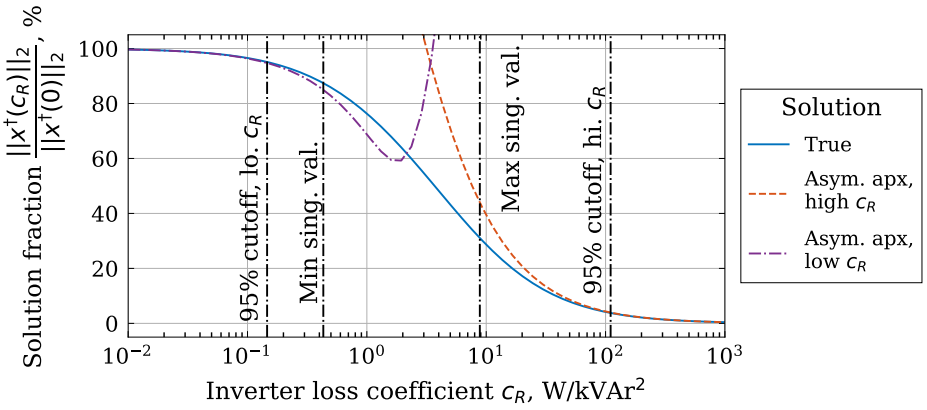

Figure 5.11: Varying the inverter loss coefficient changes the unconstrained solution $x^\dagger$ significantly (plotted here is EPRI Circuit 5 at 100% load). The 'true' solution is found by solving (5.25), whilst the asymptotic approximations are found by considering the first term of the Neumann series of (5.28) and (5.29) (as in (5.35)). The singular values are of the matrix $\Theta_{\mathrm{Q,\,lss,\,ntwk}}$ and the 95% cutoff values (whereby the solution has changed by 5% from it's nominal value) are found using the asymptotic approximation (5.35).

- For large values of c_{R} the solution asymptotically approaches zero with $1/c_R$ (from (5.28)). (The 95% cutoff value for large values of c_R is the ratio with respect to the curve $1/c_R$, which is not plotted.)
- For inverter loss coefficients between 2 and 50 W/kVAr^2 (from Figure 5.10), both network and inverter losses need to be accounted for to find an accurate solution.

5.3.2.3 Results Across Networks

The values of the maximum and minimum singular values, and these inverter loss coefficient 95% cutoff values are given in Table 5.3. It is interesting to observe that the minimum singular value is sometimes greater than the 95% cutoff for low values of c_R (if a higher accuracy is required then more terms of the Neumann series could be considered, for example). Inverter loss coefficients c_R are again assumed to be between 2 and 50 W/kVAr^2.

The first key observation from Table 5.3 is that, in all networks, the minimum singular value is always below 0.5 W/kVAr^2. As such, it is concluded inverter losses

Table 5.3: Minimum/maximum singular values of the network loss quadratic matrices $\Theta_{\mathrm{Q,\,lss,\,ntwk}}$, and the estimate of the 95% inverter loss coefficient cutoff value. For values of the inverter loss coefficient c_R between 2 and 50 W/kVAr^2, inverter losses should always be taken into account, and network losses should usually be taken into account.

Feeder	95% cutoff, low c_R, W/kVAr^2	Min. sing. value, W/kVAr^2	Max. sing. value, W/kVAr^2	95% cutoff, high c_R, W/kVAr^2
Ckt. 5	0.146	0.432	8.84	110.2
Ckt. 7	2.74e-05	2.53e-04	13.09	168.8
EULVa	0.062	0.025	59.61	622.1
Nwk. 10	0.019	0.086	6.31	39.83
123 Bus	4.86e-04	5.75e-04	1.39	16.16
Ckt. K1	8.05e-05	1.41e-03	2.65	35.58
EULVa-r	0.060	0.024	58.89	615.7

should be taken into account in all of these networks.

On the other hand, the maximum singular value is between 1 and 60 W/kVAr^2, with the inverter loss coefficient 95% cutoff value for high c_R is between 16 and 630 W/kVAr^2. Therefore, it is concluded that in some of the networks considered here, it may in fact be possible to ignore the network losses–this could occur, for example, in the IEEE 123 Bus or EPRI K1 circuit. The conclusion of this section is that inverter losses should *always* be taken into account in distribution networks with only domestic reactive power support, but it appears that in very low loss networks with small inverters that network losses can potentially be ignored with no significant impact on results. In all of the following case studies, all losses (both network and inverter losses) are modelled.

5.3.3 Impact of Load Model

The cost function linear term ψ_{Q} is the sum of a network loss component and the linear loss component. The values of each of these sensitivities is plotted in Figure 5.12 for two circuits. There are two main things to note. Firstly, there is a difference in the sign between the direction of sensitivity for losses and load, as predicted by the two-bus model. Loss sensitivities are negative, whilst load sensitivities are positive.

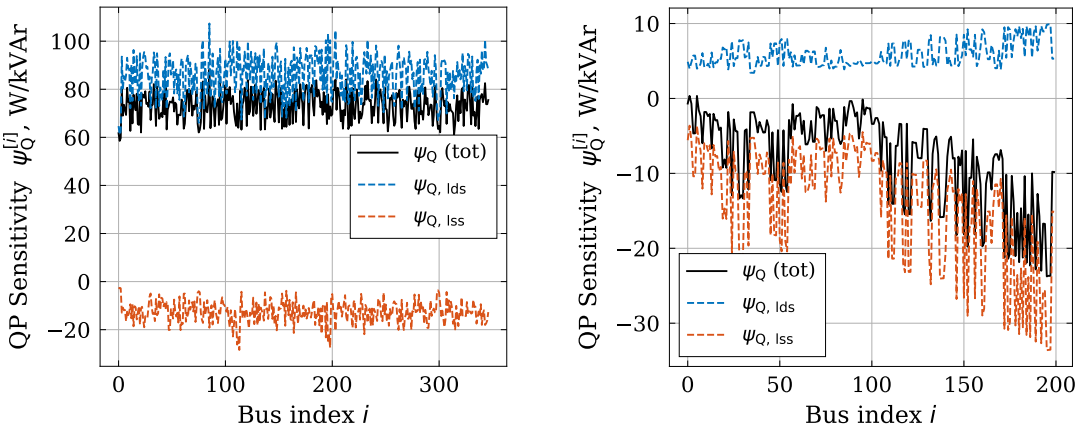

(a) EPRI K1 Circuit

(b) EULVa network

Figure 5.12: The quadratic program linear sensitivity for the EPRI K1 and EULVa network, at 100% load, with load voltage sensitivity $\alpha_{\text{CVR}} = 0.6$.

This is because load reduces with voltage, whilst compensating reactive loads (which tend to have a lagging power factor) tends to reduce the losses. The second thing of note is that either one of these quantities (load or loss sensitivity) can be larger than the other. The EPRI K1 circuit is a relatively low-loss network with a low R/X ratio; the EULVa network has a much higher R/X ratio.

Table 5.4 summarises the properties of these sensitivity vectors, as calculated at 100% loading, including calculating the angle between the load and loss sensitivities. The load sensitivity tends to be larger than the loss sensitivity, but this is not always the case. The angle between the two vectors is always greater than 90°, indicating that the action of the vectors are generally in an opposite sense.

It is clear from the norms of the loss and load sensitivities that the load model has a significant impact on the total sensitivity in all cases. Given that the unconstrained solution is linear in ψ_Q and the unconstrained cost is quadratic in ψ_Q (from (5.25)), it is concluded that the load sensitivity needs to be accounted for in all cases considered here.

Finally, it is interesting to note that the sensitivities of losses are potentially lower than may be observed in other, lossier systems. The bus with the largest individual loss sensitivity across all networks was recorded on EPRI Circuit 5, with

Table 5.4: Summary of sensitivities to reactive power injections in load, loss, and the total for both of these combined. The angle θ_ψ is calculated between the load and loss sensitivity vectors; N_Q is the number of elements in the sensitivity vector ψ_Q.

Feeder	Load sensitivity, $\frac{\|\psi_{\mathrm{Q,lds}}\|_1}{N_\mathrm{Q}}$, W/kVAr	Loss sensitivity, $\frac{\|\psi_{\mathrm{Q,lss}}\|_1}{N_\mathrm{Q}}$, W/kVAr	Total sensitivity, $\frac{\|\psi_\mathrm{Q}\|_1}{N_\mathrm{Q}}$, W/kVAr	θ_ψ, $^\circ$
Ckt. 5	64.68	24.31	40.36	168.9
Ckt. 7	75.48	4.85	70.64	140.5
EULVa	5.90	13.99	8.09	165.7
Nwk. 10	1.78	1.45	0.42	167.3
123 Bus	30.25	14.45	15.86	159.4
Ckt. K1	85.80	12.67	73.13	164.9
EULVa-r	5.90	13.82	7.93	165.6

a loss sensitivity value of 43.4 W/kVAr. This is on a similar level to the maximum sensitivities calculated in [191] as 45 W/kVAr, whilst it is less than half of the value of the sensitivity found in the rural circuit studied in [192] (the sensitivity is shown to be 100 W/kVAr). It does, however, compare favourably with the maximum sensitivity of losses to reactive power, which is estimated as 15 W/kVAr in the transmission-based case study of [193].

5.4 Constrained Optimization: Case Studies

There are three aims in the rest of this chapter. Having determined the necessity of all modelled components in the unconstrained case, this section first aims to study the constrained optimization of all circuits and demonstrate the necessity of considering all terms of the optimization. Secondly, the performance of the MI-QCQP model will be validated, by calculating the error in voltages, currents, and power at the constrained optimal point. Finally, the chapter will conclude with a sensitivity analysis in terms of CVR factor, inverter losses, and a time series simulation based on two case studies over two representative days.

For the first task of studying all terms in the objective, five separate optimizations are run with changes to either the objective function or constraints, to investigate the

causes of the reduction in cost seen.

S1 'Full' control. This utilises all controls with the full objective function.

S2 'Nominal' control. The full objective function is considered, but with no reactive power control (but with taps enabled).

S3 'Load' control. All controls are utilised, but only the load is minimized.

S4 'Loss' control. All controls are utilised, but only the losses are minimized.

S5 'Phase' control. This proposed control scheme is as the 'Full' control scheme, except all reactive power devices on the same phases are constrained to export the same reactive power.

Between them, these control schemes will be used to establish the necessity of including all terms in the model for the constrained optimization cases numerically (where the unconstrained QP case was studied analytically).

The final, 'Phase' control scheme is considered as an alternative to the Full control scheme, with reduced communication requirements (only a broadcast to all inverters would be required on each phase, rather than to all inverters individually). This method has the advantage that, if there are significant power imbalances across phases, then reactive power can be used to reduce voltages on only those phases which are loaded without causing losses on other phases, with this particularly pertinent if there are per-phase regulators.

Alternative control schemes could also be explored that are somewhere between 'Full' and 'Phase' control schemes–for example, considering reactive power setpoints spatially, based on their location with respect to tap changers. These alternative schemes may show more or less benefit compared to 'Phase' control–in fact, if there is little load unbalance then there is unlikely to be much of an advantage of 'Phase' control over a scheme which sets a uniform reactive power setpoint at all loads. A comprehensive exploration of all of the options beyond schemes S1-S5 was beyond the scope of this thesis.

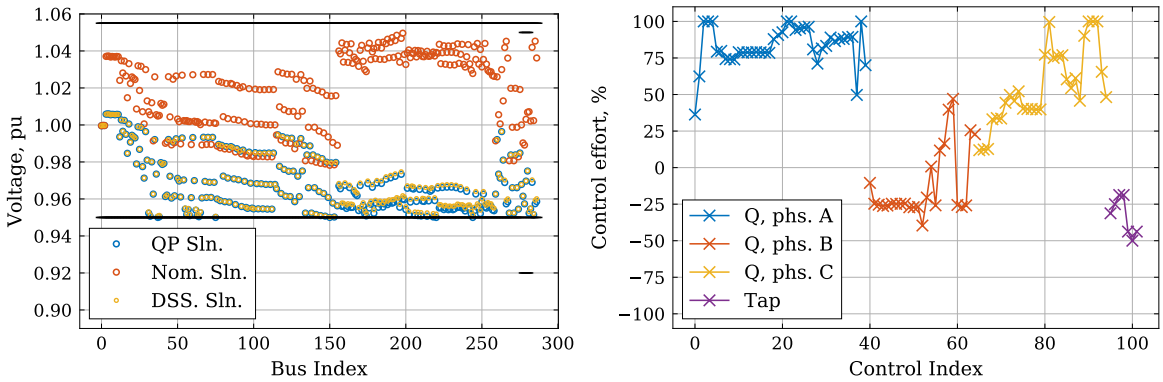

(a) 123 Bus optimal voltages

(b) 123 Bus optimal control

Figure 5.13: Solution of the 123 Bus circuit in terms of (a) voltages and (b) the optimal control solution. Three sets of voltages are plotted: the voltages according the the MI-QCQP solution (the 'QP Sln.'), with voltages as calculated using the MI-QCQP model; the solution prior to either tap or reactive power control ('Nom. Sln'); and, the solution in OpenDSS when optimal reactive power and taps are applied ('DSS. Sln'). The controls (b) are decomposed into reactive power (in terms of phase A, B, or C), and the tap. ±100% represents the maximum and minimum values of each control.

A preliminary case study will first be considered, to illustrate how the control strategies will be compared, and how the solution will be validated.

5.4.1 Preliminary Case Study: IEEE 123 Bus

The IEEE 123 Bus is first setup as outlined in Section 5.2. Having solved the 'Full' optimization, the total power on the network is reduced by 2.93% compared to the initial solution (taps and reactive power as solved for in OpenDSS). This is largely driven by a large reduction in voltage, in comparison to the initial solution, as plotted in Figure 5.13a. The corresponding controls are plotted in Figure 5.13b.

There is a large change in the tap positions, but there is also reactive power use across the whole network. In fact, it is clear that there is a strong correlation between the phase of the inverter, and the optimal reactive power control point. This is further illustrated in Figure 5.14 which plots the reactive power as located on the feeder, as well as the phase.

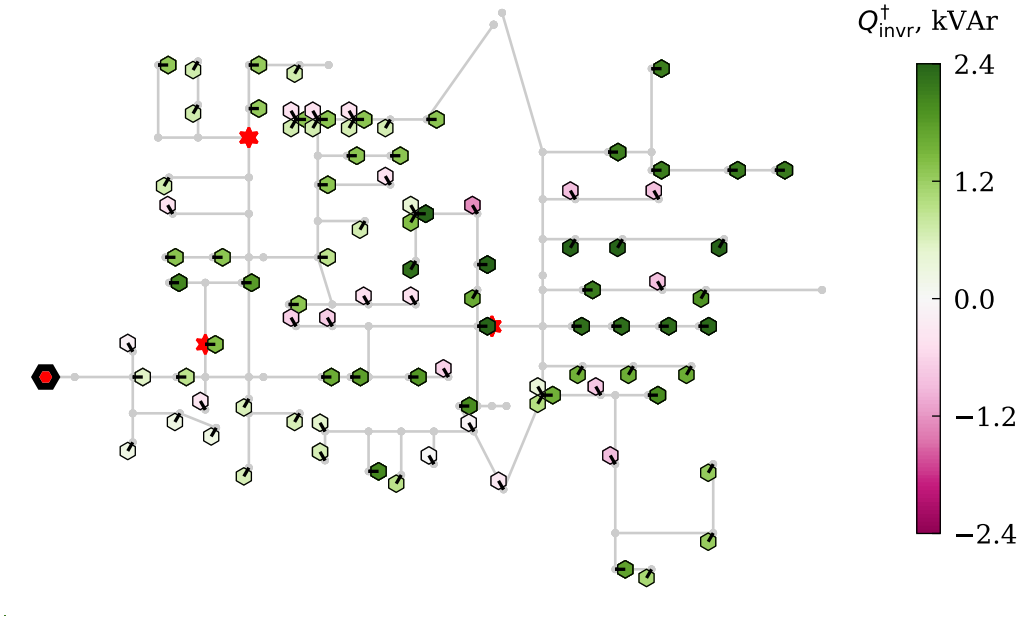

Figure 5.14: Daisy plot of the optimal control for the IEEE 123 Bus feeder, minimizing the operating cost. Each hexagon represents an inverter, with tick angles at 0°, 120°, 240° representing phase A, B and C respectively; red marks indicate a regulator. There is a strong correlation between the optimal inverters control points and the phase information, suggesting that control on a per-phase basis could perform well.

5.4.1.1 Comparative Analysis

The result of Figure 5.13 demonstrates the need for a comparison between 'Full' and 'Nominal' strategies. It is not possible as-is to evaluate the impact of the reactive power devices from this figure. Furthermore, it is not possible to determine if 'Load' or 'Loss' minimization strategies could be used as a proxy for total feeder power minimization.

Therefore, the results for control schemes S1-S5 are plotted in Figure 5.15 for three different loading points (with each loading point having a separate linearization to ensure the calculations of sensitivities remain accurate). There are a number of points of interest. As predicted, the full control case (which considers the full objective function with all controls enabled) performs the best. However, the benefits compared to Phase control is almost indistinguishable on this figure, whilst the benefits versus Nominal control (with no reactive power control) are less than 0.5%. The control

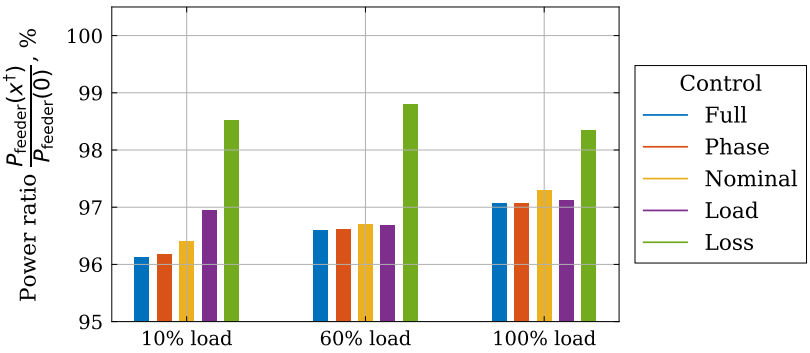

Figure 5.15: The total feeder power P_{feeder} at the optimal point $x^\dagger$ under different control schemes, compared to the solution with no control $P_{\text{feeder}}(0)$.

efficacy of the Full versus Nominal control (as calculated in (5.23)) is 68 W/kVAr.

5.4.1.2 Analysis of Approximation Error

Given a linearized model of a non-linear system, there will be a discrepancy between the true solution and the optimization solution. Additionally, in the case of mixed-integer (MI) optimization problems, if there is a non-zero 'relative gap' between the upper and lower bounds of a solution, then the global optimal point has not been reached [187, Ch. 7], [188]. Therefore, both the linearization error and MI relative gap should be checked to evaluate the performance of the algorithm.

Figure 5.16 plots the changes in voltages and currents at the optimal solution for the IEEE 123 Bus circuit at 100% load. It is observed that there are some errors in both the voltage and current injections, but that this error is small. In fact, the solution shows improved performance compared to, for example, the method of [115] which shows larger relative errors in voltages. The predicted power reduction as calculated by the MI-QCQP was 106.33 kW, whilst the reduction seen in OpenDSS was 106.43 kW. The relative mixed integer optimization gap was zero in all cases.

To consider the local error of the solution consistently across all circuits, the relative error is calculated between the MI-QCQP solution and the load flow solution from OpenDSS, as considered in previous works [139]. The relative error is evaluated

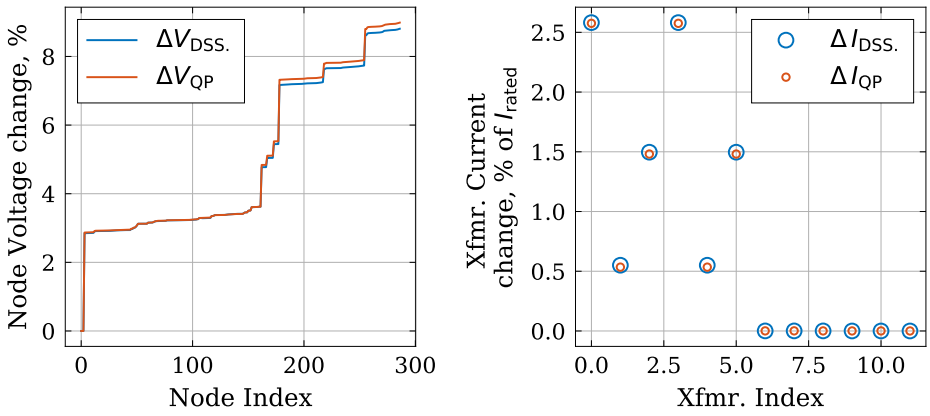

Figure 5.16: The solution error for the 123 Bus test feeder in voltages and currents, demonstrating a very good fit between the changes predicted by the linear model and the true solution from OpenDSS.

for powers, voltages and currents as follows:

$$\text{Voltage error} = \frac{\|\Delta V_{\text{QP}} - \Delta V_{\text{DSS}}\|}{\|\Delta V_{\text{DSS}}\|}, \tag{5.38a}$$

$$\text{Current error} = \frac{\|\Delta I_{\text{QP}} - \Delta I_{\text{DSS}}\|}{\|\Delta I_{\text{DSS}}\|}, \tag{5.38b}$$

$$\text{Power error} = \frac{|\Delta P_{\text{feeder, QP}} - \Delta P_{\text{feeder, DSS}}|}{|\Delta P_{\text{feeder, DSS}}|}, \tag{5.38c}$$

with voltages in pu and currents in % of I_{rated}. The subscript 'QP' and 'DSS' represent the load flow solution as calculated by the MI-QCQP and full load flow solution (i.e., from OpenDSS). Across all solutions from 123 Bus circuit, the maximum approximate voltage error was 1.8%; the current error was 7.6%, and the power error was 0.7%.

5.4.2 Results Across Feeders

Having considered the 123 Bus circuit in detail, the results across all case studies are now considered, in terms of (i) a comparison between operating strategies; (ii) a study of the solution error, and (iii) sensitivity analysis to key parameters.

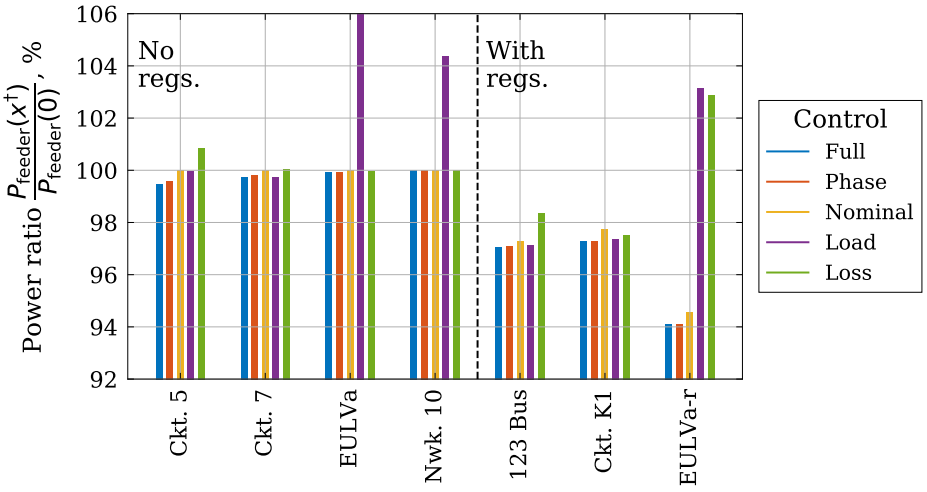

Figure 5.17: The total feeder power P_{feeder} at the optimal point $x^\dagger$ under different control schemes, compared to the nominal solution with no control $P_{\text{feeder}}(0)$, across all feeders, at 100% load. The first four circuits have no regulators ('No regs.') whilst the three final circuits have at least one regulator each ('With regs.')

5.4.2.1 Comparison Between Control Strategies

The first result that is considered is the reduction in total feeder power across all feeders, studying all five of the control schemes S1-S5. The purpose of this comparison is to consider how the benefits change between networks, and study if any of the alternative formulations can be used as an approximation for considering the full benefit that can be achieved, or if the full model must be used. The results are plotted in Figure 5.17.

The first observation based on these results is that the circuits with regulator tap control show a much greater drop in power compared to the feeders without them. This is largely driven by the use of taps, as is evidenced by the large drop in the feeder total power in the 'Nominal' control case. (In the case without regulators, this 'Nominal' power is trivially 100%). For example, the greatest demand reduction for unregulated networks is less than 1% (in EPRI Circuit 5), whilst the smallest drop in total feeder power is greater than 2.5% in regulated cases (for Full control).

The second observation that is made is that neither the 'Loss' nor 'Load' reduction schemes result in a consistent reduction in the total feeder power (compared to 'Nominal' control), in either the cases with or without regulators. For both EPRI

Table 5.5: Smart inverter benefits, as a % of load, compared to the Nominal control case (which only has tap controls activated, if there are any), calculated using the MI-QCQP model. With the exception of Network 10, the minimum ratio of phase to full load is 73%, and the maximum ratio of benefits is 98%

Control	Ckt. 5	Ckt. 7	EULVa	Nwk. 10	123 Bus	Ckt. K1	EULVa-r
Full, %:	0.524	0.250	0.068	4.5×10^{-4}	0.226	0.468	0.447
Phase, %:	0.432	0.183	0.058	1.5×10^{-4}	0.215	0.458	0.432

Circuit 5 and the 123 Bus circuit the loss reduction method is less effective than nominal control, whilst in Network 10 and the regulated EU LVa-r circuit load reduction leads to a sharp increase in the feeder total power.

Finally, it is noted that the impact of smart inverter control is typically quite modest, but that 'Phase' reactive power control is effective at capturing the majority of benefits that are seen from smart inverters, compared to 'Nominal' control. In fact, the benefits of smart inverter control considering only per-phase control under these conditions is up to 98% (see Table 5.5).

5.4.2.2 Error analysis

The error analysis of each circuit is calculated next to consider the accuracy of the MI-QCQP. That is, the voltages, currents and power calculated from the MI-QCQP are compared to the voltages, currents and powers from OpenDSS, when the solution $x^\dagger$ is applied to both models. The maximum values of each of the errors in voltage (5.38a), current (5.38b), and power (5.38c) are given in Table 5.6 across 10%, 60% and 100% loading points.

The error is 10.3% or less in all cases, although the error seen varies between networks. It is concluded that the linearization of voltages is leading to a good approximation of the non-linear power flow equations, giving confidence in the accuracy of the calculated solutions. If a higher accuracy is required, a linearization could be recalculated at this optimization solution point, and then the optimization rerun.

Table 5.6: Maximum error across all three loading points (10%, 60%, 100%), when the optimal solution $x^{\dagger}$ is applied to both OpenDSS and the MI-QCQP model. Voltage, current and power errors are as calculated in (5.38a), (5.38b) and (5.38c).

Feeder	Voltage error, %	Current error, %	Power error, %
Ckt. 5	3.177	3.170	10.310
Ckt. 7	6.789	5.541	4.083
EULVa	1.154	0.526	9.929
Nwk. 10	0.009	0.008	10.315
123 Bus	1.820	7.583	0.707
Ckt. K1	0.297	7.294	1.289
EULVa-r	0.153	0.623	2.090

5.4.3 Sensitivity Analysis

In the previous section, the sensitivity of the unconstrained QP predicted that the reactive power use would depend heavily on the loss behaviour of the inverter; but also that if a network was very lossy, the load sensitivity factor will have much less of an impact that in a network with relatively low losses. Infeasible solutions could not explicitly be considered in those cases, however, and the impact of taps was not considered either. The impact of these shall therefore be considered numerically in this section.

5.4.3.1 Inverter Losses

The first sensitivity considered is that of the losses from the inverter. Three cases are considered: a lossless inverter, an inverter with low losses, and an inverter with high losses. The benefits seen for all circuits are calculated in comparison to 'Nominal' (tap) control in Table 5.7. (Circuits in the second half of the table have voltage regulators.)

As predicted earlier in the chapter, in the circuits with no inverter losses, there is a much higher benefit than in those circuits with inverter losses. In fact, the circuits with no regulators see dramatically reduced benefits (in real power terms) - for example, there is a 50% reduction in EPRI Circuit 5. The average efficacy (in terms of the power saved per unit of reactive power control) reduces in EPRI Circuits

Table 5.7: Smart inverter load benefit (%) and efficacy (W/kVAr, defined in (5.23)). Values are as calculated using the MI-QCQP model.

	Load reduction, %			Control efficacy, W/kVAr		
Inverter losses:	None	Low	High	None	Low	High
Ckt. 5	1.009	0.524	0.458	27.1	21.8	21.6
Ckt. 7	0.369	0.250	0.221	57.4	39.6	36.9
EULVa	0.096	0.068	0.064	4.0	5.6	5.7
Nwk. 10	0.004	0.000	0.000	0.2	0.2	0.2
123 Bus	0.297	0.229	0.217	48.9	72.9	69.8
Ckt. K1	0.528	0.470	0.458	98.3	144.9	143.1
EULVa-r	0.483	0.447	0.441	18.2	31.8	33.7

5 and 7. There is little benefit in the EU LV network, and no measured benefit (to this precision) in Network 10.

In the cases with regulators, there is also a reduction in load, but the change in benefits is less pronounced. In fact, the largest drop in benefits is less than 1/3. It is interesting to see, however, that the control efficacy increases a marked amount with inverter losses. In fact, EPRI Circuit K1 has a relatively high benefit of over 100 W/kVAr. Recall that, in circuits with regulators, the action of smart inverters is to allow for a lower tap across a whole feeder, rather than acting to locally reduce the voltage (as is the case in circuits with no regulators). In fact, although the percentage reduction in load is not much greater than in, for example, Circuit 5, the efficacy in W/kVAr is much higher. This implies that if there was more reactive power available, benefits may increase; furthermore, it implies that the benefit per customer is likely to be higher.

5.4.3.2 Voltage Sensitivity Factor (α_{CVR})

The voltage sensitivity factor α_{CVR} is difficult to estimate, and it is therefore also imperative that the sensitivity with respect to this quantity is considered. The optimization is re-run over a wide range of voltage sensitivities at the 100% load point. The reduction in load and control efficacy is given in Table 5.8. (The values in the columns associated with $\alpha_{\text{CVR}} = 0.6$ match the results of the 'low' inverter losses

Table 5.8: Smart inverter load benefit (%) and efficacy (W/kVAr, defined in (5.23)) against α_{CVR}. Values are as calculated using the MI-QCQP model.

	Load reduction, %				Control efficacy, W/kVAr			
V. sensitivity α_{CVR}:	0.0	0.3	0.6	0.9	0.0	0.3	0.6	0.9
Ckt. 5	0.28	0.02	0.52	1.46	15.3	4.6	21.8	45.6
Ckt. 7	0.00	0.05	0.25	0.49	5.2	16.4	39.6	76.8
EULVa	0.19	0.12	0.07	0.03	8.2	6.9	5.6	4.1
Nwk. 10	0.01	0.00	0.00	0.00	0.7	0.4	0.2	0.7
123 Bus	0.02	0.09	0.23	0.39	10.0	26.7	72.9	102.2
Ckt. K1	0.02	0.21	0.47	0.76	8.8	59.3	144.9	242.8
EULVa-r	0.16	0.48	0.45	0.60	9.2	24.6	31.8	61.0

results of Table 5.7.)

In the unregulated networks, there appears to be a non-linear variation in the benefits that are afforded by control. For example, in the case of EPRI Circuit 5, the minimum benefit is at a voltage sensitivity of 0.3, whilst in the case of the EULVa circuit the minimum does not appear to have been reached even as the voltage sensitivity increases to 0.9. This behaviour can be explained as the linear sensitivity to load and losses act in opposite directions, as discussed previously.

In the case of networks with regulators, the pattern is that the benefits of the control increase with the voltage sensitivity, although this increase is not monotonic across all case. Because of the discrete tap position constraint, this appears to lead to a slight drop, for example, in the EULVa-r circuit. In addition to the load reduction being significantly affected, the control efficacy also increases, typically by up to an order of magnitude. It is concluded that the benefits afforded by this control need to be carefully checked against a range of voltage sensitivities before a strong estimate of the potential benefits can be confirmed.

5.4.4 Time Series Analysis using Phase Control

In this final section two case studies are considered, using the circuits with the highest load reduction values (EPRI Circuit 5 and EPRI K1). The load and generation data

is used from Chapter 3. Generators are considered as constant power devices, each following the same generation curve. Inverters are assumed to be 'off' when they are not generating. Loads are once again assumed to have a uniform voltage sensitivity of 0.6.

Two representative days are chosen (July 20th and October 15th), representing days with a large amount of generation and a large load respectively. The method of solution is as follows: first, a load flow solution is obtained from OpenDSS. The linearization is then determined at the given operating point, using the method described in Section 5.2. The control of inverter reactive power and taps is then enabled and the optimization run.

Given the strong performance of the 'Phase' control method, it is chosen for subsequent optimizations. All voltages, currents, and control points are recorded. In the case of the EPRI Circuit K1, 'Nominal' control (with only tap control) is also solved, so that the true benefits of domestic inverter control can be calculated.

5.4.4.1 Time Series Case Study I: EPRI Circuit 5

The solution for the EPRI Circuit 5 is outlined in Figures 5.18 and 5.19. Analysis of each of these figures now follows.

Powers The first thing to note is that the generation in this feeder (Figures 5.18a 5.18b) is relatively large, such that there is reverse power flow in the middle of the day in July. In October, cloud cover limits the energy that is self-consumed at the site of the generation.

Voltages The maximum and minimum voltages in the network, in terms of both MV and LV networks, are plotted in Figures 5.18c and 5.18d. The blue lines denote the voltages for Nominal control, whilst the orange lines are associated with the smart inverter Phase control. The two sets of voltage limits are visible on this graph, with the MV voltage lower constraint at 0.95 pu and the LV at 0.92 pu.

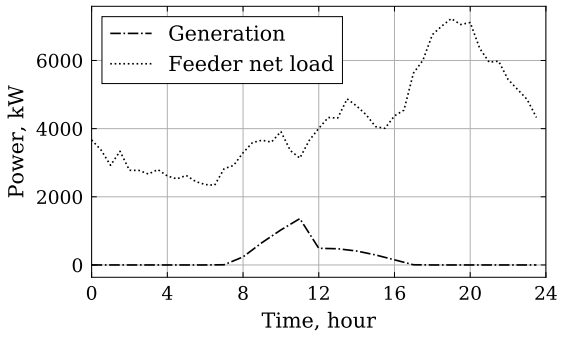

(a) Feeder powers - Oct. 15th

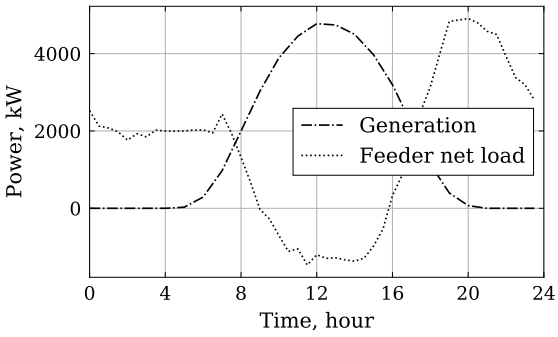

(b) Feeder powers - Jul. 20th

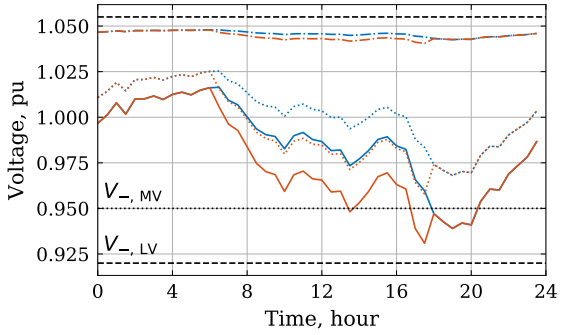

(c) MV and LV Voltages - Oct. 15th

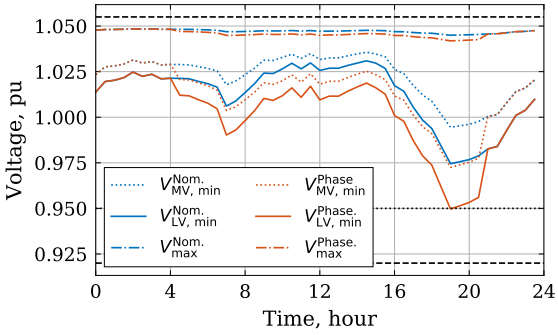

(d) MV and LV Voltages - Jul. 20th

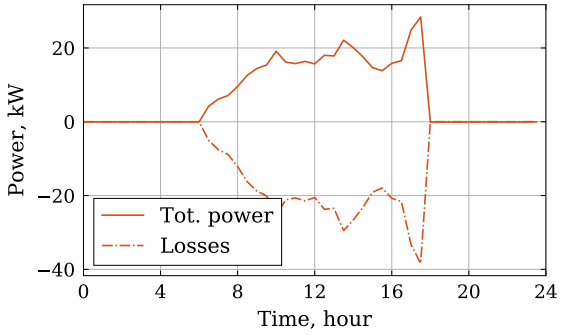

(e) Smart inverter power benefits - Oct. 15th

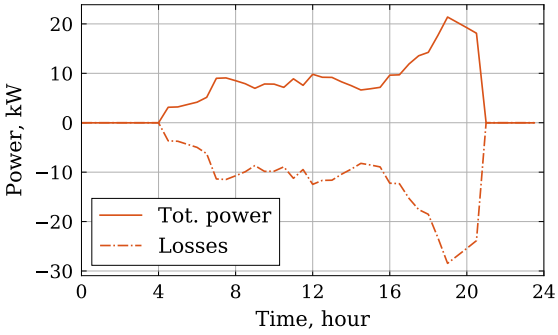

(f) Smart inverter power benefits - Jul. 20th

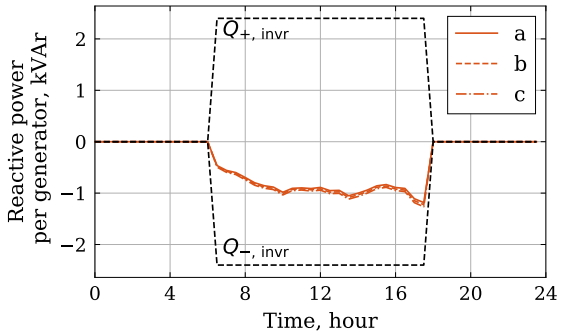

(g) Phase reactive power setpoints - Oct. 15th

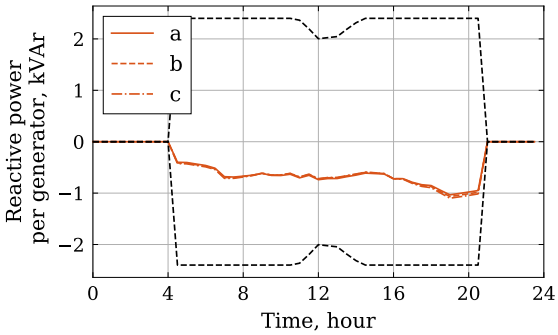

(h) Phase reactive power setpoints - Jul. 20th

Figure 5.18: Powers, voltages, benefits (in power) and phase control points for July and October days for EPRI Circuit 5.

For the first few hours of the day, the inverters are all off and so there is no reactive power provided. Once reactive power is available however, the minimum and maximum voltages all drop. The amount of voltage drop is up to 2% in the October solution, whilst the voltages drop by up to 2.5% in the July solution.

Smart inverter benefits The benefits of smart inverter control, in terms of the reduction in power, are plotted in Figures 5.18e and 5.18f. The higher peak load in the October day leads to a higher average benefit over the day, but the benefit is over a shorter time period as the inverters are off for a longer period.

Interestingly, the change in losses is negative, whilst the net power reduction is positive. The reason for the increase in losses is that the sensitivity of losses with respect to reactive power is less than half the sensitivity of loads to reactive power, with the angle between these vectors being almost 170° (as discussed in Section 5.3.3).

Phase reactive power The per-phase inverter control is given in Figures 5.18g and 5.18h. It is clear that these are all extremely correlated. It is assumed that this may be, in part, due to the constant scaling parameter applied to all domestic load profiles. If there was more diversity in load profiles, then the unbalance in the phases could increase.

Efficacy Finally, Figures 5.19a and 5.19b plot the control efficacy in term of power per unit of reactive power injection. The values observed are lower than the values in the 100% load case (which has a control efficacy of 21.8 W/kVAr). This is to be expected, as the mean load is 43% and 60% of the peak load for July and October days respectively; the peak values of load are at 95% in the October case. The efficacy for the October day is greater than for the July day, but the period over which it acts is smaller.

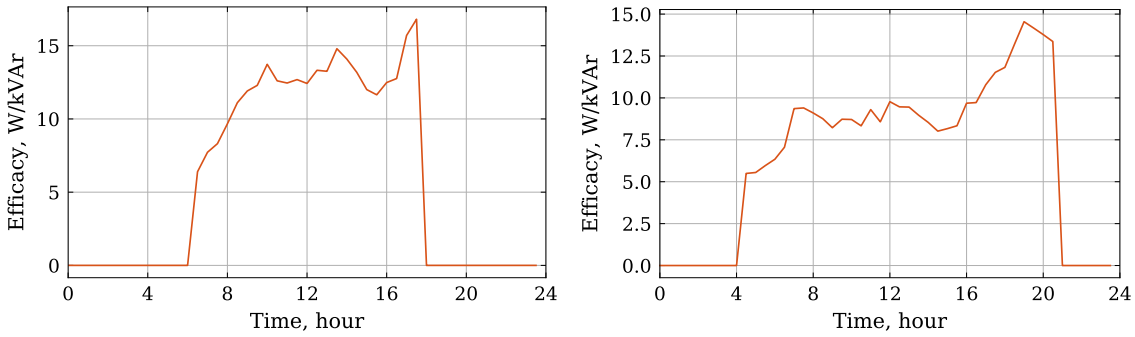

(a) Control efficacy - Oct. 15th (b) Control efficacy - Jul. 20th

Figure 5.19: Control efficacy for October and July days for EPRI Circuit 5.

5.4.4.2 Time Series Case Study II: EPRI K1

The solution for the EPRI K1 circuit is outlined in Figures 5.20 and 5.21. Analysis of each of these figures now follows, based on the comparison between Nominal control and Phase control.

Powers Figures 5.20a and 5.20b plot the power at the head of the feeder. The reduction in feeder load is not as great as compared to EPRI Circuit 5. Even in the July day, the generation is less than 50% of the feeder net load (and so even less than the total load). This is due to a larger fraction of commercial load in this feeder.

Voltages The maximum and minimum MV and LV voltages are plotted in Figures 5.20c and 5.20d. In this case, the taps allow for a much lower minimum voltage compared to EPRI Circuit 5.

The main difference between the solutions from the Nominal and Phase control is that the MV voltage for the circuit is consistently on the MV lower voltage constraint in the Phase control case. This is because the reactive power control allows for a much finer grained voltage reduction compared to only using taps.

Smart inverter benefits The benefits (in real power) of the smart inverters is plotted in Figures 5.20e and 5.20f. In this case, both the losses and load are mostly reduced throughout the day. The change in power compared to the Nominal case is

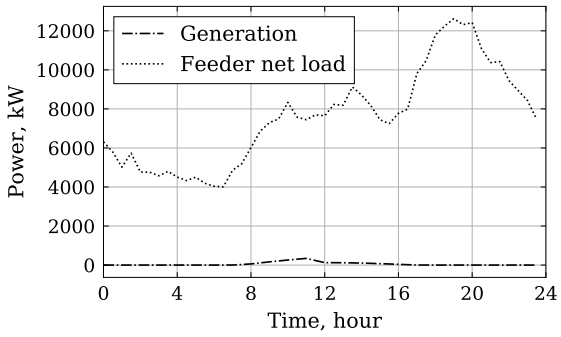

(a) Feeder powers - Oct. 15th

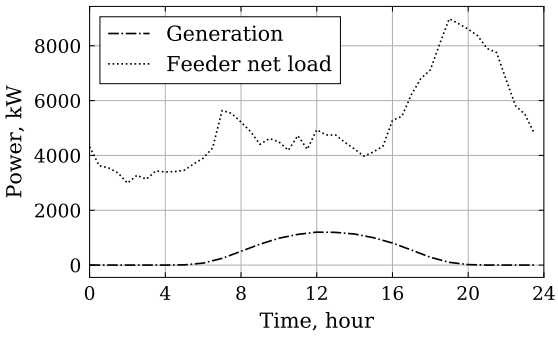

(b) Feeder powers - Jul. 20th

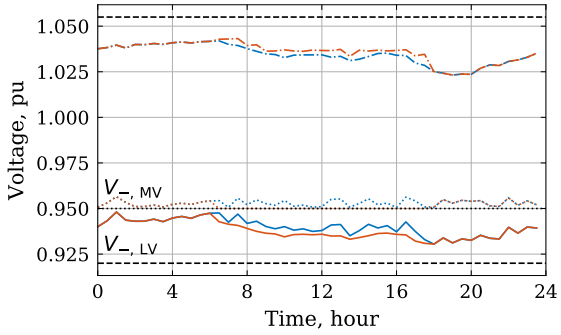

(c) MV and LV Voltages - Oct. 15th

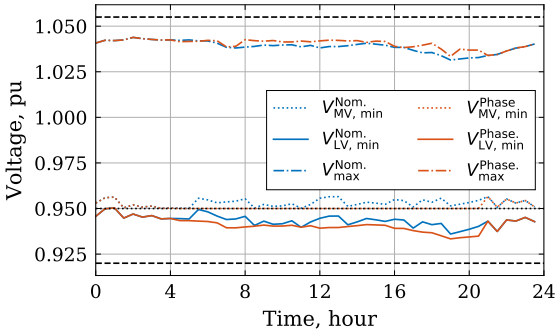

(d) MV and LV Voltages - Jul. 20th

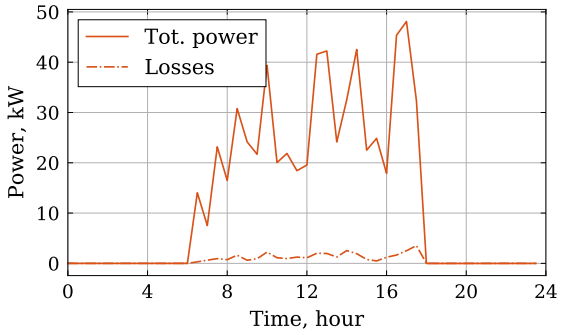

(e) Smart inverter power benefits - Oct. 15th

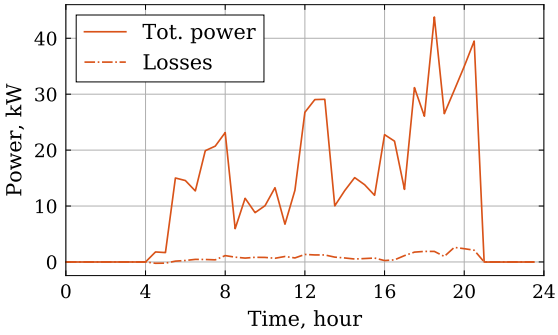

(f) Smart inverter power benefits - Jul. 20th

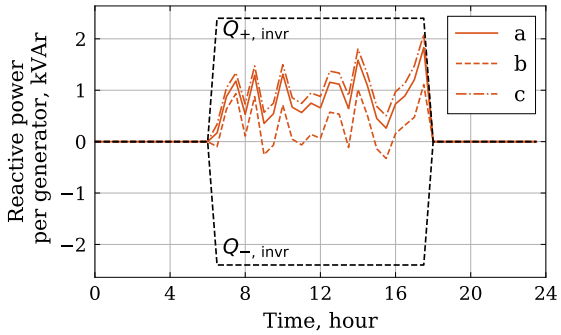

(g) Phase reactive power setpoints - Oct. 15th

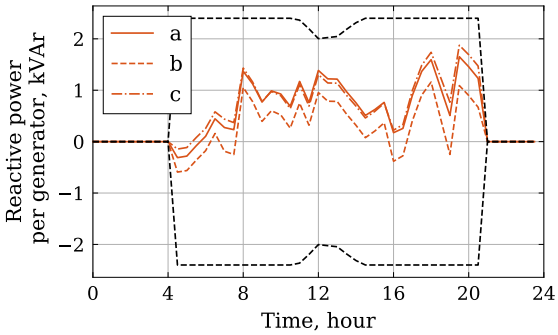

(h) Phase reactive power setpoints - Jul. 20th

Figure 5.20: Powers, voltages, benefits (in power) and phase control points for July and October days for the EPRI K1 circuit.

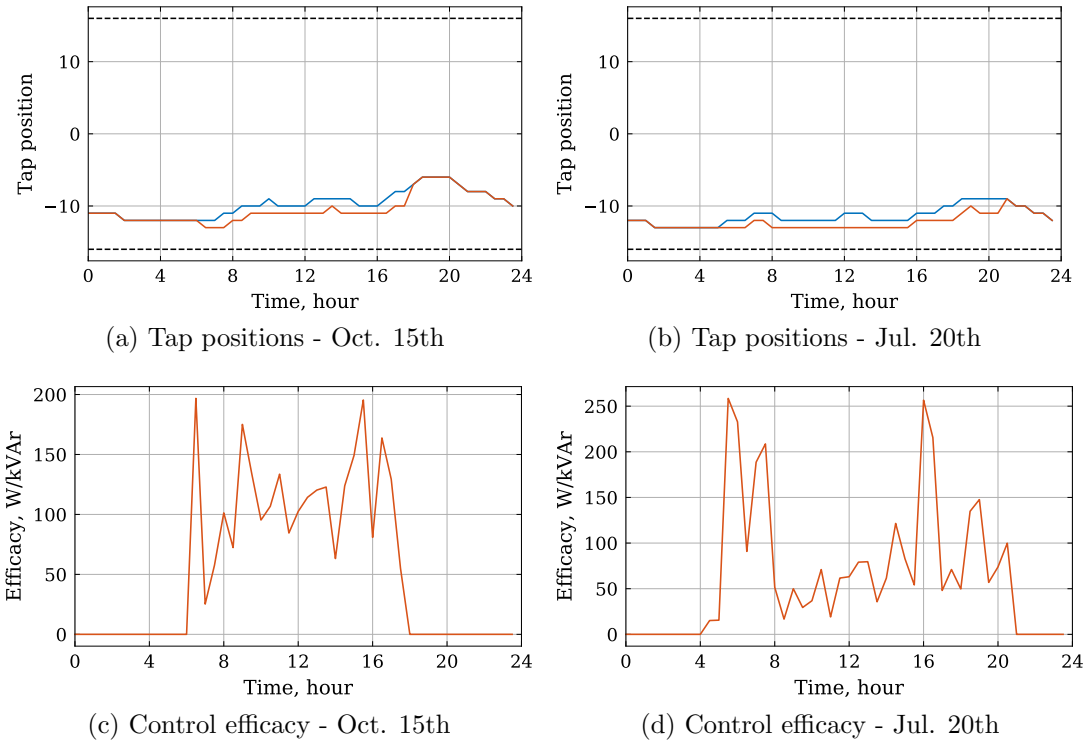

(a) Tap positions - Oct. 15th

(b) Tap positions - Jul. 20th

(c) Control efficacy - Oct. 15th

(d) Control efficacy - Jul. 20th

Figure 5.21: Tap position and control efficacy for October and July days for the EPRI K1 circuit.

relatively modest, being less than 1% of the total feeder power.

Phase reactive power The solution in reactive power of each phase are plotted in Figures 5.20g and 5.20h. In contrast to the EPRI 5 Circuit, reactive power injections are positive. That is, reactive power tends to be injected (capacitively) rather than being drawn (inductively) in EPRI Circuit 5. This is because the mechanism of power reduction is different: in this circuit, supporting the voltage at low-voltage nodes allows for the tap to be dropped across the whole circuit.

Tap positions The positions of taps are plotted in Figures 5.21c and 5.21d. The tap is lower in the case with smart inverter control. The difference in tap is between zero and two steps throughout the day.

Efficacy Finally, the efficacy of control is plotted in Figures 5.21c and 5.21d. Compared to the previous result, the efficacy of the reactive power is much greater, reach-

ing peaks of 250 W/kVAr.

5.4.4.3 Summary of Time Series Case Studies and Limitations of Approach

It has been demonstrated that there are considerable differences between the approach that uses reactive power in networks without regulators and those networks with regulators. There can clearly be benefits for using reactive power to reduce the total feeder demand. The costs of such a scheme (due to instrumentation, communications and power electronic capabilities) need to be considered carefully before it could be implemented in practise. This is particularly pertinent in systems where the marginal cost of power is low (for example, in a system dominated by solar or wind). In those cases, the peak power can instead be reduced if required as a means of acquiring flexibility.

For example, in the two cases considered above, the average energy saving per day was 170.4 kWh/day and 312 kWh/day for Circuit 5 and EPRI K1 respectively (compared to total loads of 69.2 MWh/day and 152.5 MWh/day respectively). This results in an average saving of 45.1 kWh per customer per year in the case of EPRI Circuit 5, and an average saving of 328.1 kWh per customer per year in EPRI K1. Wholesale day-ahead prices from the past 5 years have been between 30 and 70 £/MWh (on a 30 day moving-average basis) [194]. Energy savings would therefore be between £9.84 and £22.96 per customer per year for the EPRI K1 circuit and between just £1.35 and £3.16 per customer per year in the case for EPRI Circuit 5, if these prices are considered as indicative. The EPRI K1 circuit thus shows modest annual savings, whilst the savings for EPRI Circuit 5 are relatively small. It is likely that the inverter control would need to be remunerated for other benefits on top of the benefit considered here for it to prove economic to install this type of control. (This could include, for example, additional benefits due to peak demand reduction [116] or providing reactive power to the transmission system [195].)

5.5 Summary

In this chapter the following question has been considered:

How can the benefits of domestic-scale inverter reactive power control be evaluated with respect to minimising total power demand on a feeder, with load voltage sensitivity, inverter losses and distribution network losses taken into account?

There were three main contributions from this chapter. The first was a novel MI-QCQP optimization, with the innovation in the combination of inverter losses, load voltage sensitivity, and network losses in the cost function. The scalability of the optimization model is demonstrated on models with up to 9000 nodes. Both the control effort and cost reduction are demonstrated to be of interest in the solutions that are obtained. The accuracy of the MI-QCQP was demonstrated by comparing load flows solutions from both the MI-QCQP and OpenDSS at the optimization solution.

Using only tap controls to reduce voltages has been demonstrated to reduce the feeder load by up to 5%. Inverter functionality leads to further benefits, increasing the load reductions by up to 20%, with the difference in feeder load as much as 0.5%. The control efficacy (as the total savings per unit of reactive power) has been demonstrated to be as high as 240 W/kVAr in circuits with voltage regulators.

The second main contribution of this chapter is a proposed analytic method for studying if inverter losses need to be taken into account during optimizations of DG reactive powers, as these losses have been neglected in many previous works. It was demonstrated inverter losses needed to be taken into account in all circuits that were considered. This result is obtained by studying the spectral properties of the quadratic cost matrix of the optimization cost function. Load sensitivities were also shown to be larger than loss sensitivities in five of seven case studies, with these sensitivities acting in opposing senses to losses in all circuits that were studied.

The final contribution of this chapter is the proposed 'Phase' control method. This controls the reactive power output of all inverters on each phase identically.

This captures up to 97% of the benefits of 'full' inverter control of each individual inverter. Time series simulations using this control demonstrate modest benefits, reducing the total feeder power by 0.41-0.49% across two sample days.

Chapter 6

Conclusion

The main research question considered through this thesis was:

To what extent can inverter reactive power control, combined with voltage regulators, increase network efficiency and hosting capacity of distributed generation?

The research of this thesis was focussed on a range of challenges that future DSOs will face. Reactive power from DGs was identified as an asset that, if controlled appropriately, can be used to reduce curtailment, increase hosting capacity, and increase the efficiency of networks in which they operate.

Chapter roadmap Section 6.1 briefly concludes each of the three subquestions considered in each of Chapters 3-5, after which the conclusions to the main research question are drawn. Finally, promising areas for future research, based on the work undertaken in this thesis, are discussed in Section 6.2.

6.1 Conclusion of Research Questions

Chapter 3: Reactive Power, Curtailment and Losses Following the literature review, the first gap in literature was identified as follows.

There is currently no analytic method that considers the impact of reactive power

control by a distributed generator on energy losses across a wide range of network parameters and powers.

Chapter 3 addressed this gap by considering the research subquestion:

How can the impact of inverter reactive power control on the efficiency of distributed generation be analytically characterised, considering power flow up to the maximum power transfer point?.

Chapter 3 argues that the two-bus network model is ideal for the study of losses in this context.

The analytic properties of the maximum power transfer point were first considered for the two-bus network model. It was found that losses constrain the maximum power transfer, rather than stability constraints, when the impedance ratio (i.e., the R/X ratio) is greater than 0.7. It was demonstrated analytically that no reactive power should be used in purely resistive lines to try to increase generation.

Additionally, given that there are only two network parameters in the solution of the maximum power transfer problem (the impedance ratio and voltage ratio), the whole two-bus parameter space was explored. The thermal efficiency and power factors of the generation was studied, and it was demonstrated that both properties change rapidly when impedance ratios are between 0.6 and 3.

A method to convert an unbalanced network to a two-bus model was proposed, so that the analytic predictions of the two-bus model can be validated on real distribution network models. Calculations on the 34 Bus circuit demonstrated that there is a good correspondence between the model that is derived and the two-bus solution, with the relative difference between predicted solutions being less than 15% at the maximum power transfer point. This demonstrates that the two-bus model can make reasonable predictions even up to the maximum power transfer point.

The impact of reactive power control on the generation efficiency of a distributed generator was considered in the second half of Chapter 3. To study how the efficiency is impacted by voltage control, the 'relative energy loss fraction' was proposed. This

calculates the ratio of the differences between losses and generation, when reactive power is enabled (or the amount available is increased).

Bounds on the relative energy loss fraction are determined using the LinDistFlow load flow solution. There are four parameters that are shown to impact on these bounds: the reactive power before (and after) the additional control is activated; the voltage drop; and the impedance ratio.

These analytic bounds were validated in two steps. Firstly, the calculations were compared against the values calculated with the exact two-bus solution. The accuracy of the model was shown to be valid, under the condition that the increase in generation was below 20% of the potential maximum generation gain that could be realised (from a point of zero reactive power use). Beyond this point the simple LinDistFlow analytic solution could be inaccurate, and it is recommended that the exact load flow solution is used.

The second validation considered the relative energy loss fraction for six case studies (from three unbalanced networks). The absolute error between the true bounds and the LinDistFlow bounds is less than 5% in all cases. It is demonstrated that, in the extreme case considered, if losses were ignored then reactive power would be overvalued by 30%.

To conclude this first question: the two-bus model is a very good analytic model for studying the impacts of distributed generation and reactive power on losses. The Exact load flow solution provides the most accurate calculations, but the large number of terms makes interpretability challenging. On the other hand, the LinDistFlow solution introduces some error in calculations, but the algebraic simplicity makes it easier to interpret, and so at low powers this model can be used.

Chapter 4: Reactive Power and Stochastic Hosting Capacity The second gap in the literature was identified as follows.

At present, there is no method of calculating stochastic hosting capacity values of distribution networks in a computationally efficient manner, taking into account

both legacy voltage regulation equipment and reactive power control by distributed generators.

Chapter 4 addressed this gap by considering the research subquestion:

How can the stochastic hosting capacity of a distribution network be calculated in a computationally efficient manner, considering voltage regulators and reactive power control from distributed generators?

In Chapter 4, it is argued that a linear model is very well suited to answering this question, as linear models are fast and amenable to the tools of linear algebra (which are subsequently used to further improve computational efficiency).

The proposed model takes into account the reactive power of domestic generators, voltage regulators (including line drop compensation), and can consider DERMS-style regulator and reactive power control. It was shown that in many cases hosting capacity constraints can be completely cleared if regulator and power factor controls can be specified appropriately.

Three benefits of a linear model are demonstrated. Firstly, the statistics (mean and covariance) of bus voltages can be calculated in closed form, leading to immediate insights as to the areas of a network that are the weakest. These statistics also have been demonstrated to be able to reduce the computation burden, by removing buses from calculations if the likelihood of a constraint violation is very low.

Secondly, sensitivity analysis can be carried out efficiently using the linear model. This allows a network operator to determine how much the solution will change if, for example, the parameters of the assumed PDFs of generator sizes are incorrect. The sensitivities are also shown to correlate well with the error between the true (non-linear) and approximate (linear) solutions.

Finally, the linear model is extremely fast at calculating the hosting capacity. In fact, the time to calculate was shown to be less than 10 seconds even for the largest networks (compared to over an hour for the non-linear detailed method). The huge increase in computational speed makes it practical for stochastic hosting capacity

studies to carried out as a routine task by a DSO.

Therefore, it is concluded that linear models can be used to calculate the stochastic hosting capacity of a distribution network efficiently. Both voltage regulators and reactive power control can be incorporated into the calculations, each of which have a significant impact on the hosting capacity value that is obtained.

Chapter 5: Reactive Power for Reducing Total Feeder Demand Chapter 5 considered the third and final gap that was identified in the literature review.

There is no scalable method that considers the potential for domestic-scale inverter reactive power control to reduce total feeder demand, taking into account load voltage sensitivity, inverter losses and distribution network losses.

Chapter 5 addressed this gap by considering the research subquestion:

How can the benefits of domestic-scale inverter reactive power control be evaluated with respect to minimising total power demand on a feeder, with load voltage sensitivity, inverter losses and distribution network losses taken into account?

Chapter 5 approaches this problem using a MI-QCQP. This has advantages of being efficient to calculate, as there are few integer variables in the problem considered.

In contrast to the previous chapter, a Taylor-series based method was chosen for the linearization, to increase the accuracy of the calculation of the gradient at the linearization point. From the load flow linearization, all other required quantities (voltages, currents, losses and load) are calculated.

Previous works do not consider the inverter losses, network loss and load voltage response. This chapter proposes a novel analytic approach to demonstrate that each of these quantities are necessary for the solution to be accurate. It is demonstrated that, in all case studies, there would be at least a 5% difference in the solution if the inverter losses were ignored (in some cases change in cost function was over 50%).

Both networks with and without voltage regulators are studied. It is found that the operating modes of the inverters in these two types of circuit are different. For

circuits with no voltage regulators, inverters tended to draw inductive reactive power, to depress the voltage so that loads were reduced. On the other hand, where there were regulators, inverters tended to export capacitive reactive power, such that tap positions could be reduced to lower voltages (and thus loads) without impacting line losses too much.

To conclude, the proposed method utilising a MI-QCQP is well-suited to studying the potential benefits of domestic reactive power. The benefits of domestic-scale inverter reactive power can reduce feeder power by 0.5% of load, although it is worth noting that this number is sensitive to assumptions about inverter sizes and voltage-load sensitivity values.

6.1.1 Conclusions of Thesis Research Question

All three chapters of this thesis shed a different light on the main research question. Chapter 3 demonstrates that benefits of inverter reactive power control are bounded by a maximum power transfer limit, which is driven by losses in some networks. This illustrates a tension between increasing hosting capacity and increasing network efficiency. When the question is viewed from the point of maximising the hosting capacity, inverter reactive power control can increase the hosting capacity until the marginal losses equal the marginal increases in generation, or when a stability condition is hit, whichever is encountered first.

This point is further demonstrated in the second half of Chapter 3, which considers the relative energy loss fraction. All of the networks studied demonstrated an increase in losses when reactive power was used for voltage control. The fraction of losses was as high as 30% in a high penetration scenario.

It is interesting to note that voltage regulators have a large impact on the relative loss fraction that is seen when reactive power is introduced, because the power at which the voltage constraint becomes active is higher. For example, energy losses increased from 13% to 30% in simulations in the 34 Bus circuit, with the same amount of reactive power, but with an additional voltage regulator control enabled. This

illustrates that the 'attribution' of losses to reactive power can only be done in a limited sense. Nevertheless, it is demonstrated that losses tend to reduce the benefits of reactive power control by a significant margin.

Chapter 4 focuses on the research question from the point of view of domestic hosting capacity of PV. It is shown that the hosting capacity can be completely cleared in some cases by utilising fixed power factor control of DGs. The DERMS-style feasibility problem is attractive in this setting, because it allows a DSO to determine that a network upgrade will be necessary (or, that some flexibility will have to be identified from an alternative source), irrespective of tap and reactive power setpoints.

The approach of the final technical chapter complements the view taken in the previous two chapters, considering the research question from the point of view of increasing efficiency by reducing the total feeder power. Voltage regulators show a reasonable benefit of 2-5% reduction in total feeder load–enabling this control may cause an increase in tap wear, however. The average per-inverter benefits can be as high as 240 W/kVAr. In practise it might be the case that just a small number of judiciously-placed smart inverters could act to allow regulators to step down a tap, benefiting all customers. The modest increase in efficiency (up to 0.5%) from activating the smart inverter functionality for reducing feeder demand may or may not be justified.

Taking the work of the three chapters together, it is concluded that typically hosting capacity is improved more than network efficiency by the introduction of inverter reactive power control. Voltage regulators, however, show good benefits with respect to both increasing hosting capacity and reducing total feeder demand. Together, voltage regulators and inverters can interact to reduce feeder voltages, for increased CVR savings and increased DG hosting capacity.

Altogether, this work has provided a new suite of tools that could help a DSO analyse, plan and operate distribution networks with inverter-based reactive power control. The scalable methods considered in this work are an important step towards

successfully moving towards a fully decarbonised electricity system, with high penetrations of power-electronics interfaced DERs and DGs, managed in real time by a DSO.

6.2 Future Work

In this final section, four future research directions are considered, based on the work carried out in this thesis.

6.2.1 Losses and Curtailment: Distributed Droop Control

"How do a large number of domestic-scale PV inverters with distributed voltage control impact on losses?"

Chapter 3 considered the simplest analytic network model (the two-bus model), and it was demonstrated that reactive power control in networks with high R/X ratios and a large voltage rise is less effective. The result is that it appears that residential locations are not well suited to voltage control with respect to losses. An analytic model could be considered to study the impact of network parameters, including realistic residential wiring impedances and inverter loss characteristics, using a differential feeder model [77, Ch. 3]. The impact of reactive current on the losses and curtailment in such a model could be considered analytically, using either droop-style control or by finding the optimal reactive power to minimize losses. This should then be validated on large-scale networks with droop control at a large fraction of loads.

6.2.2 Stochastic Hosting Capacity: Load Flow Calculation Errors

"Can stochastic hosting capacity values be calculated in a computationally efficient way, with a guaranteed (or user-specified) error?"

The error of the linearization method of Chapter 4 was studied empirically. Previous works have determined power flow linearizations with error properties that can be calculated analytically (e.g., [196]). The results of hosting capacity calculations using a linearization (or other approximate solution method) could be made much more robustly if guarantees on the error could be determined *a priori*. It would be particularly powerful if the hosting capacity calculation error could in fact be specified explicitly by a user (which could then determine the number of steps for an iterative method, for example).

6.2.3 Stochastic Hosting Capacity: Robustness to Tap Bandwidth and Load Uncertainty

"How does uncertainty in voltage regulator tap and load impact on stochastic hosting capacity curves?"

One of the key assumptions made in hosting capacity analysis is the known load and tap positions. If, however, there is a wide voltage regulator bandwidth then it may be that the tap may not be in the position assumed in the load flow calculation, leading to a higher or lower hosting capacity value. Accounting for this in the optimization would lead to a more robust estimate of the hosting capacity. Similarly, the impact of uncertainty in load could be accounted for within the analysis.

6.2.4 Volt-Var control: Value Stacking

"How can smart inverters provide the greatest value to power systems as a whole?"

The final chapter demonstrated that in many networks the benefits of reactive power for reducing total feeder demand are modest. The benefits of reactive power control can include the minimization of tap switches, reactive power support to the transmission network and curtailment avoidance. Additionally, some inverters can provide reactive power even when they are not generating (i.e., at night). By 'value

stacking' the benefits of inverter reactive power control, the highest possible benefit could be achieved for these assets.

Appendix A

Derivations and Supporting Results

A.1 Two-Bus Derivations (Chapter 3)

Impedance angles θ_Z and the R/X ratio λ are linked by the following identities:

$$\frac{R}{|Z|} = \frac{\lambda}{\sqrt{1+\lambda^2}} = \cos(\theta_Z)\,, \qquad \frac{X}{|Z|} = \frac{1}{\sqrt{1+\lambda^2}} = \sin(\theta_Z)\,. \tag{A.1}$$

A.1.1 Two-bus Load Flow Solution

To find the load flow solution, note that the voltage drop across an impedance Z with current I_Z is given by $(V_{\text{Snd}} - V_{\text{Rcv}}) = I_Z Z$, implying that the sent power $S_{\text{Snd}} = V_{\text{Snd}} I_Z^*$ is given by

$$S_{\text{Snd}} = \frac{1}{Z^*} V_{\text{Snd}} \left(V_{\text{Snd}}^* - V_{\text{Rcv}}^*\right)\,. \tag{A.2}$$

Rearranging and taking squared magnitudes of each side yields

$$|V_{\text{Snd}}|^2 |V_{\text{Rcv}}|^2 = |V_{\text{Snd}}|^4 - 2\Re\left(Z^* S_{\text{Snd}}\right) |V_{\text{Snd}}|^2 + |Z|^2 |S_{\text{Snd}}|^2\,, \tag{A.3}$$

finally yielding the quadratic in V_{Snd}

$$|V_{\text{Snd}}|^4 - |V_{\text{Snd}}|^2 \left(|V_{\text{Rcv}}|^2 + 2\left(P_{\text{Snd}}R + Q_{\text{Snd}}X\right)\right) + |Z|^2|S_{\text{Snd}}|^2 = 0\,, \tag{A.4}$$

which can be solved to find (3.3). The losses, given by $P_{\text{lss}} = R|I_Z|^2$, can be written

$$P_{\text{lss}} = \frac{R}{|Z|^2}|V_{\text{Snd}} - V_{\text{Rcv}}|^2\,. \tag{A.5}$$

Noting that $V_{\text{Snd}}V_{\text{Rcv}}^*$ is given in terms of S_{Snd} in (A.2), (A.5) can be rewritten

$$P_{\text{lss}} = \frac{R}{|Z|^2}\left(|V_{\text{Rcv}}|^2 - |V_{\text{Snd}}|^2 + 2(P_{\text{Snd}}R + Q_{\text{Snd}}X)\right)\,. \tag{A.6}$$

Substituting (3.3) into (A.6) yields (3.4).

The identity (3.8) comes directly from (A.6), whilst (3.9) can be found by expanding (A.4) and completing the square.

A.1.2 Power at the Stability Boundary

When $D = 0$ in (3.3), the following identities can be written down:

$$\frac{\lambda P_{\text{Snd}} + Q_{\text{Snd}}}{S_{\text{SC}}\sqrt{1+\lambda^2}} = \frac{|V_{\text{Snd}}|^2}{S_{\text{SC}}|Z|} - \frac{1}{2}\,, \tag{A.7}$$

$$\frac{P_{\text{Snd}} - \lambda Q_{\text{Snd}}}{S_{\text{SC}}\sqrt{1+\lambda^2}} = \sqrt{\frac{\lambda P_{\text{Snd}} + Q_{\text{Snd}}}{S_{\text{SC}}\sqrt{1+\lambda^2}} + \frac{1}{4}}\,. \tag{A.8}$$

Adding and rearranging yields

$$\frac{P_{\text{Snd}}\sqrt{1+\lambda^2}}{S_{\text{SC}}} = \lambda\left(\frac{|V_{\text{Snd}}|^2}{S_{\text{SC}}|Z|} - \frac{1}{2}\right) + \sqrt{\frac{|V_{\text{Snd}}|^2}{S_{\text{SC}}|Z|} - \frac{1}{4}}\,. \tag{A.9}$$

But, from (A.7) and (3.4),

$$P_{\text{lss}} = \frac{\lambda}{\sqrt{1+\lambda^2}}\frac{|V_{\text{Snd}}|^2}{|Z|}\,. \tag{A.10}$$

To find (3.13), use the identity $P_{\text{Rcv}} = P_{\text{Snd}} - P_{\text{lss}}$, substituting (A.9), (A.10).

A.1.3 Derivation of Maximum Power Transfer

If the voltage angle at the sending node is θ_V and the complex argument of impedance Z is given by θ_Z then the following relations hold [81]:

$$P_{\text{Snd}} = S_{\text{SC}} \frac{|V_{\text{Snd}}|}{|V_{\text{Rcv}}|} \left(\frac{\lambda}{\sqrt{1+\lambda^2}} \frac{|V_{\text{Snd}}|}{|V_{\text{Rcv}}|} - \cos(\theta_V + \theta_Z) \right) \tag{A.11}$$

$$P_{\text{Rcv}} = S_{\text{SC}} \frac{|V_{\text{Snd}}|}{|V_{\text{Rcv}}|} \left(-\frac{\lambda}{\sqrt{1+\lambda^2}} \frac{|V_{\text{Snd}}|}{|V_{\text{Rcv}}|} + \cos(\theta_V - \theta_Z) \right) \tag{A.12}$$

$$Q_{\text{Snd}} = S_{\text{SC}} \frac{|V_{\text{Snd}}|}{|V_{\text{Rcv}}|} \left(\frac{1}{\sqrt{1+\lambda^2}} \frac{|V_{\text{Snd}}|}{|V_{\text{Rcv}}|} - \sin(\theta_V + \theta_Z) \right) \tag{A.13}$$

$$Q_{\text{Rcv}} = S_{\text{SC}} \frac{|V_{\text{Snd}}|}{|V_{\text{Rcv}}|} \left(\frac{1}{\sqrt{1+\lambda^2}} \frac{|V_{\text{Snd}}|}{|V_{\text{Rcv}}|} + \sin(\theta_V - \theta_Z) \right) . \tag{A.14}$$

Therefore, the voltage angle at which there is the maximum received power is when $\theta_V = \theta_Z$. Substituting this yields all powers.

A.1.4 Upper and Lower Bounds of Relative Loss Significance

In this section, the aim is to show that the relative loss fraction increases monotonically as curtailment is reduced along lines of constant voltage.

Using the identities $d/dP_{\text{Snd}}(\Delta P_{\text{net}}) = 1 - dP_{\text{lss}}/dP_{\text{Snd}}$ and $\Delta P_{\text{net}} = \Delta P_{\text{gen}} - \Delta P_{\text{lss}}$, differentiating (3.35) yields

$$\frac{d\epsilon_{\text{P}}}{dP_{\text{Snd}}} = \frac{1}{\Delta P_{\text{Snd}}} \left(\frac{dP^{\text{V}}_{\text{lss}}}{dP_{\text{Snd}}} - \frac{\Delta P_{\text{lss}}}{\Delta P_{\text{Snd}}} \right) . \tag{A.15}$$

Next, from (3.4) it can be observed that

$$\frac{d^2 P^{\text{V}}_{\text{lss}}}{dP^2_{\text{Snd}}} = \frac{\lambda}{1+\lambda^2} \frac{d^2 Q^{\text{V}}_{\text{Snd}}}{dP^2_{\text{Snd}}} , \tag{A.16}$$

but, as $Q^{\text{V}}_{\text{Snd}}$ is defined on the lower half of the circle (i.e. with positive curvature

with respect to P_{Snd}), it is therefore noted that

$$\frac{d^2 P_{\text{lss}}^{\text{V}}}{dP_{\text{Snd}}^2} > 0\,. \tag{A.17}$$

(This condition also trivially holds for the LinDistFlow model.) Considering the definition of a derivative, this demonstrates that

$$\frac{\Delta P_{\text{lss}}(P_{\text{Snd}}+\delta)}{\delta} < \frac{\Delta P_{\text{lss}}(P_{\text{Snd}}+\delta+\epsilon)}{(\delta+\epsilon)} < \frac{\Delta P_{\text{lss}}(P_{\text{Snd}}+\delta+\epsilon)}{\epsilon}\,, \tag{A.18}$$

for $\delta, \epsilon > 0$. Re-writing (A.15) as

$$\frac{d\epsilon_{\text{P}}}{dP_{\text{Snd}}}(P_{\text{Snd}}^{\text{X}}+\delta) = \frac{1}{\Delta P_{\text{Snd}}}\left(\frac{dP_{\text{lss}}}{dP_{\text{Snd}}}(P_{\text{Snd}}^{\text{X}}+\delta) - \frac{\Delta P_{\text{lss}}(P_{\text{Snd}}^{\text{X}}+\delta)}{\Delta P_{\text{Snd}}}\right) \tag{A.19}$$

$$= c_1\left(\frac{dP_{\text{lss}}}{dP_{\text{Snd}}}(P_{\text{Snd}}^{\text{X}}+\delta) - \frac{\Delta P_{\text{lss}}(P_{\text{Snd}}^{\text{X}}+\delta)}{\delta}\right) \tag{A.20}$$

$$= c_1 c_{\text{Rcv}}\,, \tag{A.21}$$

with $c_1(P_{\text{Snd}}) > 0$. Then:

$$c_{\text{Rcv}} = \lim_{\epsilon\to 0}\left(\frac{\Delta P_{\text{lss}}(P_{\text{Snd}}^{\text{X}}+\delta+\epsilon)}{\epsilon}\right) - \frac{\Delta P_{\text{lss}}(P_{\text{Snd}}^{\text{X}}+\delta)}{\delta}\,. \tag{A.22}$$

However, by (A.18) it is known that $c_{\text{Rcv}} > 0$, and as such, it can be concluded the gradient of ϵ_{P}, (A.15), is always positive for $P_{\text{Snd}} \in (P_{\text{Snd}}^{\text{X}}, P_{\text{Snd}}^{\text{MPT}}]$ (where $P_{\text{Snd}}^{\text{MPT}}$ denotes the power at the maximum power transfer point); as such, ϵ_{P} monotonically increases. Finally, the reasoning defining (3.36) combined with this monotonicity property implies that (3.44), (3.46) hold.

A.1.5 LinDistFlow Relative Loss Fractions

To calculate the desired result, first note that along lines of constant voltage

$$P^{\mathrm{V}}_{\mathrm{Snd}} = \frac{|V_{\mathrm{Snd}}|^2 - |V_{\mathrm{Rcv}}|^2 - Q_{\mathrm{Snd}}X}{R} \tag{A.23}$$

$$Q^{\mathrm{V}}_{\mathrm{Snd}} = \frac{|V_{\mathrm{Snd}}|^2 - |V_{\mathrm{Rcv}}|^2 - P_{\mathrm{Snd}}R}{X}\,. \tag{A.24}$$

Substituting $Q^{\mathrm{V}}_{\mathrm{Snd}}$ into the losses (3.7) yields the voltage-constrained losses $P^{\mathrm{V}}_{\mathrm{lss}}$ as

$$P^{\mathrm{V}}_{\mathrm{lss}} = \frac{R}{|V_{\mathrm{Snd}}|^2}(1+\lambda^2)P^2_{\mathrm{Snd}} + P_{\mathrm{Snd}}\lambda^2\left(1 - \frac{|V_{\mathrm{Rcv}}|^2}{|V_{\mathrm{Snd}}|^2}\right) - \frac{S_{\mathrm{SC}}\lambda\sqrt{1+\lambda^2}}{4}\left(1 - \frac{|V_{\mathrm{Rcv}}|^2}{|V_{\mathrm{Snd}}|^2}\right)^2. \tag{A.25}$$

By finding the difference between the losses at a 'base' and 'change' case, the first expression for ϵ_{P} is calculated as (3.49). Then, to derive the value as calculated using the reactive power, substitute in (A.23).

A.1.6 Loss-Minimizing Two-Bus Reactive Power

The aim of this section is to show that the optimal reactive power in the two-bus circuit is generally non-zero and positive. Differentiating (3.4) with respect to Q_{Snd} yields

$$\frac{\sqrt{1+\lambda^2}}{S_{\mathrm{SC}}\lambda}.\frac{dP_{\mathrm{lss}}}{dQ_{\mathrm{Snd}}} = \frac{1}{S_{\mathrm{SC}}\sqrt{1+\lambda^2}} - \frac{1}{2D}\frac{d(D^2)}{dQ_{\mathrm{Snd}}}\,. \tag{A.26}$$

Setting to zero and rearranging yields the quadratic

$$\frac{R}{X}Q^2_{\mathrm{Snd}} - \left(2P_{\mathrm{Snd}} + \frac{V^2_{\mathrm{Rcv}}}{R}\right)Q_{\mathrm{Snd}} + \frac{X}{R}P^2_{\mathrm{Snd}} = 0\,. \tag{A.27}$$

The optimal root is the smaller of the two roots, is denoted by $Q^{\mathrm{L}}_{\mathrm{Snd}}$, and is given by

$$Q^{\mathrm{L}}_{\mathrm{Snd}} = \frac{1}{\lambda}\left((P_{\mathrm{Snd}} + c_{\mathrm{P}}) - \sqrt{(P_{\mathrm{Snd}} + c_{\mathrm{P}})^2 - (P_{\mathrm{Snd}})^2}\right), \tag{A.28}$$

where $c_{\mathrm{P}} = V^2_{\mathrm{Rcv}}/2R$

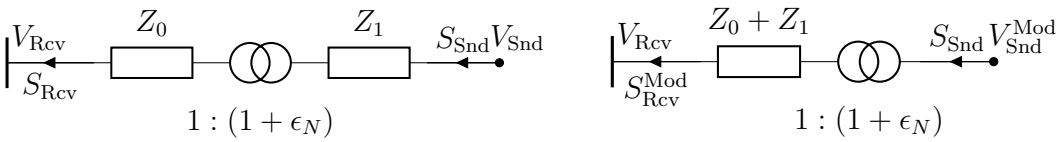

(a) 'True' two-bus model with regulator

(b) 'Proposed' simplified two-bus model with regulator

Figure A.1: The 'True' and 'Proposed' two-bus models with regulators the latter approximates the former by moving the regulator to the generator. The 'Base' model is the same as the 'Proposed' model but with the turns ratio set to unity, i.e., $\epsilon_N = 1$

A.1.7 The Loss-Voltage Crossover Point

The aim of this section is to demonstrate that the loss-voltage crossover point is quartic (so it is not practical to study the solution algebraically). The voltage constrained reactive power curve $S^{\text{V}}_{\text{Snd}}$ can be found from (3.53), and $S^{\text{L}}_{\text{Snd}}$ is found from (A.28). The crossover point $S^{\text{X}}_{\text{Snd}}$ occurs at the intersection of the these curves. Set $Q^{\text{L}}_{\text{Snd}} = Q^{\text{V}}_{\text{Snd}}$, which yields a polynomial of the form

$$\alpha(P_{\text{Snd}}) + \sqrt{\beta(P_{\text{Snd}})} = \sqrt{\gamma(P_{\text{Snd}})}\,, \tag{A.29}$$

where α is a polynomial of order 1, and β, γ are of order 2. This is therefore rationalised as a quartic polynomial, as

$$\alpha^2 \left(\alpha^2 - 2(\beta + \gamma)\right) + \beta^2 + \gamma^2 - 2\beta\gamma = 0\,. \tag{A.30}$$

This completes the proof.

A.1.8 Inclusion of Voltage Regulators in the Two-Bus Model

The aim in this section is to show that using the proposed method of including mid-feeder voltage regulators leads to reasonable two-bus model (see Figure A.1). The necessity of the model, and its accuracy, are now demonstrated by proving the following points.

(E1) Ignoring voltage regulators leads to a zeroth-order error in voltage drop.

(E2) Using the proposed method (appending regulators at the end of the feeder) leads to a first-order error in calculations of voltage drop.

(E3) Using the proposed method leads to a first-order relative error in the calculation of losses.

The first two points are important as the voltage drop determines the point at which the two-bus method reaches a constraint, and so must be calculated to a reasonable degree of accuracy. The losses must also be estimated accurately as they are required to be calculated explicitly for the relative loss fraction (Section 3.6). These models are studied using the LinDistFlow solution, as this provides linear expressions of squared voltage magnitudes in powers, and is therefore more accurate than considering voltage magnitudes in isolation [141].

Firstly, consider the voltages in the circuits as given by the LinDistFlow solution:

$$|V_{\text{Snd}}^{\text{Base}}|^2 = |V_{\text{Rcv}}|^2 \left(1 + \delta_0 + \delta_1\right) , \tag{A.31}$$

$$|V_{\text{Snd}}^{\text{True}}|^2 = |V_{\text{Rcv}}|^2 \frac{1 + \delta_0 + \delta_1(1+\epsilon_N)^2}{(1+\epsilon_N)^2} , \tag{A.32}$$

$$|V_{\text{Snd}}^{\text{Proposed}}|^2 = |V_{\text{Rcv}}|^2 \frac{1 + \delta_0 + \delta_1}{(1+\epsilon_N)^2} , \tag{A.33}$$

where the notation

$$\delta_\chi = \frac{2(P_{\text{Snd}} R_\chi + Q_{\text{Snd}} X_\chi)}{|V_{\text{Rcv}}|^2} \tag{A.34}$$

has been utilised for clarity and conciseness, and the Proposed and True models are shown explicitly in Figure A.1. Note additionally that the magnitude of δ_χ and ϵ_N must be similar for the regulator to have a reasonable impact on voltage drop, but that voltage drop is also typically much smaller than unity. This can be summarised as

$$\epsilon_N \ll 1 , \qquad \delta_\chi \ll 1 , \qquad \epsilon_N \approx \delta_\chi , \tag{A.35}$$

where $\approx$ is used to indicate that two numbers are of the same order of magnitude.

The true squared 'voltage drop' is given by

$$|V_{\text{Snd}}^{\text{True}}|^2 - |V_{\text{Rcv}}|^2 = |V_{\text{Rcv}}|^2 \frac{(2\epsilon_N + \epsilon_N^2) + \delta_0 + \delta_1(1+\epsilon_N)^2}{(1+\epsilon_N)^2}\,, \tag{A.36}$$

with this of the same order of magnitude as the regulation ϵ_N (assuming per-unit voltages close to unity).

(E1) is demonstrated by taking the difference between (A.31) and (A.32); the error is

$$|V_{\text{Snd}}^{\text{Base}}|^2 - |V_{\text{Snd}}^{\text{True}}|^2 = |V_{\text{Rcv}}|^2 \frac{(2\epsilon_N + \epsilon_N^2) + \delta_0(2\epsilon_N + \epsilon_N^2)}{(1+\epsilon_N)^2}\,. \tag{A.37}$$

Comparing terms in (A.37), and (A.36), the error is observed to be zeroth order (i.e. of the same order as the voltage drop itself). This demonstrates the necessity of the inclusion of the regulator in the model.

Showing (E2) is found by taking the difference between (A.33) and (A.32); the difference here is

$$|V_{\text{Snd}}^{\text{Proposed}}|^2 - |V_{\text{Snd}}^{\text{True}}|^2 = |V_{\text{Rcv}}|^2 \frac{\delta_1(2\epsilon_N + \epsilon_N^2)}{(1+\epsilon_N)^2}\,. \tag{A.38}$$

This represents a first-order error; this is due to the multiplication of the ϵ_N and δ_χ terms, both of which are much smaller than unity (but of a similar magnitude to the aggregate voltage drop).

Finally, to show (E3), first note that the losses calculated by the LinDistFlow models can be calculated as

$$P_{\text{Lss}}^{\text{True}} = \left(R_1 + \frac{R_0}{(1+\epsilon_N)^2}\right) \frac{P_{\text{Snd}}^2 + Q_{\text{Snd}}^2}{|V_{\text{Snd}}|^2}\,, \tag{A.39}$$

$$P_{\text{Lss}}^{\text{Proposed}} = (R_0 + R_1) \frac{P_{\text{Snd}}^2 + Q_{\text{Snd}}^2}{(1+\epsilon_N)^2 |V_{\text{Snd}}|^2}\,. \tag{A.40}$$

Taking the ratio of these two equations (to find the relative error) yields the result.

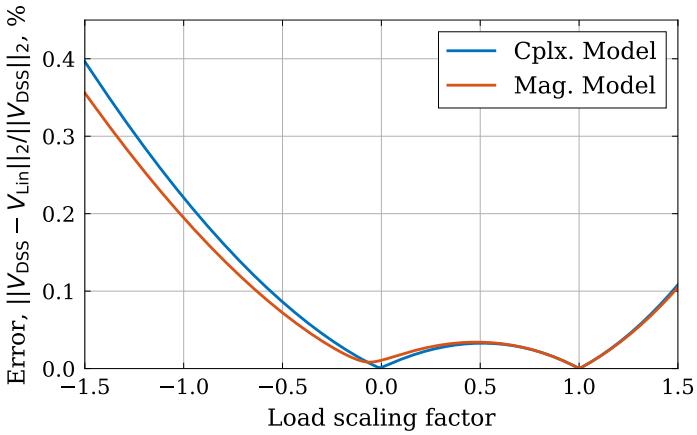

Figure A.2: IEEE 37 Bus network case study.

A.2 Fixed Point Linearization: Validation and Computational Complexity (Chapter 4)

A.2.1 Validation of Load Flow Linearization

To ensure that the model was working as expected, the linearization was repeated for one of the case studies of [139]. Admittance matrices for each circuit are obtained from OpenDSS [197]. At each load flow solution point the relative error was calculated (for the linear compared to non-linear solution), using the ratio of the 2-norm of the voltage magnitude vectors. The linearization error is plotted in Figure A.2, and the errors seen at the extreme points of (-1.5, 1.5) match the errors calculated in the previous work.

There are a number of things to note about the plotted error curves.

- The complex load flow linearization solution shows a characteristic w-shape curve, with zero error at the linearization point and at the no-load point (at the 0% load point).
- The magnitude load flow linearization solution follows the error of the complex load flow solution closely, although it noticeably does not go to zero at the no-load point.

Table A.1: Sparsity properties of nine admittance matrices, and the corresponding time required to build the linear model, t_{Lin}.

Feeder	$\text{nnz}(Y_{\text{bus}})$	$\frac{\text{nnz}(Y_{\text{bus}})}{N_V^2}$, %	t_{Lin}, s	$\frac{t_{\text{Lin}} \times 10^7}{\text{nnz}(Y_{\text{bus}})N_V}$
34 Bus	804	7.43	0.03	3.59
123 Bus	2038	2.42	0.11	1.86
Ckt. K1	9310	0.30	1.83	1.12
Ckt. J1	19679	0.11	12.89	1.55
Ckt. M1	13731	0.14	5.15	1.20
Ckt. 5	13917	0.12	6.07	1.28
Ckt. 7	17223	0.29	6.30	1.50
8500 Node	46325	0.06	60.72	1.49
Ckt. 24	33714	0.06	42.66	1.69

A.2.2 Complexity of Linearization

To consider the computational complexity of the Fixed Point linear model, the time taken to calculate the linearization is recorded for nine networks alongside the number of non-zero elements ($\text{nnz}(\cdot)$), the sparsity fraction and the time taken to compute the linear model (Table A.1).

The time required to calculate the linear model becomes quite significant for the largest networks, although only just over one minute for the largest network (times are close to matching those seen in [139]). Dividing the time required by the number of nonzero elements of the Y_{bus} and the admittance matrix dimension N_V yields a value that is consistently between 1.1 and 1.9 $\times 10^{-7}$ (except for the 34 bus network, which is much smaller than the other models). In other words, the solution appears to be approximately linear in matrix dimension and in the number of nonzero elements.

A.3 The Semidefiniteness of Quadratic Models in Losses (Chapter 5)

A.3.1 Physical Basis for Semidefinite Quadratic Loss Matrix

It is interesting to note that, in the case of the general quadratic matrices with delta loads, the quadratic matrix sometimes contains zero singular values. By substituting (5.4) and considering an appropriate incidence matrix $\Pi_{\text{branch}} \in \mathbb{R}^{N_{\text{bus}} \times N_{\text{branch}}}$ (to convert from bus voltages to branch voltages) the quadratic loss matrix $\Theta_{\text{lss, ntwk}}$ is given by

$$\Theta_{\text{lss, ntwk}} = x^{\intercal} \Re \left(M_x^{\intercal} \Pi_{\text{branch}} Y_{\text{branch}}^{*} \Pi_{\text{branch}}^{\intercal} M_x^{*} \right) x \, . \tag{A.41}$$

The definiteness of $\Theta_{\text{lss, ntwk}}$ is determined by the definiteness of the branch voltage sensitivity matrix $M_{\text{branch}} = \Pi_{\text{branch}}^{\intercal} M_x$ and the branch admittance matrix Y_{branch}.

Primitive admittance matrices associated with branch elements are usually made to be invertible by construction, and so Y_{branch} is full rank (see [138]). On the other hand, if M_{branch} is rank deficient, then $\Theta_{\text{lss, ntwk}}$ will always be rank deficient. A rank deficient M_{branch} can appear, for example, if there is a combination of both wye- and delta- loads at the same bus, with one set generating and one set absorbing reactive power. Similarly, a circulating current in a three-phase delta load will not change the load flow solution in a network.

A positive semidefinite quadratic loss model is observed, for example, in the 34 Bus network (Figure A.3a). (Numerically, the singular values are close to machine precision relative to the largest singular values of the matrix.) The two corresponding singular vectors for these singular values are plotted in Figure A.3b. The only buses which see a response are the two sets of 3× wye and 3× delta loads at buses 858 and 860. These modes correspond to modes whereby (approximately) the wye load generates the same power that is then absorbed by the delta load at the same bus. As expected, because the reactive power injections (almost) cancel, the linear response in both load and loss response to these modes is also very low (Figure A.3c).

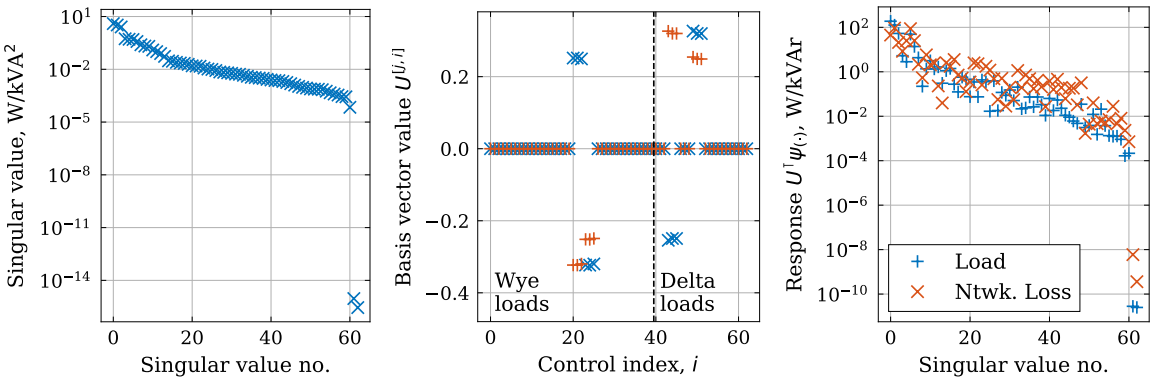

(a) Singular Values

(b) Zero-valued singular value basis vectors

(c) Load and network loss response

Figure A.3: Singular value decomposition of the 34 Bus networks, demonstrating the singular value corresponds to two buses that contain a combination of three-phase wye- and delta- connected loads.

There are two consequences of this. Firstly, the network losses matrix is not invertible. Secondly, when decomposing the matrix into the form $LL^\intercal$ (as may be required, for example, for use in a conic formulation of a quadratic constraint) the Cholesky decomposition typically requires a numerically positive definite matrix. As such, where this is required the less efficient LDL$^\intercal$ decomposition is used instead.

A.3.2 Minimum Singular Values for Asymptotic Analysis of Indefinite Systems

Any real symmetric matrix Θ can be diagonalised using the singular value decomposition as $\Theta = U\Lambda U^\intercal$, where U is unitary such that $UU^\intercal = I$ and Λ is diagonal (see, e.g., [189, Ch. 4-5]). In the case of a positive semidefinite matrix the matrix of singular values Λ will contain zeros on the diagonal.

The cost function

$$P_{\text{feeder}}(x) = x^\intercal \Theta x + b^\intercal x \tag{A.42}$$

can therefore be transformed to a new cost function, with $x = Uy$ and $c = U^\intercal b$,

yielding a new (equivalent) cost function,

$$P_{\text{feeder}}(y) = y^{\intercal}\Lambda y + c^{\intercal}y\,. \tag{A.43}$$

where Λ as a diagonal matrix with singular values along the diagonal. If the matrix Θ is positive semidefinite such that some of the diagonals of Λ are zero, then it then becomes clear that (A.43) is unbounded below if the corresponding value of $c \neq 0$. However, if all of the zero singular values (indexed by i) have $c^{[i]} = 0$, then a (non-unique) optimal solution to minimize (A.43) is

$$y^{\dagger} = -\frac{1}{2}\Lambda^{\ddagger}c\,, \tag{A.44}$$

where $(\cdot)^{\ddagger}$ denotes the pseudoinverse [198, pp. 395-396].

A value of $c^{[i]} = 0$ will occur if the singularity is in the voltage sensitivity matrix, as this will results in the linear loss and load sensitivities being zero (recall that the loss and load do not change if the nodal voltages do not change).

This is shown, for example, in Figure A.3c for the IEEE 34 Bus network. As such, the asymptotic analysis of section 5.3.2.1 for invertible quadratic loss matrices is therefore still applicable to this network (i.e., the maximum and minimum singular values of $\Theta_{\text{lss,ntwk}}$ still have exactly the same interpretation as the maximum and minimum singular values as in the invertible case).

A.3.3 Divergence of Neumann Series for Positive Definite Symmetric Matrices

As discussed in the previous section (Section A.3.2), a real symmetric matrix A can be decomposed using the singular value decomposition as $A = U\Lambda U^{\intercal}$. To demonstrate

the divergence of the Neumann Series, expand (5.31) as

$$x = \sum_{k=0}^{\infty} (\kappa A)^k \, b \tag{A.45}$$

$$= b + \kappa A b + (\kappa A)^2 b + \ldots \tag{A.46}$$

$$= \left(I + \kappa A + (\kappa A)^2 + \ldots\right) b \tag{A.47}$$

$$= \left(U\Lambda^0 U^\intercal + \kappa U \Lambda^1 U^\intercal + \kappa^2 U \Lambda^2 U^\intercal + \ldots\right) b \,, \tag{A.48}$$

where the property $UU^\intercal = I$ has been used. Collecting terms, yields

$$x = U \left(\sum_{k=0}^{\infty} (\kappa \Lambda)^k \right) U^\intercal b \tag{A.49}$$

$$= U \Xi U^\intercal b \,, \tag{A.50}$$

but, if $\kappa \|\Lambda\|_2 = 1$, then the first diagonal element of $\kappa\Lambda$ is unity for all k, and so the summation Ξ (in (A.49)) diverges.

Bibliography

[1] California Public Utilities Commission. California solar statistics. http://www.californiasolarstatistics.org, 2019. Accessed Apr. 19.

[2] S. C. Choi and R. Wette. Maximum likelihood estimation of the parameters of the gamma distribution and their bias. *Technometrics*, 11(4):683–690, 1969.

[3] M. Rylander, J. Smith, and W. Sunderman. Streamlined method for determining distribution system hosting capacity. *IEEE Transactions on Industry Applications*, 52(1):105–111, 2016.

[4] J. Nielsen. *Usability engineering*. Elsevier, 1994.

[5] BLAS (basic linear algebra subprograms). `http://www.netlib.org/blas/`, 2019. Accessed 25/07/19.

[6] IRENA. Global energy transformation: The REmap transition pathway (background report to 2019 edition). International Renewable Energy Agency, Abu Dhabi, 2019.

[7] Department for Business, Energy and Industrial Strategy (BEIS). Digest of UK energy statistics: Electricity, plant installed capacity by connection - united kingdom (5.12). `https://www.gov.uk/government/statistics/electricity-chapter-5-digest-of-united-kingdom-energy-statistics-dukes`, 2019. Accessed 08-09-19.

[8] M. H. Bollen and F. Hassan. *Integration of distributed generation in the power system*. John wiley & sons, 2011.

[9] V. M. Quezada, J. R. Abbad, and T. G. S. Roman. Assessment of energy distribution losses for increasing penetration of distributed generation. *IEEE Transactions on Power Systems*, 21(2):533–540, 2006.

[10] T. Morstyn, N. Farrell, S. J. Darby, and M. D. McCulloch. Using peer-to-peer energy-trading platforms to incentivize prosumers to form federated power plants. *Nature Energy*, 3(2):94, 2018.

[11] N. Jenkins, R. Allan, P. Crossley, D. Kirschen, and G. Strbac. *Embedded Generation*. The Institution of Engineering and Technology, 1st edition, 2000.

[12] P. Chiradeja and R. Ramakumar. An approach to quantify the technical benefits of distributed generation. *IEEE Transactions on Energy Conversion*, 19(4):764–773, 2004.

[13] L. F. Ochoa, A. Padilha-Feltrin, and G. P. Harrison. Evaluating distributed generation impacts with a multiobjective index. *IEEE Transactions on Power Delivery*, 21(3):1452–1458, 2006.

[14] Department of Energy and Climate Change. National statistics: Solar photovoltaics deployment in the UK (june 2019 update). `https://www.gov.uk/government/statistics/solar-photovoltaics-deployment`. Accessed: 11-07-2019.

[15] D. Lew, M. Asano, J. Boemer, C. Ching, U. Focken, R. Hydzik, M. Lange, and A. Motley. The power of small: The effects of distributed energy resources on system reliability. *IEEE Power and Energy Magazine*, 15(6):50–60, 2017.

[16] California Energy Commission. Building energy efficiency standards for residential and non-residential buildings. `https://ww2.energy.ca.gov/2018publications/CEC-400-2018-020/CEC-400-2018-020-CMF.pdf`, 2019. Accessed 08-09-19.

[17] S. Mohtashami, D. Pudjianto, and G. Strbac. Strategic distribution network planning with smart grid technologies. *IEEE Transactions on Smart Grid*, 8(6):2656–2664, 2016.

[18] D. Apostolopoulou, S. Bahramirad, and A. Khodaei. The interface of power: Moving toward distribution system operators. *IEEE Power and Energy Magazine*, 14(3):46–51, 2016.

[19] Office for Gas and Electricity Markets (OFGEM). Position paper on distribution system operation: our approach and regulatory priorities, 2019.

[20] N. Jenkins, J. Ekanayake, , and G. Strbac. *Embedded Generation*. The Institution of Engineering and Technology, 1st edition, 2000.

[21] M. Thomson and D. Infield. Impact of widespread photovoltaics generation on distribution systems. *IET Renewable Power Generation*, 1(1):33–40, 2007.

[22] H.-D. Chiang, J.-C. Wang, and K. N. Miu. Explicit loss formula, voltage formula and current flow formula for large-scale unbalanced distribution systems. *IEEE Transactions on Power Systems*, 12(3):1061–1067, 1997.

[23] The Energy and Climate Change Committee. Energy network costs: transparent and fair? Technical report, UK Parliament, 2014.

[24] Office for Gas and Electricity Markets (OFGEM). Electricity distribution units and loss percentages summary - fact sheet, 2010.

[25] UK Gas and Electricity Markets Authority (GEMA). *Standard Conditions of the Electricity Distribution Licence*, June 2019.

[26] T. Short, D. Brooks, B. Arritt, W. Sunderman, J. Taylor, M. Rylander, H. Sharma, A. Gaikwad, J. Smith, B. Fletcher, and M. Grady. Green circuit: Distribution efficiency case studies. Technical report, Electric Power Research Institute (EPRI), October 2010.

[27] L. Söder. Estimation of reduced electrical distribution losses depending on small scale energy production. In *12th Power Systems Computation Conference, Dresden*, 1996.

[28] C. Schwaegerl, M. Bollen, K. Karoui, and A. Yagmur. Voltage control in distribution systems as a limitation of the hosting capacity for distributed energy resources. In *18th International Conference and Exhibition on Electricity Distribution (CIRED 2005).*, 2005.

[29] S. C. Vegunta, C. F. A. Watts, S. Z. Djokic, J. V. Milanović, and M. J. Higginson. Review of GB electricity distribution system's electricity security of supply, reliability and power quality in meeting UK industrial strategy requirements. *IET Generation, Transmission & Distribution*, 13(16):3513–3523, 2019.

[30] K. Bell. Methods and tools for planning the future power system: Issues and priorities. *IET Power Networks Joint Vision*, 2015.

[31] K. P. Schneider, J. C. Fuller, F. K. Tuffner, and R. Singh. Evaluation of conservation voltage reduction (CVR) on a national level. Technical report, Pacific Northwest National Lab.(PNNL), Richland, WA (United States), 2010.

[32] K. Forsten. Green circuits: Distribution efficiency case studies. *Electric Power Research Institute (EPRI), Technical Report (1023518), Palo Alto*, 2011.

[33] P. Jahangiri and D. C. Aliprantis. Distributed volt/var control by PV inverters. *IEEE Transactions on Power Systems*, 28(3):3429–3439, 2013.

[34] I. S. C. C. 21. IEEE standard for interconnection and interoperability of distributed energy resources with associated electric power systems interfaces (IEEE std. 1547-2018), 2018.

[35] Pacific Gas and Electricity Company. Electric rule no. 21: Generating facility interconnections. `https://www.pge.com/tariffs/tm2/pdf/ELEC_RULES_21.pdf`, 2018. Accessed 09-09-19.

[36] R. Kuga. Epic 2.03a: Test smart inverter enhanced capabilities photovoltaics (PV): Smart inverter modeling report. Technical report, Pacific Gas and Electric Company, 2019.

[37] G. E. Box. Science and statistics. *Journal of the American Statistical Association*, 71(356):791–799, 1976.

[38] C. Abbey, A. Baitch, B. Bak-Jensen, C. Carter, G. Celli, K. El Bakari, M. Fan, P. Georgilakis, T. Hearne, and L. N. Ochoa. *Planning and optimization methods for active distribution systems.* CIGRE, 2014.

[39] A. Schrijver. *Theory of linear and integer programming.* John Wiley & Sons, 1998.

[40] R. B. Miller. Response time in man-computer conversational transactions. In *Proceedings of the December 9-11, 1968, fall joint computer conference, part I*, pages 267–277. ACM, 1968.

[41] S. K. Card, G. G. Robertson, and J. D. Mackinlay. The information visualizer, an information workspace. In *Proceedings of the SIGCHI Conference on Human factors in computing systems*, pages 181–186. ACM, 1991.

[42] M. Halpern, Y. Zhu, and V. J. Reddi. Mobile CPU's rise to power: Quantifying the impact of generational mobile CPU design trends on performance, energy, and user satisfaction. In *2016 IEEE International Symposium on High Performance Computer Architecture (HPCA)*, pages 64–76. IEEE, 2016.

[43] D. F. Galletta, R. Henry, S. McCoy, and P. Polak. Web site delays: How tolerant are users? *Journal of the Association for Information Systems*, 5(1):1, 2004.

[44] C. L. T. Borges and V. F. Martins. Multistage expansion planning for active distribution networks under demand and distributed generation uncertainties. *International Journal of Electrical Power & Energy Systems*, 36(1):107–116, 2012.

[45] E. Lakervi and E. J. Holmes. *Electricity Distribution Network Design.* Institution of Engineering and Technology, London, UK, 1995.

[46] K. Baker, A. Bernstein, E. DallAnese, and C. Zhao. Network-cognizant voltage droop control for distribution grids. *IEEE Transactions on Power Systems*, 33(2):2098–2108, 2018.

[47] J. Wang, C. Chen, and X. Lu. Guidelines for implementing advanced distribution management systems-requirements for DMS integration with DERMS and microgrids. Technical report, Argonne National Lab. Argonne, IL (United States), 2015.

[48] D. Pudjianto, C. Ramsay, and G. Strbac. Virtual power plant and system integration of distributed energy resources. *IET Renewable Power Generation*, 1(1):10–16, 2007.

[49] J. Deboever, X. Zhang, M. J. Reno, R. J. Broderick, S. Grijalva, and F. Therrien. Challenges in reducing the computational time of QSTS simulations for distribution system analysis. *Sandia National Laboratory, Albuquerque, NM*, 2017.

[50] M. E. Baran and F. F. Wu. Network reconfiguration in distribution systems for loss reduction and load balancing. *IEEE Power Engineering Review*, 9(4):101–102, 1989.

[51] D. L. Flaten. Distribution system losses calculated by percent loading. *IEEE Transactions on Power Systems*, 3(3):1263–1269, 1988.

[52] R. Baldick and F. F. Wu. Approximation formulas for the distribution system: the loss function and voltage dependence. *IEEE Transactions on Power Delivery*, 6(1):252–259, 1991.

[53] N. Vempati, R. Shoults, M. Chen, and L. Schwobel. Simplified feeder modeling for load flow calculations. *IEEE Transactions on Power Systems*, 2(1):168–174, 1987.

[54] C. Chen, J. Hwang, M. Cho, and Y. Chen. Development of simplified loss models for distribution system analysis. *IEEE Transactions on Power Delivery*, 9(3):1545–1551, 1994.

[55] P. N. Rao and R. Deekshit. Energy loss estimation in distribution feeders. *IEEE Transactions on Power Delivery*, 21(3):1092–1100, 2006.

[56] T. A. Short. *Electric Power Distribution Handbook, Second Ed.* CRC Press, 2nd edition, 2014.

[57] M. Braun. Reactive power supply by distributed generators. In *2008 IEEE Power and Energy Society General Meeting*, pages 1–8. IEEE, 2008.

[58] K. Turitsyn, P. Sulc, S. Backhaus, and M. Chertkov. Options for control of reactive power by distributed photovoltaic generators. *Proceedings of the IEEE*, 99(6):1063–1073, 2011.

[59] E. E. Pompodakis, I. A. Drougakis, I. S. Lelis, and M. C. Alexiadis. Photovoltaic systems in low-voltage networks and overvoltage correction with reactive power control. *IET Renewable Power Generation*, 10(3):410–417, 2016.

[60] X. Su, M. A. Masoum, and P. J. Wolfs. Optimal PV inverter reactive power control and real power curtailment to improve performance of unbalanced four-wire LV distribution networks. *IEEE Transactions on Sustainable Energy*, 5(3):967–977, 2014.

[61] E. Demirok, P. C. Gonzalez, K. H. Frederiksen, D. Sera, P. Rodriguez, and R. Teodorescu. Local reactive power control methods for overvoltage prevention of distributed solar inverters in low-voltage grids. *IEEE Journal of Photovoltaics*, 1(2):174–182, 2011.

[62] D. F. Teshome, W. Xu, P. Bagheri, A. B. Nassif, and Y. Zhou. A reactive power control scheme for DER-caused voltage rise mitigation in secondary systems. *IEEE Transactions on Sustainable Energy*, 2018.

[63] L. F. Ochoa and G. P. Harrison. Minimizing energy losses : Optimal accommodation and smart operation of renewable distributed generation. *IEEE Transactions on Power Systems*, 26(1):198–205, 2011.

[64] A. Conejo, J. Arroyo, N. Alguacil, and A. Guijarro. Transmission loss allocation: a comparison of different practical algorithms. *IEEE Transactions on Power Systems*, 17(3):571–576, 2002.

[65] A. G. Exposito, J. R. Santos, T. G. Garcia, and E. R. Velasco. Fair allocation of transmission power losses. *IEEE Transactions on Power Systems*, 15(1):184–188, 2000.

[66] T. Stetz, F. Marten, and M. Braun. Improved low voltage grid-integration of photovoltaic systems in germany. *IEEE Transactions on Sustainable Energy*, 4(2):534–542, 2013.

[67] O. Gagrica, P. H. Nguyen, W. L. Kling, and T. Uhl. Microinverter curtailment strategy for increasing photovoltaic penetration in low-voltage networks. *IEEE Transactions on Sustainable Energy*, 6(2):369–379, 2015.

[68] S. S. Sultan, V. Khadkikar, and H. H. Zeineldin. Incorporating PV inverter control schemes for planning active distribution networks. *IEEE Transactions on Sustainable Energy*, 6(4):1224–1233, 2015.

[69] L. Wang, R. Yan, and T. K. Saha. Voltage management for large scale PV integration into weak distribution systems. *IEEE Transactions on Smart Grid*, 9(5):4128–4139, 2018.

[70] K. E. Antoniadou-Plytaria, I. N. Kouveliotis-Lysikatos, P. S. Georgilakis, and N. D. Hatziargyriou. Distributed and decentralized voltage control of smart distribution networks: models, methods, and future research. *IEEE Transactions on Smart Grid*, 8(6):2999–3008, 2017.

[71] T. Stetz, K. Diwold, M. Kraiczy, D. Geibel, S. Schmidt, and M. Braun. Techno-economic assessment of voltage control strategies in low voltage grids. *IEEE Transactions on Smart Grid*, 5(4):2125–2132, 2014.

[72] S. N. Salih, P. Chen, O. Carlson, and L. B. Tjernberg. Optimizing wind power hosting capacity of distribution systems using cost benefit analysis. *IEEE Transactions on Power Delivery*, 29(3):1436–1445, 2014.

[73] S. S. Alkaabi, H. H. Zeineldin, and V. Khadkikar. Short-term reactive power planning to minimize cost of energy losses considering PV systems. *IEEE Transactions on Smart Grid*, 10(3):2923–2935, 2018.

[74] S. Kalambe and G. Agnihotri. Loss minimization techniques used in distribution network: bibliographical survey. *Renewable and Sustainable Energy Reviews*, 29:184–200, 2014.

[75] R. Dugan, M. McGranaghan, S. Santoso, and H. Beaty. *Electrical Power Systems Quality*. McGraw-Hill, 2nd edition, 2004.

[76] A. Sallam and O. Malik. *Electric Distribution Systems*. Wiley, 2nd edition, 2019.

[77] W. H. Kersting. *Distribution system modeling and analysis*. CRC press, 2006.

[78] C. Vournas. Maximum power transfer in the presence of network resistance. *IEEE Transactions on Power Systems*, 30(5):2826–2827, 2015.

[79] A. Fonseca, F. Pérez-Yauli, and G. Salazar. Loadability analysis based on short-circuit power. *IET Generation, Transmission & Distribution*, 11(10):2540–2551, 2017.

[80] H. D. Nguyen, K. Dvijotham, S. Yu, and K. Turitsyn. A framework for robust long-term voltage stability of distribution systems. *IEEE Transactions on Smart Grid*, 2018.

[81] J. Z. Zhou and A. M. Gole. VSC transmission limitations imposed by AC system strength and AC impedance characteristics. In *10th IET International Conference on AC and DC Power Transmission (ACDC 2012)*, 2012.

[82] T. Souxes and C. Vournas. System stability issues involving distributed sources under adverse network conditions. In *IREP Symposium Bulk Power System Dynamics and Control - X (IREP)*, 2017.

[83] S. Sadeghi Baghsorkhi. *Integration of Utility-Scale Variable Generation into Resistive Networks*. PhD thesis, University of Michigan, 2015.

[84] C. Vournas, I. Anagnostopoulos, and T. Souxes. Transmission support using wind farm controls during voltage stability emergencies. *Control Engineering Practice*, 59:100–110, 2017.

[85] A. Keane, L. F. Ochoa, C. L. T. Borges, G. W. Ault, A. D. Alarcon-Rodriguez, R. a. F. Currie, F. Pilo, C. Dent, and G. P. Harrison. State-of-the-art techniques and challenges ahead for distributed generation planning and optimization. *IEEE Transactions on Power Systems*, 28(2):1493–1502, 2013.

[86] A. G. Marinopoulos, M. C. Alexiadis, P. S. Dokopoulos, et al. A correlation index to evaluate impact of PV installation on joule losses. *IEEE Transactions on Power Systems*, 26(3):1564–1572, 2011.

[87] F. A. Viawan, F. Vuinovich, and A. Sannino. Probabilistic approach to the design of photovoltaic distributed generation in low voltage feeder. In *2006 International Conference on Probabilistic Methods Applied to Power Systems*, pages 1–7. IEEE, 2006.

[88] A. G. Anastasiadis, V. M. Argyropoulou, K. D. Pagonis, and N. D. Hatziargyriou. Losses in a LV-microgrid with the presence of reactive power and CHP units. *8th Mediterranean Conference on Power Generation, Transmission, Distribution and Energy Conversion*, 2012.

[89] J. Mutale, G. Strbac, S. Curcic, and N. Jenkins. Allocation of losses in distribution systems with embedded generation. *IEE Proceedings-Generation, Transmission and Distribution*, 147(1):7–14, 2000.

[90] H. A. Gil and G. Joos. Models for quantifying the economic benefits of distributed generation. *IEEE Transactions on Power Systems*, 23(2):327–335, 2008.

[91] R. Tonkoski and L. A. Lopes. Voltage regulation in radial distribution feeders with high penetration of photovoltaic. In *IEEE Energy 2030, 2008.*, pages 1–7. IEEE, 2008.

[92] P. Kumar, N. Gupta, K. R. Niazi, and A. Swarnkar. A circuit theory-based loss allocation method for active distribution systems. *IEEE Transactions on Smart Grid*, 10(1):1005–1012, 2017.

[93] A. R. Manito, U. H. Bezerra, T. M. Soares, J. P. Vieira, M. V. Nunes, M. E. Tostes, and R. C. de Oliveira. Technical and non-technical losses calculation in distribution grids using a defined equivalent operational impedance. *IET Generation, Transmission & Distribution*, 13(8):1315–1323, 2018.

[94] M. Bollen and S. Rönnberg. Hosting capacity of the power grid for renewable electricity production and new large consumption equipment. *Energies*, 10(9):1325, 2017.

[95] M. J. Reno, K. Coogan, S. Grijalva, R. J. Broderick, and J. E. Quiroz. PV interconnection risk analysis through distribution system impact signatures and feeder zones. In *2014 IEEE PES General Meeting— Conference & Exposition*. IEEE, 2014.

[96] A. Dubey and S. Santoso. On estimation and sensitivity analysis of distribution circuit's photovoltaic hosting capacity. *IEEE Transactions on Power Systems*, 32(4):2779–2789, 2017.

[97] F. Ding and B. Mather. On distributed PV hosting capacity estimation, sensitivity study, and improvement. *IEEE Transactions on Sustainable Energy*, 8(3):1010–1020, 2017.

[98] A. Navarro-Espinosa and L. F. Ochoa. Probabilistic impact assessment of low carbon technologies in LV distribution systems. *IEEE Transactions on Power Systems*, 31(3):2192–2203, 2016.

[99] J. Le Baut, P. Zehetbauer, S. Kadam, B. Bletterie, N. Hatziargyriou, J. Smith, and M. Rylander. Probabilistic evaluation of the hosting capacity in distribution networks. In *2016 IEEE PES Innovative Smart Grid Technologies Conference Europe (ISGT-Europe)*. IEEE, 2016.

[100] R. Torquato, D. Salles, C. O. Pereira, P. C. M. Meira, and W. Freitas. A comprehensive assessment of PV hosting capacity on low-voltage distribution systems. *IEEE Transactions on Power Delivery*, 33(2):1002–1012, 2018.

[101] M. S. S. Abad, J. Ma, D. Zhang, A. S. Ahmadyar, and H. Marzooghi. Probabilistic assessment of hosting capacity in radial distribution systems. *IEEE Transactions on Sustainable Energy*, 9(4):1935–1947, 2018.

[102] A. Dubey, S. Santoso, and A. Maitra. Understanding photovoltaic hosting capacity of distribution circuits. In *2015 IEEE power & energy society general meeting*. IEEE, 2015.

[103] F. Ding, B. Mather, and P. Gotseff. Technologies to increase PV hosting capacity in distribution feeders. In *Power and Energy Society General Meeting (PESGM), 2016*. IEEE, 2016.

[104] D. Schwanz, F. Möller, S. K. Rönnberg, J. Meyer, and M. H. Bollen. Stochastic assessment of voltage unbalance due to single-phase-connected solar power. *IEEE Transactions on Power Delivery*, 32(2):852–861, 2017.

[105] R. A. Shayani and M. A. G. de Oliveira. Photovoltaic generation penetration limits in radial distribution systems. *IEEE Transactions on Power Systems*, 26(3):1625–1631, 2011.

[106] S. Jothibasu and S. Santoso. Sensitivity analysis of photovoltaic hosting capacity of distribution circuits. In *Power and Energy Society General Meeting (PESGM 2016)*, 2016.

[107] S. Breker, A. Claudi, and B. Sick. Capacity of low-voltage grids for distributed generation: classification by means of stochastic simulations. *IEEE Transactions on Power Systems*, 30(2):689–700, 2015.

[108] M. Rylander and J. Smith. Stochastic approach for distribution planning with distributed energy resources. In *CIGRE Grid of the Future Symposium, Kansas City, MO*, 2012.

[109] M. Alturki, A. Khodaei, A. Paaso, and S. Bahramirad. Optimization-based distribution grid hosting capacity calculations. *Applied Energy*, 219:350–360, 2018.

[110] M. U. Qureshi, S. Grijalva, M. J. Reno, J. Deboever, X. Zhang, and R. J. Broderick. A fast scalable quasi-static time series analysis method for PV impact studies using linear sensitivity model. *IEEE Transactions on Sustainable Energy*, 10(1):301–310, 2019.

[111] H. Pezeshki, A. Arefi, G. Ledwich, and P. Wolfs. Probabilistic voltage management using OLTC and dSTATCOM in distribution networks. *IEEE Transactions on Power Delivery*, 33(2):570–580, 2018.

[112] S. Jothibasu, A. Dubey, and S. Santoso. Two-stage distribution circuit design framework for high levels of photovoltaic generation. *IEEE Transactions on Power Systems*, 2018.

[113] D. A. Quijano, J. Wang, M. R. Sarker, and A. Padilha-Feltrin. Stochastic assessment of distributed generation hosting capacity and energy efficiency in active distribution networks. *IET Generation, Transmission & Distribution*, 11(18):4617–4625, 2017.

[114] B. R. Prusty and D. Jena. A critical review on probabilistic load flow studies in uncertainty constrained power systems with photovoltaic generation and a new approach. *Renewable and Sustainable Energy Reviews*, 69:1286–1302, 2017.

[115] S. S. Guggilam, E. DallAnese, Y. C. Chen, S. V. Dhople, and G. B. Giannakis. Scalable optimization methods for distribution networks with high PV integration. *IEEE Transactions on Smart Grid*, 7(4):2061–2070, 2016.

[116] Z. Wang and J. Wang. Review on implementation and assessment of conservation voltage reduction. *IEEE Transactions on Power Systems*, 29(3):1306–1315, 2013.

[117] M. Chen, R. Shoults, J. Fitzer, and H. Songster. The effects of reduced voltages on the efficiency of electric loads. *IEEE Transactions on Power Apparatus and Systems*, pages 2158–2166, 1982.

[118] A. Bokhari, A. Alkan, R. Dogan, M. Diaz-Aguiló, F. De Leon, D. Czarkowski, Z. Zabar, L. Birenbaum, A. Noel, and R. E. Uosef. Experimental determination of the ZIP coefficients for modern residential, commercial, and industrial loads. *IEEE Transactions on Power Delivery*, 29(3):1372–1381, 2013.

[119] A. Ballanti and L. F. Ochoa. Voltage-led load management in whole distribution networks. *IEEE Transactions on Power Systems*, 33(2):1544–1554, 2017.

[120] L. Gutierrez-Lagos and L. F. Ochoa. OPF-based CVR operation in PV-rich MV-LV distribution networks. *IEEE Transactions on Power Systems*, 2019.

[121] M. H. Bollen, R. Das, S. Djokic, P. Ciufo, J. Meyer, S. K. Rönnberg, and F. Zavodam. Power quality concerns in implementing smart distribution-grid applications. *IEEE Transactions on Smart Grid*, 8(1):391–399, 2016.

[122] D. Kirshner. Implementation of conservation voltage reduction at commonwealth edison. *IEEE Transactions on Power Systems*, 5(4):1178–1182, 1990.

[123] V. Borozan, M. E. Baran, and D. Novosel. Integrated volt/var control in distribution systems. In *2001 IEEE Power Engineering Society Winter Meeting*, volume 3, pages 1485–1490. IEEE, 2001.

[124] F. Capitanescu. AC OPF-based methodology for exploiting flexibility provision at TSO/DSO interface via OLTC-controlled demand reduction. In *2018 Power Systems Computation Conference (PSCC)*. IEEE, 2018.

[125] H. V. Padullaparti, Q. Nguyen, and S. Santoso. Advances in volt-var control approaches in utility distribution systems. In *2016 IEEE Power and Energy Society General Meeting (PESGM)*, pages 1–5. IEEE, 2016.

[126] V. A. Evangelopoulos, P. S. Georgilakis, and N. D. Hatziargyriou. Optimal operation of smart distribution networks: A review of models, methods and future research. *Electric Power Systems Research*, 140:95–106, 2016.

[127] M. Farivar, R. Neal, C. Clarke, and S. Low. Optimal inverter var control in distribution systems with high PV penetration. In *2012 IEEE Power and Energy Society general meeting*, pages 1–7. IEEE, 2012.

[128] O. Gandhi, W. Zhang, C. D. Rodriguez-Gallegos, M. Bieri, T. Reindl, and D. Srinivasan. Analytical approach to reactive power dispatch and energy arbitrage in distribution systems with DERs. *IEEE Transactions on Power Systems*, 33(6):6522–6533, 2018.

[129] V. B. Pamshetti and S. P. Singh. Optimal coordination of PV smart inverter and traditional volt-var control devices for energy cost savings and voltage regulation. *International Transactions on Electrical Energy Systems*, 2019.

[130] H. Ahmadi, J. R. Martí, and H. W. Dommel. A framework for volt-var optimization in distribution systems. *IEEE Transactions on Smart Grid*, 6(3):1473–1483, 2014.

[131] Q. Zhang, K. Dehghanpour, and Z. Wang. Distributed CVR in unbalanced distribution systems with PV penetration. *IEEE Transactions on Smart Grid*, 2018.

[132] A. O'Connell. Unbalanced distribution system voltage optimisation. In *2016 IEEE PES Innovative Smart Grid Technologies Conference Europe (ISGT-Europe)*. IEEE, 2016.

[133] F. Ding and M. Baggu. Coordinated use of smart inverters with legacy voltage regulating devices in distribution systems with high distributed PV penetration–increase CVR energy savings. *IEEE Transactions on Smart Grid*, 2018.

[134] F. Ding, A. Nguyen, S. Walinga, A. Nagarajan, M. Baggu, S. Chakraborty, M. McCarty, and F. Bell. Application of autonomous smart inverter volt-var

function for voltage reduction energy savings and power quality in electric distribution systems. In *2017 IEEE Power & Energy Society Innovative Smart Grid Technologies Conference (ISGT)*, pages 1–5. IEEE, 2017.

[135] S. Satsangi and G. B. Kumbhar. Effect of load models on energy loss reduction using volt-var optimization. In *2016 National Power Systems Conference (NPSC)*. IEEE, 2016.

[136] S. Satsangi and G. B. Kumbhar. Effect of load models on scheduling of VVC devices in a distribution network. *IET Generation, Transmission & Distribution*, 12(17):3993–4001, 2018.

[137] S. Singh and S. P. Singh. Energy saving estimation in distribution network with smart grid-enabled CVR and solar PV inverter. *IET Generation, Transmission & Distribution*, 12(6):1346–1358, 2017.

[138] M. Bazrafshan and N. Gatsis. Comprehensive modeling of three-phase distribution systems via the bus admittance matrix. *IEEE Transactions on Power Systems*, 33(2):2015–2029, 2017.

[139] A. Bernstein, C. Wang, E. DallAnese, J.-Y. Le Boudec, and C. Zhao. Load flow in multiphase distribution networks: Existence, uniqueness, non-singularity and linear models. *IEEE Transactions on Power Systems*, 33(6):5832–5843, 2018.

[140] J. J. Grainger and W. D. Stevenson Jr. *Power System Analysis*. McGraw-Hill, 1994.

[141] S. Bolognani and F. Dörfler. Fast power system analysis via implicit linearization of the power flow manifold. In *2015 53rd Annual Allerton Conference on Communication, Control, and Computing (Allerton)*, pages 402–409. IEEE, 2015.

[142] B. Stott, J. Jardim, and O. Alsaç. DC power flow revisited. *IEEE Transactions on Power Systems*, 24(3):1290–1300, 2009.

[143] S. V. Dhople, S. S. Guggilam, and Y. C. Chen. Linear approximations to AC power flow in rectangular coordinates. In *2015 53rd Annual Allerton Conference on Communication, Control, and Computing (Allerton)*, pages 211–217. IEEE, 2015.

[144] Z. Li, J. Yu, and Q. Wu. Approximate linear power flow using logarithmic transform of voltage magnitudes with reactive power and transmission loss consideration. *IEEE Transactions on Power Systems*, 33(4):4593–4603, 2017.

[145] K. Christakou, J.-Y. LeBoudec, M. Paolone, and D.-C. Tomozei. Efficient computation of sensitivity coefficients of node voltages and line currents in unbalanced radial electrical distribution networks. *IEEE Transactions on Smart Grid*, 4(2):741–750, 2013.

[146] Y. Ju, C. Chen, L. Wu, and H. Liu. General three-phase linear power flow for active distribution networks with good adaptability under a polar coordinate system. *IEEE Access*, 6:34043–34050, 2018.

[147] H. Ahmadi, J. R. Martı, and A. von Meier. A linear power flow formulation for three-phase distribution systems. *IEEE Transactions on Power Systems*, 31(6):5012–5021, 2016.

[148] Y. Wang, N. Zhang, H. Li, J. Yang, and C. Kang. Linear three-phase power flow for unbalanced active distribution networks with PV nodes. *CSEE Journal of Power and Energy Systems*, 3(3):321–324, 2017.

[149] A. Garces. A linear three-phase load flow for power distribution systems. *IEEE Transactions on Power Systems*, 31(1):827–828, 2015.

[150] F. Tamp and P. Ciufo. A sensitivity analysis toolkit for the simplification of MV distribution network voltage management. *IEEE Transactions on Smart Grid*, 5(2):559–568, 2014.

[151] S. Weckx, R. DHulst, and J. Driesen. Voltage sensitivity analysis of a laboratory distribution grid with incomplete data. *IEEE Transactions on Smart Grid*, 6(3):1271–1280, 2014.

[152] V. Rigoni and A. Keane. Estimation of voltage sensitivities in low voltage feeders with photovoltaics. In *2018 IEEE PES Innovative Smart Grid Technologies Conference Europe (ISGT-Europe)*. IEEE, 2018.

[153] M. J. Reno and R. J. Broderick. Statistical analysis of feeder and locational PV hosting capacity for 216 feeders. In *2016 IEEE Power and Energy Society General Meeting (PESGM)*, pages 1–5. IEEE, 2016.

[154] Electricity Northwest (ENWL). Low voltage network solutions: LV network models. `https://www.enwl.co.uk/lvns/`, 2015. Accessed 30-09-19.

[155] IEEE Power and Energy Society. Distribution test feeders. `http://sites.ieee.org/pes-testfeeders/`, 2019. Accessed 30-09-19.

[156] K. Schneider, B. Mather, B. Pal, C.-W. Ten, G. Shirek, H. Zhu, J. Fuller, J. Pereira, L. Ochoa, L. De Araujo, R. C. Dugan, S. Matthias, S. Paudyal, T. E. McDermott, and W. Kersting. Analytic considerations and design basis for the IEEE distribution test feeders. *IEEE Transactions on Power Systems*, 33(3):3181–3188, 2017.

[157] Electric Power Research Institute (EPRI). Hosting capacity feeders J1, K1, M1. `https://dpv.epri.com/feeder_models.html`, 2019. Accessed Apr. 19.

[158] Electric Power Research Institute (EPRI). Test circuits 5, 7, 24. `https://sourceforge.net/p/electricdss/code/HEAD/tree/trunk/Distrib/EPRITestCircuits/Readme.pdf`, 2019. Accessed Apr. 19.

[159] M. E. Baran and F. F. Wu. Optimal capacitor placement on radial distribution systems. *IEEE Transactions on Power Delivery*, 4(1):725–734, 1989.

[160] T. V. Cutsem and C. Vournas. *Voltage Stability of Electric Power Systems*. Springer, 2nd edition, 2007.

[161] J. C. McLaughlin and K. L. Kaiser. 'Deglorifying' the maximum power transfer theorem and factors in impedance selection. *IEEE Transactions on Education*, 50(3):251–255, 2007.

[162] W. H. Kersting. Radial distribution test feeders. *Proceedings of the IEEE Power Engineering Society Transmission and Distribution Conference*, 2:908–912, 2001.

[163] A. P. Dobos. PVWatts version 5 manual. Technical report, National Renewable Energy Lab.(NREL), Golden, CO (United States), 2014.

[164] I. B. Engineering. Energy demand research project: Early smart meter trials, 2007-2010. UK Data Service.

[165] P. E. Gill, W. Murray, and M. H. Wright. *Practical optimization*. Academic press, 1981.

[166] R. J. Hyndman and A. B. Koehler. Another look at measures of forecast accuracy. *International journal of forecasting*, 22(4):679–688, 2006.

[167] Y. Liu, J. Bebic, B. Kroposki, J. De Bedout, and W. Ren. Distribution system voltage performance analysis for high-penetration PV. In *2008 IEEE Energy 2030 Conference*, pages 1–8. IEEE, 2008.

[168] G. H. Golub and C. F. Van Loan. *Matrix computations*. JHU press, 2012.

[169] J. R. Gilbert, C. Moler, and R. Schreiber. Sparse matrices in matlab: Design and implementation. *SIAM Journal on Matrix Analysis and Applications*, 13(1):333–356, 1992.

[170] E. Anderson, Z. Bai, C. Bischof, L. Blackford, J. Demmel, J. J. Dongarra, J. Du Croz, S. Hammarling, A. Greenbaum, A. McKenney, et al. *LAPACK Users' guide*. Society for Industrial and Applied Mathematics (SIAM), 1999.

[171] A. Bernstein and E. Dall'Anese. Linear power-flow models in multiphase distribution networks. In *2017 IEEE PES Innovative Smart Grid Technologies Conference Europe (ISGT-Europe)*. IEEE, 2017.

[172] S. Ross. *A First Course in Probability*. Prentice Hall, 8th edition, 2010.

[173] British Standards Institution. BS EN 50160:2010+A1:2015 (voltage characteristics of electricity supplied by public electricity networks), 2015.

[174] UK Power Networks. Use of system charging statement: Notice of charges effective from 1 april 2020. https://www.ukpowernetworks.co.uk/internet/en/about-us/documents/2020/eastern/Eastern%20Power%20Networks%20LC14%20Statement%202020%20V1.1.pdf, 2019. Accessed 17-09-19.

[175] W. LLP. Distribution connection and use of system agreement. https://www.dcusa.co.uk/wp-content/uploads/2019/08/DCUSA-v11.2_Public.pdf, 2006. Accessed 17-09-19.

[176] L. Korunović, S. Sterpu, S. Djokić, K. Yamashita, S. M. Villanueva, and J. Milanović. Processing of load parameters based on existing load models. In *2012 3rd IEEE PES Innovative Smart Grid Technologies Europe (ISGT Europe)*. IEEE, 2012.

[177] A. Arif, Z. Wang, J. Wang, B. Mather, H. Bashualdo, and D. Zhao. Load modeling–a review. *IEEE Transactions on Smart Grid*, 9(6):5986–5999, 2017.

[178] C. Long and L. F. Ochoa. Voltage control of PV-rich LV networks: OLTC-fitted transformer and capacitor banks. *IEEE Transactions on Power Systems*, 31:4016–4025, 2015.

[179] M. C. Kisacikoglu, M. Kesler, and L. M. Tolbert. Single-phase on-board bidirectional PEV charger for V2G reactive power operation. *IEEE Transactions on Smart Grid*, 6(2):767–775, 2014.

[180] J. Wang, G. R. Bharati, S. Paudyal, O. Ceylan, B. P. Bhattarai, and K. S. Myers. Coordinated electric vehicle charging with reactive power support to distribution grids. *IEEE Transactions on Industrial Informatics*, 15(1):54–63, 2018.

[181] UK Department for Transport. National charge point registry. https://data.gov.uk/dataset/1ce239a6-d720-4305-ab52-17793fedfac3/national-charge-point-registry, 2019. Accessed 30-08-19.

[182] IEEE Power and Energy Society. IEEE guide for loading mineral-oil-immersed transformers and step-voltage regulators. IEEE Standards Association, 2011.

[183] I. Power and E. Society. IEEE recommended practice for performing temperature rise tests on liquid-immersed power transformers at loads beyond nameplate ratings. IEEE Standards Association, 2015.

[184] C. Barteczko-Hibbert. Customer-led network revolution: After diversity maximum demand (ADMD) report (clnr-l217). *http://www.networkrevolution.co.uk/resources/project-library/*, 2015.

[185] G. Notton, V. Lazarov, and L. Stoyanov. Optimal sizing of a grid-connected PV system for various PV module technologies and inclinations, inverter efficiency characteristics and locations. *Renewable Energy*, 35(2):541–554, 2010.

[186] Mosek. Mosek fusion API. https://www.mosek.com/, 2019.

[187] L. A. Wolsey. *Integer Programming*. Wiley, 1998.

[188] Mosek Inc. The optimizer for mixed-integer problems. https://docs.mosek.com/9.0/pythonfusion/mip-optimizer.html#the-mixed-integer-optimizer-overview, 2019. Accessed: 9/4/19.

[189] L. N. Trefethen and D. Bau III. *Numerical linear algebra*. Society for Industrial and Applied Mathematics (SIAM), 1997.

[190] G. W. Stewart and J.-G. Sun. *Matrix perturbation theory*. Citeseer, 1990.

[191] D. K. Khatod, V. Pant, and J. Sharma. A novel approach for sensitivity calculations in the radial distribution system. *IEEE Transactions on Power Delivery*, 21(4):2048–2057, 2006.

[192] Q. Zhou and J. Bialek. Simplified calculation of voltage and loss sensitivity factors in distribution networks. In *Proc. 16th Power Syst. Comput. Conf.(PSCC2008)*, 2008.

[193] J. B. Gil, T. G. San Román, J. A. Rios, and P. S. Martin. Reactive power pricing: a conceptual framework for remuneration and charging procedures. *IEEE Transactions on Power Systems*, 15(2):483–489, 2000.

[194] Office for Gas and Electricity Markets (OFGEM). State of the energy market 2018, 2018.

[195] O. Gandhi, C. D. Rodríguez-Gallegos, W. Zhang, D. Srinivasan, and T. Reindl. Economic and technical analysis of reactive power provision from distributed energy resources in microgrids. *Applied energy*, 210:827–841, 2018.

[196] S. Bolognani and S. Zampieri. On the existence and linear approximation of the power flow solution in power distribution networks. *IEEE Transactions on Power Systems*, 31(1):163–172, 2015.

[197] EPRI. Opendss: EPRI distribution system simulator. https://sourceforge.net/projects/electricdss/, 2017.

[198] G. Strang. *Introduction to Linear Algebra*. Wellesley-Cambridge Press, 5th edition, 2016.